Università degli Studi di Milano
Scuola di Dottorato di Ricerca in Scienze Biochimiche, Nutrizionali e Metaboliche
Direttore: Prof. Sandro Sonnino

Dottorato di Ricerca in Scienze Biochimiche
Coordinatore: Prof. Francesco Bonomi

Biochemical studies of human MICAL1, the flavoenzyme controlling cytoskeleton dynamics

TERESA VITALI
1205
TUTOR: Prof. Maria Antonietta Vanoni

Anno accademico 2015/2016

Index

Abstract

MICAL from the "Molecule Interacting with CasL" indicates a family of cytoplasmic multidomain proteins conserved from insects to humans, which participates in the control of cytoskeleton dynamics. A unique feature of MICAL proteins is the presence of a catalytic N-terminal flavoprotein monoonoxygenase-like (MO) domain that is followed by several protein interaction domains, namely: a calponin homology (CH) domain, a LIM domain and a C-terminal region containing potential coiled-coil motifs.

In neurons MICAL1 is an essential component for the transduction of the semaphorin signaling downstream of plexin by catalyzing a NADPH-dependent F-actin depolymerization through the N-terminal flavoprotein domain. But it may also control integrin pathway and microtubules assembly through interaction with CasL and CRMP, respectively and apoptosis through interaction with NDR1. The MICAL2 and MICAL3 isoforms are implicated in vesicles trafficking and gene transcription.

The aim of this project is to contribute to define the function of human MICAL1 by characterizing the catalytic properties of the MO domain and how they are modulated by its CH, LIM and C-terminal domains and, eventually, by its interacting proteins.

The human MICAL1 form containing the isolated MO domain (55.1 kDa; pI 9) and the form comprising both the MO and the CH domains (MOCH; 68.5 kDa; pI 7.7) have been produced according to the procedures available in the laboratory, which were further optimized. The full-length MICAL1 (MICAL; 119 kDa; pI, 6.2) and the form lacking the C-terminal region (MOCHLIM; 86.4 kDa; pI, 6.7) were produced in *E.coli* cells and their purification protocols were set-up exploiting the engineered C-terminal His_6-tag. All the purified MICAL forms are stable and greater than 95% homogeneous.

MICAL forms are isolated with the correct complement of FAD bound to the MO domain and zinc ions bound to the LIM domain, which predicts the formation of two zinc fingers. The absorption spectra of all MICAL forms are similar to each other, with an extinction coefficient at 458 nm of ≈8.1 $mM^{-1}cm^{-1}$ similar to that previously determined for the isolated MO domain, indicating that the CH, LIM and C-terminal regions do not alter the conformation of the catalytic domain. However, the LIM domain causes MOCHLIM to oligomerize to yield dimers, trimers and higher order aggregates, while the full-length protein yielded stable dimers as opposed to the monomeric state of MO and MOCH forms.

All MICAL forms catalyze a NADPH oxidase (H_2O_2-producing) activity, which is associated with the MO domain. By combining steady-state kinetic measurements of the reaction as a function of pH and of solvent viscosity we concluded that the CH, LIM and C-terminal domains lead to a progressive lowering of the catalytic efficiency (MO, ≈165 $s^{-1}mM^{-1}$; MOCH, ≈18.5 $s^{-1}mM^{-1}$; MOCHLIM, ≈15 $s^{-1}mM^{-1}$; MICAL, ≈0.75 $s^{-1}mM^{-1}$) of the reaction due to an increase of K_m for NADPH from ≈20 μM (MO), to ≈130 μM (MOCH), ≈230 μM (MOCHLIM) and ≈370 μM (MICAL). The 200-fold drop of the catalytic efficiency of the full-length MICAL compared to that of MO is also due to a ≈10-fold decrease of k_{cat}. The study of the pH and viscosity dependence of the NADPH oxidase reaction of MICAL forms led us to conclude that the observed changes in the values of the kinetic parameters are not due to changes in rate determining steps of the reaction taking place within MO. The increase of K_{NADPH} correlates with a decrease of the positive charge of the protein due to the acidity of the CH, LIM and C-terminal domains. The 10-fold drop of k_{cat} observed with full-length MICAL is consistent with the proposal of an autoinhibitory role of the C-terminal region on MICAL catalytic activity. Our experiments reveal that is likely due to a conformational equilibrium between an inactive and an active conformation of MICAL, which is shifted 9:1 toward the inactive conformation in solution. The position of the C-terminal region is crucial to make the protein fully inactive .

All MICAL forms are able to depolymerize F-actin in the presence of NADPH as observed by monitoring the decrease of fluorescence of pyrenyl-actin and of the average radius of F-actin solution by dynamic light scattering. F-actin leads to an approximately 5-10-fold increase of the maximum rate of the NADPH consumption for all MICAL forms (MO, 20 s^{-1}; MOCH, 26 s^{-1}; MOCHLIM, 15 s^{-1}; MICAL, 8 s^{-1}) compared to that measured in its absence. The presence of F-actin leads to a lowering of the K_m for NADPH to similar values (11-50 μM) for all the four forms. The apparent K_m for F-actin is similar (≈4 μM) for MO, MOCH and MOCHLIM, but 10-fold higher for MICAL (≈30 μM). Also this effect can be

explained by the conformational equilibrium between an inactive and an active conformation of the full-length MICAL. The actin binding site on the MO domain may be physically accessible to F-actin only when MICAL is in the active conformation, subtracting it from the inactive/active conformational equilibrium. In this case, the high apparent K_m for actin of MICAL would reflect the coupled equilibria between inactive/active conformations and complex formation between actin and MICAL in the active conformation.

In all cases, the amount of NADPH oxidized during the reaction exceeds that of total actin present, suggesting a case of substrate recycling or an enhancement of the NADPH oxidase activity of MICAL forms when actin is bound. This finding is in contrast with the proposal that MICAL forms catalyze a (slow) NADPH oxidase activity when isolated but a fast and specific hydroxylation of actin Met44 (and Met 47) in the presence of F-actin, which leads to filament depolymerization (Hung et al. (2013) Nat Cell Biol., 15, 1445-1454). Mass spectrometry analyses of actin samples treated with MICAL forms and NADPH support the hypothesis that actin depolymerization is mediated by the H_2O_2 released by the enhanced NADPH oxidase activity of MICAL in complex with actin. A maximum of two residues are oxidized per actin molecule among which are Met44 and Met47 but also several other Met and Trp residues are oxidized with similar probability.

Overall it appears that MICAL in the free state can catalyze a basal NADPH oxidase reaction even in the cell. This activity is enhanced when the fraction of MICAL in the catalytically active state binds to actin leading to its depolymerization. Interaction of MICAL C-terminus with the cytoplasmic side of plexin upon semaphorin signaling would shift the equilibrium of inactive/active conformations toward the active form favoring the interaction with actin in proximity of plexin and its local depolymerization.

With purified MICAL forms now available, it will possible to identify its interactors and to study their effect on its activities. As a first step in this direction we produced and purified a CRMP1 form that was found to cooperate with MICAL1 in determining COS7 cells collapse in response to semaphorin signaling. We demonstrated that CRMP1 and MICAL1 MO and MOCH interact, but in a complex way: at low ionic strength the interaction, which is largely non specific due to the strong opposite charges of the proteins, leads to inhibition of the MO and MOCH NADPH oxidase activity; at higher ionic strength, where non specific interactions are removed, CRMP stimulates the NADPH oxidase activity of MO and MOCH and competes with actin for binding MICAL, but the effect is mild.

These preliminary experiments support the hypothesis that actin and microtubules dynamics may be linked through MICAL-CRMP interaction. More importantly, they show the feasibility of detailed *in vitro* studies for the identification of MICAL interacting proteins and their mutual modulatory effect. This approach, along with the detailed mechanistic studies of MICAL reactions thanks to the availability of various MICAL forms, will also open the way to the identification of molecules able to inhibit MICAL that could be beneficial to combat diseases in which MICAL has been implicated such as neurodegeneration, cancer and even vasculo- and cardiogenesis.

Abbreviations

2-ME, 2-mercaptoethanol; BrPAPS, 2-(5-bromo-2-pyridiylazo)-5-[N-n-propyl-N-(3-sulfopropyl)amino]phenol; ABP, actin binding protein; CasL, Crk (p38)-associated substrate-related protein; CH, calponine homology; Cc, critical concentration; CRMP, collapsin response mediator protein; DLS, dynamic light scattering; D-MICAL, *Drosophila melanogaster* MICAL; DTT, dithiothreitol; FAD, flavin adenine dinucleotide; FMN, flavin mononucleotide; F-actin, filamentous actin; G-actin, globular actin; HEPES, (4-(2-hydroxyethyl)-1-piperazine ethanesulfonic acid; LIM, domain found in Lin11, Isl-1 and Mec-3 proteins; MALDI-TOF, matrix-assisted laser desorption ionization - time of flight mass spectrometry; MICAL, the molecule interacting with CasL; MO, monooxygenase domain; MOCH, truncated MICAL form comprising the MO and CH domains; MOCHLIM, truncated MICAL form comprising the MO, CH and LIM domains; MRTF-A, myocardin-related transcription factor-A; MS, mass spectrometry; MST1, mammalian Ste-20-like kinase; NADPH, nicotinamide adenine dinucleotide phosphate; NDR, nuclear Dbf2-related kinases; PHBH, p-hydroxybenzoate hydroxylase; PMSF, phenylmethanesulfonyl fluoride; PVDF, polyvinylidene difluoride; Rab, Ras-related protein Rab; SDS, sodium dodecyl sulfate; SRF, serum response factor; TCA, trichloroacetic acid.

1. Introduction

MICAL1 is a member of a family of cytoplasmic multidomain proteins conserved from insect to human, which participate in the control of cytoskeleton dynamics in a variety of fundamental cellular processes, such cell migration and differentiation, cell-cell contacts, vesicle trafficking and axon growth (Hung et al., 2011; Zhou et al., 2011; Vanoni et al., 2012). Three MICAL proteins have been identified in mammals, MICAL1-3; while in drosophila only a single gene has been identified encoding MICAL (Terman et al., 2002).

A common and unique feature of MICAL proteins is the presence of a putative N-terminal catalytic flavoprotein domain that is followed by several protein-protein interactions domains, namely: a calponin homology (CH) domain, a LIM domain, a Pro-rich and coiled-coil regions (Figure 1.1). The position of such domains and the length of the interdomain regions differ for MICAL1, MICAL2 and MICAL3 (Figure 1.1; see Chapter 2).

MICAL1 and MICAL3 are ubiquitously expressed in the nervous system, while MICAL2 expression showed greater spatio-temporal selectively (Pasterkamp et al., 2006). MICAL proteins are also expressed in the heart, lung, kidney, liver, thymus, muscles, bone marrow and brain (Ashida et al., 2006; Fischer et al., 2005; Suzuki et al., 2002; Xue et al., 2011). MICAL1-3 mainly localize to the cytosol and a small fraction is associated with plasma membrane.

In mammals two proteins related to MICAL have been identified. They show sequence similarity with MICAL1-3, but they lack the N-terminal flavoprotein domain, leading to define them as MICAL-like1 and MICAL-like2 (Sharma et al., 2010). They are encoded by different genes and they are also conserved from insects to humans. MICAL-like1 has been identified as a EHD1 (protein-binding EH domain 1) interactor through the NPF (asparagine-proline-phenylanine) motif. EDH1 is responsible for receptor recycling during endocytosis. MICAL-like1 and EDH1 colocalize at the membrane of the endoplasmic reticulum (ER). Their interaction is necessary for the traslocation of EDH1 to ER and therefore, to promote endocytosis of the receptors (Rahaieng et al., 2010). MICAL-like1 is also an effector of Rab8 (Ras-related protein Rab-8A) protein that mediates vesicles secretion from the Golgi to the plasma membrane (Rahajeng et al., 2010). MICAL-like2 protein is also involved in vescicular trafficking as an effector of Rab13 (Ras-related protein Rab13 precursor) (Yamamura et al., 2008). MICAL-like2 lacks the NPF motif and the interaction with Rab13 takes place at its C-terminus resulting in the colocalization of the proteins near the perinuclear membrane and at cellular tight junctions. MICAL-like2 can also interact with E-cadeherin promoting its recycling (Yamamura et al., 2008).

The biological roles of MICAL proteins has been studied by using genetic and cell biology approaches, but a solid knowledge of their mechanism of action is still missing.

In the effort to fill this void, in this work we shall present the characterization of the catalytic properties of the N-terminal flavoprotein domain of human MICAL1 and how there are modulated by the CH and LIM domains and the C-terminal region, as an extension of the work previously done (Zucchini et al., 2011).

Each chapter is introduced by a survey of the relevant literature to complement the present introduction (Chapter 1) and is followed by a brief discussion. The overall discussion of our results and the conclusions are in Chapter 9. The Materials and Methods employed are gathered in Chapter 10.

More specifically:

Chapter 2: deals with the comparison of MICAL and MICAL-like proteins and the analysis of the three-dimensional structure of the N-terminal flavoprotein domain of mouse MICAL1, which allowed us to (i) plan the protein engineering experiments for the production of the full-length protein and of the truncated forms lacking the LIM domain (MOCH) and the C-terminal region (MOCHLIM); (ii) gain insight on the mechanism of action of MICAL and highlight potentially key residues.

Chapter 3: describes the engineering of the full-length human MICAL1 and the form lacking the C-terminal region for the expression of C-terminal His_6-tagged proteins in *E.coli* cells to facilitate their purification.

Chapter 4: focus on the set-up and optimization of the purification procedures to obtain soluble and homogeneous preparations of MICAL forms in quantities sufficient for their characterization.

Chapter 5: reports on the structural analysis of MICAL forms by determining (i) the N-terminal sequence; (ii) the mass of the intact proteins; (iii) the amounts of FAD and zinc ions associated to the N-terminal flavoprotein domain and to the LIM domain, respectively and (iv) the stability of the proteins preparations.

Chapter 6: the studies of the NADPH oxidase activity of MICAL forms under steady-state conditions to determine the effect of (i) the CH, LIM and C-terminal domains; (ii) the ionic strength, (iii) the pH and (iv) the solvent viscosity on the kinetic parameters (k_{cat}, K_{NADPH} and k_{cat}/K_{NADPH}) of the catalyzed reaction by MICAL forms.

Chapter 7: deals with the studies of the NADPH-dependent F-actin depolymerizing activity of MICAL forms by determine (i) steady-steady kinetic parameters (k_{cat}, K_{NADPH} and apparent K_m for F-actin); (ii) the intact mass of actin treated with MICAL and NADPH; and (iii) the modified actin residues by mass spectrometry.

Chapter 8: the expression and purification of mouse CRMP1 forms, which has been proposed to be an interactor and even a possible substrate of the N-terminal flavoprotein domain of MICAL1 (Schmidt et al., 2008). The mouse CRMP1 form comprising residues 8-525 was purified in quantities sufficient to (i) study its interaction with MO and MOCH forms of MICAL and (ii) its effect on their NADPH oxidase activity under various conditions.

1.1. MICAL1 as a CasL interactor

MICAL1 protein was initially identified during the search of CasL (from Crk p38-associated substrate-related protein) interactors among proteins expressed from a thymus cDNA library, from which the acronym Molecule Interacting with CasL was derived (Suzuki et al., 2002). CasL, also known as hEF1 (enhancer of filamentation 1) and NEDD9 (neural precursor expressed developmentally down-regulated protein 9), is a docking protein of the Cas family of proteins, and plays important roles in several cellular

functions, such as interleukin-2 production and cellular migration by leading to the formation of focal cell adhesion (Suzuki et al., 2002). MICAL1 was proposed to bind the SH3 domain of CasL through its Pro-rich region, as demonstrated by co-localization and co-immunoprecipitation experiments (Suzuki et al., 2002). Using same methods Suzuki et al., (2002) also demonstrated that the C-terminal region of MICAL1 can interact with vimentin, which is the main component of intermediate filaments of the cytoskeleton (Suzuki et al., 2002). Therefore, it was proposed that MICAL1 participates in the cascade of events that follow β1 integrin and/or T cell receptor stimulation by interacting with CasL, providing a physical link with cytoskeleton proteins (Suzuki et al., 2002; Vanoni et al., 2012).

1.2. MICAL in the context of axon growth

At about the same time MICAL was also found among the intracellular components of the semaphorin-plexin pathway as a novel PlexA interactor in an embryonic Drosophila cDNA library (Terman et al., 2002). Upon the discovery of MICAL several genetic and cellular biology studies have been made to identify the role of MICALs in cells. A great deal of work was done with Drosophila to elucidate MICAL function in the semaphorin-plexin signaling pathway in the context of axon growth (Terman et al., 2002). The semaphorin signaling pathway leads to a reorganization of the cytoskeleton. During neuronal development, the axon receives a multitude of extracellular signals that guide the directionality of its growth (Figure 1.2) (Schmidt et al., 2009).

Among the molecules responsible for axon guidance, are the semaphorins. Semaphorins function as axonal repellents, but they are also involved in other important cellular events such as morphogenesis and organ homeostasis. They also mediate the release of cytokines. Semaphorins are implicated in different neurodegenerative diseases and cancer (Tamagnone et al., 2004). Seven classes of semaphorins have been identified, comprising soluble and membrane proteins and they are highly conserved from insects to humans. Their conserved N-terminal domain is responsible for the interaction with their plexin receptors. The functional role of the semaphorins has been extensively studied using Drosophila as model organism. The interaction between Sema3A and PlexA leads to axon cone growth collapse (Pasterkamp and Kolodkin 2003). Drosophila mutants obtained by inactivation of the single MICAL gene showed a phenotype similar to that observed by inactivation of Sema3A (Figure 1.3; Terman et al., 2002). The same phenotype was also observed by introducing the drastic G-to-W substitution in the consensus sequence for FAD-binding in the N-terminal domain of MICAL, indicating that the flavoprotein domain is essential for MICAL function (Terman et al., 2002). The introduction of point mutations in the Drosophila MICAL gene also caused alterations of myofilaments organization and synaptic structure (Beuchle et al., 2007; Figures 1.4 and 1.5).

MICALs participate also in the Sox14-regulated dendritic pruning (Kirilly et al., 2009). In this context, Sox14 transcription factor is essential for dendritric pruning by promoting MICAL expression (Kirilly et al., 2009). These observations confirm the role of MICAL in neuronal regulation.

1.3. MICAL and actin cytoskeleton organization

The importance of the catalytic domain for MICAL function was also demonstrated in mammalian neuronal and non-neuronal cells (Giridharan et al., 2012).

Overexpression and siRNA-mediated knock down of MICAL1-3 in mammalian cells had a significant impact on the organization of actin filaments (Giridharan et al., 2012). Changes on the organization of actin filaments to yield filopodia-like protusions were observed when MICAL2 was overexpressed, while no changes were observed upon overexpression of MICAL1 and MICAL3 (Giridharan et al., 2012). Instead, when HeLa cells were transfected with the isolated N-terminal flavoprotein domain of MICAL1 and MICAL3, the number of actin filaments was reduced (Giridharan et al., 2012). In addition, the isolated N-terminal domain of MICAL1 affected also the organization of microtubules (Giridharan et al., 2012), probably in an indirect way as demonstrated by the fact the Drosophila MICAL was not able to directly interact *in vitro* with microtubules (Hung et al., 2011). On the other hand, depletion of MICAL1 and MICAL2 led to an increase of filopodia-like protusions at the cell periphery, while depletion of MICAL3 caused an increase of stress fibers and cell size (Giridharan et al., 2012). MICAL2 localizes to plasma membrane in HeLa cells and its overexpression correlated with the loss of actin stress fibers as well as actin in filopodia-like structures at the cell periphery (Giridharan et al., 2012). The same cell phenotype was observed when the isolated N-terminal catalytic domain of MICAL2 was overexpressed, indicating that the flavoprotein domain of MICAL2 is required and sufficient for actin stress fiber loss (Giridharan et al., 2012).

MICAL3 has been found among Rab8A (Ras-related protein Rab-8A) interactors (Grigoriev et al., 2011). Rab8A protein is involved in the vesicles trafficking from the trans-Golgi to plasma membrane. Rab8A is associated with exocytotic vesicles by interacting with Rab6 (Ras-related protein Rab6-A) protein. Rab8A forms a complex with MICAL3 through the C-terminal region of MICAL. Other residues in such region mediate also the interaction with ELK (ETS domain-containing protein ELK-1) protein, which is important for the docking and fusion of exocytotic vesicles (Grigoriev et al., 2011). Rab8A-ELK-MICAL3 proteins can form a triple complex in transfected HeLa cells, in which the interaction between Rab8A and ELK is more efficient when MICAL3 is present (Grigoriev et al., 2012). These results indicate a functional role of MICAL3 in the trafficking of vesicles. Moreover, as observed for MICAL1 and MICAL2, the N-terminal flavoprotein domain of MICAL3 is essential for its function. The substitution of G to W in the consensus sequence for FAD binding led to an increase of the number of secretory vesicles in the cytosol that failed to fuse with the plasma membrane (Grigoriev et al., 2011). As discussed above, MICAL-like proteins are also involved in vesicle trafficking, but they do not have any enzymatic activity and they exert their function through protein-proteins interactions (Sharma et al., 2011).

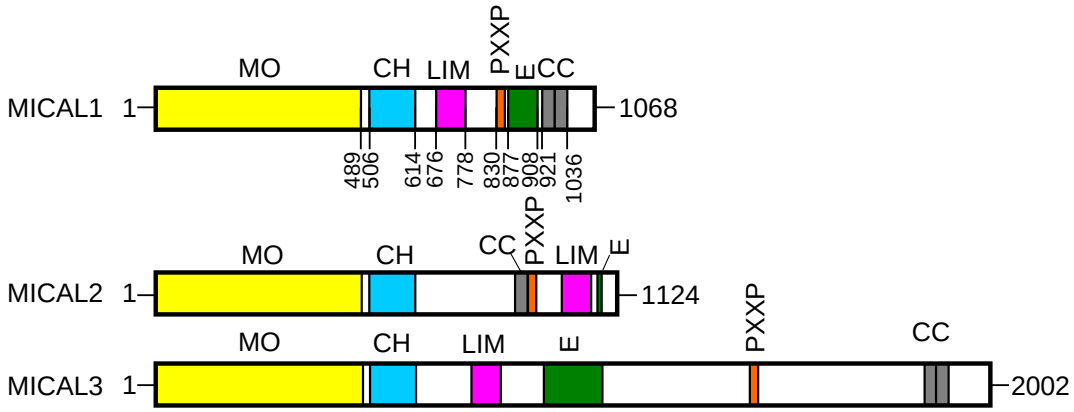

Figure 1.1. Domain organization of MICAL forms. The boundaries of the monooxygenase-like (MO), calponin homology (CH) and LIM domains, Pro- and Glu-rich region and coiled coil region are referred to the human forms.

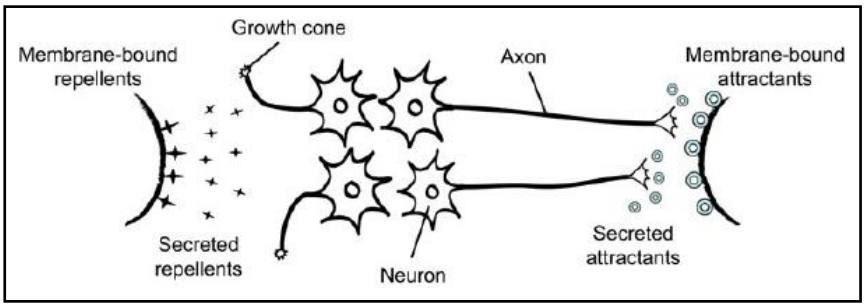

Figure 1.2. Axon guidance. During neuronal development the direction of axon extension is guided by attractive and/or repulsive signals (Zhou et al., 2010).

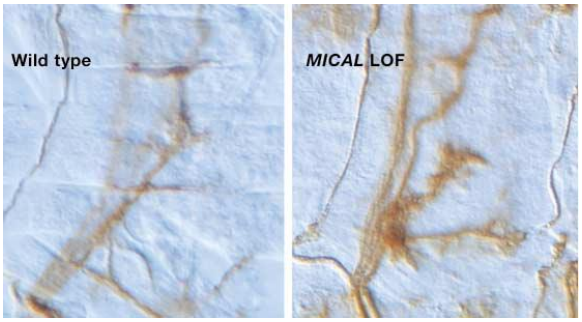

Figure 1.3. Role of MICAL during neuronal development. Development of wild-type Drosophila neurons and mutant loss of function for MICAL (MICAL LOF), in which the control of axons growth is lost (Termann et al., 2002).

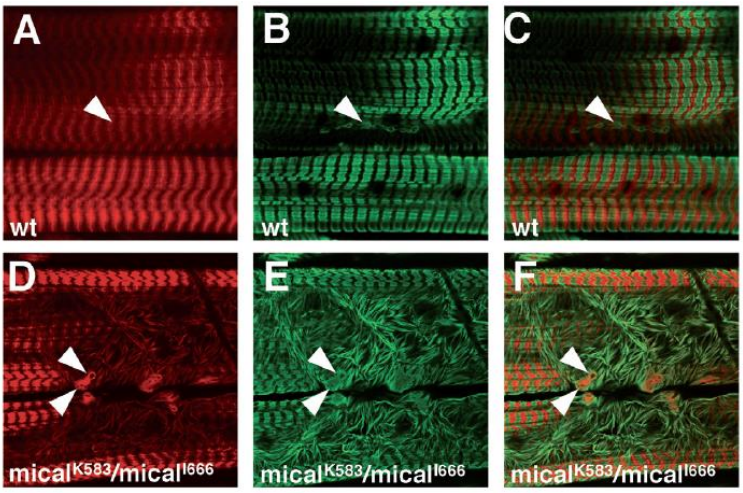

Figure 1.4. Role of MICAL in the organization of actin filaments in Drosophila muscle cells. Confocal images of wild type muscle cells (panels A-C) and of MICAL mutants (panels D-F). The larvas were stained with phalloidin-Cy3 (red) for the visualization of actin and anti-MHC (green) for myosin. The arrowheads indicate the synaptic boutons.

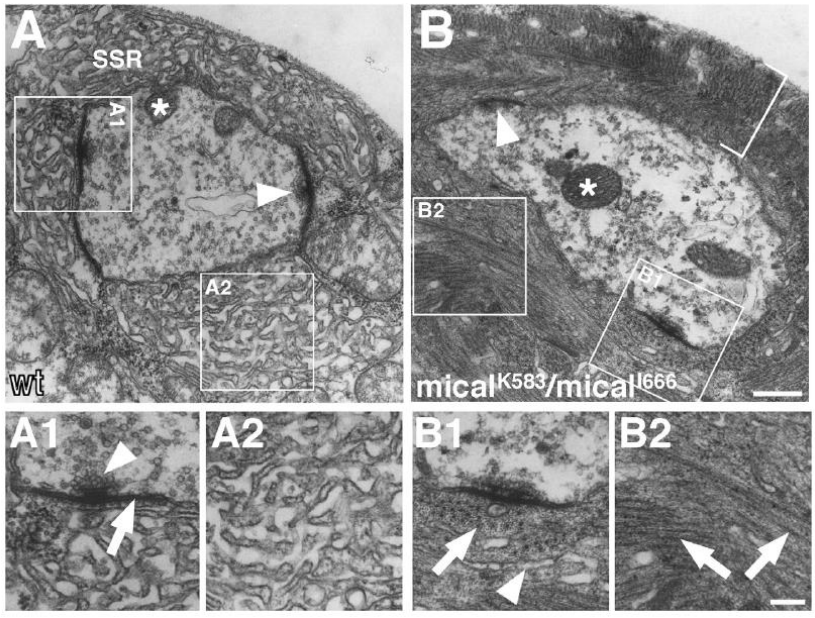

Figure 1.5. Organization of postsynaptic ultrastructures in Drosophila MICAL mutants. Electron micrographs depicting a cross-section through synaptic boutons on muscle 6 in a wild-type (A) and MICAL mutant larva (B). Active zones (arrowhead), mitochondria (asterisk) and the subsynaptic reticulum (SSR) are marked. Panels A1 and B1: zone containing electron-dense membrane thickenings (arrow) and synaptic vesicles attached to a T-bar (arrowhead). Panels A2 and B2: Enlargement of the postsynaptic area consisting of multiply folded membranes of the SSR (Beuchle et al., 2007).

1.4. MICAL and apoptosis

MICAL1 participates also in other cellular processes besides axon cone growth. In fact, it has been demonstrated that MICAL1 is involved in apoptosis by interacting with NDR (nuclear Dbf2-related) kinases (Zhou et al., 2011). NDR kinase is involved in cell proliferation, mitosis and apoptosis in response to several signalling pathways. Deletion of NDR in mouse T cells caused an unregulated cells apoptosis with consequent lymphoma development in mice (Cornils et al., 2010). NDR is activated upon phosphorylation of Thr444 by MST1 kinase (mammalian Ste-20-like kinase 1) in response to cell death receptor stimulation. MST1 binds the C-terminal region of NDR1 and at the same region takes place the interaction with MICAL1 (Zhou et al., 2011). In this case, MICAL functions as a scaffold protein by interacting with NDR through its region spanning from the LIM domain to the C-terminus. Thus, MICAL1 sequesters NDR preventing its interaction with MST1 and therefore, its phosphorylation. As a result cell apoptosis is inhibited (Zhou et al., 2011).

1.5. Hypotheses on MICAL mechanism of action

From the data obtained by genetic, molecular and cellular biology studies, several hypotheses on MICAL mechanism of action have been made (Terman et al., 2002).

Several proteins have been identified as MICAL interactors, namely: GTPases, GTPase-activating proteins, GTP-binding proteins (Weide et al., 2003), CasL (Suzuki et al., 2002), CRMP (Schmidt et al., 2008) and NDR (Zhou et al., 2011) (Figure 1.6). These observations led to propose that MICAL simply acts as a scaffold protein through its conserved protein-protein interaction domains to recruit and/or modulate the activity of interactors (Figure 1.7) (REF). This hypothesis can explain the way in which MICAL1 interferes with CasL, CRMP and NDR functions.

The scaffold model can also be applied to MICAL-like proteins that lack the catalytic domain and thus exert their functions through their protein-protein interaction domains (Sharma et al., 2011).

However, several of such studies also demonstrated the essentiality of the N-terminal flavoprotein domain of MICAL for its role in the control of the cytoskeleton dynamics leading to other hypotheses on its mechanism of action.

In 2005 the three-dimensional structure of the isolated flavoprotein domain of mouse MICAL1 has been solved (Nadella et al., 2005; Siebold et al., 2005; Chapter 2) confirming the similarity of the N-terminal domain to p-hydroxybenzoate hydroxylase (PHBH), which is the prototype of the FAD-dependent monooxygenases class of flavoproteins that catalyze the hydroxylation of aromatic compounds. The structure of the flavoprotein domain also suggested that its substrate could be an acidic protein, such as actin. On the basis of the similarity with flavoproteins of the monooxygenase class, the N-terminal domain of MICAL will be indicated as MO without actually implying that it catalyzes an hydroxylation reaction (see Chapter 6 and 7 for further discussion).

In this respect, several experiments have been carried out with the N-terminal domain of Drosophila, MICAL and with the forms comprising also the CH domain (MOCH), with the MO domain of mouse MICAL2 (Palfey et al., 2012), MOCH form of mouse MICAL1-2 (Lee et al., 2013) and with the isolated

MO domain of human MICAL1 (Zucchini et al., 2011). As will be described in Chapter 7, MICAL forms are able to catalyze a NADPH-dependent F-actin depolymerizing activity supporting this hypothesis.

The similarity of N-terminal domain to flavoproteins of the oxidase and monooxygenase classes led to the proposal that MICAL may catalyze: (i) an oxidase activity on a small molecule coupled to production of H_2O_2; (ii) an oxidase or monooxygenase activity on the side chain of its protein-substrate and (iii) a NAD(P)H oxidase activity with the production of H_2O_2 as a signaling molecule for the activation of the downstream events (Terman et al., 2002; Nadella et al., 2005; Vanoni et al., 2012; Figure 1.7).

1.6. Regulation of MICAL1 activity

In the context of actin depolymerization, it has been proposed that MICAL1 would become active only upon its interaction with plexin in response to semaphorin signal (Figure 1.8). In support of this hypothesis are the experiments carried out in COS7 and HeLa cells (Schmidt et al., 2008; Giridharan et al., 2012). The H_2O_2 produced by MICAL in the presence of NADPH was significantly reduced in the total cell extracts of COS7 cells expressing the full-length MICAL1 compared to that observed in extracts of cells transfected with truncated forms of MICAL1 (Schimdt et al., 2008; Chapter 8).

This observation led to the proposal of an inhibitory role of the C-terminal domain of MICAL1 on the activity of the MO domain (Schmidt et al., 2008).

The C-terminal domain of MICAL2 seems to have no effect on the activity of the enzyme, as deduced indirectly from the analysis of the amount of actin stress fibers, which was similar to that observed in HeLa cells expressing the truncated forms of MICAL2 comprising the MO, CH and LIM domains (Giridharan et al., 2012). The generation of chimera MICAL1-MICAL2 (composed by the MO, CH domains of MICAL1 and the C-terminal LIM domain of MICAL2) and MICAL2-MICAL1 (composed by the MO and CH domains of MICAL2 and the LIM and C-terminal domain of MICAL1) proteins, revealed that the C-terminal domain of MICAL1 was also able to interact with the MO domain of MICAL2 reducing its activity as deduced from the absence of changes on the organization of actin filaments in HeLa cells (Figure 1. 9, panels B-G; Giridharan et al., 2012). Thus, it has been proposed that the C-terminal region of MICAL1 has an autoinhibitory function to maintain MICAL in a inactive form until it binds to plexin in response to semaphorin/plexin complex formation (Figure 1.8) (Schmidt et al., 2008; Giridharan et al., 2012).

However, these experiments were limited to the analysis of the effect of human MICAL1-2 forms on the cytoskeleton (actin) organization on cells (Giridharan et al., 2012) or measuring the H_2O_2 produced in lysates of cells expressing truncated and full-length mouse MICAL1 (Schmidt et al., 2008) in a semi-quantitative way. Thus, the precise molecular mechanism by which the C-terminal domain controls the activity of the N-terminal flavoprotein domain is still missing. In this respect, the expression and purification of full-length human MICAL1, which will be described in Chapter 4, has allowed us to carry out *in vitro* experiments with the isolated protein to better understand how the C-terminal region modulates the activities of the N-terminal monooxygenase like domain (Chapters 6 and 7).

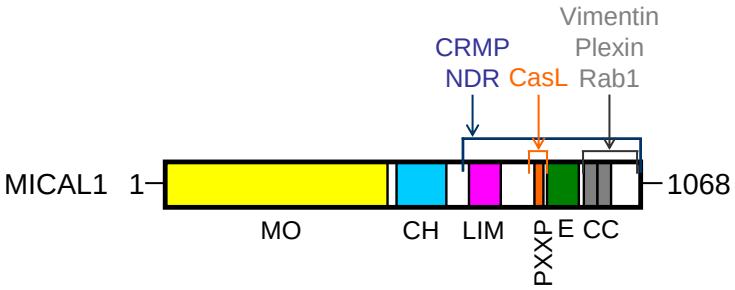

Figure 1.6. Schematic representation of the domain organization of human MICAL1 with regions responsible for the binding with interactor proteins are indicated. (The colour scheme is the same as that used in Figure 1.1).

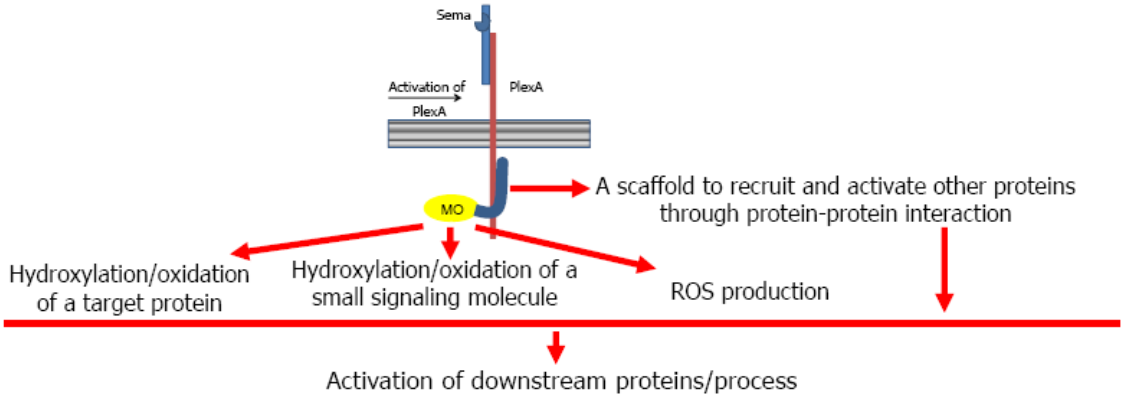

Figure 1.7. Possible mechanisms of MICAL1 function. Schematic representation of the possible mechanism of MICAL1 action upon its activation by interacting with plexin receptor in response to semaphorin signaling (the scheme is based on Kolodkin et al., 2007; Vanoni et al., 2012).

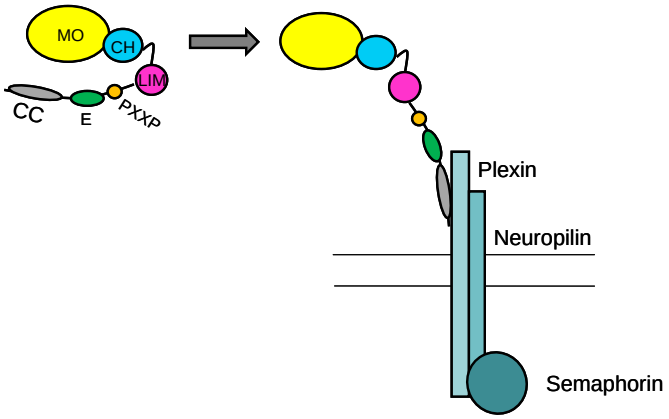

Figure 1.8. Proposed mechanism of activation of MICAL1. Schematic representations of :the possible mechanism of MICAL1 activation upon its interaction with the plexin receptor in response to semaphorin signaling (the domain colour code is the same as that used in Figure 1.1).

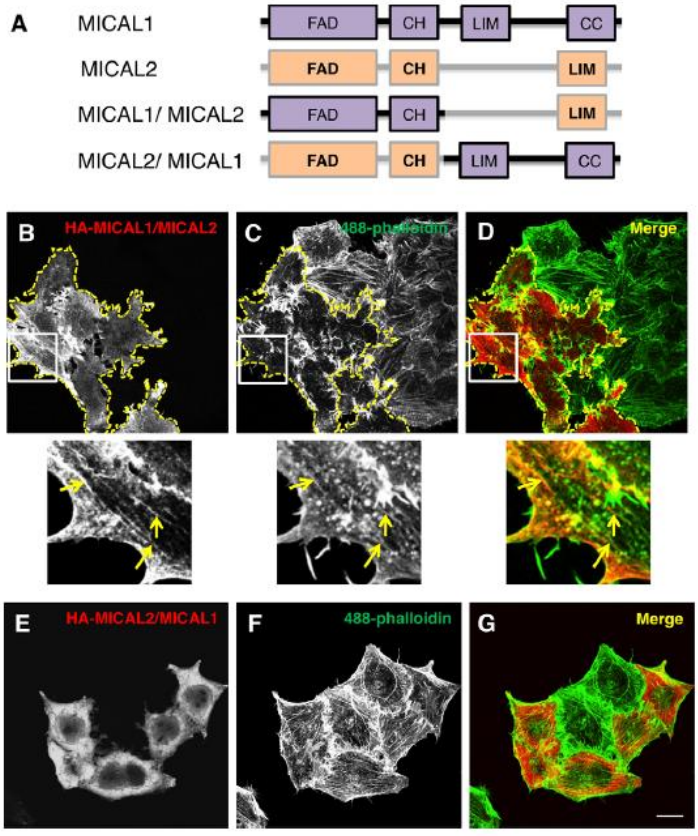

Figure 1.9. Inhibitory function of the C-terminal region of human MICAL1. Panel A: The domain organization of wild-type human MICAL1 and -2 and chimeras HA-MICAL1-MICAL2, HA-MICAL2-MICAL1 is shown. HeLa cells have been transiently trasfected with chimeric MICAL1-MICAL2 (panels B-D) and MICAL2-MICAL1 (panels E-G) forms. Cells were fixed 18 h after the transfection and incubated with anti-HA antibody (panels B and E) to localize MICAL forms, followed by incubation with phalloidin conjugated antibody (panels C and F) for actin detection. Panels D and G show the merge of the images of panels B-C and E-F, respectively. Insets and arrows show partial colocalization of the MICAL1–MICAL2 chimera with actin stress fibers. Scale bar: 10 μm. (Giridaran et al., 2012).

1.7. MICAL and disease

The mechanisms controlling cytoskeleton dynamics are far from being completely understood. In this context, understanding the molecular details of semaphorin-plexin pathway is of interest to modulate their action in pathological conditions, such as in neurodegenerative diseases, in cell mestatization and angiogenesis in cancer, pathogen infection (Vanoni et al., 2012 REF). Several observations on MICAL expression and function support its biomedical relevance. Inhibition of semaphorins seemed to prevent early events occurring in neurodegenerative diseases, like amyotrophic lateral sclerosis (ALS) and to promote axon regeneration (Kikushi et al., 2003; Kaneko et al., 2006; Schmidt et al., 2009). In rat models of spinal cord injuries, the expression levels of MICAL forms are increased (Pasterkamp et al., 2005), supporting the hypothesis that inhibition of MICAL activity would have the same effect as that observed for semaphorins inhibition. Overexpression of alternative splicing variants of MICAL2 is associated with particular aggressive prostate cancers forms (Ashida et al., 2006). The cancer cells growth was lowered by decreasing the expression level of MICAL2 variants with small RNA interfering technology (Ashida et al., 2006). Recently, MICAL proteins have been also related to melanoma cancer (Loria et al., 2015). Moreover, studies carried out using zebrafish as model organism demonstrated the role of MICALs during cardiovascular development (Xue et al., 2012). Thus, determining MICAL mechanism of action can provide information for the understanding of the semaphorin pathway as well as a way to interfere and regulate with such fundamental cellular process.

2. Sequence and structural analyses of MICAL proteins.

2.1. Primary structure of MICALs

MICAL proteins are conserved from insect to humans. Insects contain a single gene encoding MICAL. In Drosophila there are three MICAL isoforms, the so called long, medium and short variants, originated by alternative splicing (Termann et al 2002). Three different genes encoding MICAL have been found in the model organism zebrafish (*Danio Rerio*) (Xue et al., 2011). Also in mammals three MICAL proteins, MICAL1, MICAL2 and MICAL3, have been identified and they are encoded by three different genes (Termann et al., 2002); several splicing variants have been predicted (Friedburg et at., 2008) (Table 2.1 A).

As part of our studies of MICAL1, a comparative analysis of MICAL's primary structures was carried out. MICAL1-3 proteins are related to each other. Analysis of their primary structure led to identify several domains, namely: a FAD-containing domain, a calponin homology (CH) domain, a LIM (from the three gene products Lin-11, Isl-1 and Mec-3) domain and Coiled-Coil motifs. The position of the FAD-containing and CH domains is conserved at the N-terminus in the three MICAL forms. Instead, the position of the LIM domain and of the Coiled-Coil regions, as well as the presence of additional conserved regions distinguish MICAL1 from MICAL2 and MICAL3.

The primary structures of representative MICAL forms are shown in Figure 2.1 (Vanoni et al., 2012). The sequence analyses and annotations have been done also on the basis of information deriving from structural studies (Nadella et al., 2005; Siebold et al., 2005; Sun et al., 2006). In the text and in Figure 2.1 the residue numbering is given for mouse MICAL1, for which high resolution structural models are available (Nadella et al., 2005; Siebold et al., 2005).

The N-terminal region (residues 1-498) of MICALs showed sequence similarity to FAD-containing aromatic hydroxylase, of which p-hydroxybenzoate hydroxylase (PHBH) is the prototype (Entsch et al., 2005; McDonald and Palfey 2010). This hypothesis was confirmed by the determination of the three-dimensional structure of the isolated N-terminal domain of mouse MICAL1 (Nadella et al., 2005; Siebold et al., 2005).

The first ≈80 residues of the N-terminal domain form a subdomain, which has not counterpart in PHBH and contains several conserved basic residues (bold and highlighted in blue in Figure 2.1, panel A). Regions matching the consensus sequence for the formation of a Rossman fold (Wierenga et al., 1986) for FAD binding and the so called "second FAD binding region" identified by Eggink et al. (Eggink et al., 1990) are also conserved in all MICALs (residues in bold and highlighted in yellow in Figure 2.1, panel A), as are the residues important for NADPH binding (Wang et al., 2002; Siebold et al., 2005; in red and bold in Figure 2.1, panel A). Instead, other residues are conserved only within each MICAL1-3 class and can be used for their classification of MICAL proteins. In the N-terminal domain of Drosophila MICAL an additional 40 residue segment precedes such region, but it is not conserved among insect MICALs (Figure 8.1, panel A).

The calponin homology (CH) domain (residues 509-614) follows the flavoprotein domain. MICALs contain a type 2 CH domain (see below) based on sequence and structural analyses (Sun et al., 2006). In Figure 2.1 the underlined sequence corresponds to the conserved hydrophobic residues that form the core of the domain (Sun et al., 2006; Ishida et al., 2008); in bold are residues conserved in MICALs. The type 2 CH domains

contain the acting binding site (ABS) and phosphatidylinositol (4,5)-bisphosphate (PIP2) binding site are conserved in the CH domain of MICALs (Figure 2.1, panel A in which the ABS and PIP2 binding site have been identified according to Gimona et al., 2002).

The LIM domain (residues 677-742) was identified by the presence of the $CX_2CX_{16-23}HX_2CX_2CX_{16-23}CX_2C$ consensus sequence in all MICALs, with the conservation of the Cys and His residues responsible for the coordination of two zinc ions (highlighted in purple in Figure 2.1, panel B).

The interdomain region between the CH and LIM domains of MICAL2 is longer than those of MICAL1 and 3 (Figure 1.1). Within this region the formation of a coiled-coil motif has been predicted. The coiled coil region of MICAL1 and 3 has been identified at the C-terminus of the proteins.

A unique feature of MICAL1 is the presence of a Pro-rich region (PPKPP, indicated in orange in Figure 2.1, panel C) typical of proteins that interact with the SH3 domains. Several Pro-rich region can be found in MICAL2 and 3 (Figure 2.1, panels C and E), but at different positions.

All MICALs contain a Glu-rich region (shown in green in Figure 2.1, panel D), which varies for the length and can contribute to protein-protein interactions.

The C-terminal region of MICAL may form coiled-coil structures and it has been proposed to be related to proteins of Ezrin, radizin and moesin (ERM) family (Terman et al., 2002). The number of heptad repeats of hydrophobic residues and their distribution differ in MICAL1-3 (residues highlighted in grey in Figure 2.1, panel E). One coiled-coil motif of MICAL1 (residues 964-986) corresponds to the leucine zipper identified by Suzuki et al. (2002; bold and highlighted in grey in Figure 2.1, panel E). This region has the consensus sequence (S/TXV) for the formation of a PDZ binding motif as found (Termann et al. 2002; Beuchle et al., 2007), but our comparison of multiple sequences does not allow to confirm the hypothesis (Figure 2.1, panel E).

Sequence comparison of MICAL-like proteins (Table 2.1 B) has been also done. In mammals two different genes encode for MICAL-like1 and MICAL-like2 proteins, while Drosophila contains a single gene encoding a MICAL-like protein. The proteins differ from MICALs mainly for the absence of the N-terminal flavoprotein domain. They also contain the CH and LIM domains and the C-terminal region forming coiled-coil motifs. In addition, MICAL-like proteins are characterized by the presence of the asparagine-proline-phenylalanine (NPF) signature sequence, at which the interaction with EDH1 protein takes place (Sharma et al., 2010; Chapter 1).

The primary structure of the representative MICAL-like proteins is shown in Figure 2.2 in comparison with that of the isolated domain of human MICAL1.

In the CH domain the hydrophobic residues stabilizing its three-dimensional structure are conserved in both MICAL-like1 and MICAL-like2, as the residues responsible for actin (ABS) and PIP2 binding (Figure 2.2, panel A).

Zebrafish MICAL-like2 contains an additional ≈80 residues segment between the CH and LIM domain, while Drosophila lacks ≈30 residues in the interdomain region when compared to the other MICAL-like proteins (Figure 2.2, panel A).

The Cys and His residues of the LIM domain for the binding of the zincs ion are conserved, as are the other residues that also in this case do not show similarity with those of human MICAL1 (Figure 2.2, panel B).
In human MICAL1 a Pro- and Glu-rich regions following the LIM domain is present (Figure 2.1, panels C and D), corresponding regions can also be found in MICAL-like proteins (Figure 2.2, panels D and E).
MICAL-like1 proteins can be identified by the presence of two NPF motifs following the LIM domain, which are also found in the Drosophila MICAL-like protein (Figure 2.2, panels E and F).
In the C-terminal region several hydrophobic residues can form coiled-coil motifs, as found for MICAL proteins, but the hypothetical leucine zipper identified in human MICAL1 (Figure 2.1, panel E) has not a counterpart in MICAL-like proteins (Figure 2.2, panel G).

Table 2.1. Summary of MICAL (A) and MICAL-like (B) sequences from databanks. The putative full-length protein was selected when several isoforms for each one of the predicted proteins exists on the basis of sequence comparison using BLAST (blast.ncbi.nlm.nih.gov/Blast).

A

Protein	*Organism*	*Chromosome Location*	*Nucleotide*	*Protein*	*Length residues*	*Gene ID*	*UniPro/ SwissProt*
MICAL1	human	6q21	NM_022765	NP_073602	1067	64780	Q8TDZ2
MICAL2	human	11p15	NM_014632	NP_055447	1124	9645	O94851
MICAL3	human	22q11.21	NM_015241	NP_056056	2002	57553	Q7RTP6
MICAL1	mouse	10B1-B2	NM_138315	NP_612188	1048	171580	Q8VDP3
MICAL2	mouse	7E3	NM_001193305	NP_001180234	1102	320878	8QBML1
MICAL3	mouse	6F1	NM_001270475	NP_001257404	1993	194401	Q8CJ19
MICAL1	rat	20q12	NM_001106397	NP_001099867	1047	294520	D3ZBP4
MICAL2	rat	1q33		EDM_17817	1103	365352	D4A1F2-2
MICAL3	rat	4q42	NM_001191085	NP_001178014	1997	362427	
MICAL1	guinea pig	-	XM_003466042	XP_003466090	1058	100715118	H0V032
MICAL2	guinea pig	-	XM_003465749	XP_003465749	1105	100735168	
MICAL3	guinea pig	-	XM_003461762	XP_003461810	2005	100726239	
MICAL1	macaque	4	XM_002803949	XP_002803995	1065	698737	
MICAL2	macaque	14		EEH23095	1124	701439	
MICAL3	macaque	10	XM_001103660	XP_001103660	2001	710292	
MICAL1	D.rerio	23	XM_003201226	XP_003201274	1214	568573	E7F9T0
MICAL2	D.rerio	25	JX291155	AFS28884	1120	569564	
MICAL3	D.rerio	18			1994	567456	F1QH17.2
MICAL	drosophila	3R	AF520715	AAM55244	4723	41225	Q86BA1
MICAL	A.egyptis	1	CH477341	XP_001650895.1	3542	157109953	

B

Protein	*Organism*	*Chromosome Location*	*Nucleotide*	*Protein*	*Length residues*	*Gene ID*	*UniPro/ SwissProt*
MICAL-like1	human	22q.13	NM_033386.3	NP_203744.1	863	85377	Q8N3F8
MICAL-like2	human	2p22.3	NM_182924.3	NP_891554.1	904	79778	Q8IY33
MICAL-like1	mouse	15	NM_177461.1	NP_803412.1	870	27008	Q8BGT6
MICAL-like2	mouse	5G2	NM_174850.3	NP_777275.2	1009	231830	
MICAL-like1	rat	7q34	XM_006242043.2	XP_006242105.1	861	362958	
MICAL-like2	rat	12q11	XM_006248975.2	XP_006249037.1	1006	288515	
MICAL-like1	D.rerio	6	XM_001922140.4	XP_001922175.2	867	100149741	
MICAL-like2	D.rerio	3	XM_005164196.2	XP_005164253.1	802	327198	
MICAL-like1	guinea pig	6	XM_005003841.2	XP_005003898.1	844	100724657	
MICAL-like2	guinea pig		XM_003469926.3	XP_003469974.2	888	100732572	
MICAL-like	drosophila	69F5	NM_140364.3	NP_648621.1	1010	39475	

A

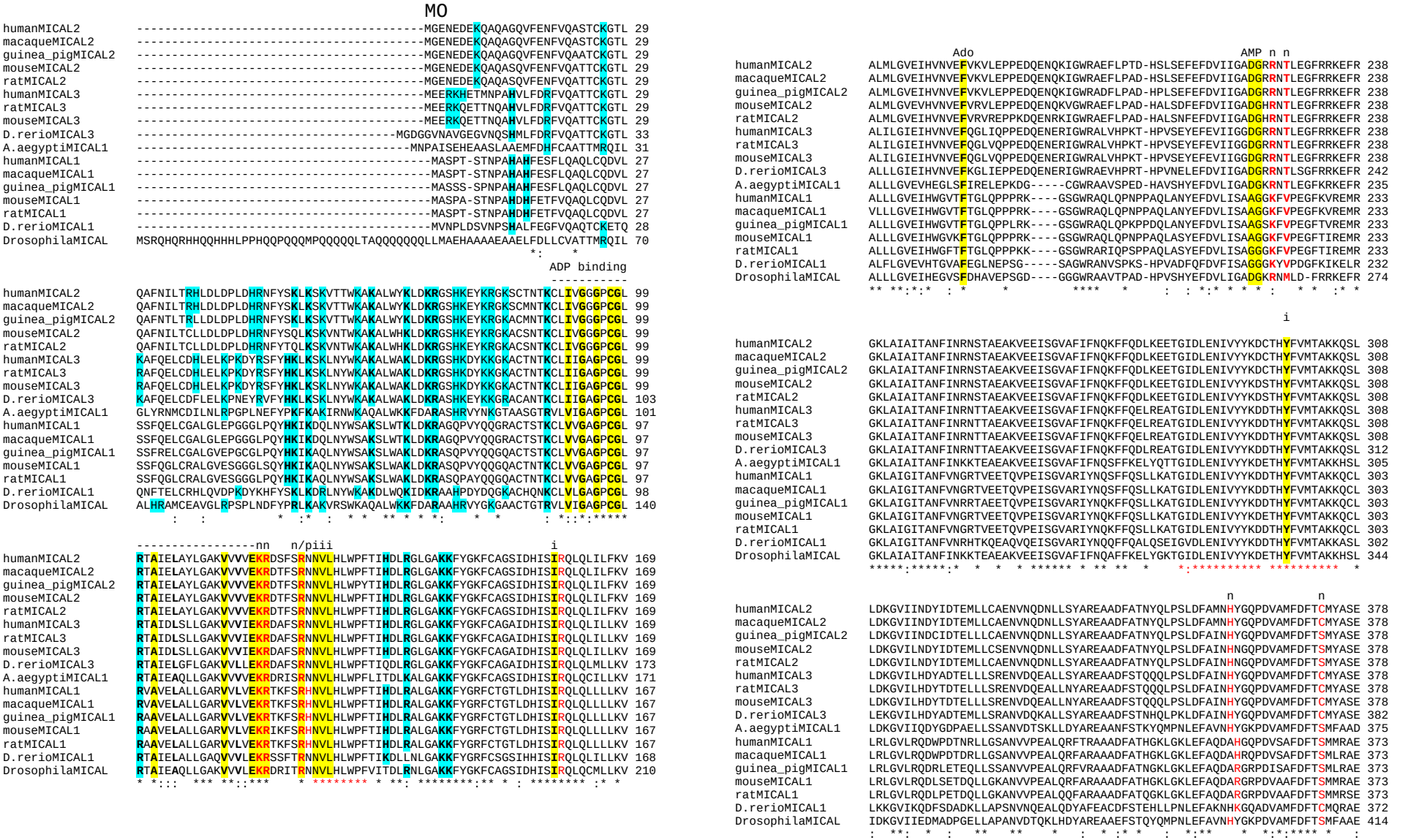

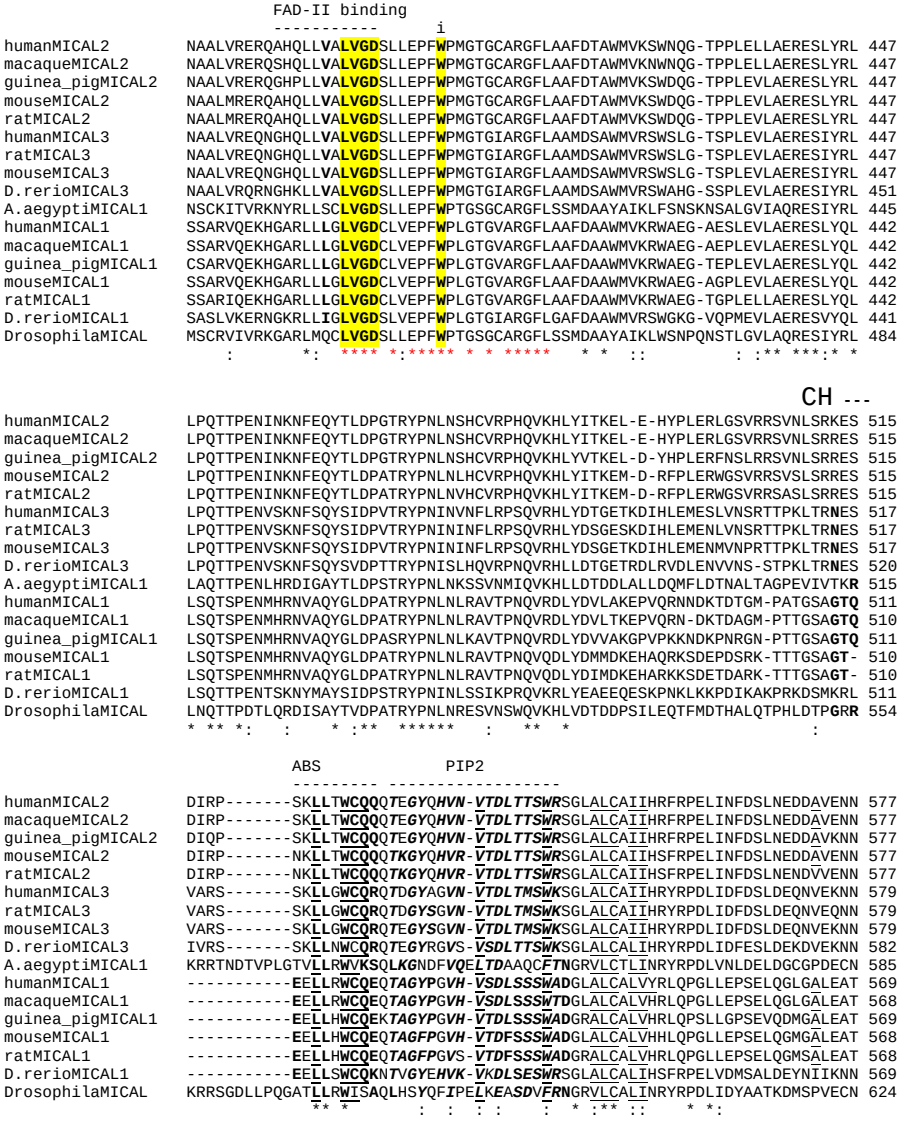

B

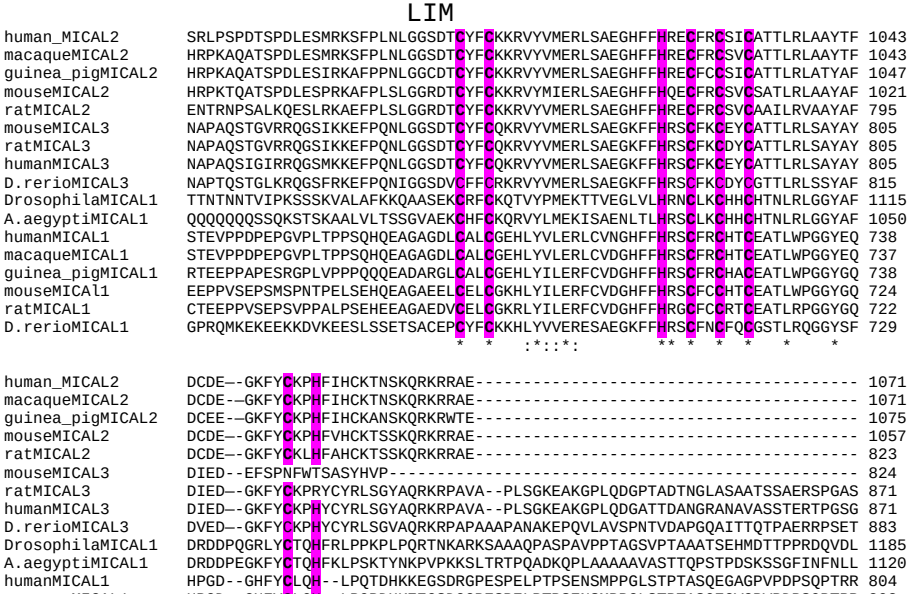

C

```
                                                PXXP
humanMICAL1          PTRRQIRLSSPERQRLSSLN---LTPDPEMEPPPKPPRSCSALAR-HALESSFVGWGLPV 857
macaqueMICAL1        PTRRRIHLSSLERQRLSSLN---LTPDPEMEPPPKPPRSCSALAR-HALESSFVGWGLPV 862
guinea_pigMICAL1     PARRLIRLSSPERQRLSSLD---INPSPEMEPPPKPPRSCSALAR-EALEGSFVGWGMPA 855
mouseMICAL1          PARRLIRLSSLERLRLSSLN---IIPDSGAEPPPKPPRSCSDLAR-ESLKSSFVGWGVPV 840
ratMICAL1            PARRLIRLSSVERLRLSSLN---IIPDSGVEPPPKPPRSCLDLAQ-ESLKSSFMGWGVLR 840
humanMICAL3          LHGSSSNMKTLGSQSFNTSDSAMLTPPSS-PPPPPPPGEEPATLR-RKLREAEPNASVVP 1487
ratMICAL3            PIRSQPVALPEARSPTSPTS--SLQPESLLA-PPTPPTPPSTQLP-ICSQPQPSSDASIP 1274
D.rerioMICAL3        LNGSVTTSQTAASDSYNNSDSTMLTPPSS--PPPPPPREEPACLQNKKSQPRTPVSPPQP 1508
D.rerioMICAL1        KISVDPDFDESTEFPAPDQ----EPPDLEESHQPPKPSELSAENTNMENQQHNINPVPAP 847
DrosophilaMICAL      FSSSSPQLYIHKPHHLAAAH---PSALDDQTPPPIPPLPLNYQRSDDESYANETREHKKQ 4542
                                              *  *
```

D

```
                          Glu-rich
humanMICAL1          SPQALVAMEKEEKESPFSSEEEEEDVPLDSDVEQALQTFMEK------------TWRRTLLRRAKEEE--  921
macaqueMICAL1        GPQALVA----EEEESSSSSEEEEDVPLDSDVEQALQTFAKTSGTMNDYP----TWRRTLLRRAKEEE--  919
guinea_pigMICAL1     SLPVF---EAMEEEESSSDNEEEEDDDEPLDPDLEQALQTMAKNAGTMD--KYPTWRRTLLRHAKEEE--  919
mouseMICAL1          APQVPEAIEKGDDEEEEEEEEEEEEPLPPLEPELEQTLLTLAKNPGAMT-KYPTWRRTLMRRAKEEE--  908
ratMICAL1            APQVPEAIEKGEEEEEEEEEEEEEELPPPLALEVEQSLLTLAKNSGDMTKYPTWRRTLMRRAKEEE--  908
humanMICAL3          AEEDVASSSSESEMEEEGEEEEEEPRLPPSDLGGVPWKEAVRIHALLKGKSEEELEASKSFGPGNEEEEE  996
ratMICAL3            TEEDAASSSSESEM-EEEEEEDEEDQLPTSDLGGVPWKEAVRIHALLKGRSEEELEASKNFEP---EEEE  992
D.rerioMICAL3        TDIEEGSSSSESDMEEEDEDAEAAG---PSDLGGVPWKEAVELHAKLKGESDPGADDDGLHDGDGEMDED 1006
D.rerioMICAL1        AGQSQPDQYVSEDDNEDDEDEDEEDLQAEHYLDCEGADFEFSDSEKRNLKRMKTLERKAKMTEIQRF---  1060
mouseMICAL3          KDKKEKDSDGAGKRRKTSQSEEEE--PPRSYKGERPTLVSTLTDRRMDAAVGNQNKVKYMATQLLAKFEE  735
                                      *:**

humanMICAL1          ------------------------------------------------------------------------
macaqueMICAL1        ------------------------------------------------------------------------
guinea_pigMICAL1     ------------------------------------------------------------------------
mouseMICAL1          ------------------------------------------------------------------------
ratMICAL1            ------------------------------------------------------------------------
humanMICAL3          EEEEYEEEEEEDYDEEEEESSEAGNQRLQQVMHAADPLEIQADVHWTHIRERGEEERMAPASESSASGAP  1066
ratMICAL3            EEEEYEDDEEE-YDEEEEESSEAGNKRLQQIITAADPLAIQADVHWTHIRERGEEERMLPPSESSTSRAP  1061
D.rerioMICAL3        EEE--EEDEEDEDEEEEEESSEARNLQIQQAIHPVDPLDIQMESHQAEGVLEMPSVSPLGSLTQPTSSTA  1081
D.rerioMICAL1        ------------------------------------------------------------------------
mouseMICAL3          ------------------------------------------------------------------------
```

E

```
                                                CC
humanMICAL1          ----------------------MKRFCKAQTIQRRLNEIEAALRELEAEGVKLELALRRQSSSPEQQKK 968
macaqueMICAL1        ----------------------MKRFRKAQTIQRRLNEIEGALRELEAEGVKLELALRRQSSSPEQQKK 966
guinea_pigMICAL1     ----------------------MKRFCKAQTIQRRLNEIEAALRELEAEGVKLELALRSQSTSPEQQKK 966
mouseMICAL1          ----------------------MKRFCKAQAIQRRLNEIEATMRELEAEGTKLELALRKESSSPEQQKK 955
ratMICAL1            ----------------------MKRFCKAQAIQRRLNEIEAAMRELETEGMKLEVALRKESSSPEKQKK 955
humanMICAL3          EELNAKLTRRVQKAARRQAKQEELKRLHRAQIIQRQLQQVEERQRRLEERGVAVEKALRGEAGMGKKDDP 1890
ratMICAL3            EELSAKLTRRVQKAARRQAKQEELKRLHRAQIIQRQLEQVEEKQRQLEERGVAVEKALRGEAGMGKKDDP 1886
D.rerioMICAL3        EELNAKLTRRVQKAARRQAKQEELKRLHRAQIIQRQLQQVEEKQRQLEERGVAVEKALRGEAGMGKKDDP 1915
D.rerioMICAL1        FSDSEKRNLKRMKTLERKAKMTEIQRFHKAQSIQRRLEEIEVTFKELEEKGVELERALRGETGTG---DE 1100
DrosophilaMICAL      SYANETREHKKQRAISKASRQAELKRLRIAQEIQREQEEIEVQLKDLEARGVLIEKALRGEAQNIENLDA 4600
humanMICAL2          LSGVLWRLQQVEEKILQKRAQNLANREFHTKNIKEKAAHLASMFGHGDFPQNKLLSKGLSHTHPPSPPSR 905
macaqueMICAL2        LSGVLWRLQQVEEKILQKRAQNLANREFHTKNIKEKAAHLASMFGHGDFPQNKLLSKGLSHTHPPSPPSC 905
guinea_pigMICAL2     LSGVLRRLQQVEEKILQKRAQNLANREFHQKNIKEKAAHLASMFGHGDFPQNKLLSKGPSHTHPPSPPPC 907
mouseMICAL2          LSGVLRRLQQVEEKVLQKRAQNLANREFHTKNIKEKAAHLASMFGHGDLPQDKLLSKRVPHAHPPSPPSC 904
ratMICAL2            QGFNNLEELPAFSSRSLGSSQEYAKESGNQNKVKYMANQLLAKFEENTRNPS-ALKQESLRKAEFPLSLG 749
mouseMICAL3          KTSQSEEEEPPRSYKGERPTLVSTLTDRRMDAAVGNQNKVKYMATQLLAKFEENAPAQSTGVRRQGSIKK 752
A.aegyptiMICAL1      ------------------------------------------------------------------------
```

```
                                Leu zipper
                               ----------------------
humanMICAL1          LWVGQLLQLVDKKNSLVAEEAELMITVQELNLEEKQWQLDQELRGYMNREENLKTAADRQAEDQVLRKLV 1038
macaqueMICAL1        LWVGQLLQLVDKKNSLVAEEAELMITVQELNLEEKQWQLDQELRGYMNREETLKTAADRQAEDQVLRKLV 1036
guinea_pigMICAL1     LWLEQLLQLVQKKNSLVAEEAELMITVQELDLEEKQWQLDHELRGYMNREETLKTAEDRQAEDEILRKLV 1036
mouseMICAL1          LWLDQLLRLIQKKNSLVTEEAELMITVQELDLEEKQRQLDHELRGYMNREETMKTEADLQSENQVLRKLL 1025
ratMICAL1            LWLEQLLQLIQKKNSLVTEEAELMITVQELDLEEKQRQLDHEFRG-INREETLKTQADRLSEDRVLRKLL 1024
humanMICAL3          KLMQEWFKLVQEKNAMVRYESELMIFARELELEDRQSRLQQELRERMAVEDHLKTEEELSEEKQILNEML 1961
ratMICAL3            KLMQEWFKLVQEKNAMVRYESELMIFARELELEDRQSRLQQELRERMAVEDHLKTEEELSEEKKILNEML 1956
D.rerioMICAL3        KLMQEWFKLVQEKNALVRYESELMIFARELELEDRQSRLQQELRERMAIDDHLKTEEELAEEKQILNEML 1985
D.rerioMICAL1        EIIDQWIELVQEKNNLLSEESDLMVASRQLELEDKQSMLEMELRRYMEMDDSEKSPEQQKHEAEILQEML 1170
DrosophilaMICAL      KLLKELLEIWRNITALKKRDEELTIRQQELQLEYRHAQLKEELNLRLSCNKLDKSSADVAAEGAILNEML 4676
humanMICAL2          LKQQREEEATWQEQEAPRRDTPTESSC--AVAAIGTLEGSPPVHFSLPVLHPLLG*               1124
macaqueMICAL2        LKQQREEEATWQEQEAPLRDTPTESSC--AVAAIGTLEGSPPVHFSLPVLHPLLG*               1124
guinea_pigMICAL      LKQEQEEEGTWQEQEGPRRDTATESSC--AVAAVSTPEGSPPVHFSLPVLHPLLG*               1128
mouseMICAL2          LNQQREEEGTWQEQEAPRRDVPTESSC--AVAAISTPEGSPPVRFSLPVLHPLLG*               1102
ratMICAL2            LNQQREEEGTWPEQEAARRDVPAESSC--AVAAISTPEGSPPGISTSFFRKALSWPLRLTRGLLNLPQSL 891
mouseMICAL3          FSPNFWTSASYHVPVALPATVMPMC----LYHPSQVLVCLEGGPAFMSPVLFNDTNS-------------- 864
A.aegyptiMICAL1      KTKPKPEALTKVDPKLELMMTTLTEPAEVLEQTD-LSKDSSLLNASSCDLPDIVNITKKQAIEAQPALKI 2939
                              :      :          :

humanMICAL1          DLVNQRDALIRFQEERRLSELALGTGAQG*                                         1067
macaqueMICAL1        DLVNQRDALIRLQEERRLSELALGIGAQG*                                         1065
guinea_pigMICAL1     EVVNQRDALIRFREECRLSELA*                                                1058
mouseMICAL1          EVVNQRDALIQFQEERRLREMPA*                                               1048
ratMICAL1            DVVNQRDALIQFQEERRLREMPV*                                               1047
humanMICAL3          EVVEQRDSLVALLEEQRLRERE EDKDLEAAMLSKGFSLNWS*                            2002
ratMICAL3            EVVEQRDSLVALLEEQRLREKEEDKDLEAAMLCKGFSLDWS*                             1997
D.rerioMICAL3        EVVEQRDSLVALLEEQRLRERE EDKDLEAVMLSKGFNLNWA*                            2026
D.rerioMICAL1        DVVDMRDSLVAFLEEKRLKEVNDQFNSSLDAKRRSTTASQVHWE*                          1214
DrosophilaMICAL      EIVAKRAALRPTASQLDLTAAGSASTSAEATGIKLTGQPHDHEESII*                       4723
ratMICAL2            LRWMQGLLQAAGHHVRDNAHNYCFMFELLSLGLLLLWAFSEVLAAMYRESEESLESIRSWLLRFVPVKLQ*961
A.aegyptiMICAL1      LDHTEKIKQITSHIPQEIQVYTLHTEDHKPAEPQPSTSGVTSDYASILKDISSGLMGTDIVEPVFYEPPPT3009

A.aegyptiMICAL1      IDRKPKSDFTTYKQILQDKAREPAEHNSQQPQRPLRKPKPTERSVSPAVAGRPFDNSICIDPWRAKRSSSI 3081
A.aegyptiMICAL1      ENLVVEQVFVKKDDKVVDTFYIVPEQQKKLKRRSKSFDRLQVPGYSGRRHSKKSLEELRDFGFDIEPPGTC 3152
A.aegyptiMICAL1      KNLVNPRLRHLNFDESDEDLSSLRNNRRRENLRKCQSSTDTSKLDVEASRVDIDRESPIPRSTDFSKWEAI 3223
A.aegyptiMICAL1      LDRGIPYYKEPPVHKKEDIKSLERKLEDLKTECKPRRKISGKTPAIPKDYDPEEYVPRINRRALDTYDVPD 3294
A.aegyptiMICAL1      SDLPKWYDPDEYVPRAQRNHAFDHEIPVSSAVRSRRLNEFDIPTSSTSRPQRSSAYEIDVPISRTGGRYYP 3365
A.aegyptiMICAL1      EPLHLDDLPMTHTLPKSKITSSHVPYTSSRTYDLPSRDVPRTRYSHRPTADSGTIVNRSQRLHEKANKYIR 3436
A.aegyptiMICAL1      SQVTKNDPNPYIREMLENESDDDAYPITTSTSHRVPITTSSFHPISTYGTSGSAAMSRIATKAITQPSRMT 3507
A.aegyptiMICAL1      HYTRKDVPSSSGSGSRSYRRGGGDHHDRRDNCTIS*                                   3542
```

Figure 2.1. Sequence comparison of MICAL forms. Regions corresponding to the monooxygenase (MO) and calponin homology (CH) domains (panel A), LIM domain (panel B), Pro-rich (panel C) and Glu-rich region (panel D) and coiled coil regions (panel E) of selected MICAL sequences (Table 2.1) have been aligned with ClustalW2 (Goujon 2010). The output reflects the degree of sequence similarity among the proteins. Sequence annotation: cyan, basic residues in the N-terminal basic region and conserved residues are in bold; yellow, residues involved in FAD binding as indicated in the sequence; in bold are the residues matching the ADP binding region and second

FAD consensus sequence; residues involved in the interaction with the isoallosaxine ring (i), pyrophosphate (p) adenosine (Ado) and AMP regions of FAD are also indicated. Red, residues proposed to be responsible of NADPH binding as deduced from the comparison with pHBH. The red stars below the aligned sequences indicate the conserved region of MO domain of MICALs. In the CH domain the underlined residues are those forming the hydrophobic core based on the structure of the CH domain of human MICAL1 (Sun et al., 2006). The regions implied in the binding of actin (ABS) and PIP2 (PIP2) as defined by Gimona et al., 2002 and Sun et al., 2006, are also indicated. Residues matching the consensus sequence for ABS are in bold and for PIP2 binding are in bold and in italic. The conserved Cys and His residues of the consensus sequence of the LIM domain are in bold and highlighted in purple. The Pro-rich regions are in bold and orange. The Glu-rich regions are in bold and green. The residues that potentially form coiled-coil motifs (CC) are highlighted in grey and those forming the putative leucine zipper are in bold. *, identical residues; :, conserved residues.

A

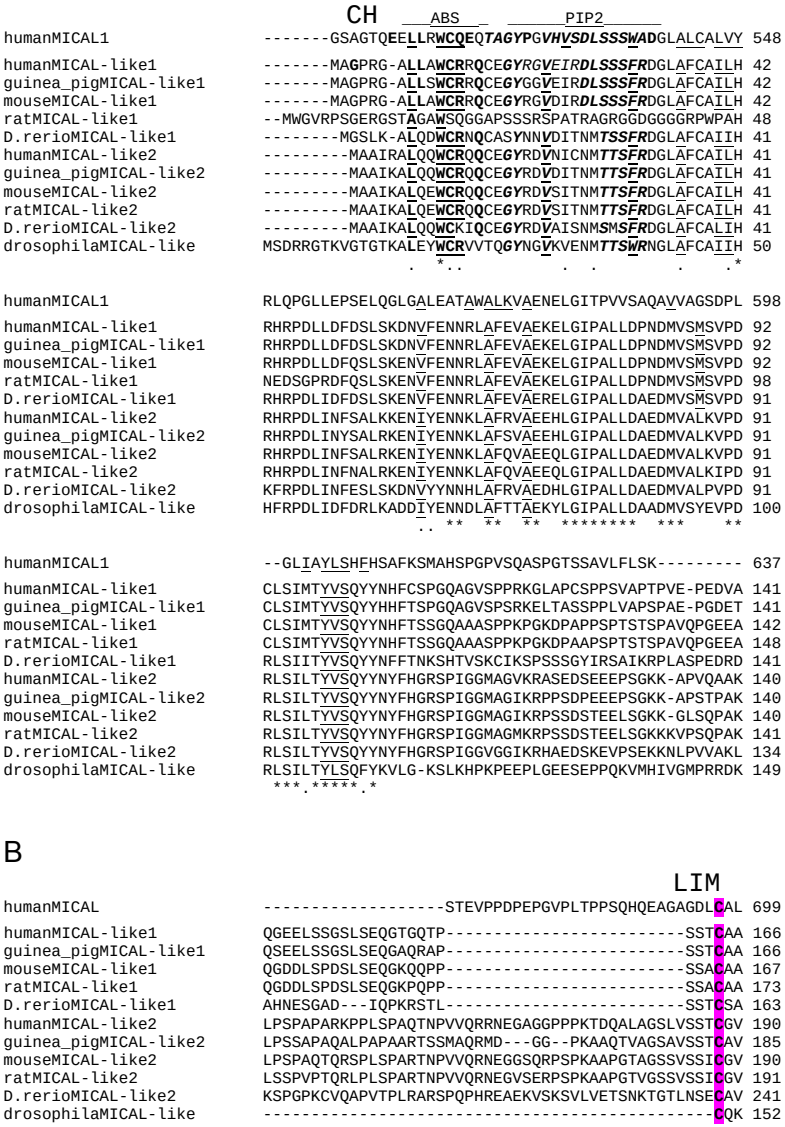
CH
ABS
PIP2
humanMICAL1
humanMICAL-like1
guinea_pigMICAL-like1
mouseMICAL-like1
ratMICAL-like1
D.rerioMICAL-like1
humanMICAL-like2
guinea_pigMICAL-like2
mouseMICAL-like2
ratMICAL-like2
D.rerioMICAL-like2
drosophilaMICAL-like

B

LIM
humanMICAL
humanMICAL-like1
guinea_pigMICAL-like1
mouseMICAL-like1
ratMICAL-like1
D.rerioMICAL-like1
humanMICAL-like2
guinea_pigMICAL-like2
mouseMICAL-like2
ratMICAL-like2
D.rerioMICAL-like2
drosophilaMICAL-like


humanMICAL1
humanMICAL-like1
guinea_pigMICAL-like1
mouseMICAL-like1
ratMICAL-like1
D.rerioMICAL-like1
humanMICAL-like2
guinea_pigMICAL-like2
mouseMICAL-like2
ratMICAL-like2
D.rerioMICAL-like2
drosophilaMICAL-like

C

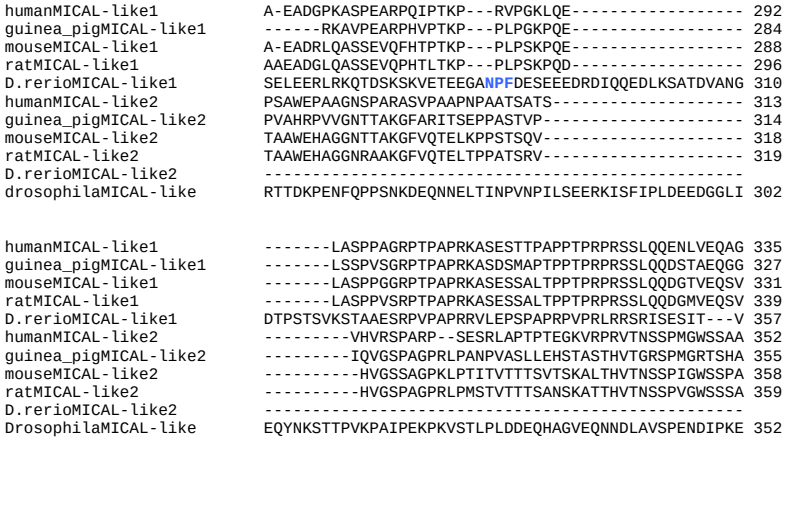
humanMICAL-like1
guinea_pigMICAL-like1
mouseMICAL-like1
ratMICAL-like1
D.rerioMICAL-like1
humanMICAL-like2
guinea_pigMICAL-like2
mouseMICAL-like2
ratMICAL-like2
D.rerioMICAL-like2
drosophilaMICAL-like

D

```
humanMICAL1                 --------------------PTRRQIRLSSPERQRLSSLNLTPDPEMEPP 830
humanMICAL-like1            SSSLVNGRLHELPVPKPRG-TPKPSEGTPAPRKDPPWITLVQAEPKKKPA 384
guinea_pigMICAL-like1       SGGLVNGRLQEPPVPKPRG-TPKLSERTPPARKDPPWITLVQAEPKKKPA 376
mouseMICAL-like1            SSGLVNGRLQEPPVPKPRG-TPKLSERMAAPRKDPPWITLVQTEPKKKPA 380
ratMICAL-like1              SGDLVNGRLQELPVPKPRG-TPKLSERMTAPRKDPPWITLVQTEPKKKPA 388
D.rerioMICAL-like1          NGDPDQTQTPQVPVPKERMHSPARKAGDTPKPKDPPWLALVQSETKRKPA 407
humanMICAL-like2            PCT-AAAASHPAVPPSAPDPRPATPQGGGAPRVAAPQTTLSSSSTSAATV 401
guinea_pigMICAL-like2       QYP-ATNSSR--SAPSIPEPCPATPQGLGPPRVSTSVTKLGLNSASPGAA 402
mouseMICAL-like2            QSSPANFNSRPVVSPSARNTHLPGSQGQTAS--KGVKTQLNLNSESSNTA 406
ratMICAL-like2              QSSTGTSGSRPVVSPSALGAHLSVPQGQAAS--KGVKTQLNSSTDSSSTA 407
D.rerioMICAL-like2          ----------------------------VP----RPVELSLAQQS---- 354
drosophilaMICAL-like        KLKISSVSIYLEDDRLVVDAIHPDNLDKQEALNNTSDALIPESQEAPIPE 402
```

Pro-rich

```
humanMICAL1                 PKPPRSCSALARHALESSFVGWGLPVSPQALVAM---------------- 856
humanMICAL-like1_human      PLPPSSSPGPPSQDSRQVENGGTEEVAQPSPTASL--------------- 419
guinea_pigMICAL-like1       PLPPGS-PRPPSRGSRQEENGTVEEVTPRGPAAGS--------------- 410
mouseMICAL-like1            PQPPSSGPGPLSQAYRQVEDGGLEEQTQKSSGTEP--------------- 415
ratMICAL-like1              PLPPSSGPGPLSQASRQVENGGLEEKTQKSPAAEP--------------- 423
D.rerioMICAL-like1          PRPPTGTAVPPSTGASPSRK---EETSRPS-------------------- 434
humanMICAL-like2            DPPAWTPSASRTQQARNKFFQTSAVPPG---------------------- 429
guinea_pigMICAL-like2       DPPAWTPSATRTQQARERFFQSPAAPT----------------------- 429
mouseMICAL-like2            VTPAWTSSASKTQQAREKFFQTPPSAPAPASAPAP-APTSKVPTVVTVPT 455
ratMICAL-like2              PTPAWTSSSSRTQQAREKFFHNLSPAPAPAPASSSSSHASRVPTVVTAPS 457
D.rerioMICAL-like2          ----WTSSAQRTQAARQKFFQSCAPATE---------------------- 378
drosophilaMICAL-like        NNTQVAIKPEDHISPRKENKIFSNTESCSKQEGVLPKQMDLESPKDKVIE 452
```

E

Glu-rich

```
humanMICAL1                 EKESPFSSEEEEEDVPLDSDVEQALQTFMEKTWRRTLLRRAKEEE----- 921
humanMICAL-like1            ESKPYNPFEEEEEDKEEEAP------------------------------ 439
guinea_pigMICAL-like1       EPRTYNPFEDEEE-VEEPSP------------------------------ 429
mouseMICAL-like1            EPKPYNPFEEEEEEEGEPAPPVPSPS------------------------ 441
ratMICAL-like1              EPKPYNPFEEEEEEE---------------------------------- 438
D.rerioMICAL-like1          --TPPNPFENEEEEE---------------------------------- 447
humanMICAL-like2            TSLSGRGPTPSLVLS---------------------------------- 444
guinea_pigMICAL-like2       SGPVGQTPAPANAPF---------------------------------- 444
mouseMICAL-like2            SKVPNVVTAPTSKVP--TVVTVPTSKVPTVVSAPTSKVPTVVSAPTSKVP 503
ratMICAL-like2              GKVSPLVNTSTSKVPSATVVTVPTSKASTVVTAPTSKAPTVVTVPISKAP 507
D.rerioMICAL-like2          LQPNTKPPLGPAEPS---------------------------------- 393
drosophilaMICAL-like        YPEDLNPFKDDDSSKGANPFD---------------------------- 480
```

F

```
humanMICAL-like1            ------------------AAPSLATSPALGHPESTPKSLHPWYGITP-TS 470
guinea_pigMICAL-like1       ------------------AAPSPAPSPAQAPSECTPKSLHPWYGITP-TS 460
mouseMICAL-like1            ----------LAPPVPSPSPAPPVPSPAPAPSEATPKSLHPWYGITP-TS 480
ratMICAL-like1              ----------------EASVPAVPSPAPAPPETTPKSLHPWYNITP-TS 470
D.rerioMICAL-like1          ------------------ESELGPEDVPGPVVAS----HPWYGITHSTE 474
humanMICAL-like2            ------------KDSSKEQARNFLKQALSALEEAGAPAPGRPSPATAAVP 482
guinea_pigMICAL-like2       ------------RDSSREQALSFLKKALSGVEAAGAQAPGKSSPAMNSCP 482
mouseMICAL-like2            ASKVSPVVDAPAQESSREQALSVLRKALPALTGSGTQAPNRSFPATSSVL 603
ratMICAL-like2              ASKVSGVVDNPAQESSREQALSVLRKALPGLTRAGSQAPSRSSPATSSVL 607
D.rerioMICAL-like2          -------------------------NLKVQEKEGNRALANGNPLHEGNA 417
drosophilaMICAL-like        ------------SSDDEVELLKAIPAQQSKGKVVPPRPPPPKIGLSSIS 517
```

```
humanMICAL-like1            SPKTKKRPAPRAPSASPLALHASRLS----HSEPPSATPSPALSVESLSS 516
guinea_pigMICAL-like1       SPKTKKRPAPRAPSASPLALHASRLS----HSEPPSATPSPALSVESLAS 506
mouseMICAL-like1            SPKTKKRPAPRAPSASPLAIHASRLS----HSEPPSATPSPALSVESLSS 526
ratMICAL-like1              SPKTKKRPAPKAPSASPLVLHASRLS----HSEPPSATPSPALSVESLSS 516
D.rerioMICAL-like1          VPGGDAGKQSPARSESPISIRRKKRP----APKAPNSSTSAFPSSQTSSP 520
humanMICAL-like2            SSQPKTEAPQASPLAKPLQSSSPRVLGLPSRMEPPAPLSTSSTSQASALP 532
guinea_pigMICAL-like2       ----KTEGPKAVPSGKPLQSDAPHTLSSTSRTEPSARLSVGSTSQVGKSP 528
mouseMICAL-like2            VTLPKNEVPQKVPSDK-LSALTTQTPNFTIKLEPSAPVNVGN---TAVFL 649
ratMICAL-like2              ITLPKNEVPPKVPSAK-LSHSTTQAFSPTPKMEPTAPLSVGSTSWTSVSL 656
D.rerioMICAL-like2          NNNNALNSDPRAKSQVKISCSSAEVSTWRQELHVRDSKGRSSYQAAPSSP 467
drosophilaMICAL-like        NPSEKPHSSPTLSHGKKMPMPTPRISISKTQTPAKPMTHQGQKSSISSSS 567
```

```
humanMICAL-like1            ES----ASQTAGAELLEPPAVPKSSSEPAVHAP-------GTPG---NPV 552
guinea_pigMICAL-like1       ES----CSQMAAGELLEPPAVPKSSSEPAVHAP-------GTPG---NSA 542
mouseMICAL-like1            ES----SSHTANAEPLEPPAVPKSSSDPAVHVP-------GTPGTSGNSV 565
ratMICAL-like1              ES----SSHTANTEPSEPPAVPKSSSDPAVHVP-------GTPGTSANSV 555
D.rerioMICAL-like1          ASSLALSTESLSSSSSDYSAVPQKAAANEQDHL-------FTKSVS-EPS 562
humanMICAL-like2            PAGRRNLAESSGVGRVGAGSRPKPEAPMAKGKSTTLTQDMSTSLQEGQED 582
guinea_pigMICAL-like2       -------ATSSGVIKEGTGSRLKPEAPTAKGP--------STSPQQSQED 563
mouseMICAL-like2            QAGKKSPSISPRVGKTSVGSRPQAEVAGVKGP--------GPISQEGQEE 691
ratMICAL-like2              QAGKKSPGISPGIGKTSAVSRPQAEVK---GP--------GPTSQEGQEE 695
D.rerioMICAL-like2          ---AIISSGGGMNGKESL-YLSAISKESSRPPSLLQTTAKASANDVQSYD 504
drosophilaMICAL-like        SEHLNSIRTFDRGADDRGSSISLPSANGPRKPLR---ASVGSPLRSEESS 614
```

```
humanMICAL-like1            SLSTNSSLASSGELVEPRVEQMPQASPGLAPRTRGSSGPQ-------PAK 595
guinea_pigMICAL-like1       SLSAHSSLSSSGELVQPSVEQTPQA------RTRGSPGPQ-------PAK 579
mouseMICAL-like1            TPSANSSLSSSGELGQPSGEQMLQA------RTKGSAGTH-------STK 602
ratMICAL-like1              TPSAHSSLSSSGELGQPSGEQMPQA------RTRGSPGTH-------STK 592
D.rerioMICAL-like1          INTPASALSQKAELQPRCSPNLSPP-----PPPPTNTSSA-------PAT 600
humanMICAL-like2            GPAGWRANLKPVDRRSPAERTLKPKEPRALAEPRAGEAPR------KVSG 626
guinea_pigMICAL-like2       GPEGWRARLKPVEKKPPAGRAQEPKEPRVPAEPKAGEAPVAPRTPVQVSG 613
mouseMICAL-like2            GPEGWRARLKPVDKKTPAGRSLEQKEP-VLAEPRIGDTSR------KASS 734
ratMICAL-like2              GPEGWRARLKPVDK-----RALEQKEP-VLAEPRAGDTPR------KASS 733
D.rerioMICAL-like2          APADWR--SKPKAAPNGP-RLNRSPDIAKDVPLTCGENKDLKVQDSQAFM 560
drosophilaMICAL-like        PTTSLSSITSPMRKKRQAPLPPIQTDFDSDPGFSKLSDEQKALLHTQLKA 664
```

```
humanMICAL-like1            PCSGATPTPLLLVGD-RSPVPSPGSSSPQLQVKSSCKENPFNRKPS---- 640
guinea_pigMICAL-like1       PCSGAAATP-LLVGD-RSPAPSPGSSSP--QLQSSCKENPFNRKPS---- 621
mouseMICAL-like1            PFSGATPTPFLLAGD-RNPAPPVGSASPQLQIKSSCKENPFNRKPS---- 647
ratMICAL-like1              PFSGATPTPFLLAGDQKSPAPPMGSSSPQMLIKSSCKENPFNRKPS---- 638
D.rerioMICAL-like1          PQTNRSARPPSLSAG---LKITPTSQTPGTPGKRTCKENPFNRKTT---- 643
humanMICAL-like2            SFAGSVHITLTPVRPDRTPRPASPGPSLPARSPSPPRRRRLAVPAS---- 672
guinea_pigMICAL-like2       HVQVGVQITLTPVQPEQTLAHAGPGTKLPEASPSSSSRRRLAIPPS---- 659
mouseMICAL-like2            SSDSSVHITLTSIQHKRKPCPAGSGPSPAALSPSPSHRKKLAVPPS---- 780
ratMICAL-like2              SSDSSIHITLTPIQQKRTPCLADSGSSLAAPSP-PSRRKKLVVPPT---- 778
D.rerioMICAL-like2          -------------------------------------------------- 578
drosophilaMICAL-like        PNLGDSTRRLIPLDQSLLSDEATESSNYDESLSTSNADEEVNVVYRRILV 714
```

```
humanMICAL-like1            PAASPATKKATKGSKPVRPPAPGHG-----------------------F 666
guinea_pigMICAL-like1       PAASPTAKKATKGPKPARPPAPGHG-----------------------F 647
mouseMICAL-like1            PSASPTVRKATKGAKPVRPPAPGHG-----------------------F 673
ratMICAL-like1              PSTSPTVRKATKGAKPVRPPAPGHG-----------------------F 664
D.rerioMICAL-like1          TSANSFVSRPPKGPRPARPPAPGHG-----------------------F 669
humanMICAL-like2            LDVCDNWLRPEPPGQEARVQSWKEEEKKPHLQGKPGRPLSPANVPALPGE 722
guinea_pigMICAL-like2       LDISANWLQSEPSEQEAQVQSWKE---KPHSQDKPGRPSALAGIPASPEK 706
mouseMICAL-like2            LDVSADWLQPEPKKQEDGTRSCKE--EKSPTRWSRERSAVLDSGLAPPGE 828
ratMICAL-like2              LDVSADWLQPELKKQDDQTRSCK---EKTATWGTRESSAILDNDLVSPDE 825
D.rerioMICAL-like2          -------------------------------------------------- 617
drosophilaMICAL-like        PPTQPENTVERSKEDQKSPIVYNDFDRNVSPLGHNKSTHGKWKRRKGPAP 764
```

G

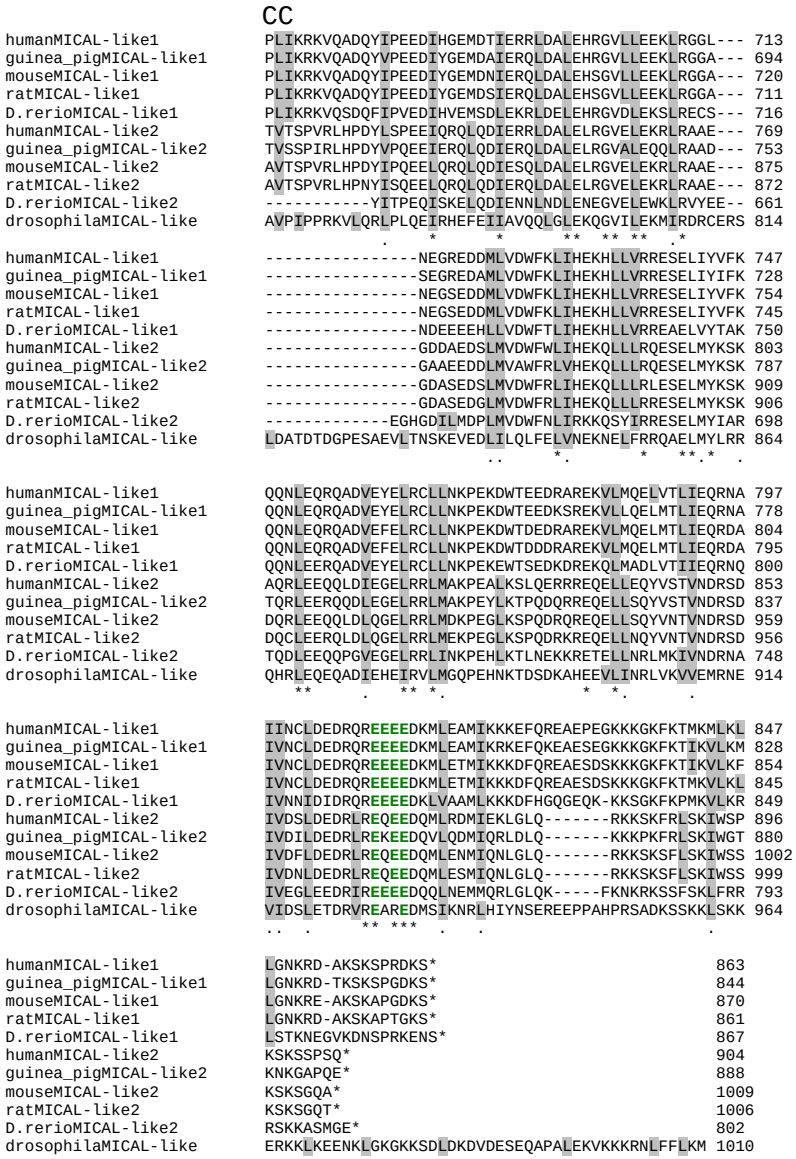

Figure 2.2. Sequence comparison of MICAL-like proteins. Annotation is as in Figure 2.1; the NPF sequence is shown in bold and blue.

2.2. Three-dimensional structures of MICAL domains.

The N-terminal domain of MICAL, which shows sequence similarity with FAD-containing aromatic hydroxylase (Figure 2.3, panel A), which is essential for several its functions.

In 2005, two independent groups (Nadella et al., 2005; Siebold et al., 2005) solved the three-dimensional structure of the isolated N-terminal domain of the mouse MICAL1 with an His_6-tag at the N-terminus of the protein (residues 1-498). In one case (Nadella et al., 2005) to favor the formation of ordered crystals Lys141 and Lys142, which were eventually found at the protein surface, were mutated to alanine (Nadella et al., 2005; PDB ID 2BRA, 2 Å resolution). Instead, no mutations were introduced to solve the structure of the isolated N-terminal domain of mouse MICAL1 in the oxidized and reduced state by Siebold et al., (2005; PDBID 2BRY; 2C4C, 1.45 Å resolution). As expected, the structures of the as-isolated (oxidized) proteins are similar to each other. A homodimer was found in the crystallographic asymmetric unit, although the protein is monomeric in solution (Nadella et al., 2005; Siebold et al., 2005; Vanoni et al., 2012).

The N-terminal domain of MICAL had a compact fold with an N-terminal four-helix bundle (residues 1-86) followed by the core region (87-442) and few disordered segments (Figure 2.3, panel B). The core region showed a fold similar to that of p-hydroxybenzoate hydroxylase (PHBH, PDB ID 1PBE), phenol hydroxylase (1PN0) and of several FAD-containing oxidases and monooxygenases. In the N-terminal flavoprotein domain of MICAL the larger portion (residues 86-234 and 367-444) contains the FAD and NADPH binding regions (Figure 2.3, panel A). The region between residues 235 and 366 forms the smaller lobe of the protein, which completes the active site. This region was defined as the monooxygenase domain by Siebold *et al*. (2005), but we will indicate it as the cap domain in order to adopt the nomenclature used for PHBH (Schreuder et al., 1989).

The topology of the N-terminal domain of MICAL is simplified compared to that of PHBH in which the polypeptide chain passes several times between the FAD- and substrate-binding domains (Figure 2.3, panels B-C and E). In MICAL, only a long two-stranded β-sheets (β 9 and 15, Figures 2.3, panel B and 2.4) connects the two domains. The C-terminus, which links the N-terminal domain to the CH domain, and the N-terminal region (residues 1-86) have no counterpart in PHBH. Several basic residues are present in the first 86 residues (H11, H13, H49, K50, K52, K61, K66, K(or R) 69, R(or K)70, K(or R)86, Figures 2.1, panel A) and in addition to several conserved residues of the FAD domain. They form one extended patch of basic potential on one face of the protein (Figure 2.5, panels A and B) (Vanoni et al., 2012). Due to its location and to the acidity of several cytoskeletal proteins, including actin, the N-terminal 1–85 basic region of MICAL has been proposed to be important to promote the interaction with the putative protein substrate (Nadella et al., 2005; Siebold et al., 2005; Vanoni et al., 2012).

On the opposite face of the protein a second basic patch is found (Figure 2.5, panels A and B), in which several basic residues are conserved among MICALs (K115, R116, R121, H122, R158, K221, R356 in Figure 2.1, panel A). Structural comparison of the N-terminal domain of MICAL with PHBH reveals that this second positively charged region may define the NADPH binding site (Figures 2.3, panel A and 2.5,

panels A and B; Vanoni et al., 2012). NADPH binds to PHBH in an extended conformation (Wang et al., 2002) stabilized by interactions with residues R33, Q34, R42, H162, R269, I164 that could correspond to K115, R116, R121, K221, V223 and S368 of MICAL (Figure 2.3, panel A). FAD also assumes an extended conformation with its adenylate moiety bound to the Rossman fold identified by the GXGXXG motif at position 91-96 of MICAL (Figures 2.1, panel A; 2.3, panel A and 2.4; Wierenga et al., 1986, 1979; Schreuder et al., 1989;) and its ribityl 3'OH is bound to residues 384-390 corresponding to Eggink's second FAD consensus sequence (Figure 2.1, panel A). The dimethylbenzene and the pyrimidine ring of FAD are both exposed to the solvent on the two opposite faces of the protein.

The side chain of the conserved Trp400 stacks against the *re* face of the isoalloxazine ring of FAD and must undergo conformational changes to allow FAD reduction following NADPH binding. The *si* face of the isoalloxazine ring makes van der Walls interactions with Ile157 and a complex network of hydrogen bonds through its N5 with Asn123, Asn243, Thr291, Tyr293 and Asp360 (Siebold et al., 2005; Vanoni et al., 2012; Figure 2.5, panel C).

Incubation of the crystals containing the N-terminal domain of mouse MICAL1 with NADPH led to determine its structure in the reduced redox state (Siebold et al., 2005; PDB ID 2C4C, 1.45 Å resolution), which corresponds to the "flavin in" conformation of PHBH (Figures 2.4 and 2.5) as opposed to the conformation similar to the "flavin out" state of PHBH observed in the oxidized MICAL forms (Nadella, et al., 2005; Siebold et al., 2005; Vanoni et al., 2012). No NADP(H) was bound to the protein preventing the identification of its binding site. The rotation (≈20°C) of the C1-C2 bond of ribityl side chain of FAD led to the switch from the "out" to the "in" conformation. When the flavin is in the "in" conformation it is shielded from the solvent at the interface between the FAD and cap domain (Figures 2.4 and 2.5). The stacking interaction between the flavin and Trp400 is lost and also the polypeptide chain undergoes conformational changes in the secondary structure elements in the cap domain (Figures 2.4 and 2.5). The difference of the relative position of FAD and cap domain of the oxidized and reduced N-terminal domain of MICAL is larger than that observed for PHBH (Figure 2.4 and 2.5). The conformational changes from the "out" to the "in" state of flavin leads to the formation of a channel connecting the protein surface to the active site (Figure 2.5, panels A and B). In this conformation the reactive C4a and N5 positions of FAD become exposed to the solvent. The residues that define the channel are conserved in MICALs suggesting an important role for MICAL function (Figure 2.1, panel A). The channel is located on the same side of the positively charged N-terminal region of the protein (Figure 2.5, panels A and B), which, in addition to the presence of the CH and LIM domains supports the hypothesis that the substrate of the N-terminal flavoprotein domain of MICAL could be the side-chain of an acidic protein. The side-chain of the protein substrate could reach the active site of MICAL through the tunnel when protein is the "flavin in" conformation upon its reduction by NADPH. Base on the similarity with PHBH the side-chain could be modified by specific hydroxylation. However, the hypothesis that the flavoprotein domain acts through a NADPH oxidase activity should not be discussed.

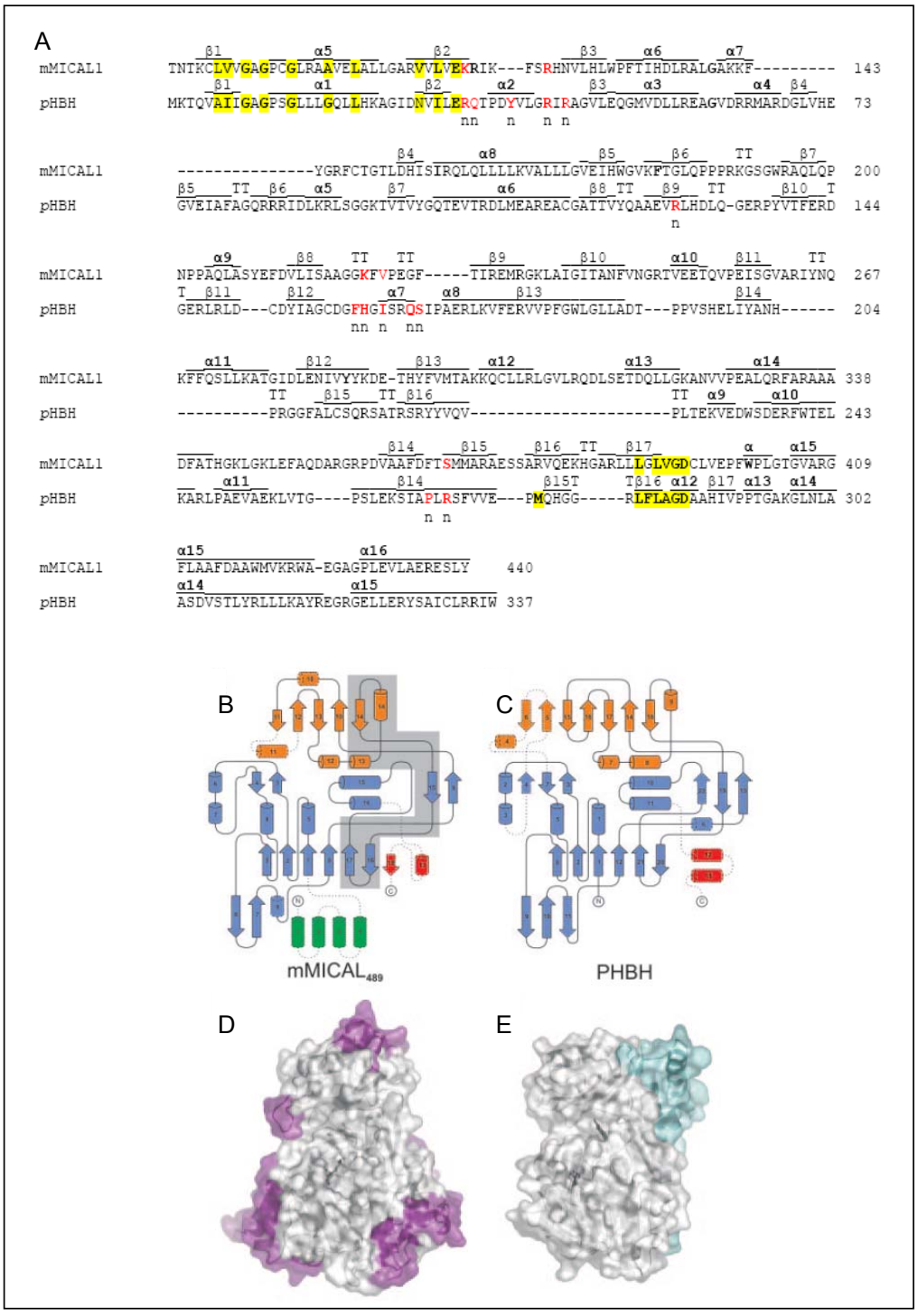

Figure 2.3. Sequence comparison between the N-terminal flavoprotein domain of mouse MICAL1 and p-hydroxybenzoate hydroxylase. Panel A: The 83-440 region of mouse MICAL1 is compared with the full-length *Pseudomonas fluorescens* p-hydroxybenzoate hydroxylase. The secondary structure elements are indicated (β strands, α helices and β turns (TT). The alignment takes into the account the three-dimensional structures of the proteins (2BRA (Nadella et al., 2005); 2BRY (Siebold et al., 2005) for mouse MICAL1 and 1 PBE (Schreuder et al., 1989) for PHBH). Colour code: highlighted in yellow, conserved residues in the consensus sequence of the binding site of the adenylate portion of FAD and in the second consensus sequence for FAD binding (Eggink et al., 1990); red, PHBH residues involved in the binding of NADPH (n) and conserved residues of MICAL in equivalent position (Vanoni et al., 2012). The topology of the N-terminal domain of mouse MICAL1 (panel B) and of PHBH (panel C) is shown, in which the shaded area indicates the region that is deleted in MICAL1 isoform b. Note that this species has not been experimentally detected in cells. Solvent-accessible surface of MICAL (panel D) and of PHBH (panel E) with their unique parts are shown in purple for MICAL and in cyan for PHBH (Siebold et al ., 2005).

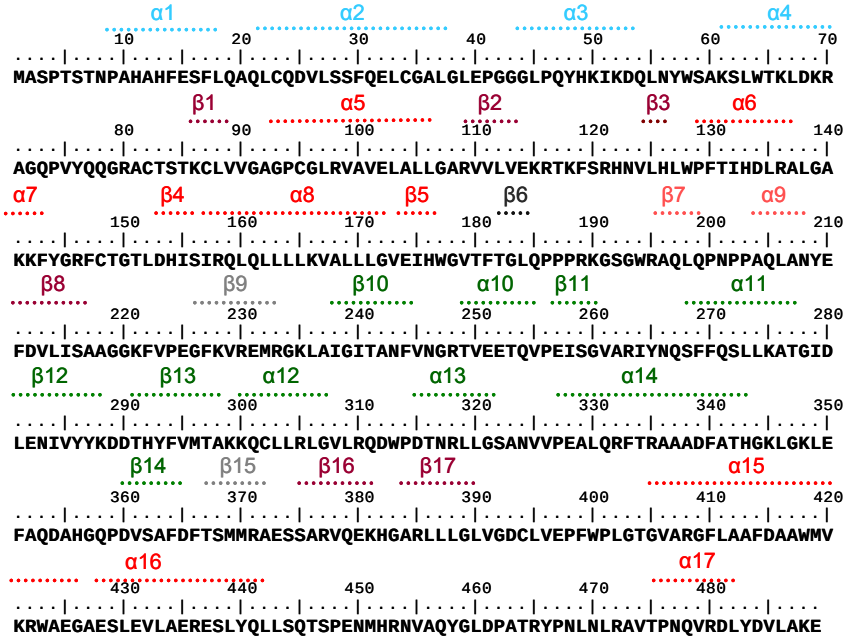

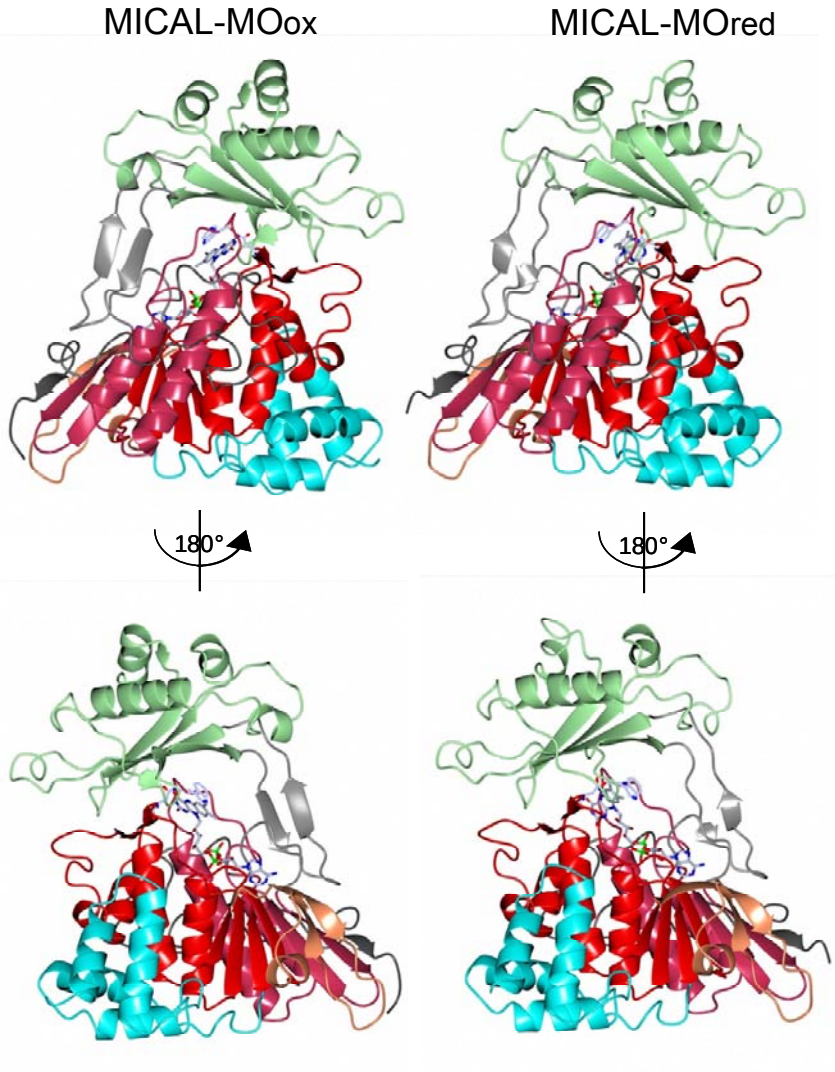

Figure 2.3 Comparison of the primary, secondary and ternary structures of the flavoprotein monooxygenase-like domain of mouse MICAL1. Left panel: Sequence of the N-terminal domain of human MICAL1, in which the residues corresponding to secondary structure elements are identified based on its three-dimensional structure. Right panel: The structures of the "as isolated" mouse MICAL1 monooxygenase domain in the oxidized ("flavin out") state (2BRY, chain A, MICAL-MOox) and of the NADPH-reduced ("flavin in") species (2C4C, chain A, MICAL MOred) as determined by Siebold *et al.* (2005) are shown in two orientations. Color scheme is as follows: blue, residues 1–85; red, residues 86–177, 208–217; coral, 178–208; grey, 218–237 (β9) and 366–375 (β15); green, 238–365; dark red, 376–442; dark grey, 443–489. FAD, Trp400 and Asn123 are shown in sticks with carbon in light grey, nitrogen in blue, oxygen atom in red and phosphorus in green. The CCP4MG program was used to generate the figure (Vanoni et al., 2012)

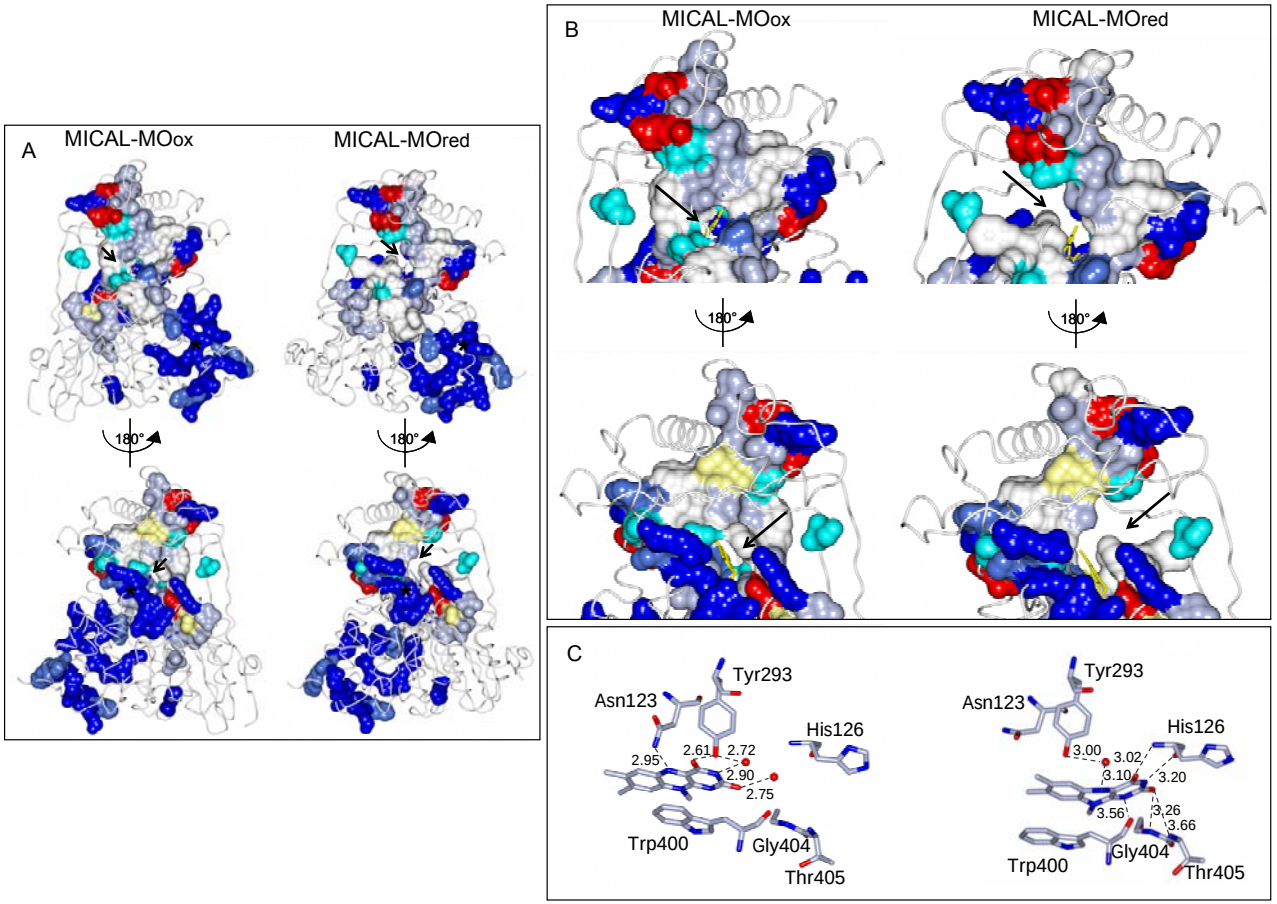

Figure 2.5. Comparison of the "flavin out" (MICAL-MO$_{ox}$) and "flavin in" (MICAL-MO$_{red}$) conformations. Panel A: The stars indicate the positively charge residues (spheres) in the 1-86 region (upper panels) and those in the putative NADPH binding site (lower panels). Panel B: detail of panel A. The arrow indicates the solvent exposed part of FAD, and the opening of the tunnel that leads to the putative active site in the reduced form. Panel C: FAD environment in the "flavin out" and "flavin in" conformations. The view is obtained by vertically flipping the models in Figure 2.2 with an approximately 45° rotation. The FAD ribityl side chain is cut at C1'. The conserved residues surrounding the FAD isoalloxazine ring (arrows) and comprising residues 121-130, 278-300 and 390-405 (red stars in Figure 2.1) are shown. Color code: light grey, Phe, Tyr, Trp; grey, Gly, Ala, Val,Leu, Ile; cyan, Ser, Thr, Gln, Asn; light yellow, Cys, Met; blue, Arg, Lys, His; red, Asp,Glu. The view is similar to that in Figure 2.2 to highlight the formation of the tunnel leading from the protein surface to the isoalloxazine ring in the "flavin in" (right) conformation (Vanoni et al., 2013).

The structures of the isolated CH domain of human MICAL1 (PDB ID 2DK9 Sun et al., 2006; PDB ID 1WYL Jin et al., 2006), MICAL2 (PDB ID 2E9K, no accompanying publication) and MICAL3 (PDB ID 2D88, no accompanying publication) have been solved by NMR, confirming its sequence-based identification.

The CH domain is a protein interaction domain mainly found in actin- and microtubule-binding proteins. Invariant core residues define the CH domain, which are crucial for the stabilization of its three-dimensional structure. Three types of CH domains have been identified (Gimona et al., 2002). One type 1 and one type 2 CH domain form the F-actin binding region of several cytoskeleton proteins, (such as spectrin, α-actinin); the overall affinity for F-actin is in the low μM range (Gimona et al., 2002). Tandem CH domains can bind F-actin thanks to their conformational changes from an "open" (free state) to a "closed" conformation upon interaction with the actin filament (Galkin et al., 2012). The single type 2 CH domain is not sufficient to interact with F-actin. On the contrary type 1 CH domain alone is able to bind F-actin, but with a 10-fold lower affinity compared to the complete actin binding region composed by type 1 and type 2 CH domains. Thus, in the tandem type1-type2 CH domain, the type 2 CH region that has not an intrinsic ability to interact with F-actin, may function an initial docking site that contributes to the interaction with F-actin. This role has been also proposed for type 3 CH domains (Galkin et al., 2012).

The architecture of the CH domain is conserved among the three types of domains. The three-dimensional structure of the CH domain of human MICAL1 consists of six α-helices and one 3_{10} helix. The CH domain is composed by four long helices (A, B, D and F alpha-helix in Figure 2.6, panel A) and stabilized by hydrophobic interactions (Sun et al., 2006). Helix A forms the first hydrophobic region that makes contacts with residues in helix B, D and F. The presence of a crossing angle of 70° between the first and third helix is typical of the type 2 CH domain. The fold of the CH domains of human MICAL2 (PDB ID 2E9K; Tomizawa 2007, no associated publication) and of human MICAL3 (PDB ID 2D88; Tomizawa 2006, no associated publication) is very similar to that of the CH domain of human MICAL1 (not shown). The type 2 CH domain alone can not bind F-actin. Thus, it has been proposed that the CH domain of MICAL may assist or establish an initial interaction with F-actin (protein-substrate) favoring that with the N-terminal FAD-containing domain (Siebold et al., 2005; Sun et al., 2006).

The LIM domain was named by its initial discovery in three homeodomain proteins Lin11, Isl-1 and Mec-3 (Bach 1990); LIM domains are composed of ≈55 amino acids with the general sequence $CX_2CX_{16-23}HX_2CX_2CX_{16-23}CX_2C$, where C is cysteine, H is histidine and X is any amino acid. LIM domains bind two Zn^{++} ions through the conserved Cys and His residues. LIM domains are found in both nuclear and cytoplasmic proteins where they function in molecular recognition to assemble multiprotein complexes (Bach et al., 2000). The three-dimentional structure of the isolated LIM domain of human MICAL1 has been solved in 2005 (PDB ID 2CO8, Sato (2005), no associated publication; Figure 2.6, panel B), showing the typical structural features of the LIM domain. It is composed by two zinc fingers formed by 2 antiparallel β-hairpins. The first zinc finger contains β-hairpin 1 and 2 and the second zinc finger

contains β-hairpin 3 and 4. The conserved Cys and His residues (Figure 2.1, panel B) of the tetrahedral zinc coordination establishes the secondary structure of the LIM domain (Kadrmas 2004) (Figure 2.6, panel B). The C- and N-terminal regions of the domain do not have a secondary structure (Figure 2.6, panel B). Overall, the LIM domain has an elongated conformation compared to that of the CH and N-terminal domains of MICAL (Figures 2.6, panel B).

Based on the sequence analysis several coiled-coil motifs have been predicted in the C-terminal region of MICAL. The isolated C-terminal region of MICAL has not been produced and purified yet so that the three-dimensional structure is not available. However, it is well known that the coiled-coil motifs form amphipathic α-helixes, which mediate protein-protein interactions by binding to the coiled-coil motif of the interactor (an example of coiled-coil motif formed by residues 860-960 of the heavy and light chain of myosin (PDB ID 1I84, Wendt et al., 2001) is shown in Figure 2.6, panel C).

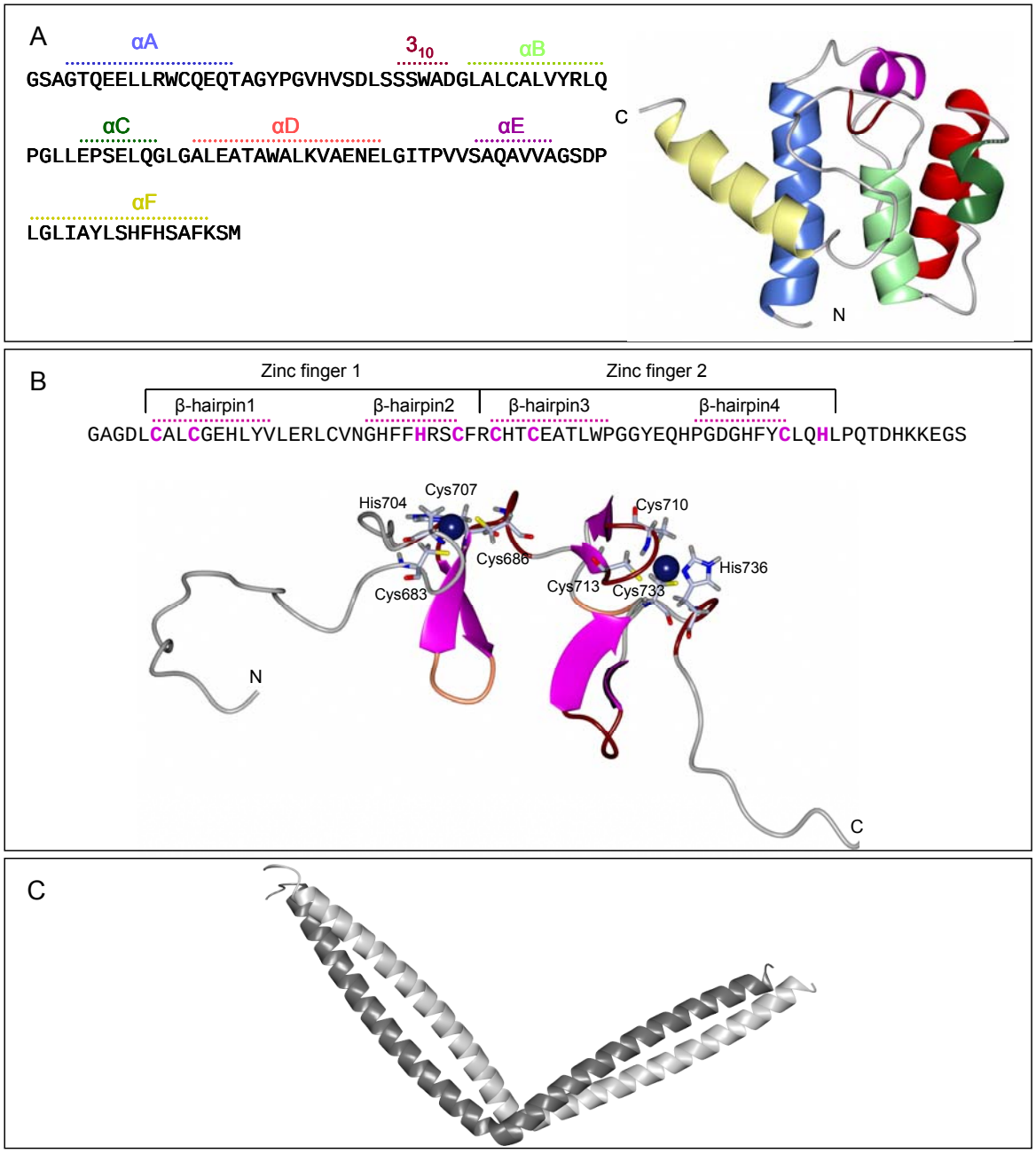

Figure 2.6. Three-dimensional structures of the CH, LIM domains and coiled-coil motif. Panel A: The secondary structures elements of the CH domains are indicated (upper panel) in the CH domain sequence of human MICAL1 (upper panel). The three-dimensional structure of one chain (chainA) of the CH domain of human MICAL1 (PDB code 2KD9; Sun et al 2006) is shown. Color code: blue, helix A; light green, helix B; dark green, helix C; red, helix D; purple, helix E; yellow, helix F; dark red, 3_{10}, helix; unstructured region, grey. The N- and C-terminus are indicated. Panel B: The conserved Cys and His residues of the consensus sequence of the LIM domain are in bold and purple; residues forming the 4 β-hairpins and the 2 zinc finger are also indicated. In the three-dimentional structure of chain 1A of the LIM domain of human MICAL1 obtained by NMR (PDB code 2CO8) the Cys and Hys residues (in sticks) coordinating the binding of Zn^{++} (dark blue sphere) are shown. Color code: purple, β-sheet; β-3 turn, coral; β-5 turn, dark red. Panel C: coiled-coil motif formed by residues 860-960 of the heavy (dark grey) and light (light grey) chains of myosin (PDB ID 1I84, Wendt et al., 2001). To draw the figures the program CCP4 has been used (McNicholas et al., 2011).

3. Engineering the DNA coding for human MICAL1 and the truncated forms containing the MO, CH and LIM domains (MOCHLIM)

3.1. Introduction

The DNA encoding human MICAL1 has been engineered for the production of the full-length protein (MICAL) and the form lacking the C-terminal region (MOCHLIM) in *E.coli* cells to study how the catalytic properties of the N-terminal MO domain can be modulated by the additional domains, namely the CH, LIM domains and the C-terminal region containing the Pro/Glu-rich regions and the coiled coil motifs that may mediate protein-protein interactions. The engineering of DNA to express the human MICAL1 form containing both the MO and CH domains was previously done (Vitali T 2012) and its characterization was extended during this work.

The cloning strategy for MOCHLIM and MICAL was the same as that used for the production of the isolated MO domain (Zucchini et al., 2011) and MOCH. The pDON-MICAL1 plasmid was used as the template for the PCR amplification of fragments of interest. The PCR primers (Table 10.3) were designed to introduce at the 5' end of the amplification product *Eco*RI and *Nde*I restriction sites and at the 3' end a stop codon (TAG or TAA) between engineered *BamH*I and *Xho*I restriction sites. The presence of such restriction sites allowed us to clone the PCR product in a pET23b vector using *Nde*I and *Xho*I digestion for the expression of the C-terminally His_6-tagged fusion protein. *Nde*I and *BamH*I restriction could be used for the production of the protein without tag. The PCR product could also be cloned into pET28b vector using the *Nde*I and *BamH*I restriction enzymes to obtain the protein form with a N-terminal His_6-tag (Figure 3.1and 3.2). For the amplification of the DNA encoding MOCHLIM, two reverse primers were synthetized (MOCHLIMRev2 and MOCHILMRev4, Table 10.3) for the production of two protein forms spanning residues 1-771 and 1-783, respectively.

The isolated MO domain was produced "as is" and with the hexahistidinyl-tag at the C-terminus or at the N-terminus of the protein to determine (i) the effect of the His_6-tag and of its position on the properties of the MO domain; (ii) the best protein form in terms of stability, activity and purification yield. The three MO forms showed similar properties (Zucchini et al., 2011), indicating that the presence of the His_6-tag did not alter the stability and the activity of the MO domain. The form carrying the C-terminal His_6-tag (MO-His) could be purified in larger quantities compared to the others and this form was used for MICAL-MO characterization (Zucchini et al., 2011). For these reasons MICAL, MOCHLIM and MOCH forms were first produced with the hexahistdinyl-tag at the C-terminus of the protein.

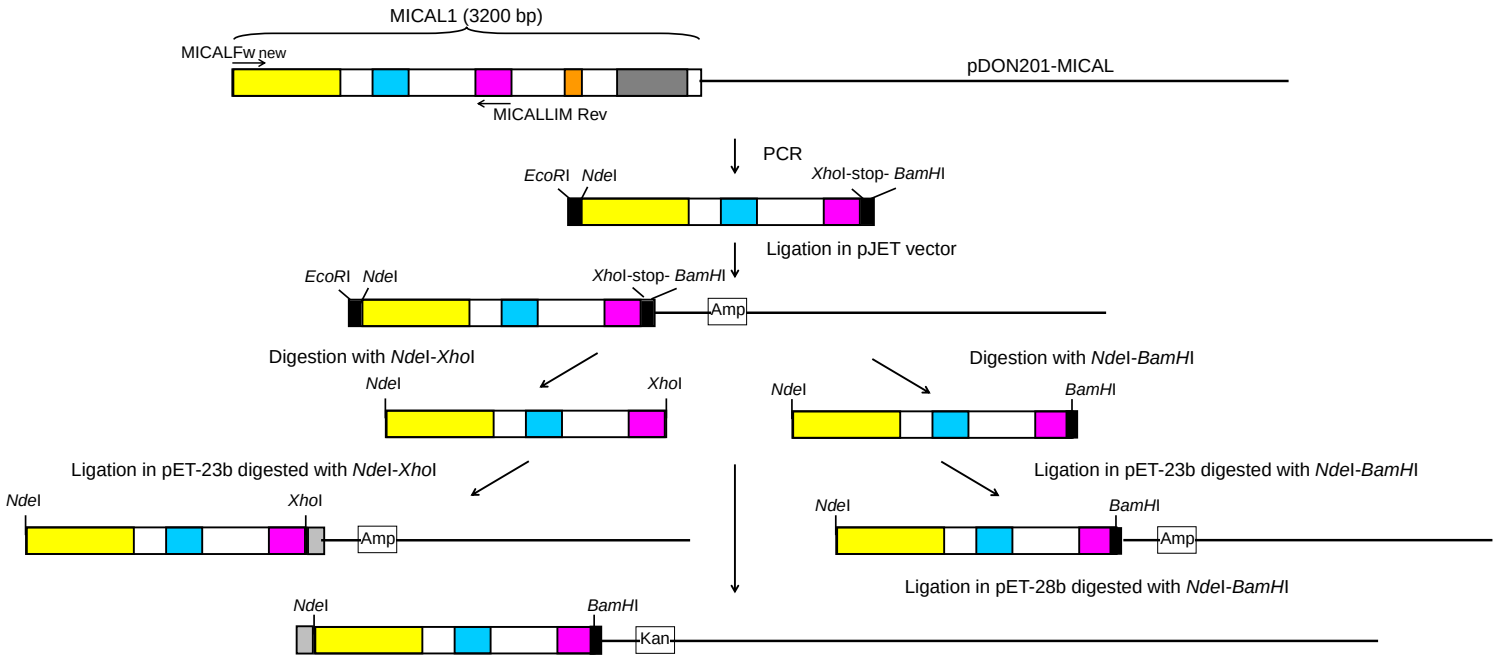

Figure 3.1. Scheme of the construction of plasmids for the production of MOCHLIM forms of human MICAL1 without or with a His_6-tag at the C- or N-terminus of the protein. Color code is: MO domain, yellow; CH domain, cyan; LIM domain, purple; Pro rich region, orange; coiled-coil motif, dark grey; His_6-tag, light grey.

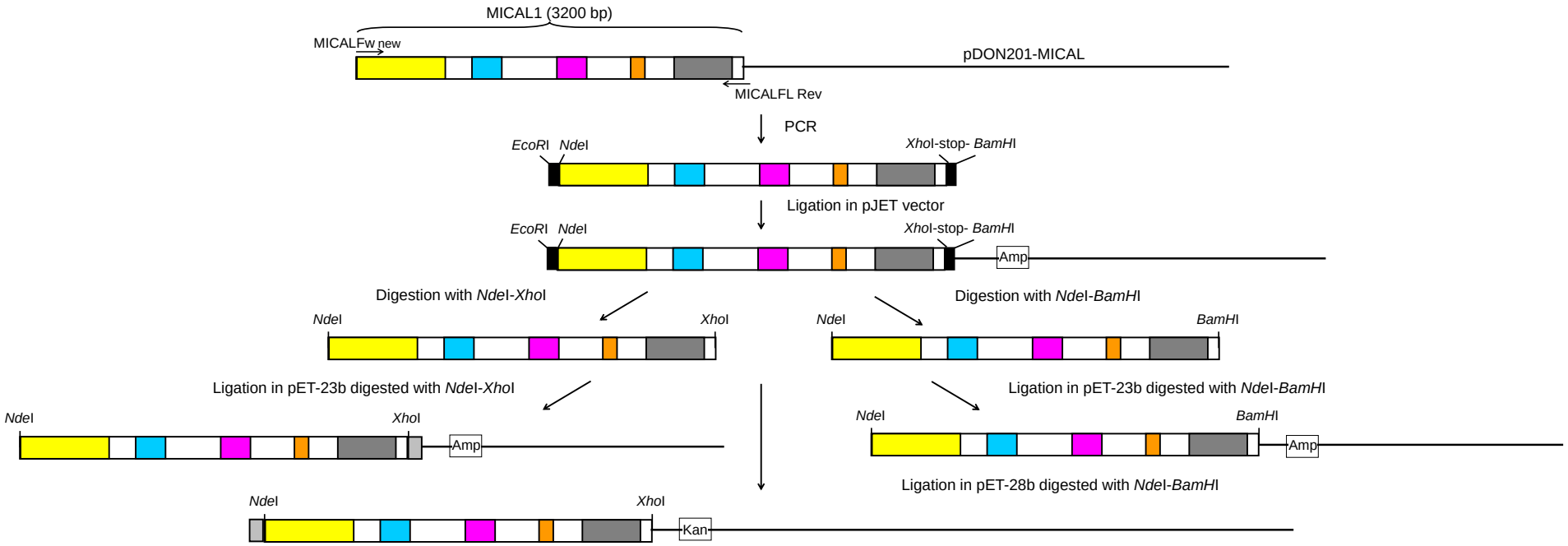

Figure 3.2. Scheme of the construction of plasmids for the production of human MICAL1 without or with a His_6-tag at the C- or N-terminus of the protein. Color code is as in Figure 3.1.

3.2. PCR amplification and cloning of DNA encoding human MICAL1 and MOCHLIM forms in pJET1.2 blunt-end vector

pDON-MICAL1 plasmid encoding the full-length human MICAL1, received from Prof. Jeroen Pasterkamp (University Medical Center Utrecht, NL), was used as the template for the amplification of the DNA fragments of interest as described in Materials and Methods (Chapter 10). PCR products encoding MOCHLIM (1-771 and 1-783) and MICAL (1-1068) were purified from agarose gels to check their size and to determine their concentration by comparing the intensities of the sample bands with the signals of samples of linearized pUC18 vector loaded at known amounts on the same gel (Figure 3.3). The fragments had sizes similar to the expected ones: 2238 bp for MOCHLIM2, 2247 bp for MOCHLIM4 and 3200 bp for MICAL (Figure 3.3). All fragments were obtained in quantities sufficient for further work (Figure 3.3).

The fragments were cloned into pJET1.2 blunt-end vector, as described in Materials and Methods, to obtain the corresponding pJET derivatives (pJET-MOCHLIM2, pJET-MOCHLIM4 and pJET-MICAL), which were transformed into *E.coli* DH5α cells for their propagation, purification and maintenance. Transformants were selected on LB-Amp plates and 10-20 of the resulting clones were analyzed by colony PCR using the pJETFw and pJETRev primers included in the pJET1.2 blunt-end cloning kit (Table 10.4). All the clones analyzed for pJET-MOCHLIM2 and pJET-MICAL and six clones for pJET-MOCHLIM4 plasmids were positive. The plasmids from two of the positive clones for each construct were purified and analyzed by restriction enzymes digestion followed by agarose gel electrophoresis to verify the presence of the correct restriction sites introduced by PCR amplification and the size of the DNA fragments. The purified plasmids contained *BamH*I, *Nde*I, and *Xho*I restriction sites as expected (Figure 3.4). An exception was pJET-MOCHLIM4 plasmid from clone number 6 that lacked *BamH*I and one of the *Xho*I restriction site (Figure 3.4). The inserts of the samples (pJET-MICAL clone 1 and 2, pJET-MOCHLIM2 clone 1 and 2 and pJET-MOCHLIM4 clone 7, Figure 3.4) were sequenced to confirm the presence of the desired mutations and to rule out undesired ones. The pJETFw and pJETRev primers were used first, then sequencing was completed with *ad hoc* designed primers (Table 10.4). The sequence of each selected clone was correct. Thus, we continued the work with clone 1 for pJET-MOCHLIM2, clone 7 for pJET-MOCHLIM4 and clone 2 for pJET-MICAL.

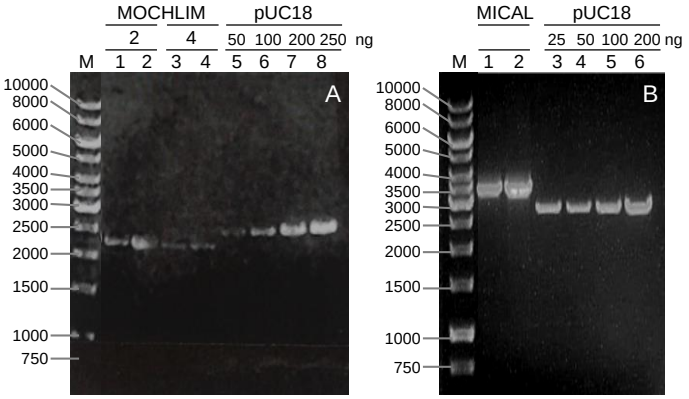

Figure 3.3 Analysis of PCR products of the amplification of DNA fragments encoding MOCHLIM2, MOCHLIM4 and MICAL. Agarose gel electrophoresis of the products of the amplification reaction reaction of the DNA fragments enconding MOCHLIM2 and MOCHLIM4 (panel A) and MICAL1 (panel B) after purification. Known amounts of linearized pUC18 plasmid were also loaded on the gel to allow quantification of the PCR products.

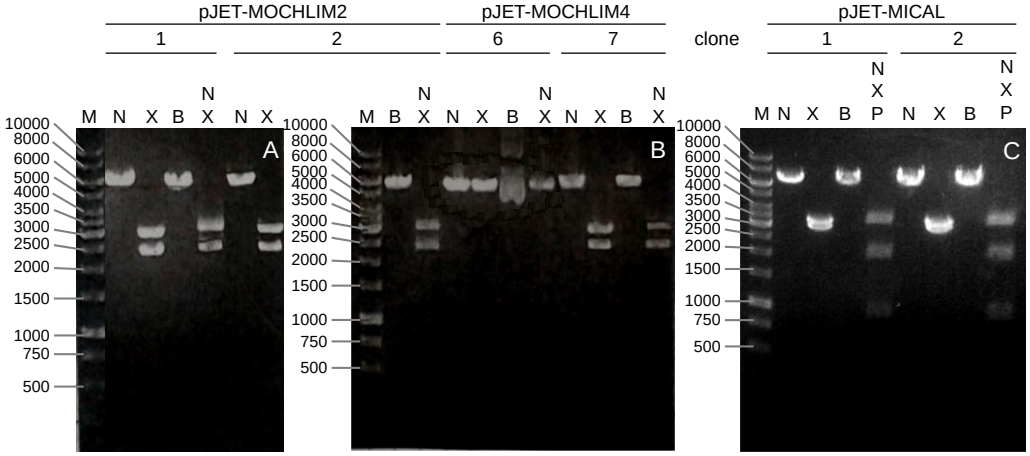

Figure 3.4. Restriction analysis of pJET-MOCHLIM2, pJET-MOCHLIM4 and pJET-MICAL clones. Single digestion with *Nde*I (N), *Xho*I (X), *BamH*I (B); double digestion with *Nde*I and *Xho*I (NX) and triple digestion with *Nde*I, *Xho*I and *Pvu*I of 300 ng of pJET-MOCHLIM2, pJET-MOCHLIM4 and pJET-MICAL plasmids.

3.3. Subcloning of MOCHLIM2, MOCHLIM4 and MICAL DNA fragments into the pET23b vector

The pJET derivatives were used for the construction of the pET23b derivatives (pET-MOCHLIM2, pET-MOCHLIM4 and pET-MICAL) for the production of the C-terminally His_6-tagged fusion protein. The pJET plasmids and the pET23b vector were digested with *Nde*I and *Xho*I. For the construction of pET-MICAL plasmid, the pJET derivative was also digested with *Pvu*I to distinguish between the digested pJET vector (2900 bp) and the DNA fragment encoding the enzyme (3216 bp) that lack *Pvu*I sites. The fragments of interest were purified from excised agarose gel bands and quantified following analytical electrophoresis. The procedure yielded the plasmids in quantities sufficient for further work.

The DNA fragments encoding the MICAL forms were ligated with the digested pET23b vector using different vector/insert molar ratios (1:2 and 1:4) and 60 ng of vector. At the end of the ligation, aliquots (200 µl) of *E.coli* DH5α cells, previously made competent with the RbCl method, were transformed with 4 µl of ligation mixture. The transformants were selected on LB-Amp plates. Analysis of the plates indicated that the ligation was successful. The number of colonies on the plates inoculated with cells transformed with the complete ligation mixture was much higher than that obtained for the negative control (ligation mixture without insert). To identify the clones containing the fragments of interest we carried out colony PCR on several (10-20) colonies using T7 promoter and T7 terminator primers that anneal onto the pET23b vector. We expected amplification products of 2316 bp for MOCHLIM2, 2342 bp for MOCHLIM4 and 3202 bp for MICAL. We obtained 10 positive clones for both pET-MOCHLIM2 and pET-MOCHLIM4 and 17 positive clones for pET-MICAL. Two for each one of the plasmids from the positive colonies were purified and subjected to restriction analysis that demonstrated the presence of the correct restriction sites and that the size of the fragments was similar to the expected one (Figure 3.5). Therefore, pET-MOCHLIM2 clone 2, pET-MOCHLIM4 clone 1 and pET-MICAL clone 14 were used for the expression of MOCHLIM (1-771 aa), MOCHLIM (1-786 aa) forms and full length MICAL (1-1068 aa) of human MICAL1 (Figure 3.6).

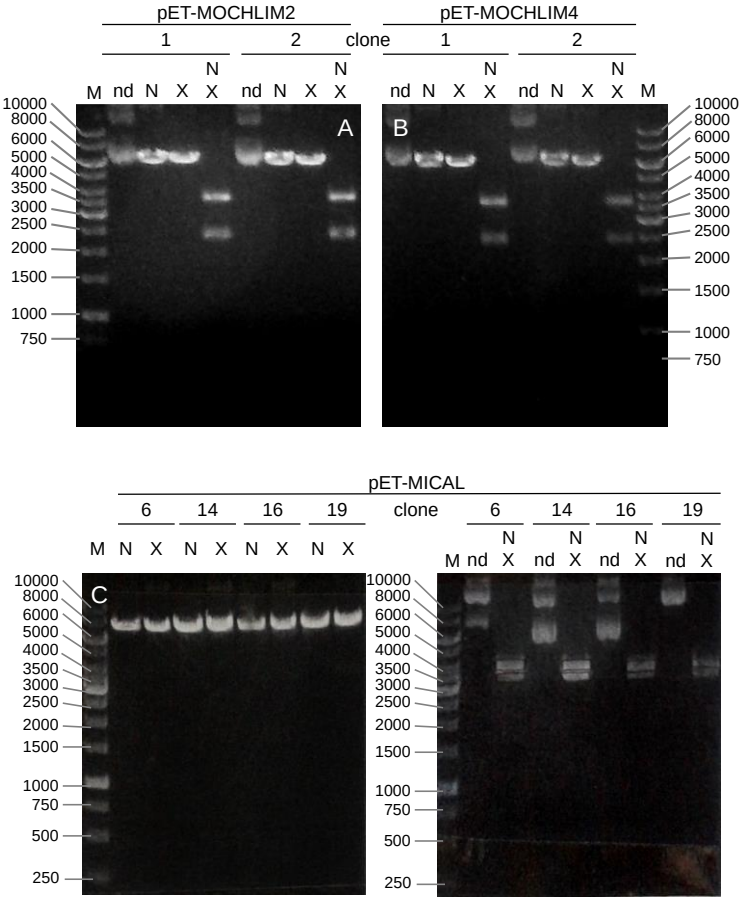

Figure 3.5. Restriction analysis of pET-MOCHLIM2, pET -MOCHLIM4 and pET-MICALFL clones. 300 ng of plasmids pET-MOCHLIM2 (panel A), pET-MOCHLIM4 (panel B) and pET-MICALFL (panel C) plasmids were loaded as is (nd, not digested); after single digestion with *Nde*I (N), *Xho*I (X); double digestion with *Nde*I and *Xho*I (NX).

A

Human MICAL1 protein sequence (code GenBank: BAB86289.1)

```
MASPTSTNPAHAHFESFLQAQLCQDVLSSFQELCGALGLEPGGGLPQYHKIKDQLNYWSAKSLWTKLDKRAGQPVYQQGRACTSTK
CLVVGAGPCGLRVAVELALLGARVVLVEKRTKFSRHNVLHLWPFTIHDLRALGAKKFYGRFCTGTLDHISIRQLQLLLLKVALLLG
VEIHWGVTFTGLQPPPRKGSGWRAQLQPNPPAQLANYEFDVLISAAGGKFVPEGFKVREMRGKLAIGITANFVNGRTVEETQVPEI
SGVARIYNQSFFQSLLKATGIDLENIVYYKDDTHYFVMTAKKQCLLRLGVLRQDWPDTNRLLGSANVVPEALQRFTRAAADFATHG
KLGKLEFAQDAHGQPDVSAFDFTSMMRAESSARVQEKHGARLLLGLVGDCLVEPFWPLGTGVARGFLAAFDAAWMVKRWAEGAESL
                                                        MO
                                                        |
EVLAERESLYQLLSQTSPENMHRNVAQYGLDPATRYPNLNLRAVTPNQVRDLYDVLAKEPVQRNNDKTDTGMPATGSAGTQEELLR
WCQEQTAGYPGVHVSDLSSSWADGLALCALVYRLQPGLLEPSELQGLGALEATAWALKVAENELGITPVVSAQAVVAGSDPLGLIA
              CH
              |
YLSHFHSAFKSMAHSPGPVSQASPGTSSAVLFLSKLQRTLQRSRAKENAEDAGGKKLRLEMEAETPSTEVPPDPEPGVPLTPPSQH
                                                                                LIM2
                                                                                |
QEAGAGDLCALCGEHLYVLERLCVNGHFFHRSCFRCHTCEATLWPGGYEQHPGDGHFYCLQHLPQTDHKKEGSDRGPESPELPTPS
       LIM4
       |
ENSMPPGLSTPTASQEGAGPVPDPSQPTRRQIRLSSPERQRLSSLNLTPDPEMEPPPKPPRSCSALARHALESSFVGWGLPVQS

PQALVAMEKEEKESPFSSEEEEEDVPLDSDVEQALQTFAKTSGTMNNYPTWRRTLLRRAKEEEMKRFCKAQTIQRRLNEIEAALRE
LEAEGVKLELALRRQSSSPEQQKKLWVGQLLQLVDKKNSLVAEEAELMITVQELNLEEKQWQLDQELRGYMNREENLKTAADRQAE
                                  CC
                                  |
DQVLRKLVDLVNQRDALIRFQEERRLSELALGTGAQG
```

B

MO	$_{1}$MASPTSTN.....TPNQVRDLYDVLAK$_{490}$	LEHHHHHH
MOCH	$_{1}$MASPTSTN.....AYLSHFHSAFKSMA$_{616}$	LEHHHHHH
MOCHLIM2	$_{1}$MASPTSTN.....HKKEGSDRGPESPE$_{771}$	LEHHHHHH
MOCHLIM4	$_{1}$MASPTSTN.....PELPTPSENSMPPG$_{783}$	LEHHHHHH
MICAL	$_{1}$MASPTSTN.....RRLSELALGTGAQG$_{1068}$	LEHHHHHH

C

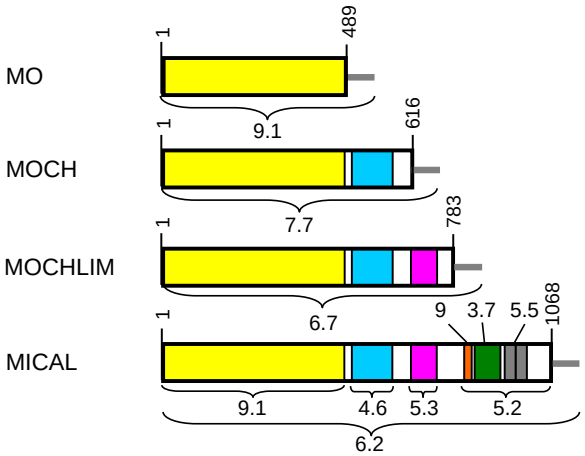

Figure 3.6. Amino acid sequence of human MICAL1 and of the truncated MO, MOCH and MOCHLIM forms. Panel A: Sequence of human MICAL1 (code GenBank: BAB86289.1) with the domains highlighted as follows: MO, yellow; CH, cyan; LIM, purple. Panel B: The starting and ending sequence of the MO, MOCH, MOCHLIM and MICAL forms produced in this work are indicated. The sequence introduced by cloning into pET23b vector is in grey. Panel C: The MO, CH and LIM domain, Pro- and Glu-rich and the coiled coil regions are indicated as in Figure 1.1. The grey bars indicate the His_6-tag at the C-terminus of the protein. The isoelectric points of the isolated domains and region are indicated, as well as that of the MICAL forms calculated with Compute pI/Mw tool (http://web.expasy.org/compute_pi/).

4. Expression and purification of human MICAL1 and of the MO, MOCH and MOCHLIM truncated forms

The isolated MO domain of human MICAL1 (MO) and the form containing both the MO and the CH domains (MOCH) can be produced in *E.coli* cells in a soluble form. The purified proteins contained FAD bound in stoichiometric amounts and were catalytically active (Zucchini et al., 2011; Vitali 2012; Chapters 5 and 6). For the overexpression of the MO form *E.coli* Rosetta(DE3) strain, which contains the pRARE plasmid encoding rare tRNA (AUA, AGG, AGA, CUA, CCC, and GGA for Ile, Arg, Leu, Pro and Gly tRNAs, respectively) and confers resistance to chloramphenicol (Chl), was used. The MOCH form was produced in *E.coli* BL21(DE3) strain containing the p18 plasmid (Castanié et al., 1997), which encodes the GroE chaperon and also confers resistance to Chl. In pilot experiments MOCHLIM2 (residues 1-771), MOCHLIM4 (residues 1-783) and full-length MICAL1 were produced in both *E.coli* Rosetta(DE3) and BL21(DE3, p18) cells. MO and MOCH forms were used as positive controls in each expression experiment to compare the quantity and, more importantly, the quality of the produced recombinant proteins.

4.1. Expression of human MICAL1 forms in E.coli cells

The pET derivatives encoding the MO, MOCH, MOCHLIM2, MOCHLIM4 and MICAL (pET-MO, pET-MOCH, pET-MOCHLIM2, pET-MOCHLIM4 and pET-MICAL) forms of human MICAL1 carrying the His_6-tag at the C-terminus of the protein, were used to transform competent *E.coli* Rosetta(DE3) or BL21(DE3, p18) cells. For pilot experiments, 2-6 l of *E.coli* cultures were set-up. The transformants were selected on LB-Amp-Chl plates and used to inoculate 50-200 ml of LB medium supplemented with Amp (0.1 mg/ml) and Chl (0.025 mg/ml, see Materials and Methods, Chapter 10). Cultures were grown at 25°C, under stirring, until the OD_{600} value was ≈1. The cell cultures were transferred at 4°C and the day after the cells were harvested under sterile conditions by centrifugation, resuspended in LB medium and used to inoculate four-six 2 l flasks containing 500 ml selective LB medium each, to obtain an initial OD_{600} value of ≈0.05. The cultures were grown at 25°C, under stirring. When the OD_{600} value was ≈1, the expression of the MICAL forms (and of GroE for BL21(DE3, p18) cells) was induced by adding isopropyl-β-thiogalactoside (IPTG, 0.1 mM final concentration). The cultures were transferred at 15°C and harvested after 24 h. To maintain selective pressure Amp (0.1 mg/ml) was added every 8-15 h after the IPTG addition. Immediately before and at different times after the induction of protein expression aliquots of the cell cultures were withdrawn and used to prepare total cell extracts for SDS-PAGE analysis.

All MICAL forms were produced in *E.coli* cells after the addition of IPTG, as observed by comparing the total cell extracts before (0 h) and after ITPG addition (3, 16, 24 h, Figure 4.1). The level of protein expression was similar for all MICAL forms when expressed in *E.coli* Rosetta(DE3) or BL21(DE3, p18) cells. In both cases MOCHLIM forms showed the lowest expression levels. The protein bands corresponding to MO, MOCHLIM and full-length MICAL had a molecular mass similar to the expected one (Table 5.1) indicating that the proteins were produced in their full-length form. On the contrary, the

observed molecular mass of ≈62 kDa for MOCH was significantly lower than the theoretical value of 68.5kDa, suggesting a possible degradation of the enzyme during its expression. As described in Chapter 5, previous analyses had demonstrated that MOCH was produced in the full-length form, but had an anomalous electrophoretic migration under denaturing conditions.

4.2. Small-scale purification of human MICAL1form

Pilot small-scale purifications of MOCHLIM and full-length MICAL on Ni-NTA Sepharose affinity chromatography were carried out from 2-6 g of *E.coli* Rosetta(DE3) or BL21(DE3, p18) cells to compare the quality of MICAL produced in the two *E.coli* strains. MO and MOCH forms were also purified as positive controls for *E.coli* Rosetta(DE3) and BL21(DE3, p18) cells growth, respectively, and for the purification procedure.

For MICAL, cells (2 g) were resuspended in homogenization buffer (buffer A, 50 mM Na-phosphate buffer, pH 7.5, 100 mM NaCl, 10% glycerol, supplemented with protease inhibitor cocktail (Sigma P8849; 50 µl/g cell), 1 mM 2-mercaptoethanol (2-ME), 1 mM PMSF and DNase) and disrupted by sonication. The crude extract obtained after centrifugation was incubated with Ni-NTA Sepharose resin (1 ml) on a wheel for 1 h at 4°C. The suspension was poured into a column and the resin was allowed to settle. The unbound proteins were collected in the flow-through (FT). The weakly bound proteins were removed by flowing 5 volumes each of buffer A (fractions 1-5) and of buffer A + 20 mM imidazole (fractions 6-10). Bound proteins were eluted by flowing 5 volumes of buffer A + 100 mM imidazole (fractions 11-15), followed by 5 volumes of buffer A + 500 mM imidazole (fractions 16-20; Figure 4.2). The fractions were analyzed by recording the absorption spectrum (Figure 4.2, panels A, C) and by SDS-PAGE (Figure 4.2, panels B, D); the NADPH oxidase activity of the selected fractions was also measured in 20 mM Hepes/KOH buffer, pH 7 in the presence of 100 µM NADPH, at 25°C.

MICAL eluted with 100 mM imidazole as demonstrated by the absorption spectra of the fractions that showed the presence of flavin (Figure 4.3, panels A and B). The peak fraction exhibited a NADPH oxidase activity with a specific activity, expressed as U/ml/A_{458}, of 0.4 that was ≈5-fold lower than that measured for the MOCH form used as a control. The SDS-PAGE analysis of the fractions (Figure 4.2, panels B, D) confirmed that the flavin signal was associated with MICAL that migrates as a ≈120 kDa band, which represented ≈70% of the total protein content (Figure 4.2, panels C, D).

These results indicated that MICAL was produced in a soluble form, with bound FAD, in both *E.coli* Rosetta(DE3) and in BL21(DE3) cells in the presence of GroE. Moreover, the absorption spectrum of the full-length MICAL was very similar to that of the MO domain under similar conditions, with the characteristic long-wavelength absorbance band in the 500-600 nm region (Figure 4.3).

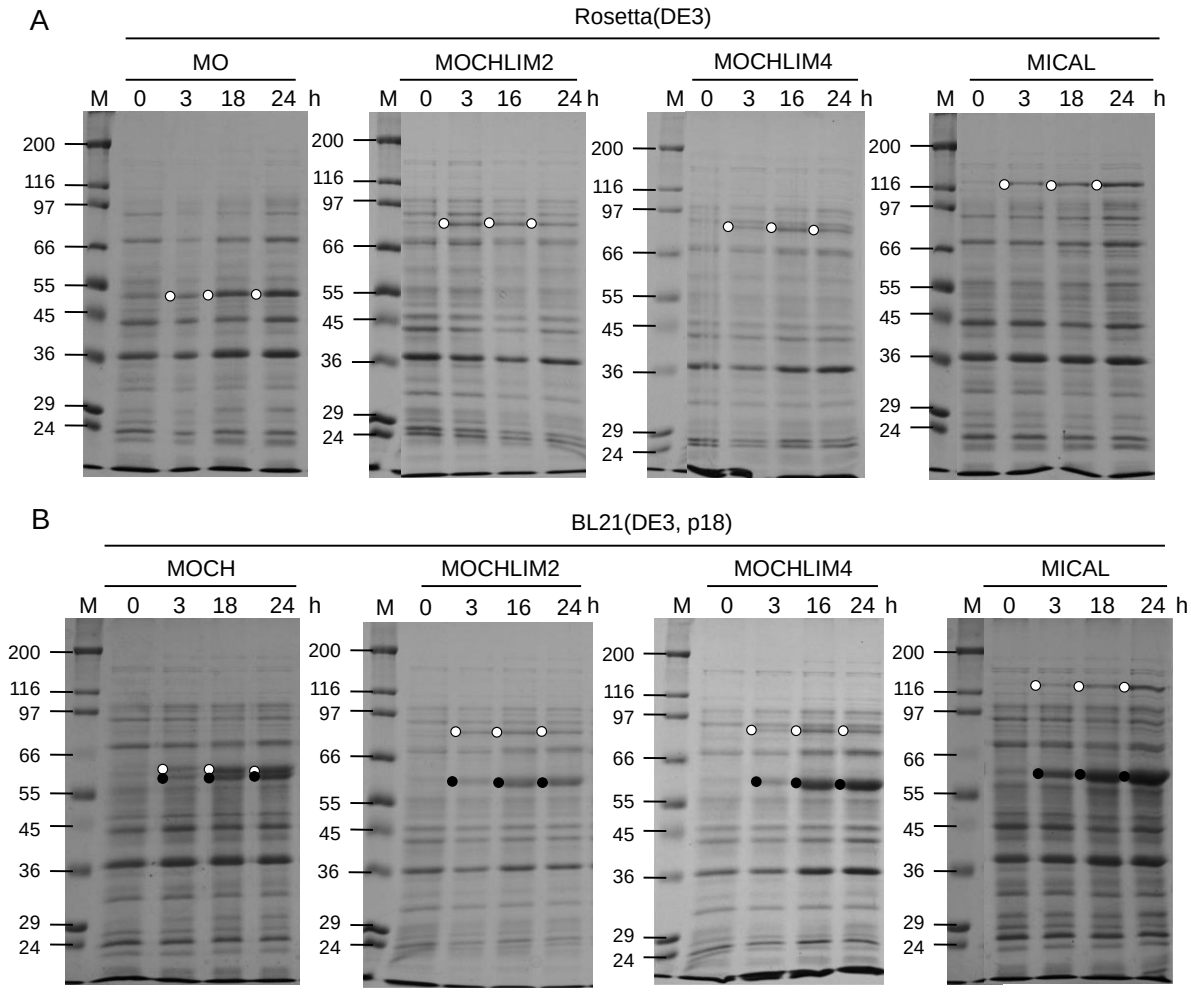

Figure 4.1. Production levels of human MICAL forms in E.coli cells. E. coli Rosetta(DE3) (panel A) or BL21(DE3, p18) (panel B) cells harboring the pET-derivatives for the production of human MICAL1 and MOCHLIM forms were grown in 0.5 l LB supplemented with 0.1 mg/ml ampicillin and 0.025 mg/ml choloramphenicol up to an OD_{600} of ≈1. The temperature was lowered to 15°C and IPTG (0.1 mM final concentration) was added. Small aliquots of the culture were harvested before IPTG addition (0 h) and at the indicated times after induction. For comparison, samples obtained by culturing *E. coli* Rosetta(DE3) and BL21(DE3, p18) cells harboring the pET-derivatives for the production of MO and MOCH, respectively, are shown. Aliquots of total cell extracts were analyzed by SDS-PAGE on 10% acrylamide+bis-acrylamide gels. The empty circles indicate the bands corresponding to the MICAL forms; the full circles indicate the bands corresponding to GroEL (59.7 kDa) encoded by p18. M, standard proteins of mass indicated in the figure in kDa.

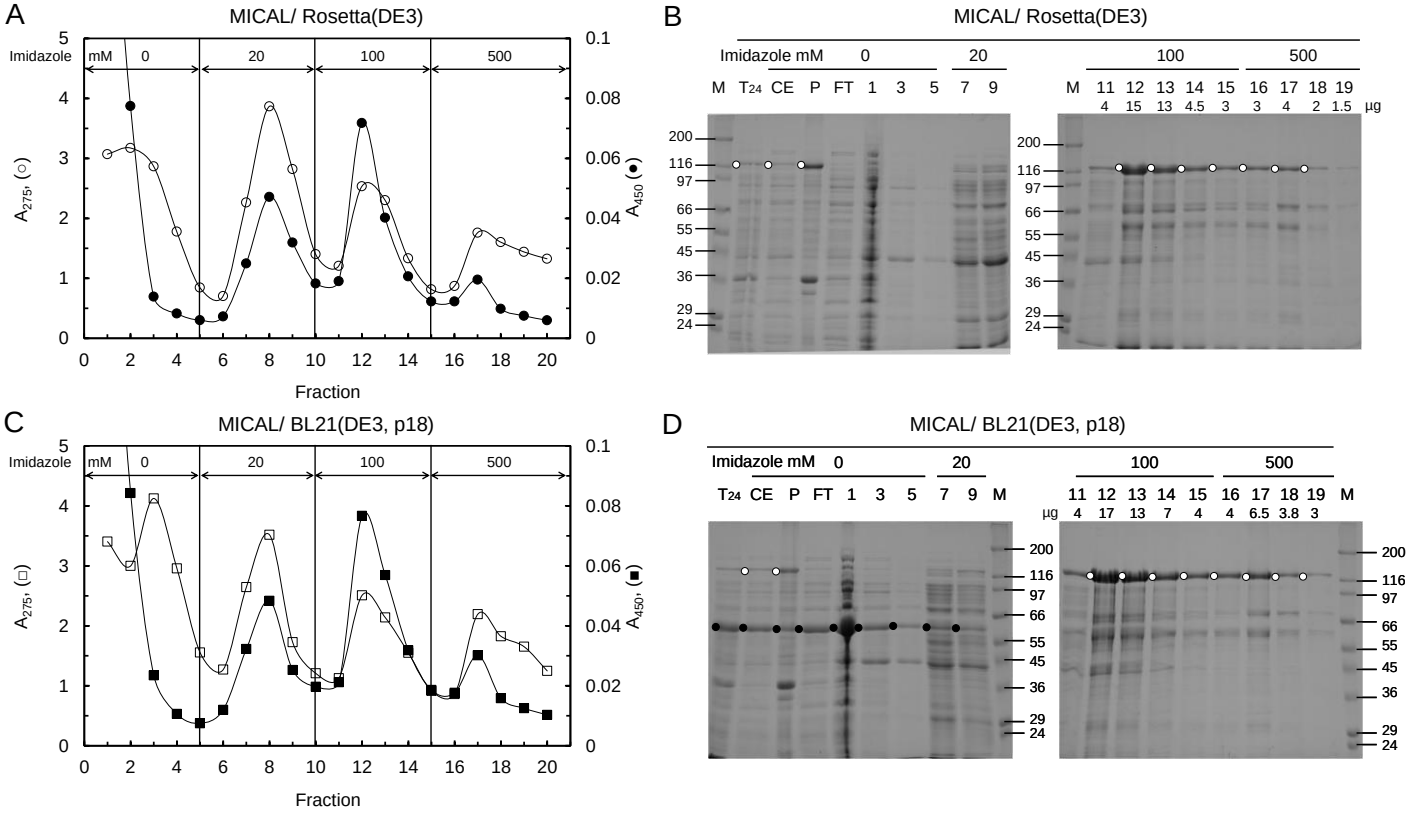

Figure 4.2. Small-scale purification of human MICAL1 – Ni-NTA Sepharose affinity chromatography. The homogenate from 2 g of *E.coli* Rosetta(DE3) (panels A and B) and BL21(DE3, p18) (panels C and D) cells was incubated with 1 ml of Ni-NTA Sepharose at 4°C for 1 h. The resin was packed into a column. The bound MICAL was eluted by increasing imidazole concentration (0, 20, 100 and 500 mM). Panels A and C: elution profile showing absorbance values at 275 nm (empty symbols) and at 450 nm (full symbols). Panels B and D: SDS-PAGE analysis on 10% (AcA + bisAcA) gels of aliquots of: total cell extract (T_{24}); crude extract (CE); pellet obtained after centrifugation of the homogenate (P); unbound proteins collected during sample loading (column flow-through, FT); aliquots of individual fractions numbered as in panels A and C; M, standard proteins of mass indicated in the figure in kDa. The quantity of MICAL loaded (µg) was calculated from the absorbance at 450 nm using the extinction coefficient of MO (8.1 $mM^{-1}cm^{-1}$) and the theoretical mass of MICAL (119 kDa).

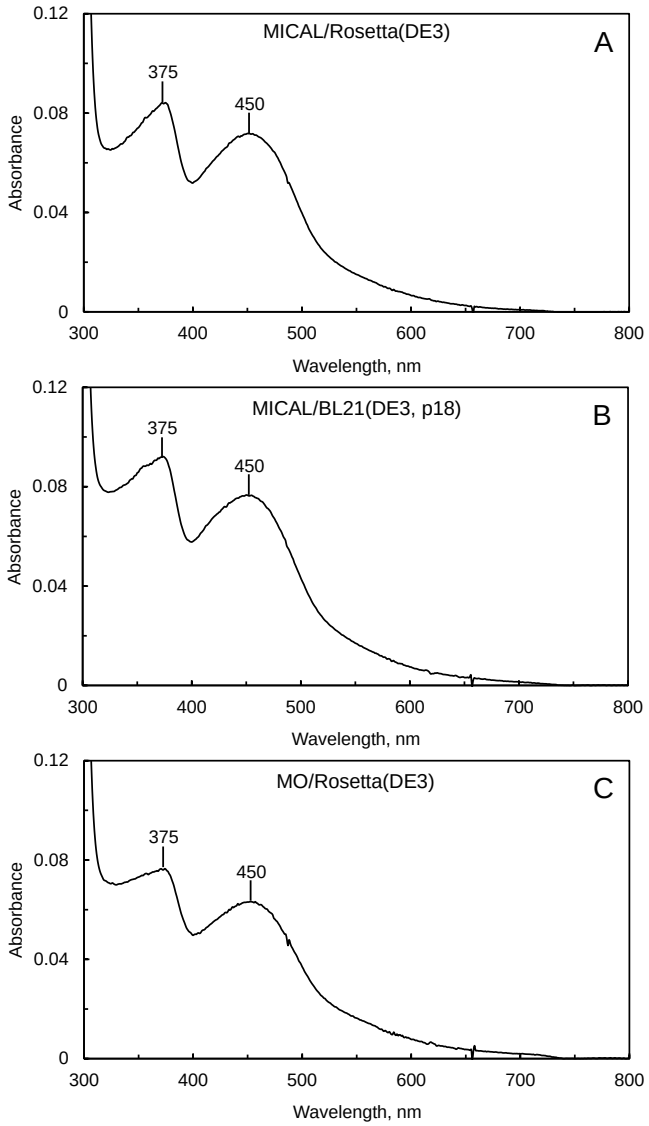

Figure 4.3. Absorption spectra of MICAL and of the isolated MO domain after affinity chromatography on Ni-NTA Sepharose. Absorption spectra of fraction 12 eluted with 100 mM imidazole during the chromatographies shown in Figure 4.2. For comparison, panel C shows the spectrum of the corresponding fraction obtained by chromatographying *E.coli* Rosetta(DE3) cells that had expressed MO under same conditions.

MOCHLIM2 (residues 1-771) and MOCHLIM4 (residues 1-783) were produced at levels lower than MO, MOCH and full-length MICAL (Figure 4.1) in both *E.coli* strains tested. To determine the quality of protein forms produced both in *E.coli* Rosetta(DE3) and in BL21(DE3) in the presence of GroE small scale purifications were carried out starting from 6 g of cells.

For these experiments the procedure was that described for MICAL in the previous paragraph with minor modifications. The crude extracts (Table 4.1), were incubated with Ni-NTA Sepharose resin (2 ml) previously equilibrated in buffer A or, in subsequent experiments, in buffer A + 20 mM imidazole to minimize the non-specific binding of proteins. From the elution profiles (Figure 4.4, panels A, C, E, G) and SDS-PAGE analyses of the collected fractions (not shown), we concluded that MOCHLIM eluted with 100-200 mM imidazole. The flavin signal was associated with both MOCHLIM2 and MOCHLIM4 produced either in *E.coli* Rosetta(DE3) or in BL21(DE3, p18) cells (Figure 4.4, panels B, D, F, H). On the basis of the absorption spectra, fractions containing MOCHLIM were pooled, concentrated (Table 4.1 and Figure 4.4, panels B, D, F, H) and stored overnight on ice at 4°C to verify the stability and solubility of the enzyme preparations.

At this stage MOCHLIM preparations were stable after concentration and storage overnight on ice at 4°C independently from the protein form and from the *E.coli* background used for their production. The absorption spectra were similar to each other and to that of the MO domain at this stage of purification (Figure 4.4, panels B, D, F, H and Figure 4.3, panel C). The degree of purity of the enzyme preparations after affinity chromatography was also similar for MOCHLIM2 and MOCHLIM4 regardless of the *E.coli* strain used for their expression. MOCHLIM represented greater than 70% of the total protein present in the peak fractions. However, we observed several contaminating proteins with mass lower than that of MOCHLIM (≈87 kDa). In particular, the main contaminant had an apparent mass of ≈66 kDa (inserts of panels B, D, F, H in Figure 4.4).

The concentrated fractions containing MOCHLIM were used to test additional chromatographic steps for further purification and to establish which construct yielded protein of higher quality for further work.

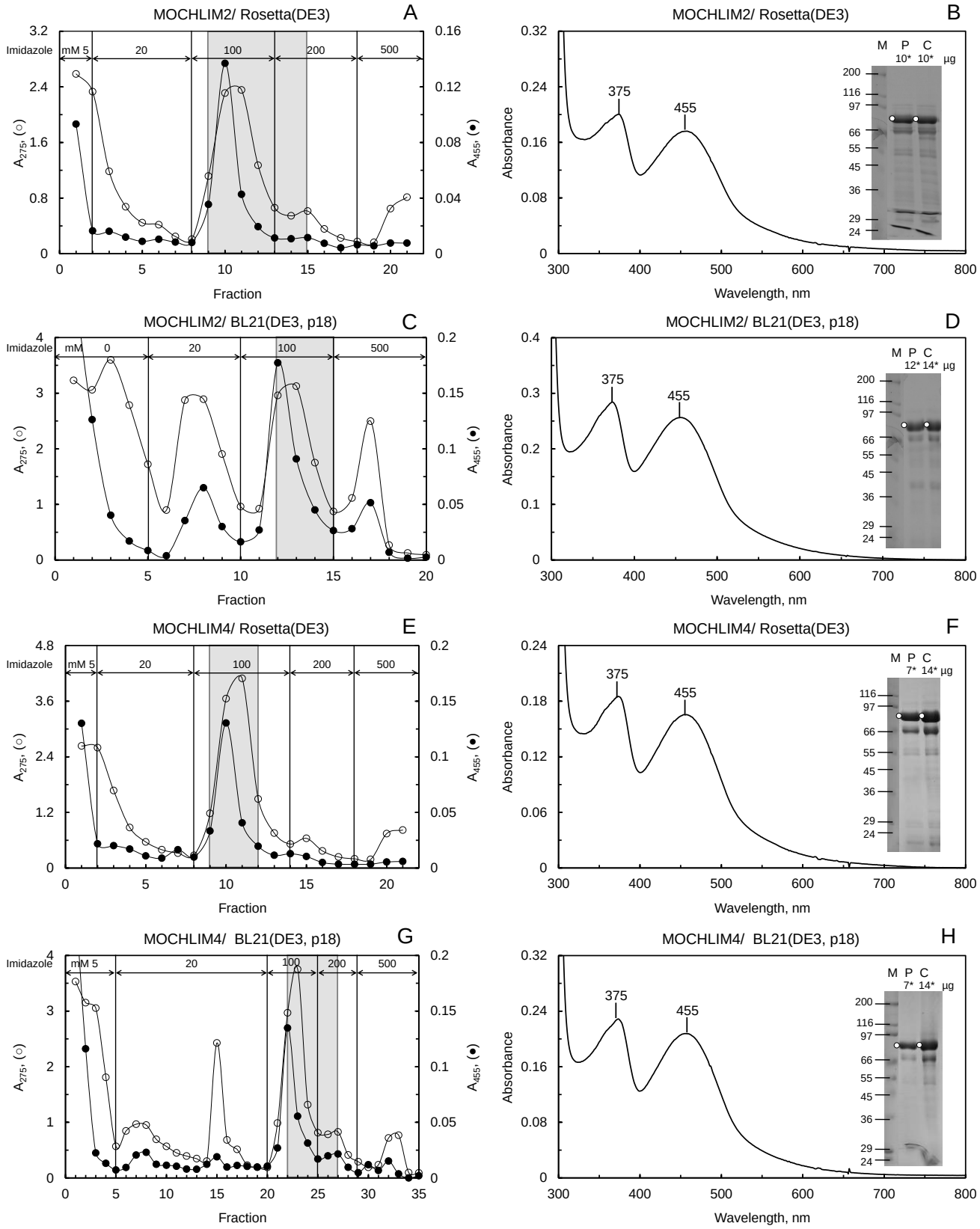

Figure 4.4. Small-scale purification of MOCHLIM forms – Ni-NTA affinity chromatography. Crude extracts from 6 g of *E.coli* Rosetta(DE3) or BL21(DE3, p18) cells that had produced MOCHLIM2 or MOCHLIM4 were subjected to chromatography on Ni-NTA Sepharose resin as described in the legend of Figure 4.2. The host *E.coli* strain and the protein form under study are indicated. The insets of panels B, D, F and H show the SDS-PAGE analysis of the pooled fractions (P) from the corresponding chromatographies (panels A, C, E and G; shaded area) and the final sample after concentration (C). Other symbols are as in the legend of Figure 4.2.

4.3. Set-up of the purification protocol of MOCHLIM

MOCHLIM samples after Ni-NTA chromatography were used for further protein purification by gel filtration and ion exchange chromatographies. Similar tests were made for MICAL.

Size exclusion chromatography of MOCHLIM was carried out to evaluate its efficacy in the removal of contaminating proteins.

Aliquots (500 µl, ≈2 mg) of the partially purified MOCHLIM2 and MOCHLIM4 forms were gel filtered in buffer B (50 mM Na-phosphate buffer, pH 7.5, 100 mM NaCl, 10% glycerol, 1 mM EDTA, 1 mM DTT) on a Superose12 column connected to an FPLC apparatus. The elution profile of the chromatography was similar for both MOCHLIM forms with a main peak containing the enzyme followed by a second peak corresponding to proteins with a lower mass, an example is shown in Figure 4.5. The absorption spectrum in the visible region of the fractions containing MOCHLIM showed that the absorbance maximum was shifted from 455 nm observed after Ni-NTA Sepharose to 458 nm (Figure 4.6) that is characteristic of the homogeneous MO domain. On the basis of the value of the UV/Vis ratio (A_{275}/A_{458}), which is a measure of the degree of purity of flavoenzymes, fractions with the minimal values (≈22) were pooled and concentrated with a Centricon YM30 centrifugal filter device (Table 4.1).

Gel filtration of MOCHLIM forms allowed to remove only part of the contaminating proteins, as demonstrated by the UV/Vis ratio of ≈22, which must be compared with the theoretical value of 16 for homogeneous holoenzyme, and by SDS-PAGE (insets in panels C, F and I of Figure 4.6). In fact, the main contaminating species of ≈66 kDa partially coeluted with MOCHLIM. The intensity of the band increased after protein concentration suggesting that it could be a product of proteolytic degradation of MOCHLIM (insets in panels C, F and I of Figure 4.6). Both MOCHLIM forms were able to catalyze a NADPH oxidase reaction with an initial velocity, expressed as v/[E], a measure of the apparent turnover assuming that all the protein present is MOCHLIM, of 0.7-0.8 s^{-1}. This value is only ≈2-fold and ≈3-fold lower than that measured for MOCH (≈1.3 s^{-1}) and MO (≈2.5 s^{-1}) under the same conditions (Table 4.1).

The gel filtration allowed us to observe a difference in the proteins produced in *E.coli* Rosetta(DE3) cells compared to those expressed in BL21(DE3, p18) cells. In the latter case the absorption spectrum was better resolved in the 300-375 nm region (Figure 4.6, panels C, F and I). Moreover, the absorbance maxima in the UV region were at 275 and 265 nm for MOCHLIM forms produced in *E.coli* BL21(DE, p18) and Rosetta(DE3) cells, respectively (Figure 4.6, panels A, D and G). The absorbance maximum at 265 nm of the enzyme obtained from *E.coli* Rosetta(DE3) cells could indicate the presence of cellular compounds that interact with the protein, such as non-specific interaction between DNA fragments and MOCHLIM through the LIM domain. Furthermore, the electrophoretic pattern of the proteins produced in *E.coli* BL21(DE3, p18) cells showed a higher degree of purity than that observed for the proteins expressed in Rosetta(DE3). In the latter case several faint protein bands below MOCHLIM suggested proteolytic degradation (insets in panels C, F and I of Figure 4.6). Thus, from these results coexpression of MOCHLIM with GroE in *E.coli* BL21(DE3, p18) seemed to give protein of higher quality.

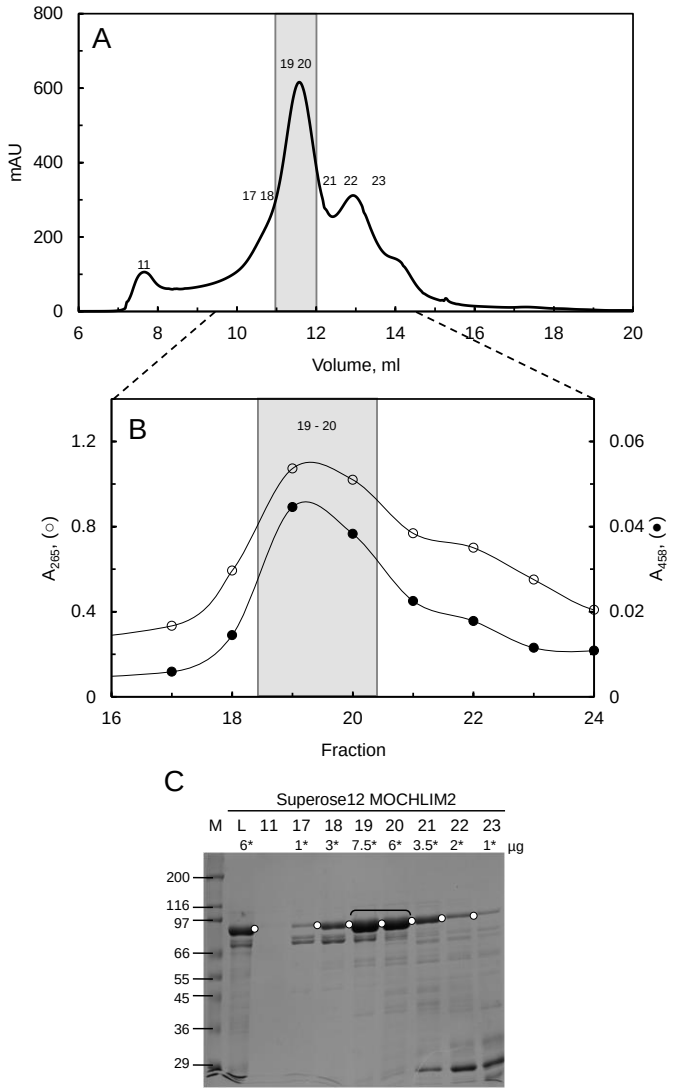

Figure 4.5. Small-scale purification of MOCHLIM – Gel filtration. Panel A: Gel filtration of MOCHLIM2 expressed in *E.coli* Rosetta(DE3) after Ni-NTA Sepharose affinity chromatography from 6 g of cells (Figure 4.4 panels A-B) on a Superose12 column in buffer B. Fractions enriched in MOCHLIM were pooled (shaded area) and concentrated. Panel B: detail of the gel filtration profile obtained by recording the absorption spectrum of the individual fractions. Panel C: SDS-PAGE analysis of the sample loaded onto the column (L) and of the fractions collected during the gel filtration numbered as in panel B.

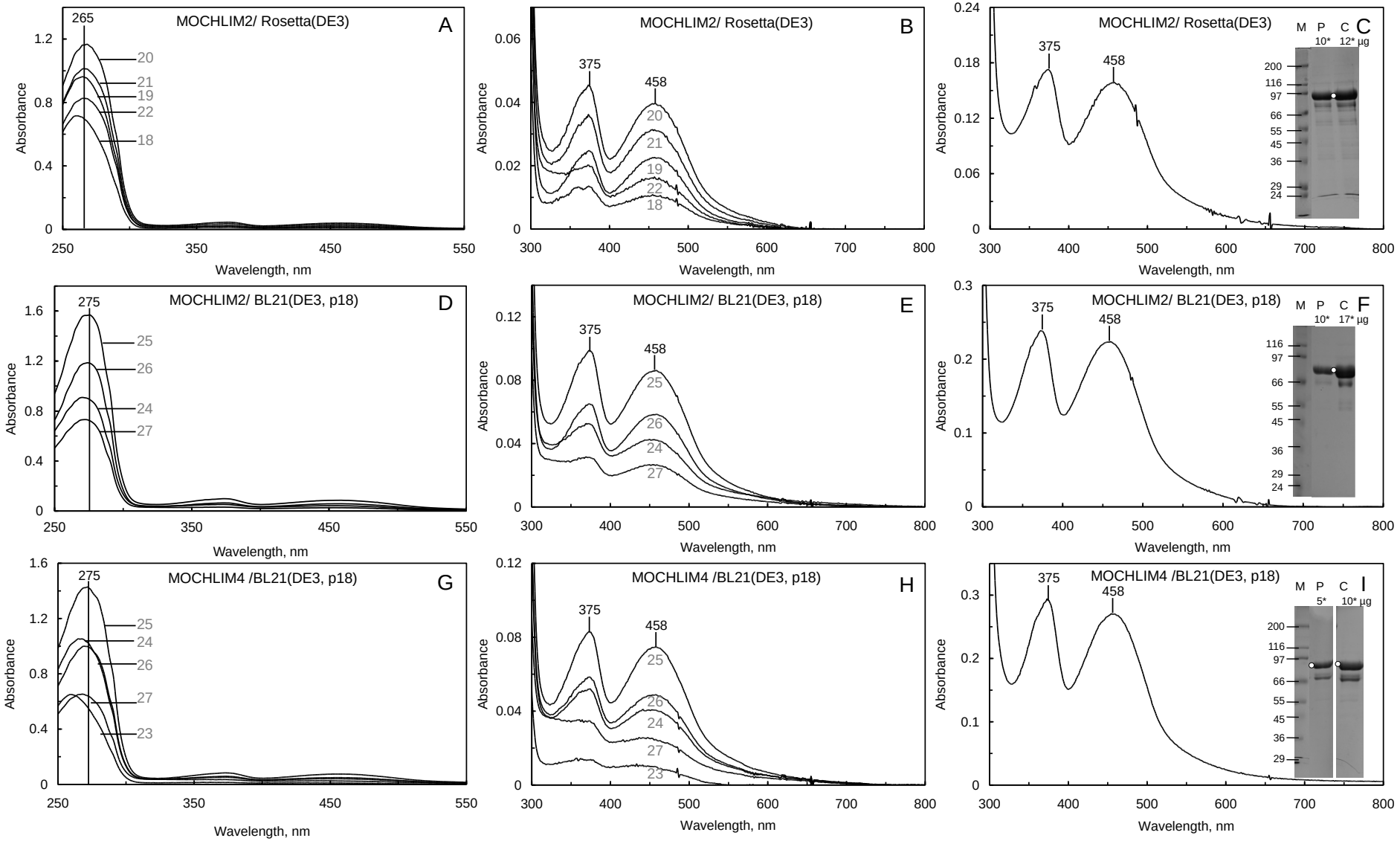

Figure 4.6. Comparison of the absorption spectra of the MOCHLIM forms after gel filtration on Superose12. MOCHLIM2 produced in *E.coli* Rosetta(DE3) and in BL21(DE3, p18) and MOCHLIM4 produced in BL21(DE3, p18) cells after Ni-NTA affinity chromatography (Figure 4.4) were gel filtered on a Superose12 column in buffer B as described in the legend of Figure 4.5. In panels A, B, D, E, G and H the absorption spectra of the fractions enriched in MOCHLIM are shown on two scales. Note that the elution profiles were in all cases similar to that shown in Figure 4.5 so that the different fractions numbers indicated do not correspond to different elution volumes. The absorbance spectra of the final samples are shown in panels C, F and I. The SDS-PAGE analyses of the pooled fractions (P) and of the same fractions after concentration (C) are shown in the insets.

Since gel filtration did not resolve MOCHLIM from contaminants, the efficacy of anion exchange chromatography was tested, taking also into account the isoeletric point of MOCHLIM (pI, 6.6).

To verify if anion exchange chromatography could allow us to obtain homogeneous MOCHLIM preparation, MOCHLIM4 expressed in *E.coli* Rosetta (DE3) cells and purified by affinity chromatography (Figure 4.4, panels E, F) was further chromatographed on a MonoQ column equilibrated with buffer B without glycerol (50 mM Na-phosphate, pH 7.5, 100 mM NaCl, 1 mM EDTA, 1 mM DTT).

The enzyme solution was first dialyzed versus buffer B without glycerol with good recovery (Table 4.1). Then, it was loaded onto a MonoQ column, which was washed with 5 volumes of equilibration buffer followed by a linear 100-500 mM NaCl gradient in 60 column volumes. 0.5-1 ml fractions were collected (Figure 4.7, panels A, B).

Under these conditions MOCHLIM did not bind to the resin, presumably due to the high ionic strength of the buffer and it coeluted with several contaminants (Figure 4.7, panels C and D). Protein bands of ≈22 and 21.5 kDa, not present in the starting sample, bound to MonoQ and eluted at ≈130 mM NaCl. These observations indicated that proteolytic events were taking place. Thus, the fractions containing the enzyme (fractions 3-6) were pooled, concentrated (Figure 4.7, panels C; Table 4.1) and diluted 4-fold in buffer without NaCl to lower its concentration from 100 to 25 mM. The sample was loaded on to the MonoQ column equilibrated in 50 mM Na-phosphate buffer, pH 7.5, 25 mM NaCl, 1 mM EDTA, 1 mM DTT. Under these conditions MOCHLIM bound to the resin and eluted at ≈160 mM NaCl (Figure 4.7, panel E, F). Fractions 18-19 that contained the enzyme were pooled (Figure 4.7, panel G; Table 4.1). The electrophoretic analysis of the samples (Figure 4.7, panel H) indicated that the anion exchange chromatography removed most of the contaminants, but only part of the ≈66 kDa protein. Moreover, the electrophoretic pattern of the enzyme after concentration showed the appearance of novel protein bands with lower mass than that of MOCHLIM (Figure 4.7, panel H), strongly suggesting an ongoing proteolytic degradation of MOCHLIM.

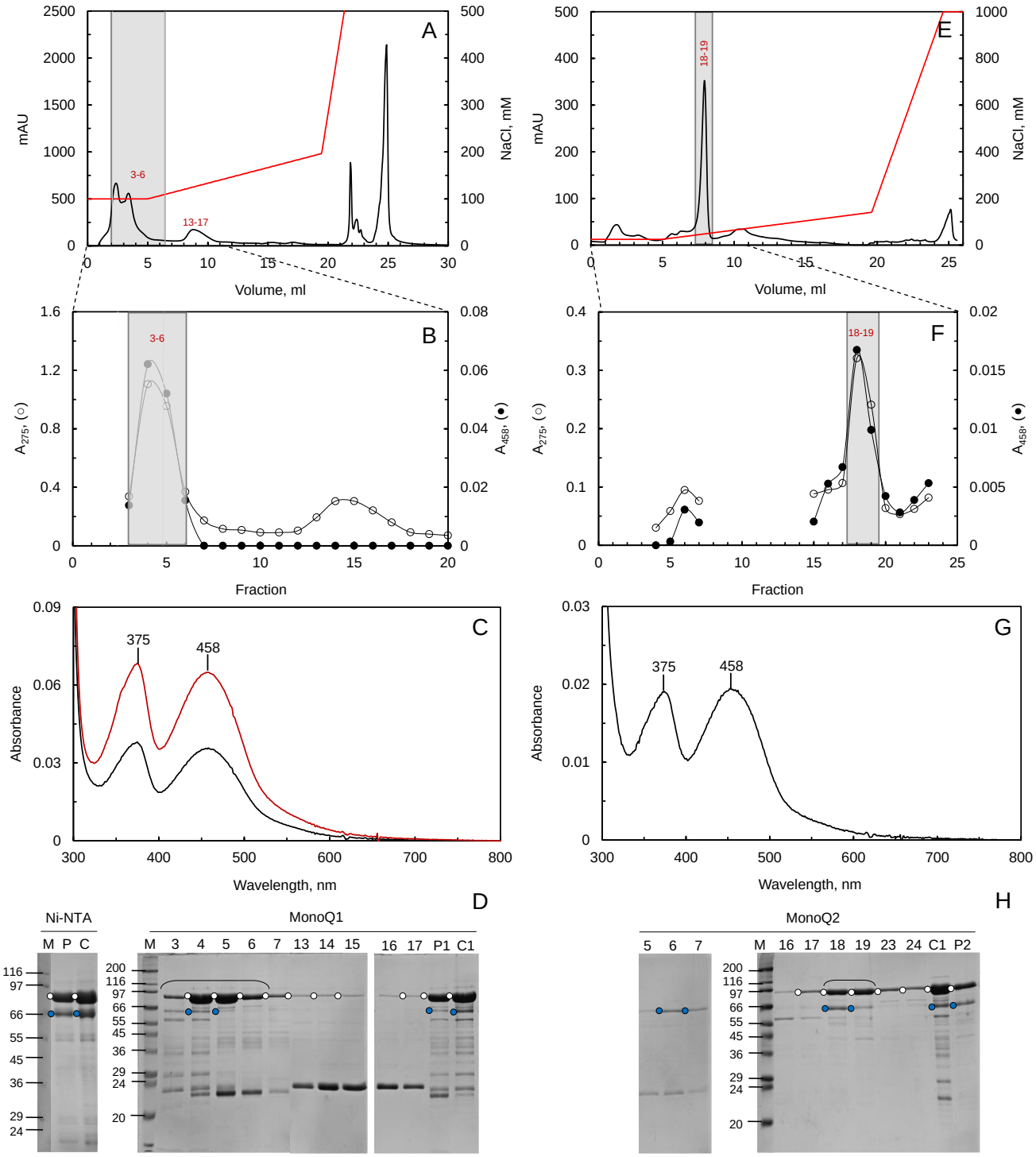

Figure 4.7. Small-scale purification of MOCHLIM – Anion exchange chromatography. The MOCHLIM4 produced in *E.coli* Rosetta(DE3) cells and purified by Ni-NTA affinity chromatography (Figure 4.4, panels E, F) was loaded onto a MonoQ column equilibrated in buffer B without glycerol (50 mM Na-phosphate buffer, pH7.5, 100 mM NaCl, 1 mM EDTA, 1 mM DTT) and eluted by applying a linear NaCl gradient (panels A and B). Under these conditions MOCHLIM and most of the contaminants did not bind to the resin (panels C and D). Thus fractions 3-6 were pooled (black line panel C, 0.38 mg/ml, 4.46 µM), concentrated (red line panel C, 0.69 mg/ml, 8.1 µM) and diluted 4-fold in 50 mM Na-phosphate buffer, pH 7.5, 1 mM EDTA, 1 mM DTT (black line panel C, 0.17 mg/ml, 2 µM) to lower NaCl concentration to 25 mM. The sample was loaded onto MonoQ column equilibrated in 50 mM Na-phosphate buffer, pH 7.5, 25 mM NaCl, 1 mM EDTA, 1 mM DTT and developed by applying linear NaCl gradient (panels E and F). Peak fractions containing MOCHLIM (shaded area in panels E and F) were pooled. The absorption spectrum of the pooled fractions (18-19, 0.20 mg/ml, 2.35 µM) is shown in panel G. Panel H shows the SDS-PAGE analysis of the fractions from the second MonoQ column, numbered as in panel F, the pooled peak fractions (P2) the sample loaded (C1) from the first chromatography (panels A-D).○, full-length MOCHLIM form (87 kDa); ●, ≈66 kDa protein species.

Table 4.1. Small-scale purification of MOCHLIM forms from E.coli Rosetta(DE3) and BL21(DE3, p18) cells. Summary of the quantitation of MOCHLIM forms obtained during the purifications shown in: Figure 4.4 (A-B), 4.5 and 4.6 (A-C) (MOCHLIM 2 expressed in Rosetta(DE3) cells), Figure 4.4 (C-D) and 4.6 (D-F) (MOCHLIM 2 expressed in BL21(DE3, p18) cells), Figure 4.4 (G-H) and 4.6 (G-I) (MOCHLIM 4 expressed in BL21(DE3, p18) cells) and Figure 4.4 (E-F) and 4.7 (MOCHLIM 4 expressed in Rosetta(DE3) cells). The protein concentration was determine with the Bradford method ([a]) or from the absorbance at 458 nm, by using the extinction coefficient of 8.1 $mM^{-1}cm^{-1}$ of MO (Zucchini et al., 2001) and the calculated mass of 85.6 and 86.4 kDa of MOCHLIM2 and MOCHLIM4, respectively ([b]). The NADPH oxidase activity was carried out in 20 mM Hepes/KOH buffer, pH 7, 100 µM NADPH at 25°C.

			Bradford[a]				Absorbance[b]				Activity		
E.coli strain	Protein form	Sample	ml	mg/ml	mg	yield, %	mg/ml	mg	yield, %	µM	UV/Vis	U	U/mg[a]
Rosetta(DE3)	MOCHLIM2	Crude extract	27	12	324	100							
		Ni-NTA Sepharose	13	1.14	14.8	4.6	0.39	5.1	100	4.57			
		Concentration	2.10	5.82	12.2	3.8	1.84	3.9	76	21.6			
		Superose12	3.0	0.55	1.65	0.5	0.40	1.2	24	4.7	26.86	0.90	0.55
		Concentration	0.48	2.58	1.23	0.4	2.0	0.95	19	23.3	23.30	0.66	0.54
BL21(DE3, p18)	MOCHLIM2	Crude extract	25	18	452.5	100							
		Ni-NTA Sepharose	7.0	3.9	27.2	6.0	0.8	5.60	100.00	9.41			
		Concentration	1.5	16	24.0	5.3	2.7	4.05	72.32	31.76			
		Superose12	2.5	1.3	3.33	0.73	0.66	1.66	29.62	7.78			
		Concentration	0.57	2.94	1.68	0.37	2.35	1.34	23.93	27.57	22.33	0.91	0.55
BL21(DE3, p18)	MOCHLIM4	Crude extract	25.00	9.53	238.25	100.00							
		Ni-NTA Sepharose	11.00	1.03	11.33	4.76	0.50	5.50	100.00	5.81			
		Concentration	2.00	4.91	9.82	4.12	2.21	4.42	80.36	25.70			
		Superose12	2.80	0.81	2.27	0.95	0.61	1.69	30.81	7.04	21.55		
		Concentration	0.44	3.86	1.70	0.71	3.05	1.34	24.37	35.42	19.70	0.98	0.58
Rosetta(DE3)	MOCHLIM4	Crude extract	25	10.29	257	100							
		Ni-NTA Sepharose	7.50	1.29	9.68	3.76	0.56	4.20	100	6.57			
		Concentration	2.00	4.00	8.00	3.11	1.76	3.52	84	20.64			
		Dialysis	2.00	3.95	7.90	3.07	1.60	3.20	76	18.76			
		MonoQ1	4.00	0.51	2.04	0.79	0.38	1.52	36	4.46			
		Concentration	1.10	0.77	0.85	0.33	0.69	0.76	18	8.09			
		MonoQ2	0.90	0.34	0.31	0.12	0.20	0.18	4.3	2.35			

4.4. Large-scale production of MICAL and of the MO, MOCH and MOCHLIM forms

To obtain the proteins forms in quantities sufficient to carry out their characterization, 12 l cell cultures were set up in a fermentor.

On the basis of the results obtained during the previous experiments with MICAL and MOCHLIM forms we decided to coexpress the proteins in *E.coli* BL21(DE3) cells with GroE to favor protein folding. In the preliminary analyses MOCHLIM2 and MOCHLIM4 showed similar properties in terms of the quantity and quality (stability, activity). Thus, we focused on MOCHLIM4 form, which is 10 residues longer than MOCHLIM2, since the additional residues could promote the folding and stability of the LIM domain.

The cells were cultured as described in Material and Methods (Chapter 10). After a series of preliminary experiments, cells were harvested 24 and 40 h after the addition of IPTG for MOCHLIM and MICAL, respectively. The analysis of the total cell extracts at different times (Figure 4.8) showed the appearance of protein bands expected for the MICAL forms after IPTG addition and their expression levels were similar to those obtained in cells cultured in 2 l flasks (Figure 4.1). MO and MOCH forms were produced in *E.coli* Rosetta(DE3) and in BL21(DE3, p18) cells, respectively.

The cells were used for the purification of the four MICAL forms. For MO and MOCH, the available procedures were modified to improve purity of the final preparations. For MOCHLIM and MICAL several tests were made on the basis of preliminary experiments (Figures 4.2-4.6) to set-up novel purification procedures.

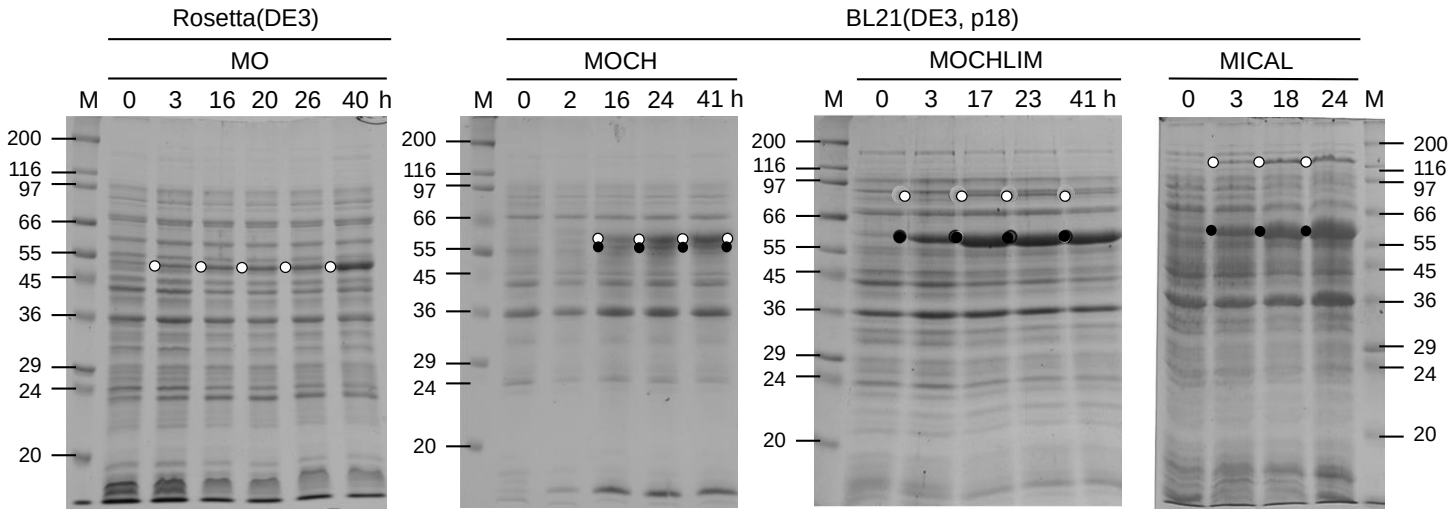

Figure 4.8. Large-scale production of MICAL forms in E.coli cells. E. coli Rosetta(DE3) or BL21(DE3, p18) cells harboring the pET-derivatives for the production of human MICAL1 forms were grown in a fermentor in 12 l LB supplemented with 0.1 mg/ml ampicillin and 0.025 mg/ml choloramphenicol up to an OD_{600} of ≈ 1. The temperature was lowered to 15°C and IPTG (0.1 mM) was added. Small aliquots of the culture were harvested before IPTG addition (0 h) and at the indicated times after induction. For comparison samples obtained from culturing, under the same conditions, *E. coli* Rosetta (DE3) and BL21(DE3, p18) cells harbouring the pET derivatives for the production of MICAL MO and MOCH, respectively, are shown. Aliquots of total cell extracts were analyzed by SDS-PAGE on 12% (AcA+bis-AcA) gels. The empty circles indicate the bands corresponding to the MICAL forms; the full circles indicate the bands corresponding to GroEL (59.7 kDa) encoded by p18.

4.5. Large-scale purification of MO

30 g of *E.coli* Rosetta(DE3) cells that had produced MO were used for its purification. The crude extract (Table 4.2 A) in buffer A containing 50 mM Na-phosphate, pH 7.5, 100 mM NaCl, 10% glycerol, 1 mM PMSF, 1 mM 2-ME, 1% protease inhibitors cocktail was directly loaded on a Ni-NTA Sepharose column (30 ml) equilibrated in buffer A + 20 mM imidazole in the cold room. The weakly bound proteins were removed by flowing 1 volume of buffer A + 20 mM imidazole, 1 mM 2-ME (fractions 1-38, Figure 4.9, panel A) and 10 volumes of buffer A + 50 mM imidazole, 1 mM 2-ME (fractions 39-70, Figure 4.9, panel A). The column was connected to a FPLC apparatus with UV and conductivity detectors, thermostatted at 4°C. The bound proteins were eluted by applying a linear 50-200 mM imidazole gradient in 10 column volumes (Figure 4.9, panel B). Fractions enriched in MO, as judged by the absorption spectrum (Figure 4.9, panel C) and SDS-PAGE analysis (not shown), were pooled, concentrated and dialyzed against buffer B (Figure 4.9, panel D; Table 4.2 A). The NADPH oxidase activity of the pooled fractions and of the preparation after concentration and dialysis was measured (Table 4.2 A). After dialysis an aliquot of the enzyme was diluted to determine the value of the UV/Vis ratio (A_{275}/A_{458}) that was 11.5 (Figure 4.9, panel E) similar to the theoretical value of 11 expected for MO containing a stoichiometric amount of FAD (see Chapter 5). The recovery of the protein after concentration and dialysis, and the quality of absorption spectrum with absorbance maxima at 375 and 458 nm (Figure 4.9, panel D) in the visible region were comparable to those obtained previously (Zucchini et al., 2011) and confirmed the enzyme stability. Moreover, the activity of the protein, expressed as v/[E], increased after concentration and dialysis, from 1 to 1.8 s^{-1} due to the combination of the removal of imidazole from the sample and the smaller amount of enzyme solution used to carry out the assay, leading to a decrease of the ionic strength of the reaction mixture. In fact, as better described in Chapter 6, the isolated MO domain is very sensitive to ionic strength and type of ions of the medium (Zucchini et al., 2011). MO preparation at the end of Ni-NTA Sepharose chromatography was nearly homogeneous as demonstrated by the value of the UV/Vis ratio and the SDS-PAGE analysis. MO represented >90% of the total protein content and the main contaminating protein band with a mass of ≈68 kDa (Figure 4.9, panel F) could be removed by gel filtration, which was routinely carried out prior to each experiment to also exchange the buffer.

The enzyme solution was divided in small aliquots and stored at -80° after flash-freezing in liquid nitrogen. MO was stable after long-term storage at -80°C (see Chapter 5).

The contaminants present in trace amounts in the MO preparation from Ni-NTA Sepharose were removed by gel filtration on a Superose12 column in buffer B or "F-buffer no ATP" (9.5 mM Tris/HCl, pH 7.7, 45 mM KCl, 0.18 mM $CaCl_2$, 1.8 mM MgCl, 1.3 mM DTT) prior to each experiments to also transfer the protein in the appropriate buffer. The protein behavior during chromatography was independent from the buffer used. Thus, only the results obtained from the gel filtration of the enzyme in "F-buffer no ATP" will be shown.

Aliquots up to 500 µl of protein solution (Table 4.2 B) were loaded on a Superose12 column and 0.5 ml fractions were collected. On the basis of the absorption spectrum (Figure 4.10, panels A-C) fractions 15-

16 were pooled (Figure 4.10, panels D, E; Table 4.2 B) and concentrated (Figure 4.10, panel F; Table 4.2 B).

The resulting MO preparation showed absorbance maxima at 276, 375 and 458 nm and a A_{276}/A_{458} ratio of 10.2. The contaminants were successfully removed as shown by the elution profile in which two peaks with a lower absorbance were observed before and after the main peak containing MO (Figure 4.10, panel A) and by SDS-PAGE analysis of the individual fractions (Figure 4.10, panel C).

The enzyme was used immediately for experiments or was stored at -80°C after flash-freezing of small aliquots in liquid nitrogen. Under these conditions the enzyme in buffer B or in F-buffer without ATP was stable.

Table 4.2. Large-scale purification of MO. Quantitation of MO prepared from 30 g of *E.coli* Rosetta(DE3) cells as described in the text. A: Recovery after Ni-NTA Sepharose, concentration and dialysis as described in the legend of Figure 4.9. B: Example of final purification and buffer exchange by gel filtration on Superose12 column as described in the legend of Figure 4.10. The indicated quantities of MO are referred to two chromatographic runs. 500 µl of sample were loaded in each run and the corresponding peak fractions were combined before concentration. The NADPH oxidase activity was carried out in 20 mM Hepes/KOH buffer, pH 7, 100 µM NADPH at 25°C [a]Protein concentration was determined with the Bradford method. [b]Protein concentration determined from the absorbance at 458 nm, by using the extinction coefficient of 8.1 $mM^{-1}cm^{-1}$ of MO (Zucchini et al., 2001) and the calculated mass of 55.1 kDa of MO.

A

		Bradford[a]			Absorbance[b]			Activity			
Sample	ml	mg/ml	mg	yield, %	mg/ml	mg	yield, %	µM	U	%U	U/mg[a]
Crude extract	140	16.29	2280	100	-	-	-	-	-	-	-
Ni-NTA Sepharose	45	0.50	22.5	0.99	0.4	18	100	7.26	25	100	1.11
Concentration	3.3	5.14	16.9	0.74	4	13	72	72.6	27	108	1.59
Dialysis	3.1	5.03	15.6	0.68	3.76	12	67	68.2	28	112	1.8

B

		Bradford[a]			Absorbance[b]				
Sample	ml	mg/ml	mg	yield, %	mg/ml	mg	yield, %	µM	A_{276}/A_{458}
Ni-NTA Sepharose	1	4	4	100	3	3.1	100	56	11.5
Superose12	2.3	1.25	2.875	71.875	0.93	2.15	70	16.93	10.20
Concentration	0.9	2.2	1.98	49.5	1.94	1.75	57	35.26	-

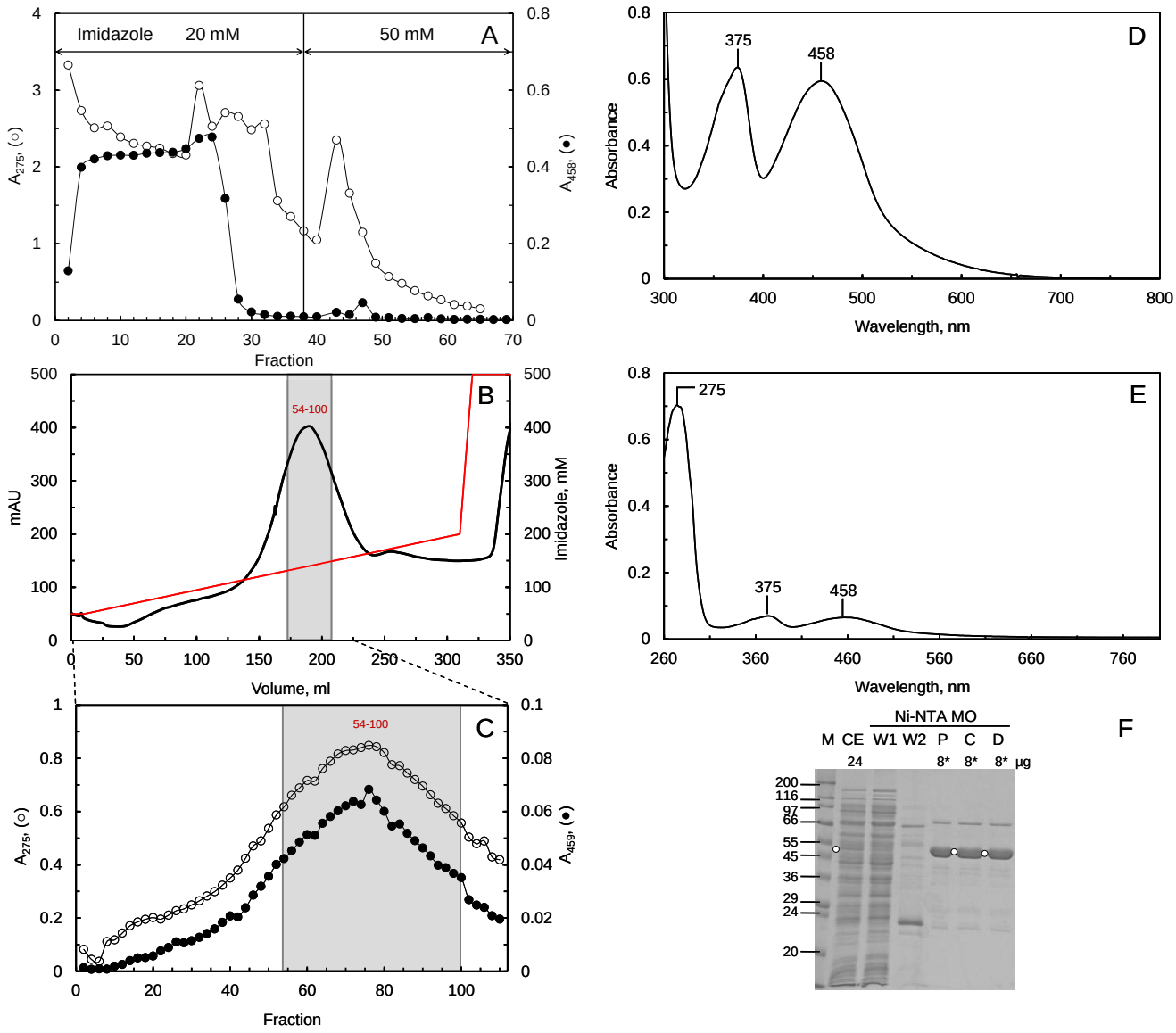

Figure 4.9. Large-scale purification of MO – Ni-NTA affinity chromatography. The crude extract from 30 g of *E.coli* Rosetta(DE3) cells that had expressed MO (Figure 4.8) was loaded onto 30 ml of Ni-NTA Sepharose column in buffer A + 20 mM imidazole. The column was rinsed with equilibration buffer and buffer A + 50 mM imidazole in the cold room (panel A). The column was connected to an FPLC apparatus and bound proteins were eluted by applying an imidazole gradient (panels B and C). Based on the elution profiles (panels B and C), quality of the absorbance spectra of the individual fractions and SDS-PAGE (not shown) the fractions in the shaded area were pooled, concentrated and dialyzed against buffer B. The absorption spectrum of the final protein preparation (panel D, 3.76 mg/ml, 68 µM) and of the sample after 6-fold dilution in buffer B (panel E, 0.63 mg/ml, 11 µM) are shown. Panel F shows the SDS-PAGE analysis of: crude extract (CE); fraction 22 eluted with buffer A + 20 mM imidazole (W1, panel A); fraction 45 eluted with buffer A + 50 mM imidazole (W2, panel A); the pooled MO containing fractions before (P) and after concentration (C) and dialysis (D). The indicated quantity of protein loaded was determined with the Bradford method for the crude extract and from the A_{458} of MO for the other samples.

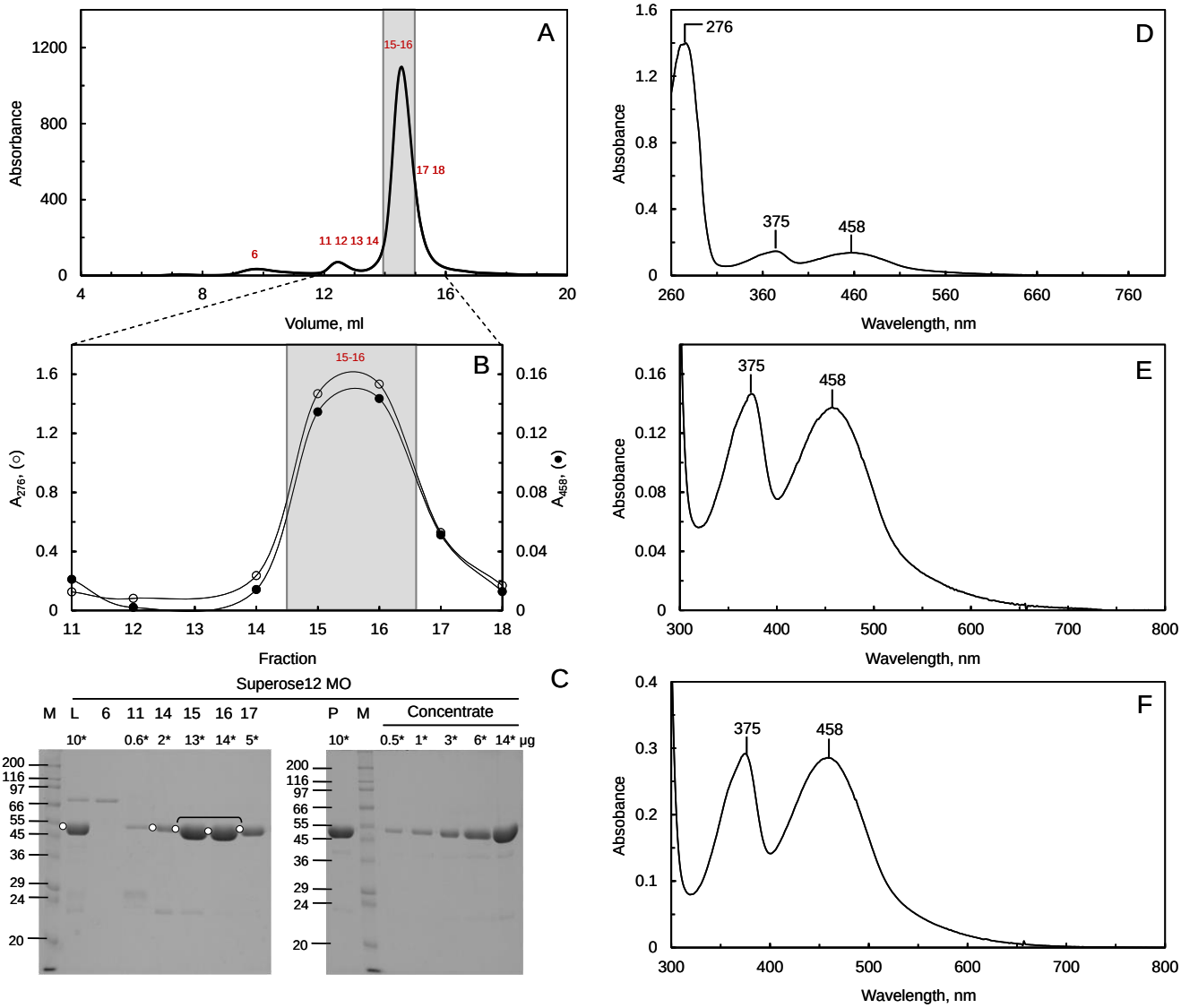

Figure 4.10. Purification of MO – Gel filtration. An aliquot of MO preparation after affinity chromatography (Figure 4.9) was gel filtered on a Superose12 column in F-buffer no ATP to remove the ≈68 kDa contaminant and for buffer exchange. Panel A: elution profile obtained with on-line A_{280} detection. Panel B: detail of the elution profile shown in panel A, obtained by recording the absorption spectrum of individual fractions. Panel C: SDS-PAGE analysis of MO after Ni-NTA chromatography loaded on Superose12 (L); fractions collected during gel filtration numbered as in panel B; fraction 15-16 pooled (P); different amounts of the MO preparation after concentration (Concentrate), calculated with the protein concentration determined by the A_{458} of the sample using the extinction coefficient of 8.1 $mM^{-1}cm^{-1}$ and a mass of 55.1 kDa calculated for MO. Panels D and E: absorption spectra of the pooled fractions 15-16 (0.93 mg/ml, 16.93 µM) on two different scales. Panel F: fractions 15-16 after concentration (1.94 mg/ml, 35 µM).

4.6. Large-scale purification of MOCH

The crude extract (Table 4.3 A) was obtained by sonication of ≈30 g of *E.coli* BL21(DE3, p18) cells, which had overexpressed the protein (Figure 4.8), and centrifugation at 18000 rpm for 1 h at 4°C. It was directly loaded on to a column containing Ni-NTA Sepharose (25 ml) equilibrated in buffer A + 20 mM imidazole at 4°C. The column was washed overnight with 13 column volumes of buffer A+ 20 mM imidazole, 1 mM PMSF, 1 mM 2-ME to remove weakly bound proteins (Figure 4.11, panel A). The day after, the column was connected to an FPLC apparatus and to a water bath at 4°C. Protein elution was effected by applying a linear 20-200 mM imidazole gradient in buffer A. When the first protein peak emerged from the column, the concentration of imidazole was held constant at ≈70 mM for 2 column volumes (Figure 4.11, panel B). In this way, an increase of purity of MOCH, present in the second main peak, was obtained (Figure 4.11, panel C). From the absorption spectra (Figure 4.11, panel C) and SDS-PAGE (not shown) of individual fractions, those enriched in MOCH were pooled (fractions 47-67; Table 4.3 A). The protein solution (Pool 47-67; Table 4.3 A) was concentrated by ultrafiltration (Figure 4.11, panel D) and dialyzed against buffer B (Figure 4.11, panels E, F; Table 4.3 A).

MOCH was stable as demonstrated by the greater than 85% of protein recovery after concentration and dialysis (Table 4.3 A), calculated from the enzyme concentration determined from the absorption spectrum and the extinction coefficient of 8.1 $mM^{-1}cm^{-1}$ (Zucchini et al., 2011), and by the quality of the absorption spectra (Figure 4.11, panel E). The final preparation showed a A_{276}/A_{458} ratio value of 17.5 (Figure 4.11, panel F) to be compared with the theoretical value of 14 and to the value of 19.3 for the enzyme solution obtained with the original protocol. At this stage MOCH preparation was still contaminated (inset of panel F in Figure 4.11) by protein species that were similar to those observed for MO after Ni-NTA Sepharose (Figure 4.9, panel F) and could be removed by gel filtration. As an alternative, MOCH could be further purified by anion exchange chromatography.

Such additional purification steps, especially gel filtration, were often performed before certain experiments also for buffer exchange. In fact, MOCH after affinity chromatography and dialyzed in buffer B was stable at -80°C after flash-freezing of small aliquots in liquid nitrogen.

As described above for MO, also the MOCH preparation after Ni-NTA Sepharose chromatography contained contaminants that could be removed by gel filtration on a Superose12 column in buffer B or in 20 mM Hepes/KOH buffer, pH 7, 100 mM NaCl, with similar results. Thus, only an example of gel filtration of MOCH in buffer B is shown.

Aliquots (up to 500 µl) of MOCH solution (≈5 mg/ml, Table 4.3 B) after Ni-NTA Sepharose affinity chromatography were loaded on a Superose12 column equilibrated and eluted with buffer B at 0.5 ml/min and 0.5 ml fractions were collected. The elution profile was similar to that observed for MO, with a main peak containing MOCH and two minor peaks corresponding to the contaminating proteins (Figure 4.12, panels A, B), as confirmed by the SDS-PAGE analysis (Figure 4.12, panel C). Fractions with an A_{276}/A_{458} value ≤16 were pooled (fractions 12-14, Figure 4.12, panels D, E; Table 4.3) and concentrated (Figure 4.12, panel F; Table 4.3 B).

The MOCH preparation at the end of gel filtration had a UV/Vis ratio of 15.7 (Figure 4.12, panel D) which was lower than the initial value of 17.5 in agreement with the removal of most of the contaminants (Figure 4.12, panel C). The yield was only 60% of MOCH (Table 4.3 B), also due to the fact that some side fractions were discarded.

As an alternative to gel filtration, MOCH could be further purified after affinity chromatography by anion exchange on a MonoQ column. The column was equilibrated in 20 mM Na-phosphate buffer, pH 7.5, 40 mM NaCl. At this pH the overall charge of MOCH is ≈0 (pI 7.67) so that it should not bind the resin as opposed to the contaminating proteins, according to pilot experiments.

An aliquot of MOCH solution (black thick line in Figure 4.13, panel A; Table 4.3 C) in buffer B was dialyzed against 20 mM Na-phosphate buffer, pH 7.5, 40 mM NaCl (see Materials and Methods for the details). At the end of the dialysis the enzyme (red thin line in Figure 4.13, panel A; Table 4.3 C) was loaded on a MonoQ column equilibrated in the dialysis buffer. The column was developed by flowing 20 volumes of the equilibration buffer, followed by a linear 40-500 mM NaCl gradient in 60 column volumes and 0.5 ml fractions were collected. Fractions enriched in MOCH (Figure 4.13, panels B, C) and with a UV/Vis value ≤ 16 were pooled (fractions 23-32; black thick line in Figure 4.13, panel D; Table 4.3 C) and concentrated (red thin line in Figure 4.13, panel D; Table 4.3 C). Under these conditions MOCH bound very weakly to the resin and eluted with the equilibration buffer, while contaminating proteins bound to the resin and high concentrations of NaCl were required for their elution (Figure 4.13, panel A).

At the end of chromatography, the UV/Vis ratio of the preparation was 14.8 close to the theoretical value of 14 (see Chapter 5). The electrophoretic pattern showed only traces of contaminants (Figure 4.13, panel F) that were similar in mass to those observed after gel filtration. However, the protein yield was only 40% (Table 4.3 C) of the starting sample compared to 60% from size exclusion chromatography (Table 4.3 B).

Table 4.3. Large-scale purification of MOCH. Quantitation of MOCH prepared from 30 g of *E.coli* BL21(DE3, p18) cells as described in the text. A: Recovery after Ni-NTA Sepharose, concentration and dialysis as described in the legend of Figure 4.11. B: Example of final purification and buffer exchange by gel filtration on Superose12 column as described in the legend of Figure 4.12. The indicated quantities of MOCH are referred to two chromatographic runs. 400 and 350 µl of sample were loaded onto Superose12 column and the corresponding peak fractions were combined before concentration. C: Example of final purification of MOCH by anion exchange chromatography on a MonoQ column as described in the legend in Figure 4.13. [a]Protein concentration was determined with the Bradford method. [b]Protein concentration was determined from the absorbance at 458 nm, by using the extinction coefficient of 8.1 $mM^{-1}cm^{-1}$ of MO (Zucchini et al., 2001) and the calculated mass of 68.5 kDa of MOCH.

A

		Bradford[a]			Absorbance[b]			
Sample	ml	mg/ml	mg	yield, %	mg/ml	mg	yield, %	µM
Crude extract	150	19	2850	100		-	-	-
Ni-NTA Sepharose	38	0.95	36.1	1.3	0.54	20.4	100	6.3
Concentration	5.8	-	-		3.13	18.2	89	36
Dialysis	5.6	5.25	29.4	1	3.13	17.6	86	36

B

		Bradford[a]			Absorbance[b]				
Sample	ml	mg/ml	mg	yield, %	mg/ml	mg	yield, %	µM	A_{276}/A_{458}
Ni-NTA Sepharose	0.75	5.25	3.94	100	3.01	2.26	100	44	17.50
Superose12	2.8	1.1	3.08	78	0.60	1.68	70	16	15.69
Concentration	0.8	2.35	1.88	48	1.76	1.41	58	34	-

C

		Bradford[a]			Absorbance[b]				
Sample	ml	mg/ml	mg	yield, %	mg/ml	mg	yield, %	µM	A_{276}/A_{458}
Ni-NTA Sepharose	0.8	9.5	7.6	100	6.7	5.36	100	98	-
Dialysis	1.1	6.5	7.15	94	4.54	4.99	93	66	18.5
MonoQ	4.5	0.66	2.97	39	0.57	2.57	48	8.3	14.5
Concentration	1	2.4	2.4	32	2.07	2.07	37	30	-

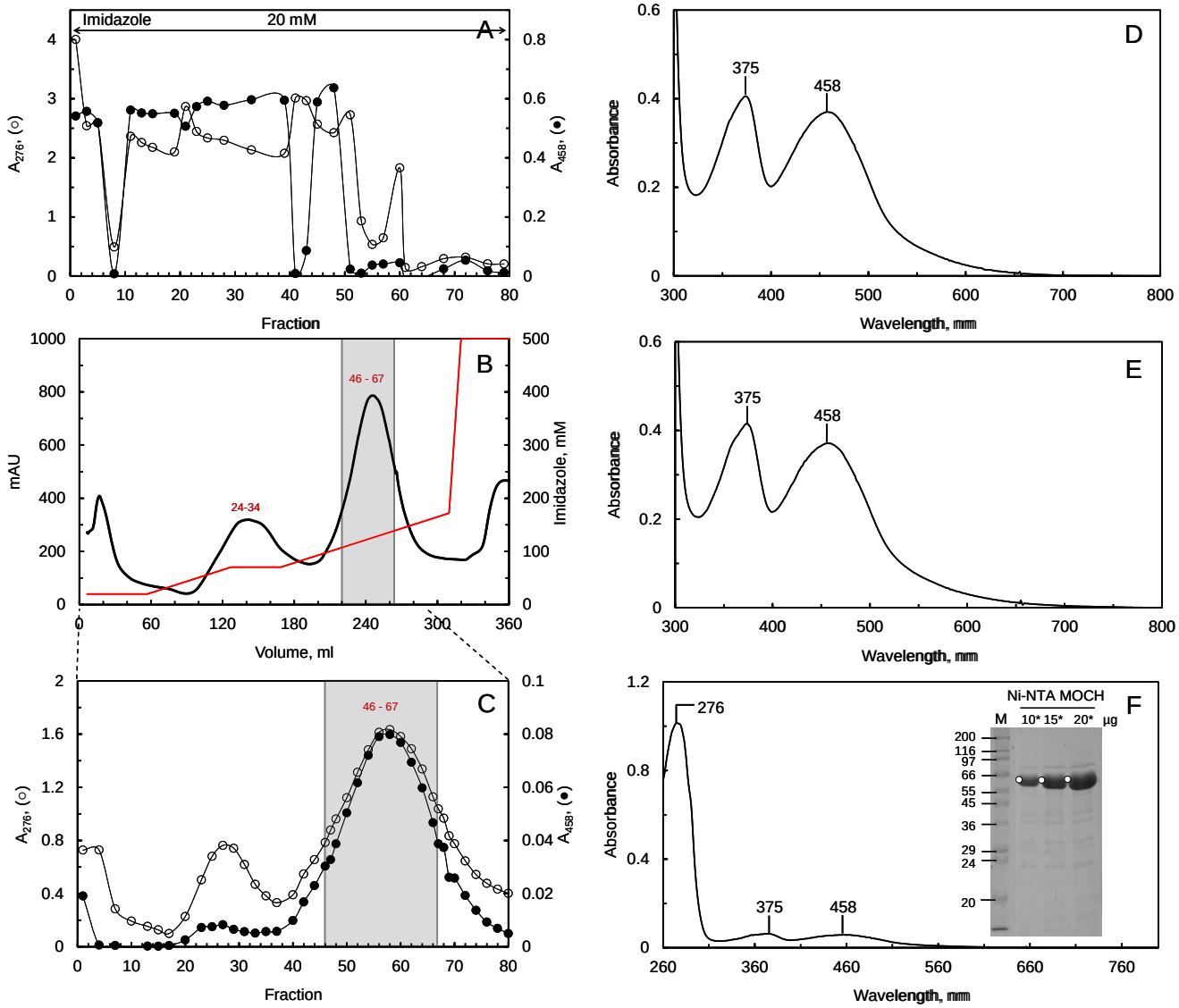

Figure 4.11. Large-scale purification of MOCH – Ni-NTA affinity chromatography. A crude extract from ≈30g of *E.coli* BL21(DE3, p18) cells that had produced MOCH (Figure 4.8) was prepared and chromatographed on a Ni-NTA Sepharose column as described in the legend of Figure 4.9. Panel A: elution profile obtained by measuring the absorption spectrum of fractions during the initial rinsing of the column with buffer A + 20 mM imidazole. Panel B: elution profile obtained during the imidazole gradient and on-line detection of A_{280} of the eluate. Panel C: detail of the elution profile shown in panel B obtained by measuring the absorption spectra of the individual fractions. The absorption spectrum of pooled fractions 46-67 after concentration (panel D, 3.13 mg/ml, 36 µM) and dialysis (panel E, 3.13 mg/ml, 36 µM) are shown. Panel F shows the spectrum of an aliquot of the final MOCH preparation after 6.5-fold dilution in buffer B (0.48 mg/ml, 7 µM). The inset shows the SDS-PAGE analysis of the final MOCH sample.

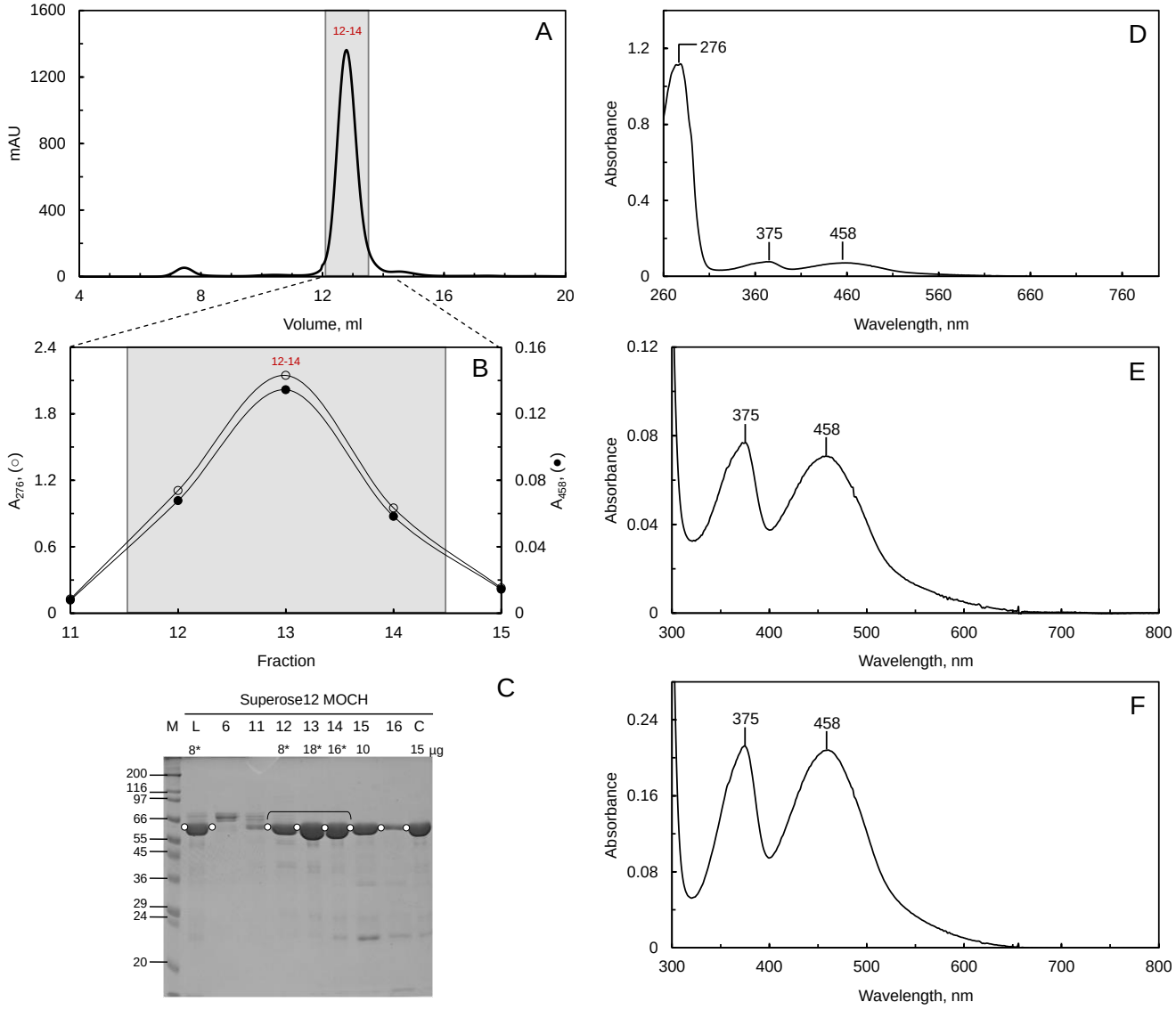

Figure 4.12. Purification of MOCH – Gel filtration. An aliquot of MOCH preparation after affinity chromatography (Figure 4.11) was gel filtered on a Superose12 column in buffer B in the FPLC to remove the ≈68 kDa contaminant and for buffer exchange. Panels A-F are as in Figure 4.10. MOCH concentration was: 0.6 mg/ml, 16 µM (pooled fractions 12-14, panels D and E) and 1.76 mg/ml, 34 µM (after concentration, panel F).

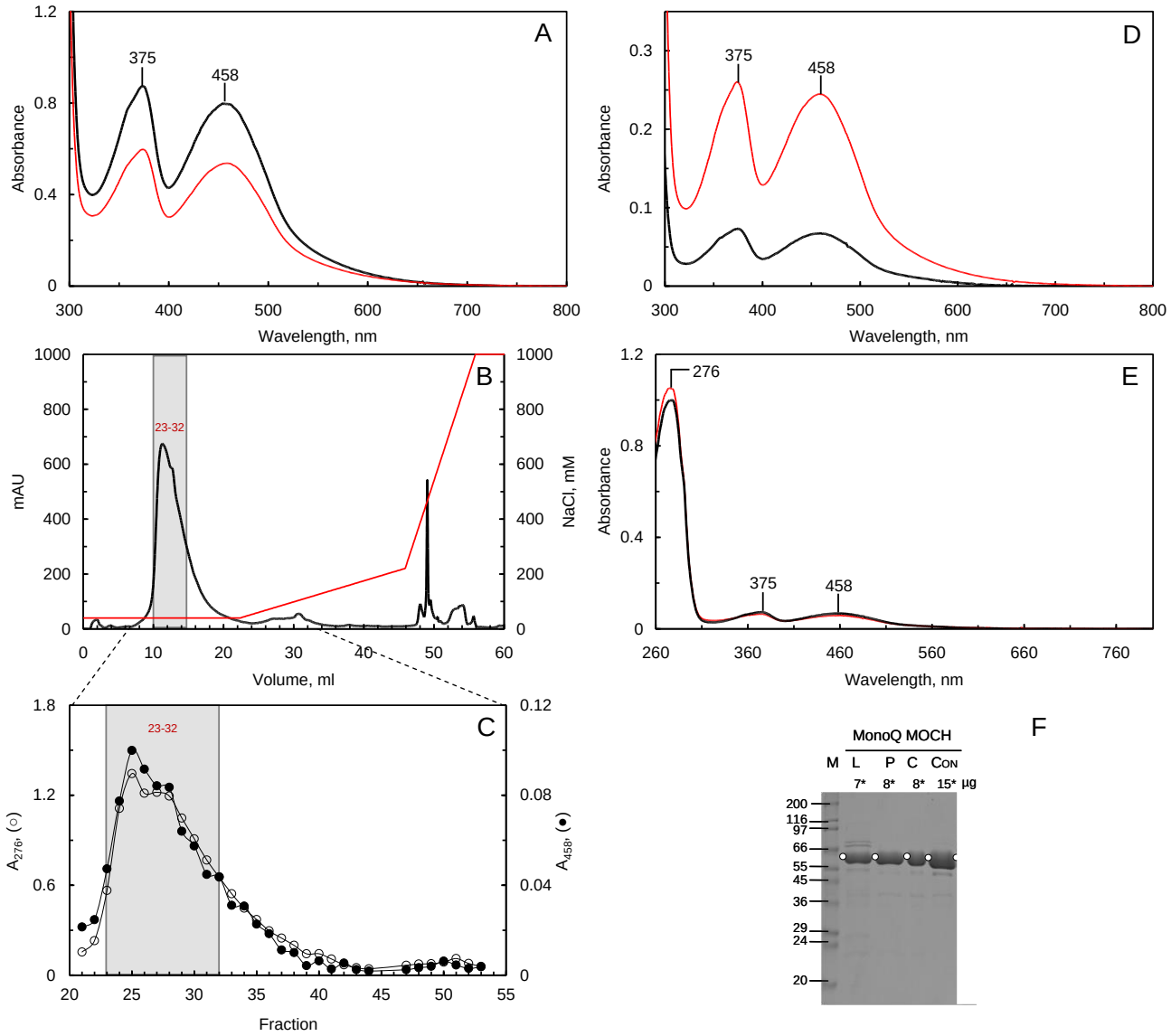

Figure 4.13. Purification of MOCH – Anion exchange chromatography. An aliquot of MOCH after Ni-NTA Sepharose chromatography (Figure 4.11) was dialyzed against 20 mM Na-phosphate buffer, pH 7.5, 40 mM NaCl and chromatographed in the FPLC onto a MonoQ column equilibrated with the dialysis buffer and eluted with a NaCl gradient. Panel A: absorption spetrum of MOCH after Ni-NTA Sepharose (black thick line, 6.7 mg/ml, 98 µM, 0.8 ml, 5.36 mg) and after dialysis (red thin line; 4.54 mg/ml, 66 µM, 1.1 ml, 4.99 mg). Panel B: elution profile of the MonoQ column with on-line detection of A_{280}. The NaCl gradient is indicated in red. Panel C: detail of the elution profile of panel B obtained by recording the absorption spectrum of the individual fractions. Panel D: absorption spectrum of the pooled fractions 23-32 before (black thick line, 0.57 mg/ml, 8.3 µM) and after concentration (red thin line, 2.07 mg/ml, 30 µM). Panel E: comparison of the absorption spectrum of MOCH before (red thin line) and after (black thick line) anion exchange chromatography after dilution to determine the UV/Vis ratio. Panel F: SDS-PAGE analysis of: MOCH loaded onto the MonoQ column (L); pooled fractions 22-32 before (P) and after concentration (C). CON indicates a sample of the final concentrated enzymes (C) after overnight incubation on ice at 4°C.

4.7. Large-scale purification of MOCHLIM

In order to set-up the purification procedure of MOCHLIM we needed to control its proteolytic degradation, that led to appearance of the ≈66 kDa , ≈62 kDa, ≈55 kDa and 22 and 21.5 kDa bands (Figure 4.7). The 62 kDa species clearly derived from that of 66 kDa, which was fully lost when the sample had to be treated over long period of time as during large scale purification. It derived from proteolytic cleavage of MOCHLIM in the region between the CH and the LIM domains as shown by the N-terminal sequencing ($_2$ASTPN$_6$) and by its mass of 71.2 kDa determined by MALDI-TOF. By checking the effect of incubating partially purified MOCHLIM from Ni-NTA affinity and anion exchange chromatographies, with 1 mM PMSF and 0.5% protease inhibitors cocktail (Sigma P8849), we found that the latter was sufficient to prevent MOCHLIM degradation (Figure 4.14).

Due to the cost of the reagent we decided to add the protease inhibitors cocktail at 0.5% to pooled fractions after each chromatographic step and to the dialyzed samples. PMSF (1 mM final concentration) was included in all buffers to further inhibit serine proteases.

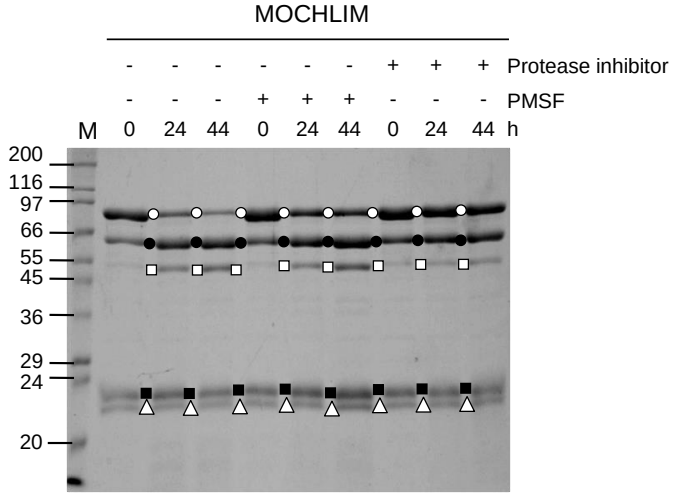

Figure 4.14. Effect of the protease inhibitors on the proteolytic degradation of MOCHLIM form. Aliquots of MOCHLIM4 purified by Ni-NTA Sepharose and anion exchange chromatographies were diluted 2-fold in buffer in the absence and presence of 1 mM PMSF or 0.5% protease inhibitors cocktail (Sigma Aldrich P8849). After 0, 24 and 44 h at 4°C aliquots of each sample were denatured by incubation at 100°C for 5 min. ○, full-length MOCHLIM form (87 kDa); ●, 62 kDa protein species; □, 55 kDa;■, 22 kDa; Δ, 21.5 kDa.

30 g of *E.coli* BL21(DE, p18) cells containing MOCHLIM4 forms, grown in fermentor and harvested 24 h after the induction of protein expression (Figure 4.8), were homogenized by sonication in buffer A + 20 mM imidazole. The crude extract obtained after centrifugation (Table 4.4 A) was loaded on a Ni-NTA Sepharose column (15 ml), preequilibrated in buffer A + 20 mM imidazole, in the cold room. The column was washed with ≈10 column volumes of buffer A + 20 mM imidazole, 1 mM PMSF, 1 mM 2-ME (Figure 4.15, panel A) and 5 column volumes of buffer A + 50 mM imidazole, 1 mM PMSF, 1 mM 2-ME to remove the unbound and weakly bound proteins (fractions 1-20, Figure 4.15, panel B). The bound proteins were eluted by applying a linear 50-200 mM imidazole gradient in 9 column volumes (Figure 4.15, panel B). Fractions enriched in MOCHLIM were pooled, supplemented with 0.5% protease inhibitor cocktail (Table 4.4 A), concentrated by ultrafiltration (Table 4.4 A) and dialyzed against buffer B + 1 mM PMSF (Figure 4.15, panels D and E; Table 4.4 A). Protease inhibitors cocktail (0.5% v/v, final concentration) was added to the final MOCHLIM solution. The other half of the sample was further concentrated by ultrafiltration with 87% of protein recovery (Figure 4.15, panel F).

The absorption spectrum of MOCHLIM showed absorbance maxima at 276, 375 and 458 nm (Figure 4.15, panel E). The A_{274}/A_{458} ratio of 19 to be compared with the theoretical value of 16 (see Chapter 5), indicated that the MOCHLIM preparation was not homogeneous at this stage. SDS-PAGE showed that the main contaminant species had mass of 22 and 21.5 kDa and only traces of the ≈66 kDa degradation products were also present (Figure 4.15, panel G), indicating that the addition of the protease inhibitors cocktail before concentration and after dialysis was sufficient to control proteolytic degradation of MOCHLIM.

The final MOCHLIM preparation was divided in small aliquots and stored at -80°C after flash-freezing in liquid nitrogen. Under these conditions MOCHLIM was stable both after long-term storage at -80°C and after overnight incubation on ice at 4°C (see Chapter 5).

The MOCHLIM preparation obtained by Ni-NTA Sepharose chromatography, which was stabilized by the addition of the protease inhibitors cocktail contained two main contaminanting species of 22 and 21.5 kDa as well as trace amounts of other proteins, which were more likely residual *E.coli* proteins and degradation products of MOCHLIM. Such contaminants could be easily removed by gel filtration on a Superose12 column on a small scale or on a Superdex200 column on a large scale. Only results of the preparative Superdex200 column are shown here. An example of chromatography on a Superose12 column is shown in Chapter 5.

The MOCHLIM preparation after the Ni-NTA Sepharose affinity chromatography (Figure 4.15) was concentrated (Figure 4.16, panel A; Table 4.4 B) and gel filtered on a Superdex200 column (150 ml) equilibrated and eluted with buffer B + 1 mM PMSF at 4°C. 1.5 or 5 ml fractions were collected. The elution profile was qualitatively similar to that obtained during pilot purification experiments on a Superose12 column (Figure 4.16, panel B), with a main peak containing the enzyme and two peaks with low absorbance. SDS-PAGE analysis of the fractions showed that the proteins with mass just lower than that of intact MOCHLIM were in the first chromatographic peak (fractions 25-30, Figure 4.16, panels B, C) with some MOCHLIM. A peak containing the protein species of 22 and 21.5 kDa (fractions 60-70,

Figure 4.16, panels B, C) was well resolved from the main peak containing MOCHLIM (fractions 40-50, Figure 4.16, panels B, C). On the basis of the absorption spectrum, fractions were pooled (fractions 43-48, Figure 4.16, panel D; Table 4.4 B) and concentrated (Figure 4.16, panel E; Table 4.4 B). The final MOCHLIM preparation was pure, stable and no degradation of the enzyme during this final purification step occured. MOCHLIM showed absorbance maxima at 278, 375 and 458 nm. The A_{278}/A_{458} ratio value of 15.9 (Figure 4.16, panel F) was similar to the theoretical value of 16 indicating that MOCHLIM was homogeneous with the correct complement of FAD. Protein purity was confirmed by SDS-PAGE (Figure 4.16, panel C). The NADPH oxidase activity of the final enzyme preparation was measured. The v/[E] value, which, assuming that all the protein present is MOCHLIM, would correspond to apparent turnover, was 1.1 s^{-1}. This value was comparable with the values measured for the MOCHLIM preparations obtained by gel filtration on Superose12 column under same conditions.

Similar results were obtained for gel filtration of MOCHLIM on a Superose12 column. Such chromatography was also used to exchange the buffer prior to several experiments.

MOCHLIM was also stable upon storage at -80°C after flash-freezing in liquid nitrogen or if kept on ice up to 48 h (see Chapter 5).

Table 4.4. Large-scale purification of MOCHLIM. Quantitation of MOCHLIM prepared from 34 g of *E.coli* BL21(DE3, p18) cells as described in the text. A: Recovery after Ni-NTA Sepharose, concentration and dialysis as described in the legend of Figure 4.15. B: Half of the MOCHLIM preparation obtained by Ni-NTA chromatography was concentrated and gel filtered onto Superdex200 column as described in the legend of Figure 4.16. The NADPH oxidase activity was measured in 20 mM Hepes/KOH buffer, pH 7, in the presence of 100 µM NADPH at 25°C. [a]Protein concentration was determined with the Bradford method. [b]Protein concentration was determined from the absorbance at 458 nm, by using the extinction coefficient of 8.1 $mM^{-1}cm^{-1}$ of MO (Zucchini et al., 2001) and the calculated mass of 86.4 of MOCHLIM.

A

		Bradford[a]			Absorbance[b]			
Sample	ml	mg/ml	mg	yield, %	mg/ml	mg	yield, %	µM
Crude extract	200	20	4100	100		-	-	-
Ni-NTA Sepharose	42	1.09	45.78	1.12	0.8	33.6	100	12.6
Concentration	12	3.5	42	1.02	2.62	31.44	93	30
Dialysis	12	3	37	0.91	2.48	29.76	88	29

B

		Bradford[a]			Absorbance[b]				Activity		
Sample	ml	mg/ml	mg	yield, %	mg/ml	mg	yield, %	µM	A_{278}/A_{458}	U	U/mg[a]
Ni-NTA Sepharose	6	3	18	100	2.57	15.57	100	31.25	19	-	-
Concentration	3.3				4.26	14	91	49			
Superdex200	8.7	1.5	13.05	43	1.2	10.4	64	13. 9	16.5	-	-
Concentration	2.2	5	11	37	4.33	9.5	59	50.1	15.9	8.8	0.77

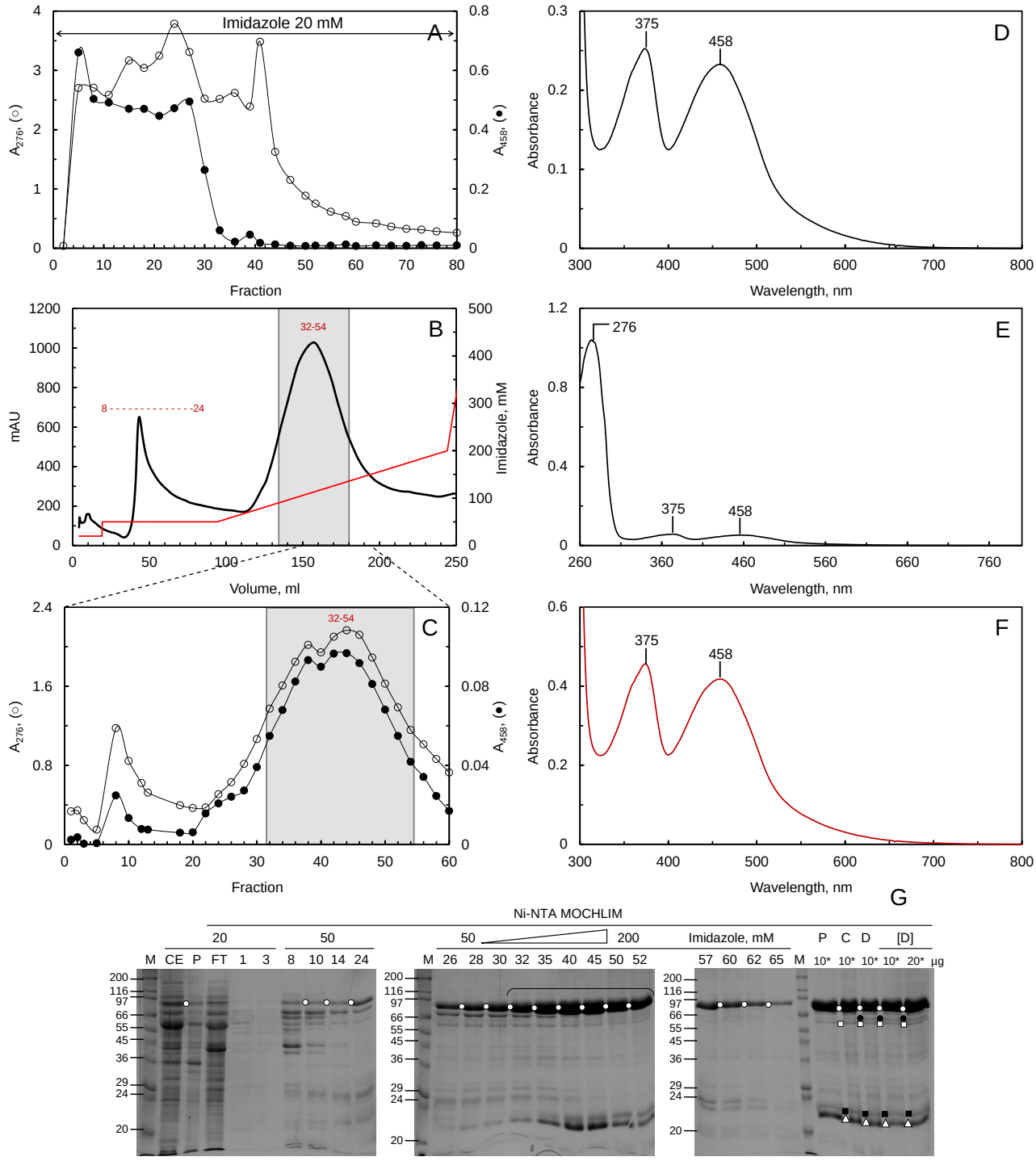

Figure 4.15. *Large-scale purification of MOCHLIM – Ni-NTA affinity chromatography.* A crude extract from ≈30g of *E.coli* BL21(DE3, p18) cells that had produced MOCHLIM (Figure 4.8) was homogenized and used to purify MOCHLIM on a Ni-NTA Sepharose column as described in the legend of Figure 4.9. Panel A: elution profile obtained by measuring the absorption spectrum of fractions during the initial rinsing of the column with buffer A + 20 mM imidazole. Panel B: elution profile obtained during the imidazole gradient and on-line detection of A_{280} of the eluate. Panel C: detail of the elution profile shown in panel B obtained by measuring the absorption spectra of the individual fractions. The absorption spectra of the concentrated fractions 32-54 after dialysis against buffer B + 1 mM PMSF (2.6 mg/ml, 30 µM; panel D) and after 5-fold dilution in dialysis buffer (0.52 mg/ml, 6 µM; panel E) are shown. Half of the MOCHLIM preparation was further concentrated (4.45 mg/ml, 51 µM; panel F). Panel G: SDS-PAGE analysis of: crude extract (CE); pellet obtained after centrifugation (P); unbound proteins eluted during rinsing of the column with buffer A + 20 mM imidazole (fraction 28 in panel A, FT); fractions numbered as in panel C; the pooled fractions 32-54 (P) after concentration (C) and after dialysis (D); the final sample was further concentrated ([D]) prior to storage at -80°C. Bands corresponding to full-length MOCHLIM (○, 87 kDa), and its presumed degradation products (●, 66 kDa; □, 62 kDa; ■, 22 kDa; Δ, 21.5 kDa) are indicated.

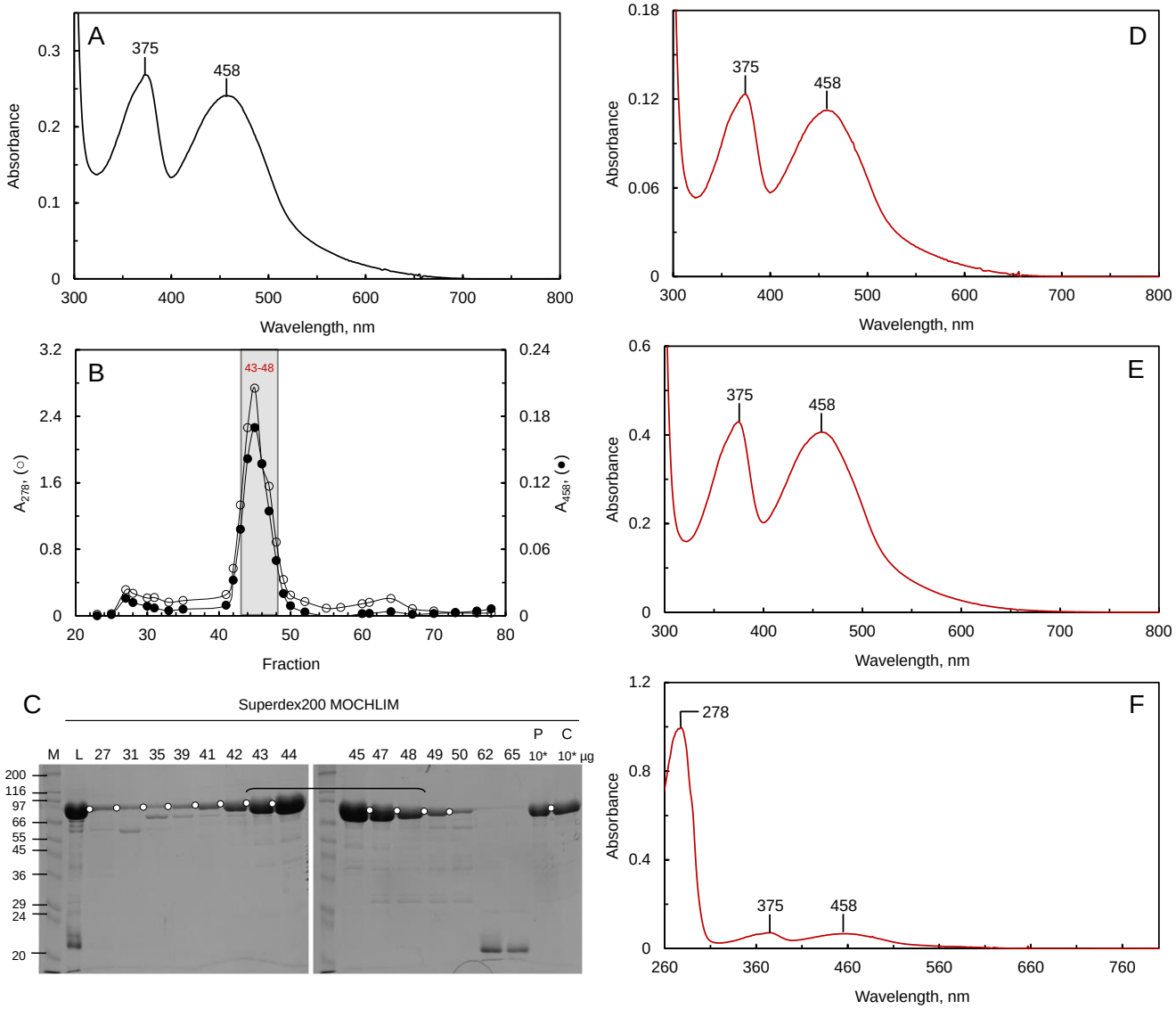

Figure 4.16. Large-scale purification of MOCHLIM – Gel filtration. To remove the contaminating proteins present in the MOCHLIM preparation obtained by Ni-NTA Sepharose affinity chromatography (Figure 4.15), half of the final sample was concentrated for its further purification on a Superdex200 column (150 ml) equilibrated and developed in buffer B + 1 mM PMSF in the cold room. The absorption spectrum of MOCHLIM solution from Ni-NTA Sepharose after concentration (4.26 mg/ml, 49 µM) is shown in panel A. The elution profile obtained by recording the absorption spectra of the individual fractions is shown in panel B. Panel C shows the SDS-PAGE analysis of: MOCHLIM from Ni-NTA Sepharose after concentration loaded onto Superdex200 column (L); fractions numbered as in panel B; the pooled fractions 43-48 (shaded area in panel B) before (P) and after concentration (C); the other symbols are as in the legend of Figure 4.15. Panels D and E: the absorption spectra of the pooled fractions (1.2 mg/ml, 14 µM) and after concentration (4.3 mg/ml, 51 µM) are shown. An aliquot of the final MOCHLIM preparation was diluted 7-fold (0.62 mg/ml, 7 µM) in equilibration buffer to determine the UV/Vis ratio (panel F).

4.8. Large-scale purification of full-length MICAL

The crude extract (Table 4.5) obtained by homogenization of 30 g of *E.coli* BL21(DE, p18) cells in buffer A + 5 mM imidazole, 1 mM PMSF, 1 mM 2-ME, 1% protease inhibitors cocktail was loaded onto Ni-NTA Sepharose column (15 ml) equilibrated in buffer A + 5 mM imidazole. The removal of the weakly bound proteins to the resin was carried out as described for the purification of the MOCH form. The bound proteins were eluted by applying a 20-200 mM imidazole linear gradient in buffer A in 10 column volumes (Figure 4.17, panel A). As done for MOCH, the concentration of imidazole was held constant at ≈56 mM imidazole for 4 column volumes to resolve MICAL from some contaminants (Figure 4.17, panel A). MICAL started to elute at ≈80 mM imidazole. To try to separate it from the other *E.coli* proteins also bound to the resin, imidazole concentration was held constant to ≈115 mM for one column volume. After this step the gradient was resumed (Figure 4.17, panel A). To the pooled fractions (fractions 29-46, Table 4.5) 0.5% (v/v) protease inhibitor cocktail was added as done for MOCHLIM to prevent proteolysis. The sample was concentrated by ultrafiltration (Figure 4.17, panel D; Table 4.5) and dialyzed against buffer B + 1 mM PMSF.

At this stage, the absorption spectrum of the MICAL preparation showed maxima at 278, 375 and 458 nm, but the spectrum was less resolved in the 300-400 nm region compared to that of the other MICAL forms at the same purification step. Indeed, the calculated value of the UV/Vis ratio was 27 (Figure 4.17, panel E) to be compared with the theoretical value of 18, indicating that other proteins in addition to MICAL were present. The SDS-PAGE analysis confirmed the presence of contaminants. Among them, were protein species of ≈68 and 62 kDa (Figure 4.17, panel C). The first was present also in MO and MOCH preparation after Ni-NTA Sepharose, suggesting that it is an *E.coli* protein. The 62 kDa species may correspond to the MOCH form derived from proteolysis as found for MOCHLIM. However, no sign of proteolytic degradation was observed during concentration and dialysis indicating that the addition of the protease inhibitor cocktail to the enzyme before concentration and after dialysis was sufficient to prevent a possible degradation resulting in a stable MICAL preparation. MICAL form showed more contaminants compared to the other forms after Ni-NTA Sepharose chromatography. Thus one or more purification steps were required to obtain a homogeneous protein preparation.

MICAL was further purified by anion exchange chromatography. In order to identify suitable conditions, several small-scale purifications on MonoQ column were carried out. The most satisfying protocol we designed is here described.

The dialyzed MICAL from Ni-NTA Sepharose chromatography was loaded onto a Q-Sepharose column (10 ml) equilibrated with buffer B + 1 mM PMSF. The column was washed with equilibration buffer (4 column volumes) and then connected to an FPLC apparatus for the elution of the bound proteins by applying a linear 100-500 mM NaCl in 60 column volumes. The interaction between MICAL and the resin was weak and the protein started to elute during the initial washing of the column with the equilibration buffer. Complete MICAL elution was obtained at the early stages of the applied NaCl gradient (Figure 4.18, panel A). Fractions enriched in MICAL, which had a A_{278}/A_{458} value <21, were pooled (fractions 11-33, Figure 4.18, panel B; Table 4.5) and 0.5% of protease inhibitor cocktail was

added. The sample was concentrated (Figure 4.18, panel D; Table 4.5) and dialyzed against buffer B + 1 mM PMSF (Figure 4.18, panel D; Table 4.5).

The spectrum of the final enzyme preparation was well resolved in the 300-350 nm region suggesting that the protein was stable, with maxima at 278, 375 and 458 nm (Figure 4.18, panels D, E). The A_{278}/A_{458} ratio was 19 (Figure 4.18, panel E), a value similar to the theoretical one of 18 and much lower than that of 27 of the enzyme prior to anion exchange chromatography. SDS-PAGE confirmed that MICAL preparation was almost pure containing only traces of the of ≈68 kDa protein species (Figure 4.18, panel C). However, the yield of the procedure was low so that only 25% of MICAL was recovered in this step (Table 4.5). Such a low yield was in part due to the fact that we had to discard almost half of the fractions containing MICAL in order to remove the ≈68 kDa contaminant.

The final MICAL preparation was stored at -80°C after flash-freezing in liquid nitrogen.

Table 4.5. Large-scale purification of full-length MICAL. Quantitation of MICAL prepared from 30 g of *E.coli* BL21(DE3, p18) cells by Ni-NTA Sepharose and anion exchange chromatography onto Q-Sepharose resin as described in the legend of Figure 4.17.and 4.18, respectively. [a]Protein concentration was determined with the Bradford method. [b]Protein concentration was determined from the absorbance at 458 nm, by using the extinction coefficient of 8.1 $mM^{-1}cm^{-1}$ of MO (Zucchini et al., 2001) and the calculated mass of 119 of MICAL.

	Bradford[a]				Absorbance[b]				
Sample	ml	mg/ml	mg	yield, %	mg/ml	mg	yield, %	A_{278}/A_{458}	μM
Crude extract	160	19	3040	100	-	-	-	-	
Ni-NTA Sepharose	35	1.18	41.3	1.36	0.78	27.3	100	-	6.55
Concentration	7.5	4.48	33.6	1.11	3.24	24.3	89	-	27.2
Dialysis	7.5	4.33	32.5	1.07	3.16	23.7	87	27	26.6
Q-Sepharose	22	0.45	9.9	0.33	0.3	6.6	24	-	2.5
Concentration	3.5	2.08	7.28	0.24	1.8	6.3	23	-	15.1
Dialysis	3.5	2.03	7.11	0.23	1.7	5.95	22	19	14.3

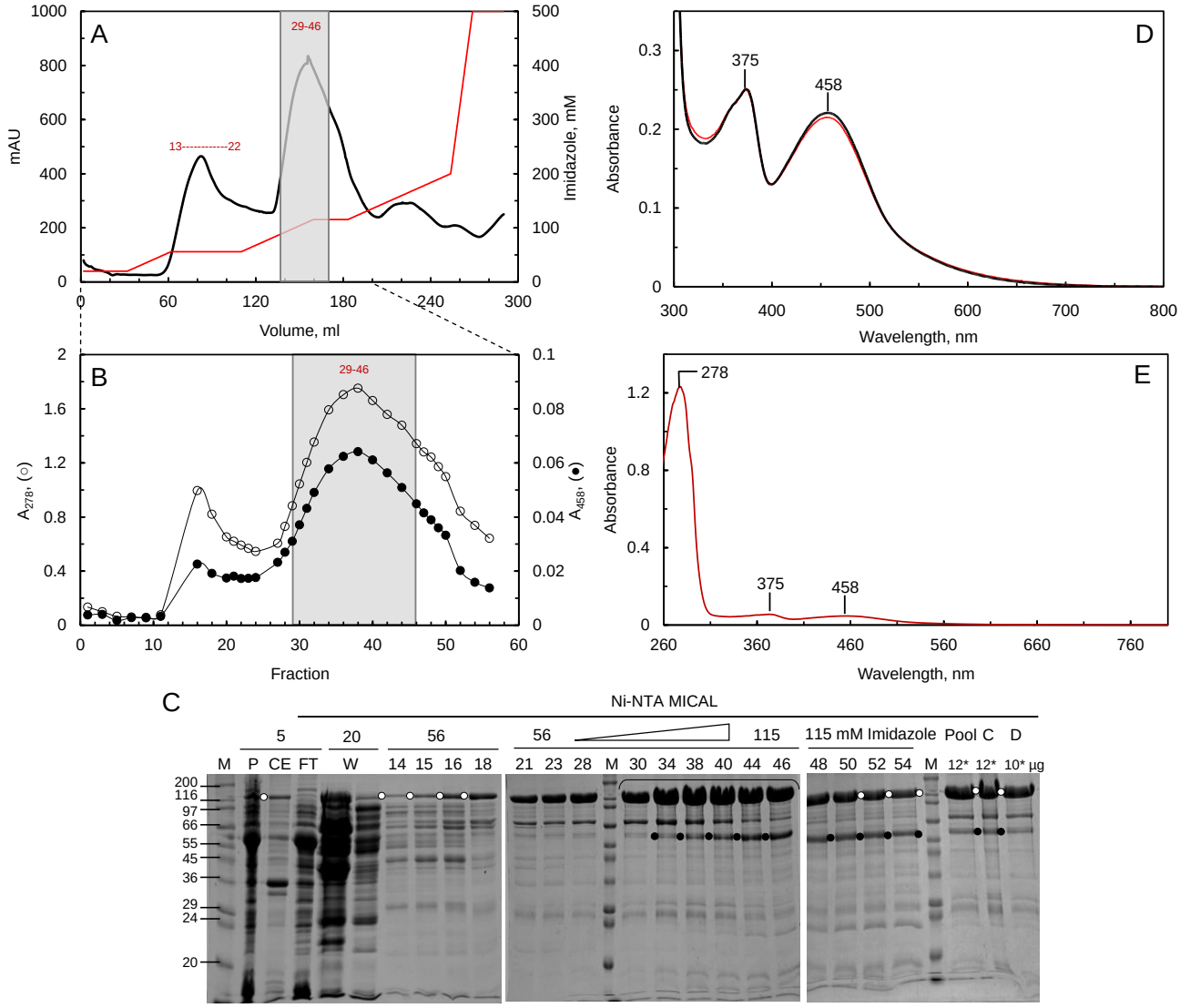

Figure 4.17. Large-scale purification of MICAL – Ni-NTA affinity chromatography. The crude extract of 30 g of *E.coli* BL21(DE3, p18) cells that had produced MICAL (Figure 4.8) form was loaded on Ni-NTA Sepharose column, the unbound and weakly bound proteins were removed with buffer A + 20 mM imidazole, 1 mM PMSF, 1 mM 2-ME. Panel A: Elution profile of the bound proteins by applying a linear imidazole gradient in buffer A + 1 mM PMSF (red line) with on-line detection at A_{280} (black line). Panel B: details of panel A obtained by recording the absorption spectra of the individual fractions. Panel C: SDS-PAGE analysis of: pellet (P) obtained by centrifugation of the crude extract (CE); the weakly bound proteins were removed by flowing buffer A + 20 mM imidazole (W); fractions eluted during the development of imidazole gradient numbered as in panel B; the pooled fractions (29-49, shaded area in panels A and B) before (Pool) and after concentration (C) and dialysis (D); ○, full-length MICAL (120 kDa); ●, protein species of ≈62 kDa; the quantity of protein loaded is calculated from the absorption spectrum. Panel D: the absorption spectra of MICAL after concentration (black thick line; 3.24 mg/ml, 27 µM) and after dialysis against buffer B + 1mM PMSF (red thin line, 3.16 mg/ml, 26 µM) are shown. Panel E: absorption spectrum of an aliquot of the final MICAL preparation diluted 6-fold (0.53 mg/ml, 4.5 µM) in dialysis buffer + 1 mM PMSF is shown.

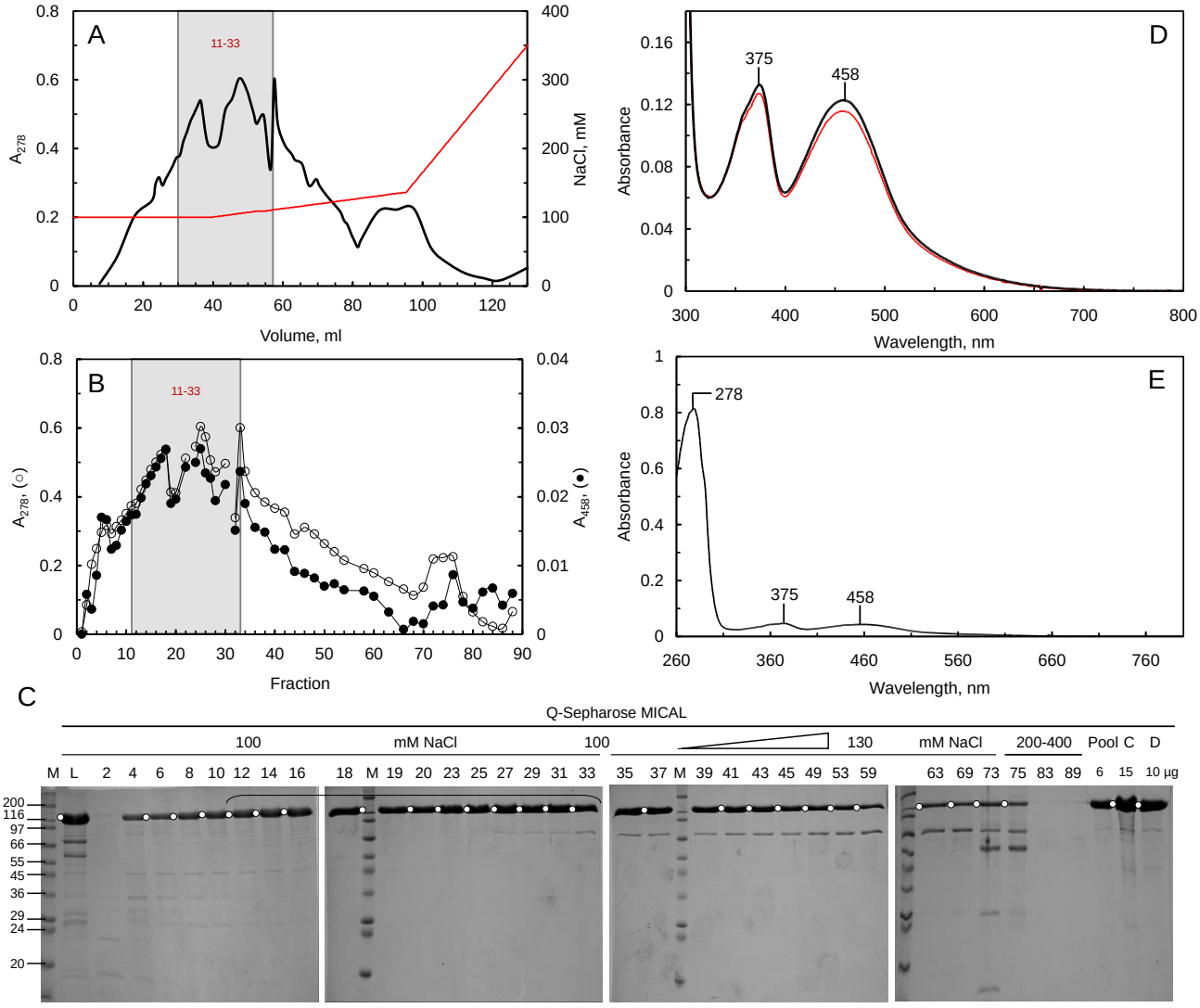

Figure 4.18. Large-scale purification of MICAL – Anion exchange chromatography. To remove the contaminating proteins from the MICAL preparation obtained by Ni-NTA affinity chromatography showed in Figure 4.17, the enzyme solution was further chromatographed onto a Q-Sepharose column (10 ml) equilibrated in buffer B + 1 mM PMSF and developed by applying NaCl gradient. The protein solution was loaded onto the column and washed with the equilibration buffer in the cold room. The the column was connected to an FPLC apparatus to elute the proteins bound to resin with increasing NaCl in buffer B + 1 mM PMSF (panel A). The individual fractions were analyzed by recording the absorption spectrum (panel B). Panel C shows the SDS-PAGE analysis of: MICAL solution from Ni-NTA Sepharose loaded onto Q-Sepharose column (L); fractions numbered as in panel B; fractions 11-30 were pooled (P, shaded area in panels A and B), concentrated (C) and dialyzed (D) against buffer B + 1 mM PMSF; the other symbols are as in the legend of Figure 4.17. The absorption spectra of MICAL preparation after concentration (black thick line; 1.8 mg/ml, 15 µM) and dialysis (red thin line, 1.7 mg/ml, 14 µM) are shown in panel D. An aliquot of the final preparation was diluted 3-fold (0.57 mg/ml, 4.76 µM) in dialysis buffer to determine the UV/Vis ratio (panel E).

5. Structural characterization of the purified MICAL forms.

5.1. N-terminal sequence and mass of MICAL forms

To verify the integrity of the MICAL forms we produced and purified (see Chapters 3 and 4), their N-terminal sequence and mass were experimentally determined in the laboratory of Prof. Gabriella Tedeschi (Dipartimento di Scienze Veterinarie e Sanità Pubblica, Università degli Studi di Milano).

The mass of MO observed in SDS-PAGE was similar to the calculated mass (Table 5.1). The N-terminal sequence of MO was that of MICAL (ASPTN) after post-traslational removal of Met1 and its mass determined by MALDI-TOF was similar to the theoretical one (Figure 5.1, panel A; Table 5.1). These results confirmed the integrity of the protein we prepared during this work .

On the contrary, MOCH migrated as ≈62 kDa band on SDS-PAGE (Figure 4.1), leading to the hypothesis that degradation of the protein had occurred during its expression. However, the N-terminal sequence of the purified protein was that of MO and the mass obtained by MALDI-TOF was similar to the calculated one (Figure 5.1, panel A; Table 5.1) indicating that MOCH was expressed and purified in its full-length form. This result was also confirmed by the mass spectrometry analysis of peptides obtained after MOCH tryptic and chymotrypitic digestion (not shown). Thus, the isolated band of ≈62 kDa (Figure 4.11- 4.13) was intact MOCH, which showed an anomalous migration on SDS-PAGE.

MOCHLIM was sensitive to proteolytic degradation (Figure 4.14) resulting in a truncated form of ≈62 kDa on SDS-PAGE, which most likely corresponded to a form comprising the MO and CH regions. The analysis of purified MOCHLIM under conditions that blocked proteolysis showed that it was intact with only small traces of contaminants or degradation products (Figure 5.1, panel B). Indeed, the N-terminal sequence of MOCHLIM was ASPTN and its mass was consistent with the expected one (Figure 5.1, panel B; Table 5.1).

Also the full-length form of purified MICAL showed post-traslational modification with the removal of Met1 and a mass similar to the calculated one (Figure 5.1, panel C; Table 5.1) demonstrating its integrity. As observed for MOCHLIM, only small amounts of degradation products or *E.coli* contaminating proteins were present in the final enzyme preparation (Figure 5.1, panel C).

All together these results demonstrated the integrity and purity of all the isolated MICAL forms.

Table 5.1 Mass of MICAL forms. The theoretical mass of MICAL, MO, MOCH and MOCHLIM was calculated using the Compute pI/Mw tool at www.expasy.ch by taking into account the post-translational removal of the starting Met residue and is expressed in Da. The calculated values are compared with those obtained by SDS-PAGE and MALDI-TOF.

Protein	*calculated*	*SDS-PAGE*	*MALDI-TOF*
MO	55005	54500 ± 700	54915
MOCH	68338	61700 ± 1500	68222
MOCHLIM	86348	87900 ± 1300	87615
MICAL	118920	121050 ± 600	119084

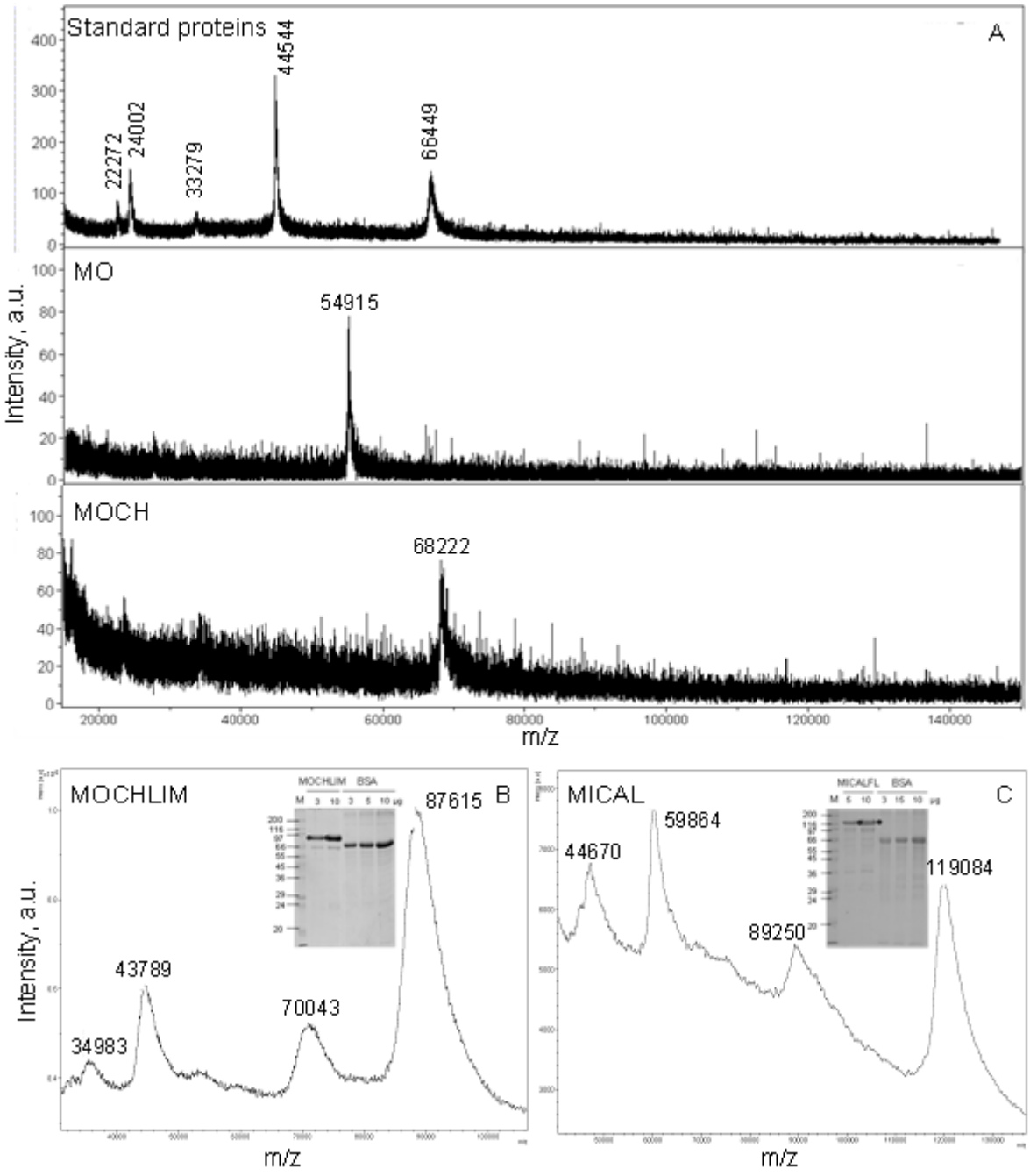

Figure 5.1. MALDI-TOF analysis of MICAL forms. Aliquots of MICAL forms (10-20 mg/ml in 50 mM Na-phosphate buffer, pH 7.5, 100 mM NaCl) were analyzed by MALDI-TOF. The mass spectrum of standard proteins, MO and MOCH is shown in panel A. In panels B and C the peaks at 87615 and at 119084 correspond to MOCHLIM and MICAL respectively; other peaks may be degradation products and/or *E.coli* contaminating proteins observed in trace in the SDS-PAGE of the sample (insets). The mass of MICAL forms determined by MALDI-TOF are also indicated in Table 5.1.

5.2. Determination of the FAD content and of the extinction coefficient in the visible region of MICAL forms.

MICAL1 catalyzes a NADPH oxidation reaction thanks to its N-terminal monooxygenase-like domain. An important aspect was the determination of the stoichiometry of FAD bound to the purified MICAL forms.

All MICAL forms were freshly transferred into 50 mM Na-phosphate buffer, pH 7.5, 100 mM NaCl by gel filtration on a Superose12 column (for MO and MOCHLIM, as described in Chapter 4) or by anion exchange chromatography (for MOCH and MICAL, Chapter 4). The protein solutions were concentrated to a final concentration of ≈20 μM. The absorption spectrum was recorded (red line in Figure 5.2) and the protein concentration was determined with the Bradford method (Bradford).

The sample was diluted 2-fold with a 10% trichloroacetic acid (TCA) solution and incubated 15 min at room temperature. The treatment caused immediate denaturation and release of FAD. The released FAD was recovered in the supernatant after centrifugation at 14900xg for 30 min at 4°C. From the absorption spectrum of the supernatant (black line in Figure 5.2) the FAD concentration, the stoichiometry and the extinction coefficient at 458 nm of MICAL forms were calculated (see Materials and Methods, Chapter 10).

For all MICAL forms greater than 0.8 mol of FAD per mol of protein was found (Table 5.2) with the protein concentration determined with the Bradford method. The calculated extinction coefficient at 458 nm of bound FAD was similar for all MICAL forms (Table 5.2) and similar to the value determined for the isolated MO domain (8.1 $mM^{-1}cm^{-1}$ Zucchini et al., 2011).

Protein denaturation with buffer containing guanidine is an alternative to TCA treatment as a method to determine the stoichiometry and the extinction coefficient of bound FAD. This method also allows determine the value of A_{280}/A_{448} ratio of the denatured protein, which is a measure of the percentage of the holoprotein present, independently from the protein concentration determined with the Bradford method.

As done for protein precipitation with TCA, MICAL, MOCH and MOCHLIM were gel filtered in 50 mM Na-phosphate buffer, pH 7.5, 100 mM NaCl, 10% glycerol, 1 mM EDTA and concentrated to ≈20 μM. The absorption spectra of the proteins were recorded before (red line in Figure 5.3) and after 2-fold dilution with 20 mM Tris/HCl buffer, pH 8, 500 mM NaCl, 6 M guanidine (black line in Figure 5.3).

The absorption spectra of MOCH and MOCHLIM were stable up to ≈15 min after the addition of guanidine, while for MICAL formation of turbidity was observed after ≈10 min maybe due to an incomplete denaturation of the protein and formation of aggregates.

For the calculation of the FAD content, the extinction coefficient and the value of A_{280}/A_{448} ratio the average of the absorbance values recorded during the first 15 min was used for MOCH and MOCHLIM. For MICAL the absorbance values obtained immediately after the dilution in buffer containing guanidine were used.

The amount of bound FAD (≈0.8 mol per mol of protein and the extinction coefficient at 458 nm, Table 5.2) were similar to those determined by TCA denaturation. The values of the A_{280}/A_{448} ratio were also

similar to the theoretical ones (Table 5.2) indicating that at least 90% of the MICAL proteins were present in the holoenzyme form. The lower percent of holoenzyme calculated with the protein concentration determined with the Bradford method may be due to a systematic overestimation of protein content with the method.

Table 5.2. Flavin content of MICAL forms. The FAD content was determined on the supernatant obtained by TCA precipitation of the proteins and their removal by centrifugation or by denaturation in guanidine. The protein concentration was calculated with the Bradford method with bovine serum albumin as the standard protein using the theoretical protein mass (Table 5.1). Quantitation of FAD content was carried out on two different protein preparations for MOCHLIM and MICAL. For MO and MOCH the determination was done with 2-3 experiments using proteins from the same preparation. The theoretical A_{280}/A_{448} was calculated as described in Materials and Methods (Chapter 10).

	Denaturation method					
	5%TCA		*3 M Guanidine*			
Protein	*FAD/protein*	ε_{458}	*FAD/protein*	ε_{458}	A_{280}/A_{448}	A_{280}/A_{448}
	mol/mol	$mM^{-1}cm^{-1}$	*mol/mol*	$mM^{-1}cm^{-1}$	*experimental*	*calculated*
MO	0.8 ± 0.03(2)	7.9 ± 0.054 (2)				
MOCH	0.84 ± 0.02(3)	7.92 ± 0.22 (3)	0.8	8.02	10.99	9.46
MOCHLIM	0.81±0.017(2)	8.14 ± 0.07 (2)	0.79 ± 0.02(2)	8.42 ± 0.007 (2)	10.52 ± 0.17 (2)	10.38
MICAL	0.83±0.005(2)	7.56 ± 0.56 (2)	0.76	8.48	13.56	12.49

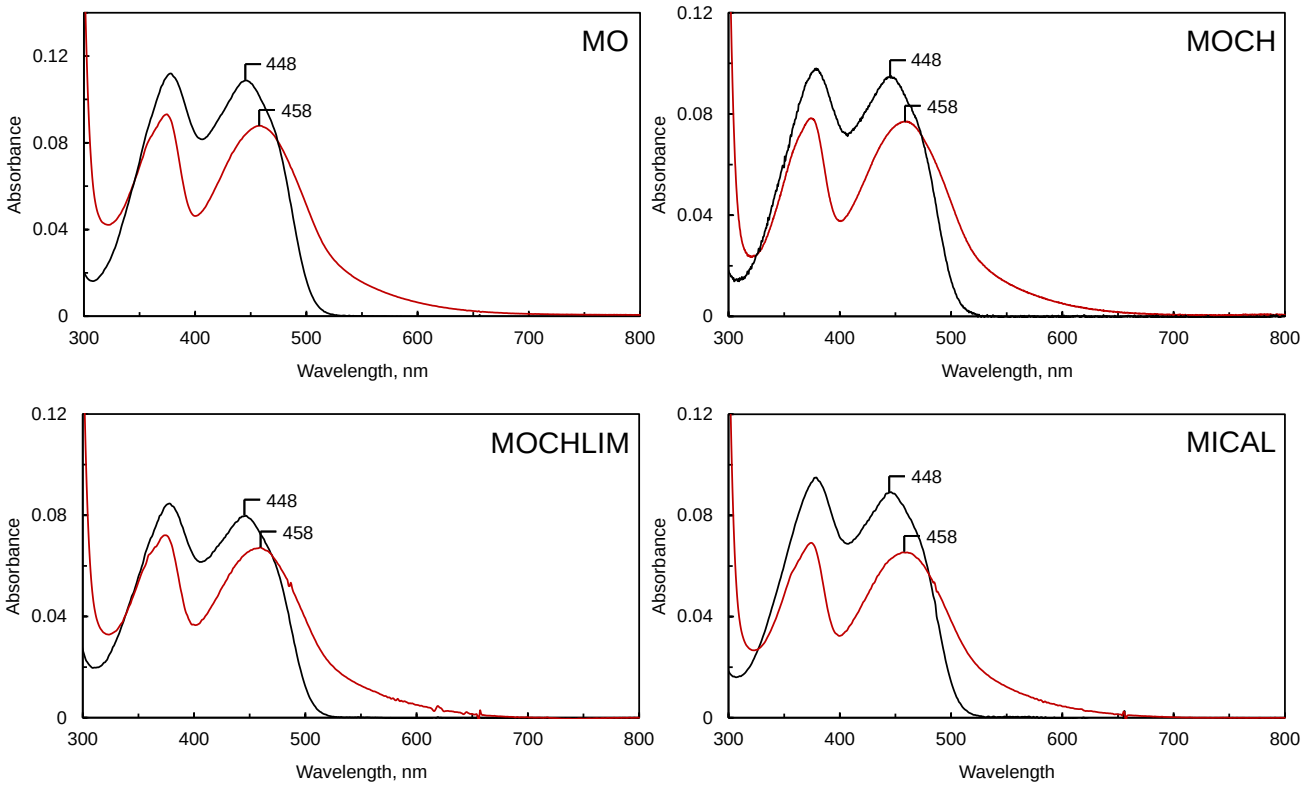

Figure 5.2. Absorption spectra of MICAL forms before and after denaturation with 5% TCA. The spectra of MICAL forms were recorded before (red line) and after addition of an equal volume of 10% (w/v) TCA and centrifugation (black line). The spectra of the native enzymes are corrected to take into account the 2-fold dilution. Initial protein concentration was: MO, 26 μM; MOCH, 24 μM; MOCHLIM, 22 μM; MICAL, 22 μM. The amounts of FAD present and the extinction coefficients at 458 nm of MICAL forms are in Table 5.2.

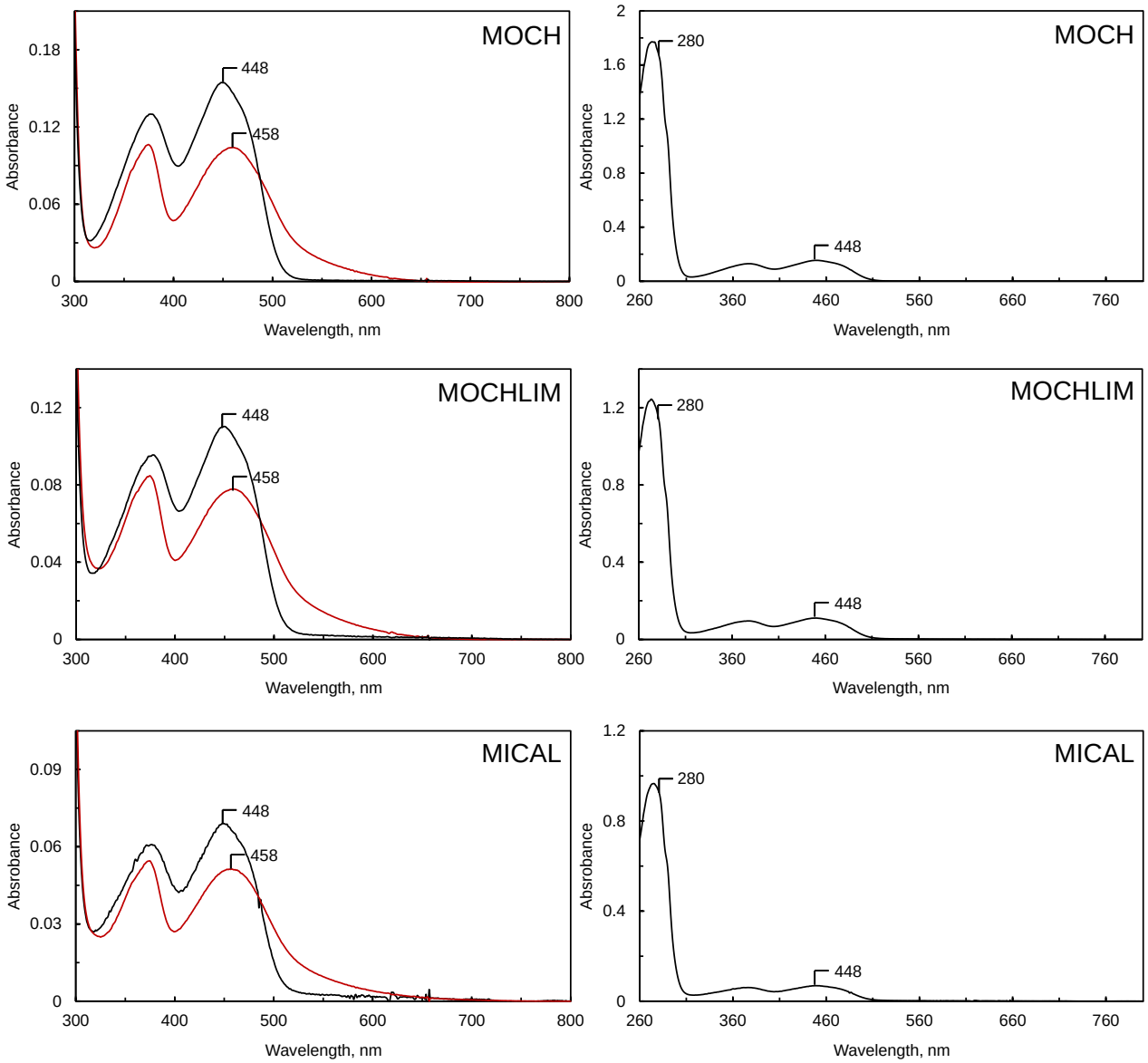

Figure 5.3. Absorption spectra of MICAL forms before and after denaturation with 3 M guanidine. Left panels: The absorption spectra of MICAL forms were recorded before (red line, left panels, the spectra are corrected for 2-fold dilution) and after 2-fold dilution with buffer 20 mM Tris/HCl, pH 8, 500 mM NaCl, 6 M guanidine (black line). The initial protein concentration was: MOCH, 32 μM; MOCHLIM, 22 μM; MICAL, 14 μM. The FAD stoichiometry, protein extinction coefficients at 458 nm and the A_{280}/A_{458} values of MICAL forms are indicated in Table 5.2.

5.3. Determination of the Zn^{++} content associated to LIM domain

The LIM domain, as described in Chapter 2, is characterized by the presence of a consensus sequence ($CX_2CX_{16-23}HX_2CX_2CX_{16-23}CX_2C$), in which the Cys and His residues are responsible for the coordination of two zinc ions (Kadrmas et al., 2004). The three dimensional structure of the isolated LIM domain of human MICAL1 (Figure 2.5) demonstrated the presence of the expected 2 Zn^{++} ions (PDB ID 2CO8)

Since the presence of zinc ions in the LIM domain is essential for its secondary and ternary structures determining its stability and functionality, it was important to verify the stoichiometry of zinc bound to the purified MOCHLIM and MICAL forms.

The zinc content of MICAL forms was determined using the colorimetric method developed by Bennie et al., (1985) to quantify the zinc content of serum samples. The method was modified by us to lower the quantity of sample required for the analysis, as described in Materials and Methods (Chapter 10). Several control experiments were also done to ensure that buffer composition did not interfere with the method and to identify the optimal concentration range of zinc ions (Chapter 10).

Aliquots (0.025-0.2 ml, 0.2-3 µM) of the supernatants obtained by TCA denaturation of MICAL forms (see above) were added to 0.75 ml of 1 M Hepes/NaOH buffer, pH 8, 125 µM BrPAPS and the absorption spectrum was recorded for ≈10 min until no more changes in the spectrum were observed. The amount of zinc present was calculated using the extinction coefficient of 130 $mM^{-1}cm^{-1}$ at 550 nm for the Zn^{++}-BrPAPS complex. MO and MOCH forms were used as control samples to detect non-specifically associated zinc ions. For MOCHLIM and MICAL ≈1.5 mol of Zn^{++} per mol of protein was determined, when the protein concentration was calculated with the Bradford method (Table 5.3), which most likely systematically overestimates the protein content by 15-20%. In fact, by taking into account the FAD bound to the protein 1.9 mol of Zn^{++} per mol of FAD was calculated (Table 5.3).

Table 5.3. Zinc content of MICAL forms. The zinc content was determined on the supernatant obtained by TCA precipitation of the proteins and their removal by centrifugation (see Table 5.2). The protein concentration was calculated with the Bradford method with bovine serum albumin as the standard protein using the theoretical protein mass (Table 5.1). FAD quantitation is taken from the data in Table 5.2.

Protein	*Zn^{++}/protein mol/mol*	*FAD/protein mol/mol*	*Zn^{++}/FAD mol/mol*
MO	0.07	0.8	0.08
MOCH	0.04	0.84	0.05
MOCHLIM	1.5 ± 0.1	0.81	1.8 ± 0.1
MICAL	1.6 ± 0.1	0.83	1.9 ± 0.1

5.4. Determination of the mass and oligomeric state of MICAL forms.

The isolated MO domains of mouse MICAL1 and human MICAL are monomeric in solution (Nadella et al., 2005; Zucchini et al., 2011). To verify if the presence of the additional domains, which mediate protein-protein interactions, alters the quaternary structure of the proteins, we determine the mass of MICAL forms by gel filtration and by dynamic light scattering (DLS).

Aliquots of (500 µl) of MOCH (3 mg/ml), MOCHLIM (2.8 mg/ml) and MICAL (2.25 mg/ml) solutions were gel filtered on a Superose12 column that had been calibrated with proteins of known mass (see Materials and Methods, Chapter 10). Under these conditions MOCH appeared to be monomeric in solution, while MOCHLIM and MICAL may form dimers (Figure 5.4; Table 5.4).

Table 5.4. Mass determination of MICAL forms by gel filtration. Protein samples (2-3 mg/ml, 0.5 ml) were gel filtered on a calibrated Superose12 column in buffer B. The monomer mass was calculated as in Table 5.1.

Protein	*Elution volume, ml*	*Mass observed*	*Mass calculated*	*Oligomeric state*
MOCH	12.75	78427	68338	1.15
MOCHLIM	11.6	207107	86428	2.39
MICAL	11.4	236775	118920	1.99

MICAL forms were also analyzed by DLS, which also yields information on the degree of polydispersion of the protein samples. MOCH form was confirmed to be monomeric as found by gel filtration, while MOCHLIM and MICAL appeared to oligomerize (Figure 5.5; Table 5.5). Aliquots of MOCHLIM and MICAL at varying concentrations obtained after centrifugation at 10000xg for 1 h at 4°C were analyzed in greater detail. For MOCHLIM formation of dimers, trimers and tetramers and higher order aggregates depending on protein concentration (Table 5.5). While for protein solutions <2 mg/ml the calculated values of the radius corresponded to an apparent trimer or dimer (Table 5.5). MICAL was found to be as a dimer for all the protein concentration tested (Table 5.5).

Thus, either the LIM domain and the C-terminal region of MOCHLIM and of MICAL stabilize a dimer or these protein forms are monomeric but elongated. So that the globular species of 190 kDa would be 5.6 nm and dimerization would lead to an increase of only 1.9 nm, which corresponds to a extended stretch of ≈10 residues.

Table 5.5. Mass determination of MICAL forms by dynamic light scattering (DLS). Protein samples were analysed by DLS at 15°C. Instrument conditions: acquisition time, 15 s; sensitivity, 80-100%, solvent, glycerol 10%; pH, 7.5; concentrations are indicated in the table.R, [a] value of the sample radius;R_c, [b] the value of water shell radius (0.2 nm) is subtracted to the value of sample radius (R); [c]percentage of polydispersion; [d]mass of the sample calculated using the Rc value; [e]mass calculated as in Table 5.1; [f] sample obtained after ultracentrifugation at 100000xg for 1 h at 4°C in rotor TLA100.3 a Beckmann TL100 centrifuge. Buffer B: 50 mM Na-phosphate, pH 7.5, 100 mM NaCl, 10% glycerol, 1 mM EDTA, 1 mM DTT.

Protein	*mg/ml*	*μM*	*R, nm*[a]	*Rc, nm*[b]	*Pd, %*[c]	*Mass experimental*[d]	*mass calculated*[e]	*Apparent Oligomeric state*
MOCH	0.5	7.3	4.1	3.9	6	81000	68330	1.18
MOCHLIM	0.6	7.0	5.6	5.4	10	174000	86428	2.02
MOCHLIM[f]	0.24	2.8	5.9	5.7	12	198000		2.3
	0.65	7.5	7.2	7	34	320000		3.7
	1	11.6	6.8	6.6	15	278000		3.2
	2.1	24.3	9.7	9.5	46	653000		7.6
	4	46.3	10.2	10	45	736000		8.5
MICAL	0.5	4.2	6.1	5.9	13	214000	118920	1.8
	2	16.8	6.7	6.5	20	269000		2.26
	5	42.0	8.1	7.9	36	424000		3.56
MICAL[f]	0.22	1.8	6.2	6	27	223000		1.87
	0.6	5.0	6.3	6.1	28	232000		1.95
	1.2	10.0	6.2	6	14	223000		1.87
	2	16.8	6.1	5.9	30	214000		1.8
	4	33.6	6.3	6.1	14	232000		1.95

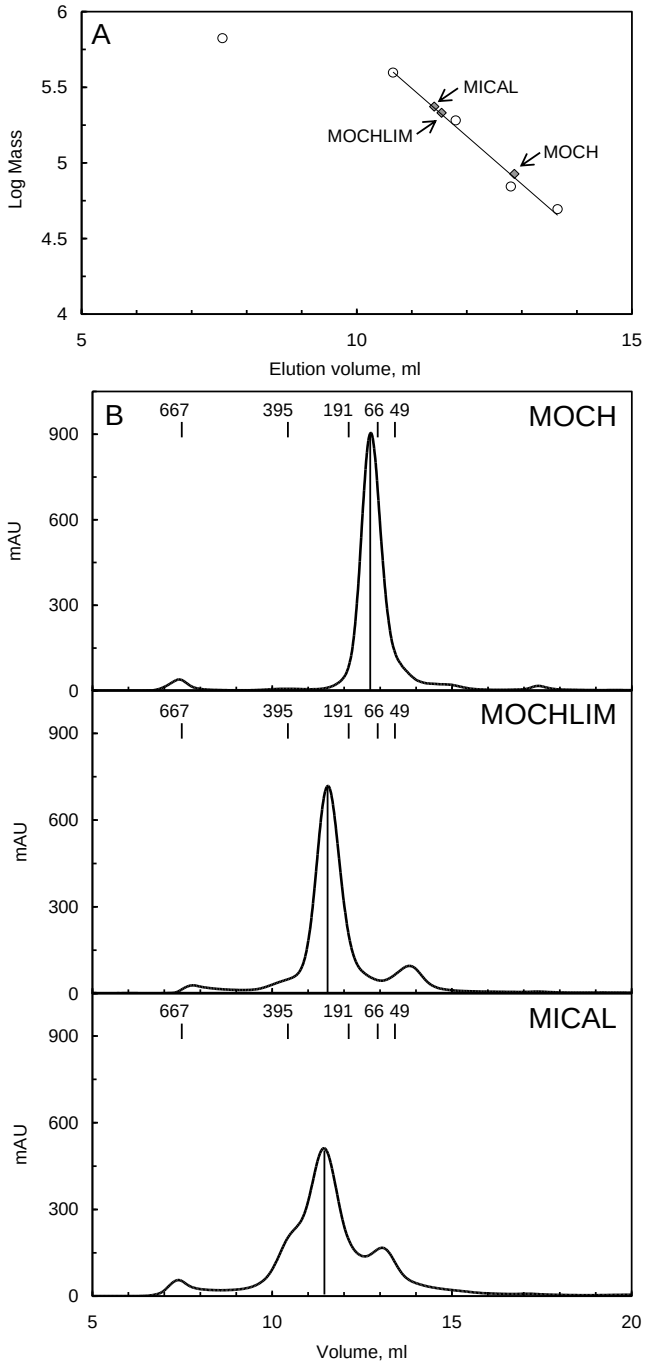

Figure 5.4. Mass determination of MICAL forms by gel filtration. Aliquots (400 µl) of MOCH (3 mg/ml), MOCHLIM (2.8 mg/ml) and MICAL (2.25 mg/ml) were gel filtered in buffer B on a calibrated Superose12 column. Panel A: Calibration curve obtained by gel filtration of standard proteins (○) from which thyroglobulin (667 kDa) is excluded and elution position of MICAL forms (♦). The calculated mass of MICAL forms is indicated in Table 5.4. Panel B: Elution profiles obtained by gel filtration of MICAL solutions. The additional peaks correspond to small amounts of contaminating proteins (see Chapter 4). The elution volume of the standard proteins is indicated.

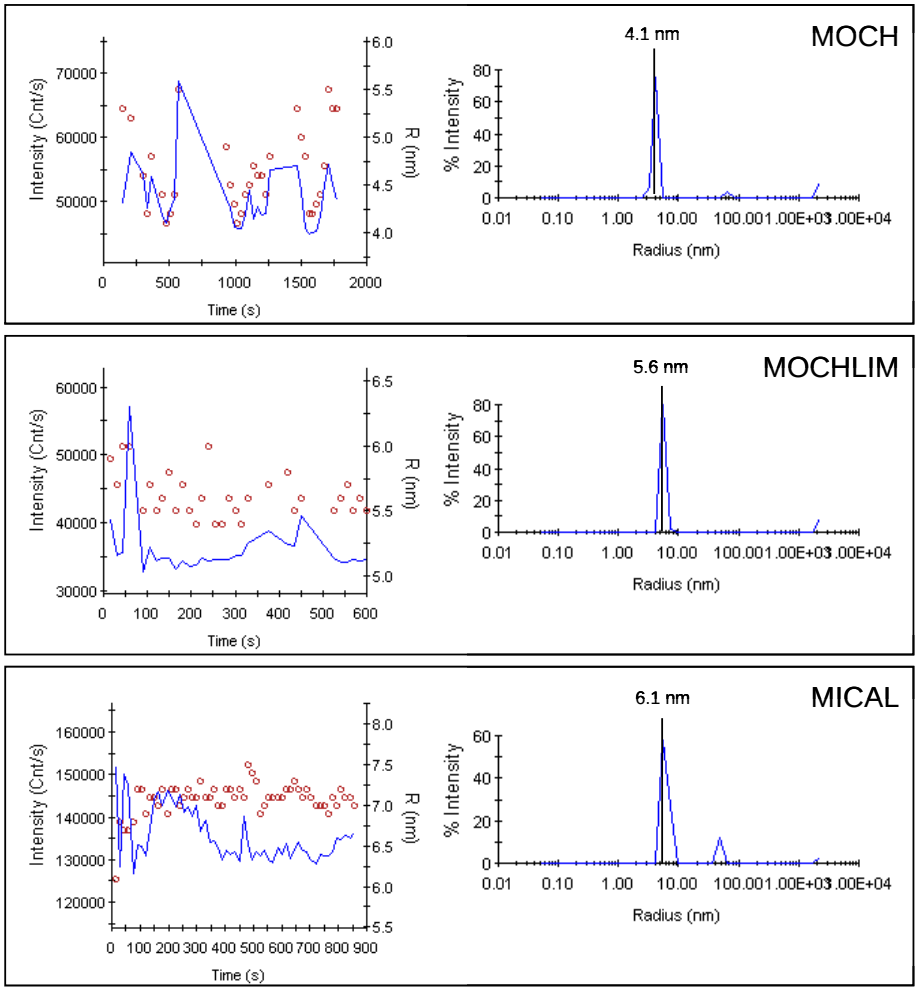

Figure 5.5. Determination of the apparent mass of MICAL forms by dynamic light scattering. Aliquots of MOCH (0.5 mg/ml, 7.3 µM), MOCHLIM (0.6 mg/ml, 6.95 µM) and MICAL (0.5 mg/ml, 4.2 µM) at the end of the purification were analyzed by DLS by recording signals for up to 30 min (left panels). The calculated radius (right panels) was corrected for the contribution of the water shell (0.2 nm) to determine the apparent mass of the proteins (Table 5.4). DLS conditions: acquisition time, 15 s; temperature, 15°C; sensitivity, 90%; solvent, 10% glycerol; pH, 7.5; concentration, 0.5 mg/ml.

5.5. Stability of human MICAL1 forms

A fundamental step prior to mechanistic and structural studies on a protein is the definition of the stability of the preparations upon storage and during the experiments. In particular for MOCHLIM and MICAL, which showed sensitivity to proteolysis, it was also important to establish the absence of proteolytic degradation. The absorption spectra, the NADPH oxidase activity and the electrophoretic pattern of samples were taken as a measure of the quality and stability of the protein preparations.

The absorption spectrum of protein-bound FAD is very sensitive to changes of protein environment. Shift of the absorbance maxima or changes at wavelength greater than 500 nm may reflect conformational changes, but also protein denaturation and formation of aggregates.

MO, MOCH and MOCHLIM solutions that had been stored at -80°C showed absorption spectra (black line in Figure 5.6, panels A-C) similar to those recorded at the end of the purification (grey line in Figure 5.6, panels A-C). No changes were observed for MOCH and MOCHLIM also after storage on ice at 4°C for 15 h (Figure 5.6, panels E-F). For MICAL, small changes were observed in its spectrum, in which the absorbance maximum shifted from 458 nm (grey line in Figure 5.6, panel D) to 456 nm (black line in Figure 5.6, panel D) with an increase of absorbance at 325 nm suggesting a tendency of the protein to aggregate. Such aggregates could be removed by centrifugation at 100000xg for 1 h at 4°C (not shown).

Aliquots of the enzymes were also used for SDS-PAGE analysis, after thawing, during the experiments and up to 20 h incubation on ice at 4°C. In all cases, the different samples of MICAL forms showed a similar electrophoretic pattern (Figure 5.7) indicating their stability.

The stability of the proteins, under various conditions, was also determined by monitoring the NADPH oxidase activity. As shown in Figure 5.8 there was no activity loss when the proteins were thawed after storage at -80°C. Furthermore, all MICAL forms were stable for up to 23 h in buffer B (for MO and MOCH) or in buffer B supplemented with 0.5% protease inhibitors cocktail (for MOCHLIM and MICAL) when kept on ice at concentrations greater than 1 mg/ml.

The stability of MICAL forms was measured as a function of pH, also in the light of the planned studies of the pH dependence of their NADPH oxidase activity. Aliquots of MO and MOCH were diluted 10-fold to a final concentration of ≈0.2 mg/ml in mixed buffer A and MOCHLIM was diluted in mixed buffer B, at varying pH. The enzymes solutions were incubated at 25°C and their NADPH oxidase activity was measured at different incubation times under standard conditions. For MO and MOCH, the activity of the protein solutions at varying pH was similar to that measured for the stock enzyme (Figure 5.9). Only a small decrease of the activity (15%) was observed for MO when diluted in buffers at pH greater than 7.5 (Figure 5.9), indicating that the enzyme is more stable in an acidic medium. On the contrary, MOCHLIM solutions showed a progressive loss of activity upon dilution in all buffer tested (Figure 5.9), suggesting that at this concentration MOCHLIM is not stable.

Thus, the pH did not alter the stability of MO, MOCH and MOCHLIM.

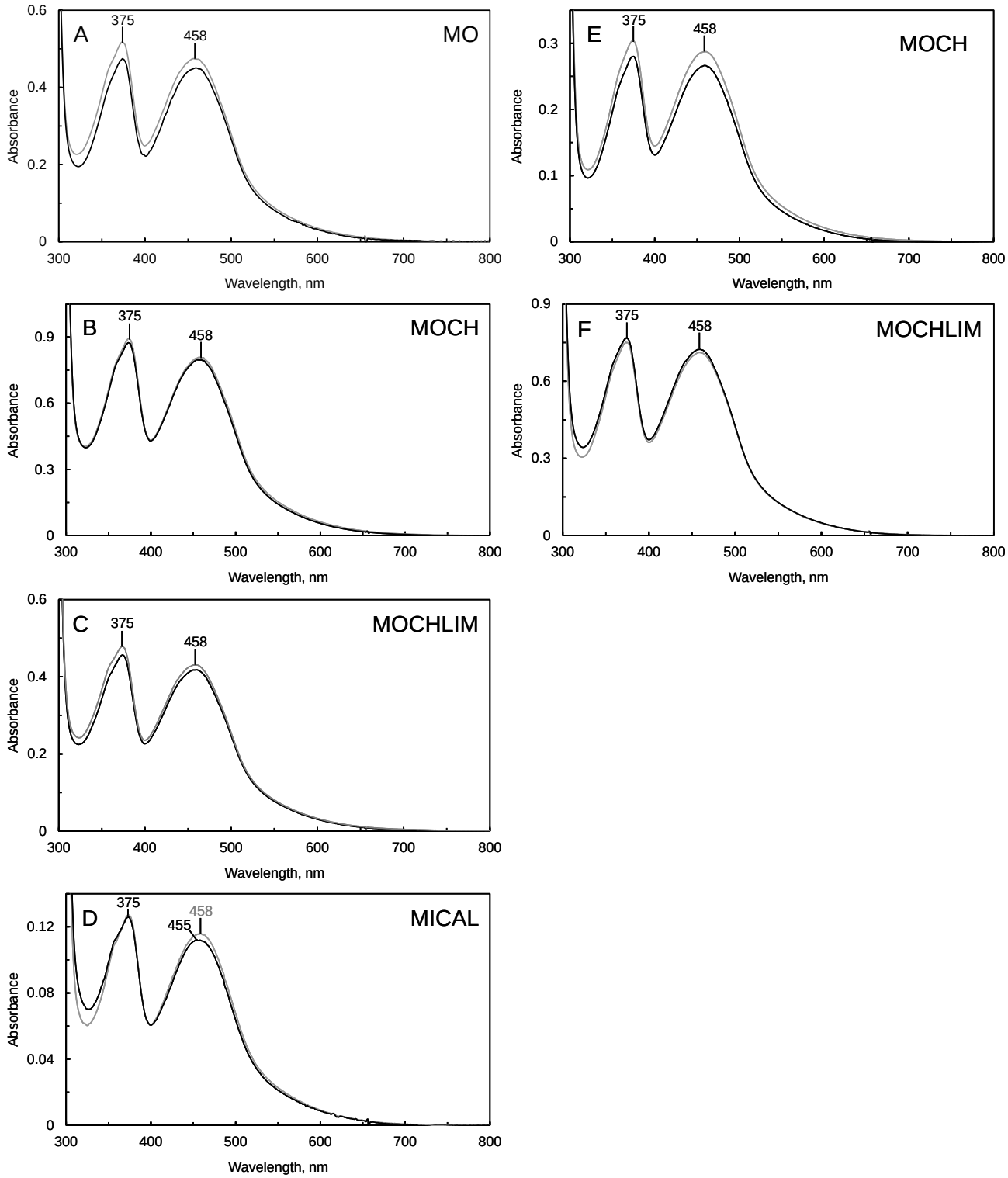

Figure 5.6. Comparison of the absorption spectra of MICAL forms at the end of the purification and after storage. Panels A-D: grey, the absorption spectra recorded at the end of the purification; black, spectra recorded after thawing of the protein samples that had been stored at -80°C after flash-freezing in liquid nitrogen. Proteins were conserved in buffer B (for MO and MOCH) or buffer B supplemeted with 0.5% of protease inhibitors cocktail (for MOCHLIM and MICAL) and their concentration was: MO, 3.2 mg/ml, 58 µM; MOCH, 6.8 mg/ml, 99 µM; MOCHLIM, 4.6 mg/ml, 53 µM; MICAL, 1.7 mg/ml, 14 µM. Panels E-F: grey, absorption spectra of MOCH (2.4 mg/ml, 35 µM) in 20 mM Hepes/KOH buffer, pH 7, 100 mM NaCl and of MOCHLIM (4.5 mg/ml, 52 µM) in buffer B at the end of the gel filtration; black, spectra recorded after storage on ice at 4°C for 15 h.

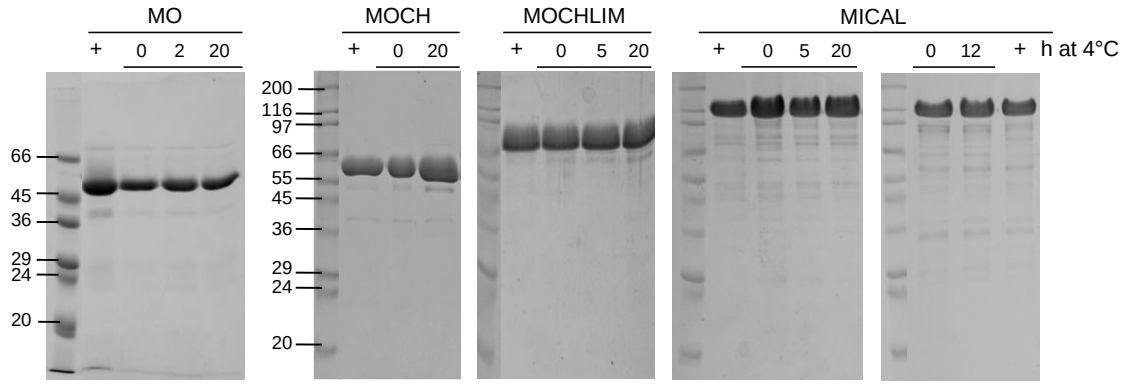

Figure 5.7. Check of the stability of MICAL forms by SDS-PAGE. The electrophoretic pattern of the protein preparations at the end of their purification (+) is compared to that of the proteins that had been stored at -80°C immediately after thawing (0 h) and at different subsequent times during which the proteins were kept on ice at 4°C. MO, 10 and 5 µg; MOCH, 10 and 15 µg; MOCHLIM, 15 µg; MICAL, 10 and 15 µg.

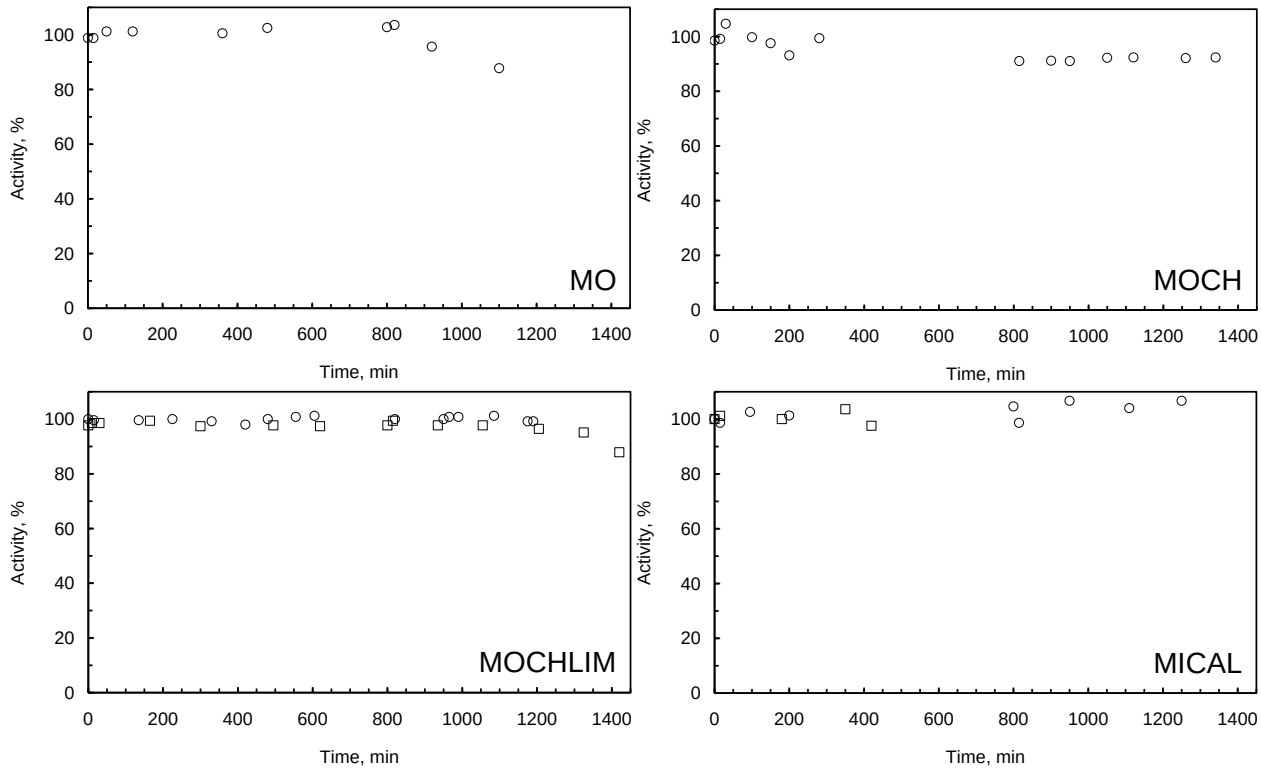

Figure 5.8. Stability of MICAL forms. Aliquots of purified MO (1 mg/ml), MOCH (3 mg/ml), MOCHLIM (○, 1 mg/ml; □, 5 mg/ml); MICAL (○, 5 mg/ml; □, 10 mg/ml) were thawed and kept on ice. Their NADPH oxidase activity was measured in 20 mM Hepes/KOH buffer, pH 7 in the presence of 100 µM NADPH at 25°C and indicated times. The residual activity is expressed as percentage with the respect of that of the sample at the end of the purification.

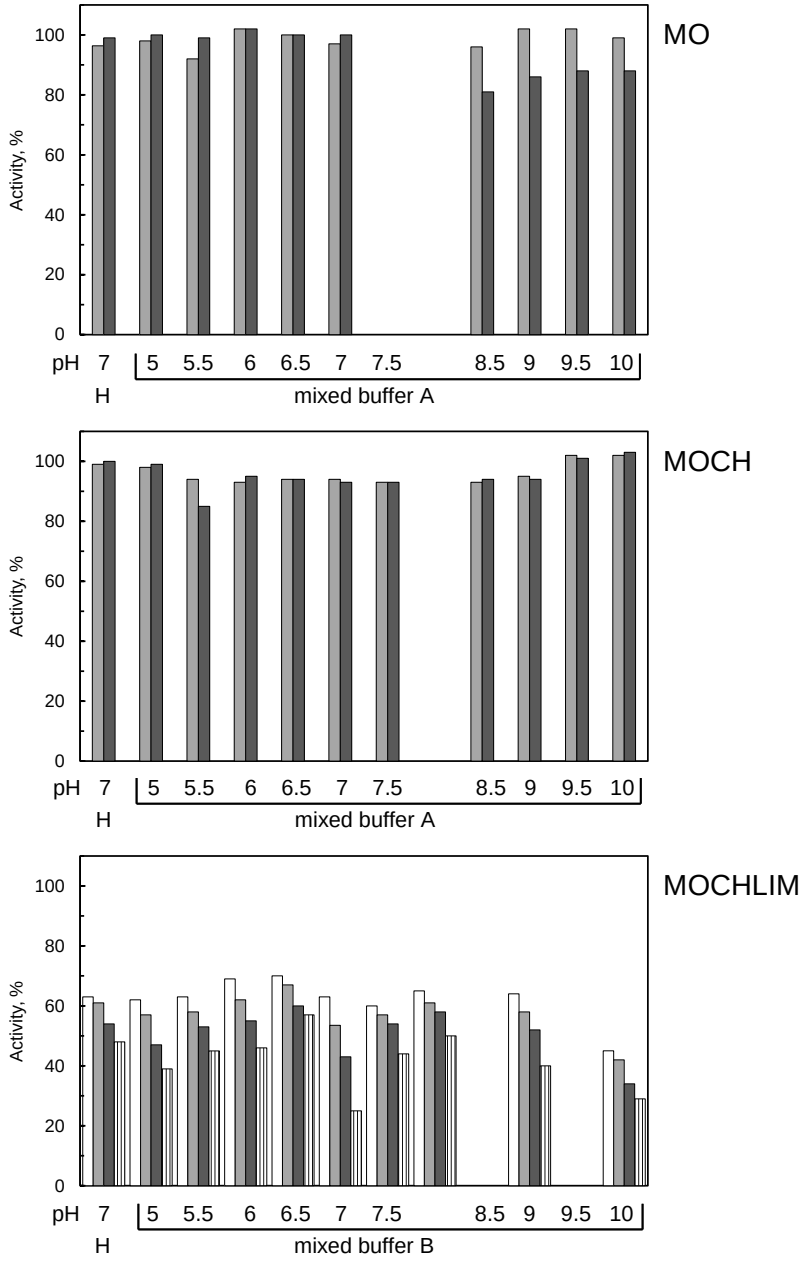

Figure 5.9. pH dependence of the stability of MO, MOCH and MOCHLIM. Aliquots of MO, MOCH and MOCHLIM were diluted 10-fold in mixed buffer A (MO and MOCH) or mixed buffer B (MOCHLIM) at varying pH or in 20 mM Hepes/KOH buffer pH 7 (H) to a final concentration of ≈0.2 mg/ml and incubated at 25°C. The NADPH oxidase activity was determined under standard conditions on aliquots withdrawn at different times: immediately after the dilution (white), after 10 min (light grey), 20 min (dark grey) and 30 min (black lines). The activity is expressed as percentage of that of the starting stock solution.

Aliquots of MOCH (2.35 mg/ml, 34 μM) in 20 mM Hepes/KOH buffer, pH 7 were diluted 2-fold in buffer at varying pH. At subsequent times and after incubation for 16-36 h of samples on ice at 4°C their absorption spectra were recorded and their activity was measured. The activity was similar to that measured for the protein stock solution (Figure 5.10, panel A) and their spectra were similar for all the samples (Figure 5.10, panel B). Only small changes were observed at pH > 8 that could be associated with partial denaturation of the enzyme.

No evidence of a pH dependence of the intensity of the charge-transfer (CT) complex between FAD and Trp400 was obtained. Such pH dependence of CT complex was observed, for example for NikD flavoprotein (Venci et al., 2002). The long-wavelength absorption band of NikD is due to the formation of a CT complex between FAD and Cys42. Such band disappears as the pH decreased and it is coupled to an increase of absorbance at 455 nm (Figure 5.10, panel C). Analysis of nikD absorbance changes at 550 nm (or other wavelengths) as a function of pH yields a p*K*a value of 7.3 (Figure 5.10, panel C) suggesting that the CT interaction can occur only when an ionisable group in the donor is unprotonated (Venci et al., 2005).

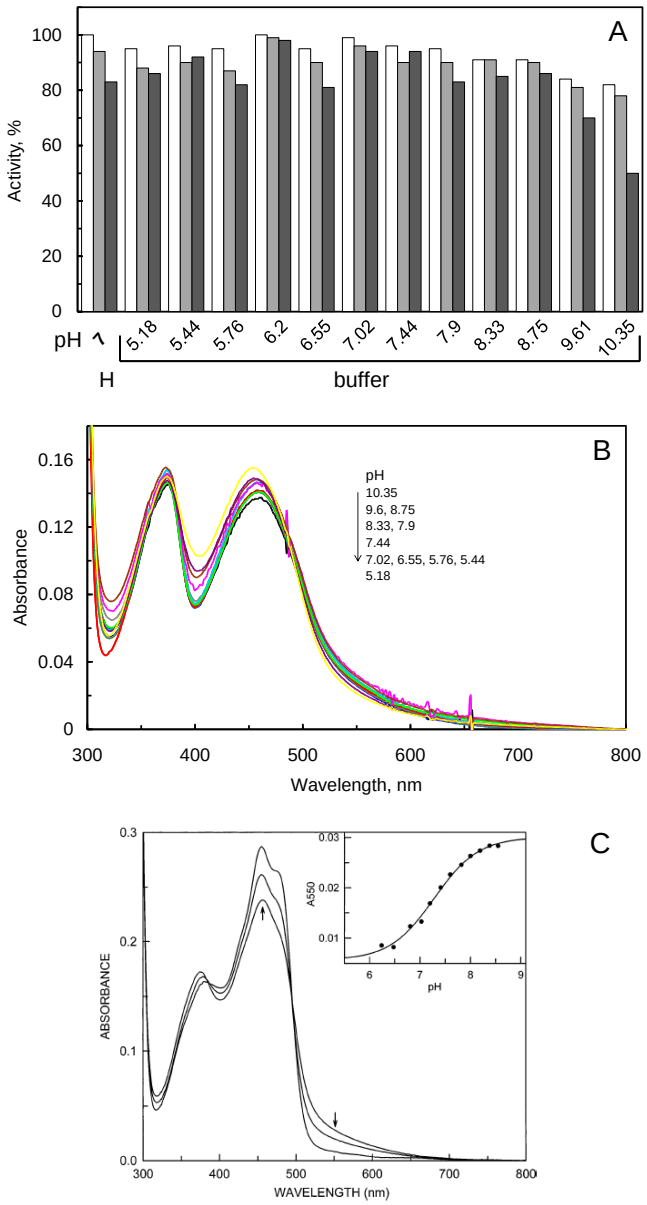

Figure 5.10. Stability of MOCH in mixed buffer at varying pH. The stability of MOCH (1 mg/m, 17 μM) in 10 mM Hepes/KOH, 125 mM formic acid, 50 mM imidazole, 50 mM Tris, 50 mM NaCl buffer at varying pH was determined by measuring the NADPH oxidase activity and by recording the absorption spectra at different times. Panel A: The NADPH oxidase activity of MOCH solutions kept at 4°C were measured at different times (white, 15 min; light grey, 15 h; dark grey, 30 h) is expressed as percentage of that of the protein stock solution in 20 mM Hepes/KOH buffer, pH 7, 100 mM NaCl (H). Panel B: The absorption spectra of MOCHLIM solutions after 2-fold dilution in 250 mM formic acid, 100 mM imidazole, 100 mM Tris varying pH recorded at 17°C. Panel C: Spectra were recorded at pH 8.55, 7.41 and 6.48 in 100 mM K-phosphate buffer at 25°C. The arrows indicate the direction of absorbance changes as the pH lowers. The insert shows the fit of the observed absorbance change at 550 nm to pH titration curve yielding a pK_a value of 7.3 (Venci et al., 2002).

6. The NADPH oxidase activity of human MICAL1 and MO, MOCH, MOCHLIM forms

6.1. Introduction

Organisms have integrated flavin species in the form of flavin coenzymes during the long history of evolution (Miura, 2003). Flavin coenzymes are remarkably efficient in the sense that a single molecular entity, the isoalloxazine system, which is the reactive portion of the flavin can cope with a wide range of reactions. The versatility of flavins makes flavoproteins able to partecipate in a variety of important cell processes (Figure 6.1). In addition to flavoenzyme-catalyzed redox reactions, where flavins accept and donate electrons from and to substrates, they can also accept and emit photons. Enzyme-bound flavins can use received photons in catalysis, as in DNA photolyase, which repairs damaged DNA in a light-dependent fashion (Miura, 2003; Sancar 2008). Flavin functions as a light emitter in bacterial luciferase, which emits photons during oxygenation of alkyl aldehydes (Massey, 2000). Apart from chemical attractiveness, flavin has aesthetic benefits. It has a yellow colour when it is in the oxidized state. It can assume other colours as well: red, pink, green, purple, blue, etc., depending on the redox, ionic, or electronic state. In fact, ionic states of flavins or reaction intermediates are often named after their characteristic colors, such as red flavosemiquinone, blue flavosemiquinone, purple intermediate, green complex, etc (Miura 2003).

The isoalloxazine ring is a tricyclic system formed by the fusion of the hydrophobic dimethylbenzene moiety with the hydrophilic pyrimidine ring and a pteridine moiety (Figure 6.2). It can exist in the oxidized state, in the 2-electron fully reduced state and in the one-electron reduced state in the neutral (blue semiquinone) or the anionic form (red semiquinone) (Figure 6.3). The oxidation or reduction of the flavin cofactor may occur by two one-electron transfer steps or by one two-electrons transfer step. The side chain of the flavin cofactor is not directly involved in redox processes, but plays important roles in stabilizing the protein-coenzyme complex, in modulating coenzyme reactivity and assisting catalysis. The flavin coenzyme is often tightly but non-covalently bound to the apo-protein, although several enzymes containing covalently bound flavin exist, with consequences on the isoalloxazine reactivity.

The three most common types of flavin cofactors are: riboflavin (vitamin B2) and its derivatives flavin mononucleotide (FMN) and flavin adenine dinucleotide (FAD). Riboflavin is converted to FMN by riboflavin kinase that catalyzes the phosphorylation of the ester linkage at the terminal hydroxyl group of the ribityl side chain. FAD synthetase catalyzes the adenylation of FMN to generate FAD (Figure 6.2; Barile et al., 2013).

Under anaerobic conditions the free flavin can be present in solution in both the oxidized and the reduced states; the equilibrium between these forms is rapidly set up with only 5% of radical stabilized in an equimolar mixture of oxidized and reduced flavin (Massey 2000). On binding to the apo-protein this equilibrium can change dramatically resulting in no stabilization of semiquinone or in its complete stabilization. The flavin coenzymes can also form charge-transfer complexes (CT), which are novel electronic states that do not belong to any of the three redox states mentioned before, but are those in which partial charge is transferred to/from an acceptor/donor molecule of the three flavin redox states

(Miura 2003). They are formed upon interaction between the highest occupied molecular orbital (HOMO) of an electron donor and the lowest unoccupied molecular orbital (LUMO) of an electron acceptor (Miura, 2003). Free flavins have typical absorption spectra in the visible and near UV region (300-700 nm) that change when bound to the protein. In particular, the protein environment influences the absorption spectrum that becomes the identity signature of the specific enzyme. Moreover, since the absorption spectrum depends on the oxidation state of the flavin, absorption spectroscopy allows monitoring the events that take place during the catalytic cycle. Figure 6.3 shows the absorption spectra in the visible region of FAD bound to D-amino acid oxidase in different redox, ionic, and charge-transfer states (Miura, 2003).

Flavoprotein reactions often involve two separate half-reactions. The most common reaction is the reduction of the enzyme-bound flavin by the substrates that are dehydrogenated in a two-electron reduction step. To complete the catalytic cycle the resulting reduced flavin is re-oxidized by its oxidizing substrate in two- or one-electron transfer steps. For many other flavoenzymes the substrate or one of the substrates is molecular oxygen (Scheme 6.1). In this reaction, the reduced flavin (I) donates one-electron to O_2 (a) to yield a radical pair (II). This radical pair (II) can collapse (b) into a flavin C4a-peroxide (IV) that (c) becomes electrophilic hydroperoxide (V). The peroxide species can eliminate hydrogen peroxide (e) to yield oxidized flavin (VI). As an alternative (j), a second electron transfer from the radical pair (II) gives the same products (VI). The radical pair (II) can also dissociate (k) into flavin radical (III) and superoxide (Massey, 2000).

Several classifications of flavoproteins have been made on the basis of the type of the catalyzed reaction, the nature of the reducing and oxidizing substrates, physico-chemical properties and their structural features. Conventionally, flavoproteins are classified depending on their reactivity with oxygen distinguishing flavoproteins oxidases, monooxygenases and dioxygenases, electron-transferases and dehydrogenases (Table 6.1). The oxidases, such as for example D-amino acid oxidase, glucose oxidase or glycolate oxidase, react very rapidly with molecular oxygen with the production of hydrogen peroxide without the formation of any detectable intermediate. The monooxygenases can react with oxygen leading to the formation of the C4a-hydroperoxide intermediate after the reduction of flavin by NAD(P)H that is their physiological reductant. After the hydroxylation of the substrate, the flavin goes back to the oxidized state by dehydration. The prototype of this class of flavoproteins is p-hydroxybenzoate hydroxylase (PHBH) that has been extensively studied (see below). The electron-transferases, like flavodoxin, ferredoxin-$NADP^+$ reductase, NADPH-cytochrome P450 reducatse, catalyze a single-electron transfer reaction and interact very slowly with oxygen producing superoxide and flavin semiquinone. In this classification some important flavoproteins do not find an appropriate placement like flavoproteins that contain auxiliary redox center, such as metal- and heme-containing flavoproteins and flavoprotein disulfide reductases.

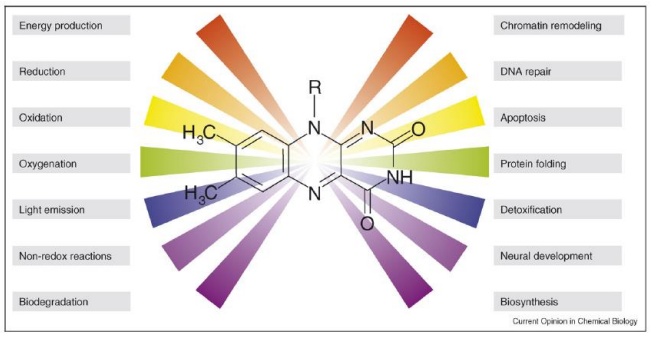

Figure 6.1. Biological processes involving flavoproteins function (Joosten and Van Berkel 2007).

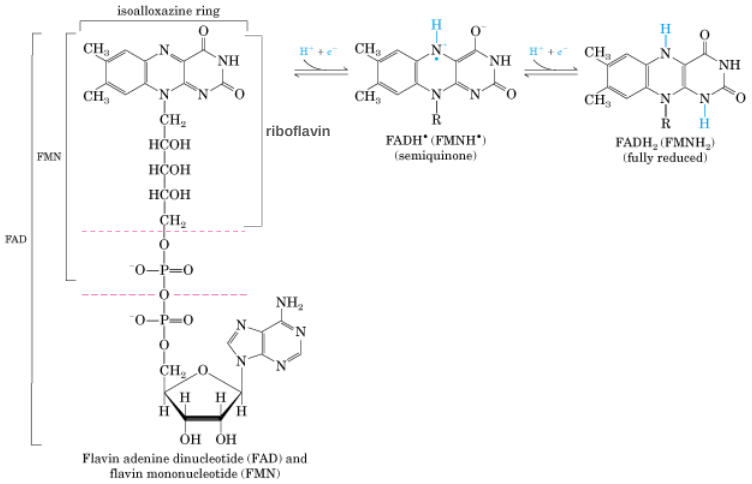

Figure 6.2. Structure of riboflavin, FMN and FAD in the oxidized (left), semiquinoid (middle) and reduced (right) state (Voet, D. and Voet, J. (2012), *Biochemistry*, 4th edn, Wiley, New York).

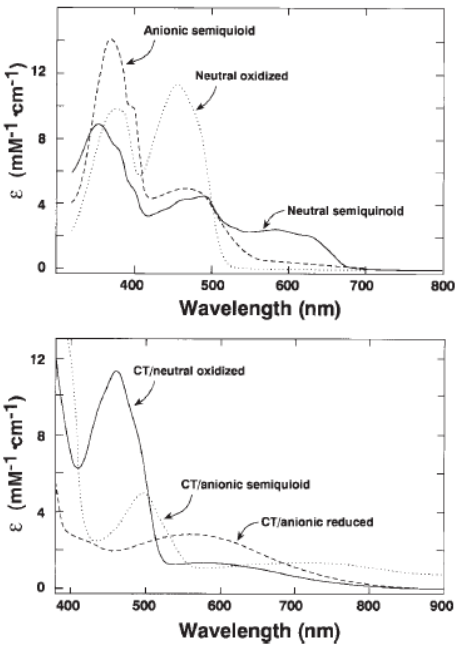

Figure 6.3. Absorption spectra of D-amino acid oxidase. Top panel: neutral oxidized (dotted line), anionic semiquinoid (dashed line), and neutral semiquinoid (solid line) states of flavin bound to D-amino acid oxidase. Bottom panel: charge-transfer states of neutral oxidized bound-flavin (solid line), anionic semiquinoid flavin (dotted line), and anionic reduced flavin (dashed line). (Miura, 2003).

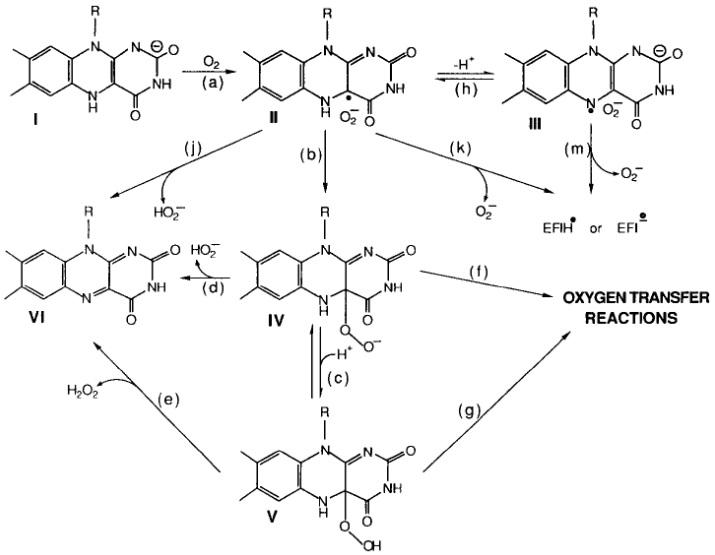

Scheme 6.1. Possible pathways in the reaction of reduced flavin with O_2. (Massey 2000).

Table 6.1 Classification of flavoproteins.

Class	*Reaction*
Oxidases	$S_{red} + O_2 \leftrightarrow S_{ox} + H_2O_2$
Monooxygenases	$S + NAD(P)H + O_2 \leftrightarrow SOH + NAD(P)^+ + H_2O$
Electron-transferases	$S_{red} + A_{ox} \leftrightarrow S_{ox} + A_{red}$
Dehydrogenases	$S_{red} + NADP^+ \leftrightarrow S_{ox} + NADPH$

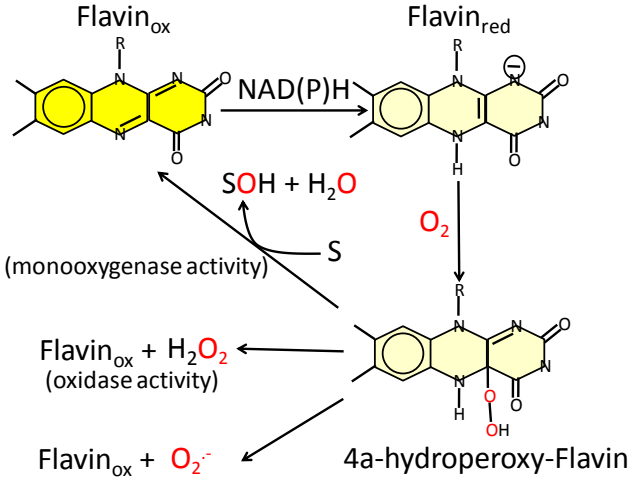

Scheme 6.2. Reaction scheme of FAD-dependent monooxygenases. The flavin reduced by NAD(P)H interacts with O_2 leading to the formation of C4a-hydroperoxy-FAD with (1) the hydroxylation of the bound substrate (S) or (2) H_2O_2 production when absent (Vanoni et al., 2012).

Flavin-dependent monooxygenases, to which MICAL N-terminal domain is structurally related (Chapter 2), catalyze the incorporation of one atom of molecular oxygen into the oxidable substrate, while the other oxygen atom is reduced to water (Scheme 6.2). Typically, oxygen activation involves the formation of a flavin C4a-oxygen adduct. They catalyze hydroxylation, Baeyer-Villiger oxidation, sulfoxidation, epoxidation and halogenation reactions with high selectivity and constitute the largest family of flavoenzymes (Huijbers et al., 2013). On the basis of their structural and functional properties a division into six groups has been proposed (Huijbers et al., 2013). Groups A and B comprise single-component enzymes that have NAD(P)H as the reducing substrate. Groups C, D and F contain monooxygenases that need a reductase partner protein to be reduced. Internal flavoprotein monooxygenase that reduce the flavin coenzyme through substrate oxidation are included in groups G and H (Table 6.2 and Figure 6.4).
Monooxygenases of group A are encoded by a single gene, contain a typical Rossman-fold for FAD binding and use NAD(P)H as electron donor. PHBH is the prototype of this group of monooxygenases. PHBH catalyzes the hydroxylation of *p*-hydroxybenzoate (pOHB) to form 3,4-dihydroxybenzoate in three steps: (i) reduction of the enzyme cofactor (FAD) by NADPH in response to binding of pOHB to the enzyme, followed by (ii) oxidation of reduced FAD by oxygen to form a 4a-hydroperoxide intermediate, which (iii) oxygenates pOHB to form 3,4-dihydroxybenzoate (Entsch et al., 2005; Scheme 6.3). The process has evolved to be carefully controlled to prevent the wasteful production of hydrogen peroxide (k_{10} in scheme 6.3), which would be the product of the reaction in the absence of pOHB. In the early work with the enzyme, it was found that the rate of reductive half-reaction increased by a factor of $2x10^5$ after the binding of pOHB, without significant changes in the dissociation constant for NADPH. Both the rate of dissociation and of association of pOHB with the enzyme is 10^4-fold lower when the flavin is reduced. Thus, substrate stays on the enzyme so that it can be attacked by the flavin-C4a-hydroperoxide as soon as it is formed. Moreover, with pOHB bound to the active site, the reduced enzyme reacts 10^5-fold faster with oxygen than the reduced flavin does in aqueous solution. Another important aspect of the catalytic cycle of PHBH is the presence of conformational changes that take place during the different steps of the catalytic cycle and that also represent another control mechanism of the reaction. On the basis of PHBH structures and kinetic data, a model of the reaction has been proposed. In the absence of the substrate, the enzyme is mainly in the "open" conformation with an open channel to facilitate substrate binding; binding of pOHB leads to a flavin shift from the "open" to the "flavin in" conformation; deprotonation of the substrate causes the conversion from the "flavin in" to the "flavin out" conformation in which the isoalloxazine ring of the flavin is exposed to the solvent and can be reduced by NADPH; the positive electrostatic field of the active site pulls the reduced flavin back to the "in" conformation, where it can react with oxygen in a protected environment and it hydroxylates the substrate through the formation of the C4a-hydroperoxide (Figure 6.5; Brender et al., 2005).

Table 6.2 . Classification of FAD-dependent monooxygenases. (Van Berkel et al., 2013).

Group	Cofactor	Electron donor	Protein fold	Reaction	Prototype
A	FAD	NAD(P)H	Rossmann (GR-2)	Hydroxylation	*p*-Hydroxybenzoate 3-hydroxylase
				Sulfoxidation	MICAL
B	FAD	NAD(P)H	Rossmann (FMO)	Baeyer–Villiger oxidation	Cyclohexanone monooxygenase
				Heteroatom oxygenation	Dimethylaniline monooxygenase
				N-Hydroxylation	L-Ornithine monooxygenase
				Oxidative decarboxylation	Indole-3-pyruvate monooxygenase
C	FMN	$FMNH_2$	Tim-barrel (luciferase)	Light emission	Alkanal monooxygenase
				Baeyer–Villiger oxidation, epoxidation	Diketocamphane monooxygenase
				Desulfurization, sulfoxidation	Alkanesulfonate monooxygenase
				Hydroxylation	Long-chain alkane monooxygenase
D	FAD/FMN	$FADH_2$/$FMNH_2$	Acyl-CoA dehydrogenase	Hydroxylation	*p*-Hydroxyphenylacetate 3-hydroxylase
				N-Hydroxylation	KijD3 sugar *N*-oxygenase
E	FAD	$FADH_2$	Rossmann (GR-2)	Epoxidation	Styrene monooxygenase
F	FAD	$FADH_2$	Rossmann (GR-2)	Halogenation	Tryptophan 7-halogenase
G	FAD	Substrate	Rossmann (MAO)	Oxidative decarboxylation	Tryptophan 2-monooxygenase
H	FMN	Substrate	Tim-barrel (glycolate oxidase)	Oxidative decarboxylation	Lactate 2-monooxygenase
				Oxidative denitration	Nitronate monooxygenase

GR, glutathione reductase; FMO, flavin-containing monooxygenase; MAO, monoamine oxidase; MICAL, molecule interacting with CasL.

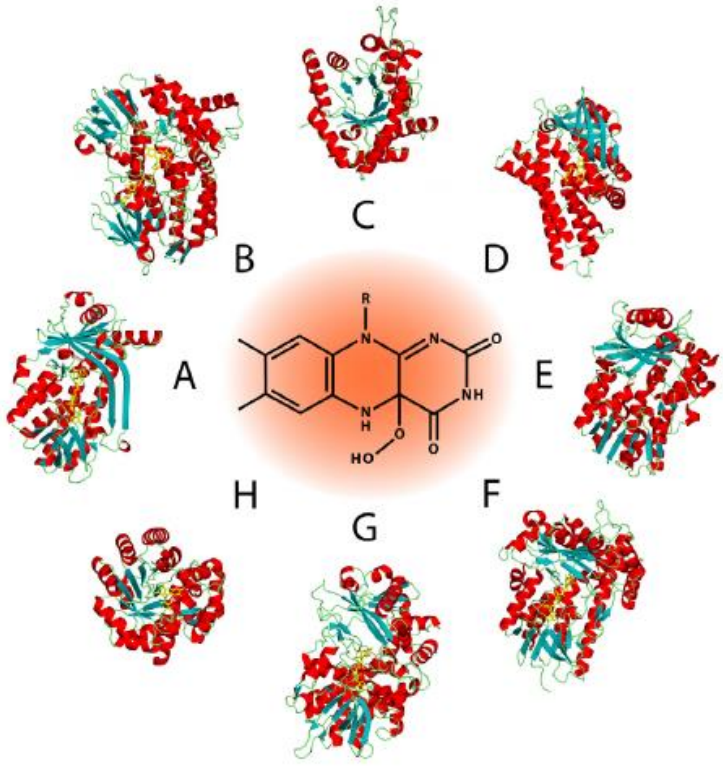

Figure 6.4. Protein folds of FAD-dependent monooxygenases. A, hydroxybenzoate hydroxylase PHBH; B, phenylacetone monooxygenase; C, bacterial luciferase; D, hydroxylphenylacetate hydroxylase; E, styrene monooxygenase; F, tryptophan-halogenase; G, tryptophan monooxygenase; H, nitronate monooxygenase. Folds are indicated in Table 6.2. (Van Berkel et al., 2013).

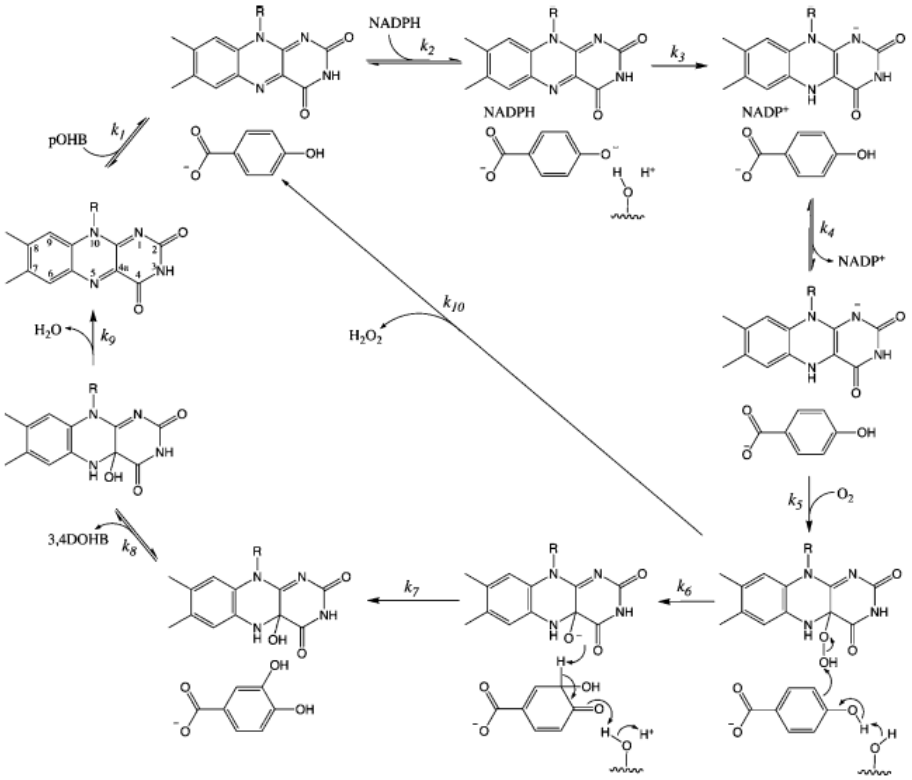

Scheme 6.3 Catalytic cycle of PHBH. In the figure, the numbered isoalloxazine ring represents the oxidized enzyme without ligands bound. Note that k_1 to k_{10} represent the rate constants for the chemical reactions and ligand interactions in the forward reaction of the catalytic cycle. (Entsch et al., 2005).

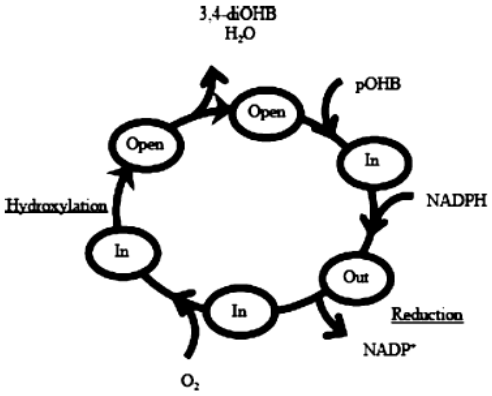

Figure 6.5. Conformational cycle of PHBH. During the reaction cycle, the isoalloxazine ring of the flavin moves between conformations in which the flavin is exposed to solvent (designated "out" and "open") and ones in which it is sequestered from solvent ("in") as substrate (p-hydroxybenzoate, pOHB) is converted into product (3,4-dihydroxybenzoate, diOHB). (Brender et al., 2005).

The three-dimensional structure of the isolated flavoprotein domain of mouse MICAL1 was solved in 2005 (Nadella et al., 2005; Siebold et al., 2005), revealing its structural similarity to enzymes of PHBH the family (Chapter 2). However, the N-terminal domain of mouse MICAL1 was reported to catalyze a NADPH oxidase activity with a k_{cat} of 77 s^{-1} and a K_m for NADPH of 222 μM (Nadella et al., 2005) that is very high for a monooxygenase in the absence of the substrate to be oxidized.

The MO domain of human MICAL1 was produced in our laboratory in *E.coli* cells in quantities sufficient to carry out its characterization (Zucchini et al., 2011; Chapter 4).

The isolated MO domain of human MICAL1 was found to catalyze a NADPH oxidase activity with an apparent K_m for NADPH of 20 μM and a k_{cat} of 4 s^{-1} in 20 mM Hepes/KOH buffer, pH 7 (Table 6.3; Zucchini et al., 2011). These values are one order of magnitude lower than those reported for the mouse MO (Nadella et al., 2005). The discrepancies could be explained in various ways. The activity of the mouse enzyme was measured in presence of 0.1 M NaCl, which causes an increase of the K_m for NADPH with a mild effect on the k_{cat} (2.6 s^{-1}) of the human MO domain (Table 6.3). Another important aspect is the activity assay used to monitor the NADPH oxidase reaction. For the mouse enzyme a coupled assay with horseradish peroxidase and amplex red was used to monitor the NADPH-dependent H_2O_2 production (Nadella et al., 2005). Instead, for the human protein the NADPH oxidation was directly monitored spectrophotometrically at 340 nm. Control experiments carried out in our laboratory demonstrated that NADPH consumption is stimulated in the presence of amplex red and HRP and H_2O_2. With this information it appears that the NADPH oxidase activity of mouse and human MO should be similar to each other, if measured under similar conditions.

With human MO, the NADPH oxidase reaction was also carried out in the oxygen electrode (Table 6.4) showing an average of 0.87 mole of O_2 consumed per NADPH. The rate of the reaction decreased 2-fold in the presence of catalase without affecting the NADPH consumption (Zucchini et al., 2011). End-point spectrophotometric methods were used to quantify the H_2O_2 produced and 1 mole of H_2O_2 was detected per mol of NADPH being oxidized (Table 6.4, Figure 6.5, Zucchini et al., 2011). These results are consistent with those expected for an authentic NADPH oxidase reaction producing H_2O_2.

Table 6.3. Steady-state kinetic parameters of the NADPH oxidase activity of the MO domain human MICAL. Assays were carried out in 20 mM Hepes/KOH buffer, pH 7, in the presence of the indicated NADPH concentration ranges at 25°C. Apparent k_{cat} and K_{NADPH} values and their associated errors were determined by fitting the data to the Michaelis-Menten equation. (Zucchini et al., 2011).

Enzyme	NADPH (μM)	NADH (μM)	NaCl (M)	Glycerol (%)	$K_{NAD(P)H}$ (μM)	k_{cat} (s^{-1})	$k_{cat}/K_{NAD(P)H}$ (s^{-1} mM^{-1})
MICALHis	4–160	–	–	–	28 ± 2	4.0 ± 0.1	143 ± 11
	40–650	–	0.1	–	499 ± 28	2.6 ± 0.1	5.2 ± 0.4
	20–200	–	–	–	28 ± 3	4.4 ± 0.1	157 ± 17
	–	80–670	–	–	580 ± 24	0.28 ± 0.01	0.48 ± 0.03
	10–300	–	–	–	26 ± 4	3.9 ± 0.1	150 ± 23
	10–300	–	–	10	93 ± 11	2.9 ± 0.1	31.2 ± 4
HisMICAL	20–200	–	–	–	40 ± 2	4.4 ± 0.1	110 ± 6
MICAL	20–200	–	–	–	41 ± 2	4.8 ± 0.1	117 ± 6

Table 6.4. Comparison of the rates of oxygen consumption and NADPH oxidation in the NADPH oxidase reaction of MO. Parallel assays were setup in cuvettes and in the oxygen electrode chamber. Small aliquots (up to 10 µl) of MO solutions were added to start the assays that were monitored spectrophotometrically or with the oxygen electrode (Zucchini et al., 2011).

Enzyme	NADPH, µM	Catalase, µg	v/E, s^{-1}		Ratio
			Oxygen	NADPH	O_2/NADPH
MICAL	200	0	3.0	3.3	0.91
	400	0	3.0	3.6	0.83
HisMICAL	187	0	3.7	4.4	0.84
	94	0	3.2	3.6	0.89
	47	0	2.6	2.9	0.89
	28	0	2.1	2.4	0.88
	187	10	1.7	3.8	0.44
	94	10	1.7	3.3	0.51
	47	10	1.3	2.6	0.50
	28	10	1.1	2.2	0.50
MICALHis	200	0	2.8	3.1	0.90
	200	10	1.6	3.1	0.51

The NADPH oxidase activity of MO was found to be very sensitive to ionic strength and specific anions. Increasing concentrations of neutral salts in the standard 20 mM Hepes/KOH buffer, pH 7 and buffer salts led to a decrease of k_{cat}/K_{NADPH} mainly due to an increase of K_m for NADPH (Zucchini et al., 2011; Figure 6.7). The stronger effect was exerted by phosphate, followed by chloride and acetate anions and no specific effect was observed as a function of their counter ions (Na^+, K^+, Ca^{++}, Mg^{++}) (Figure 6.7). The sensitivity to ionic strength of the affinity for NADPH is also a property of PHBH to which MICAL-MO is structurally related. In PHBH the interaction between NADPH and enzyme is controlled by electrostatic interactions, thus specific ions may compete with the phosphate group of NADPH for positively charged residues on the enzyme (Ortiz et al., 2004).

In addition to the ionic strength, also solvent viscosity has been observed to have an effect on the kinetic parameters of the NADPH oxidase activity of the isolated MO domain of human MICAL1 (Zucchini et al., 2011).

Enzymatic catalysis is a dynamic process where internal and external motions of protein and solvent molecules contribute to the sequence of catalytic steps. Critical protein dynamics must take place in the active site of the enzyme (Sitnitsky 2008). Therefore, solvent viscosity may have significant effects on the enzyme dynamics and activity by influencing the rate at which the substrate associates to the enzyme and the product is released and also on the rate at which conformational changes along the reaction path take place. (Sampson et al., 1992; Simpoulos et al., 1994; Eser et al., 2010). Varying solvent viscosity is a potential route to explore enzyme function and mechanism. The data (rate constants, equilibrium constants, k_{cat}, k_{cat}/K_m etc) are plotted as the ratio of the relevant parameters in the absence of viscogen to that in its presence as a function of the relative solvent viscosity (Figure 6.8). A slope of 0 is expected when the parameter value is determined by the rate of chemical steps. A slope of 1 is expected when diffusional events (i.e.: access of the substrate or the release of product to/from the active site of the enzyme) fully determine the value of the parameter under study. A slope greater than 1 is expected when

conformational changes that take place during the catalytic cycle contribute to the value of the parameter (Sampson et al., 1992; Simpoulos et al., 1994; Eser et al., 2010), (Figure 6.8).

From the three dimensional structure of the MO domain of mouse MICAL1 conformational changes are predicted to take place during the catalytic cycle (Nadella et al., 2005; Siebold et al., 2005; Chapter 2). In a minimal scheme they would imply: (i) movement of Trp400 to allow hydride transfer from the NADPH nicotinamide ring to the flavin, (ii) the subsequent "flavin in"/"flavin out" transition (Scheme 6.3). With human MICAL-MO the slope of a plot of the the solvent viscosity effect on k_{cat}/K_{NADPH} was ≈3, which indicates that a conformational change contributes to determine the value of the parameter. The plot of the effect of solvent viscosity on k_{cat} had a slope of 1. Stopped-flow studies of the reaction between MO and NADPH demonstrated that turnover is limited by the rate of flavin reduction by NADPH, which would have predicted no viscosity effect on k_{cat} (Zucchini et al., 2011). Thus, the slope of 1 may reflect the fact that the conformational change seen in k_{cat}/K_{NADPH} partially contributes also to the value of k_{cat} making the observed viscosity effect greater than 0.

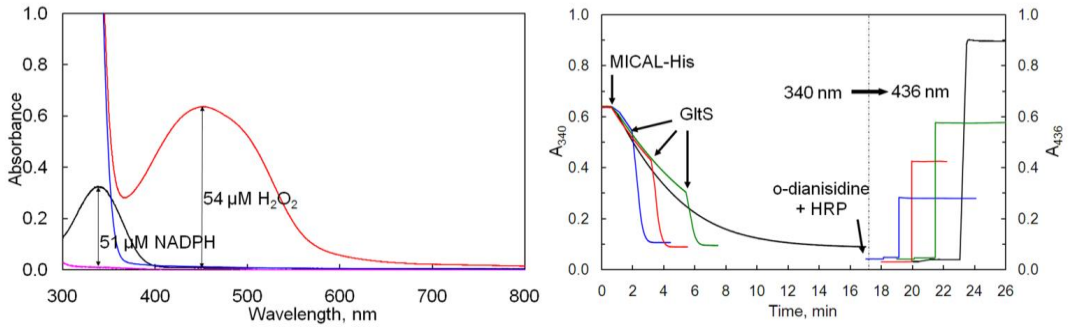

Figure 6.6 End-point assays of H_2O_2 produced during the NADPH oxidase activity of MICAL. Left panel: His-MO was incubated with 51 µM NADPH (black line) in 20 mM Hepes/KOH buffer, pH 7.0, until all NADPH was consumed (purple line). o-dianisidine (0.4 mM, 50 µl) was added (blue line) followed by horseradish peroxidase (HRP, 1 µg). The spectrum at the end of the reaction is shown (red line) along with the calculated concentration of H_2O_2 formed. Right panel: MO-His was incubated with 100 µM NADPH in 20 mM Hepes/KOH buffer, pH 7.0 in the presence of 2.5 mM 2-oxoglutarate and 5 mM L-glutamine, and the reaction was monitored at 340 nm. At the indicated times an aliquot of glutamate synthase (GltS, 10 µl, 40 µg) was added to bring the reaction to completion. The spectrophotometer wavelength was switched to 436 nm and o-dianisidine (0.4 mM) and HRP (1 µg) were added. The reaction was allowed to reach completion before calculating the concentration of H_2O_2 formed. The black line shows an assay in which the reaction was allowed to reach completion in the absence of GltS (Zucchini et al., 2011).

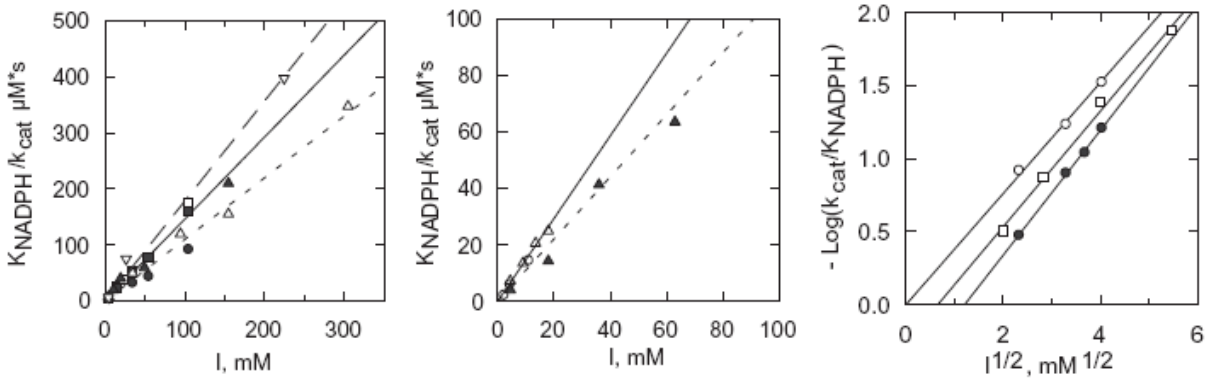

Figure 6.7. Effect of ionic strength and type of ions on MO NADPH oxidase reaction. Left and middle panels: the slopes of double reciprocal plots (K_{NADPH}/k_{cat}) obtained by measuring initial velocities in the presence of varying NADPH and different concentrations of salts or buffers are plotted as a function of the ionic strength (I) of the assay mixture. Left panel: the following salts were added to the standard assay buffer (20 mM Hepes/KOH, pH 7.0): ●, sodium acetate; Δ, magnesium acetate; □, NaCl; ■, KCl; ▲, calcium chloride; , sodium phosphate. Center panel: assays were carried out with different concentrations of Hepes/KOH buffer (○), Tris–chloride (Δ) or Tris–acetate (▲). The continuous line is the common fit of the data obtained with the chloride salts; the dotted line is the common fit obtained with the acetate salts; the dashed line is the fit to the data obtained with sodium phosphate. Right panel: assays were carried out with different concentrations of imidazole–chloride (○), imidazole–acetate (□) or Bis–Tris–acetate (●) (Zucchini et al., 2011).

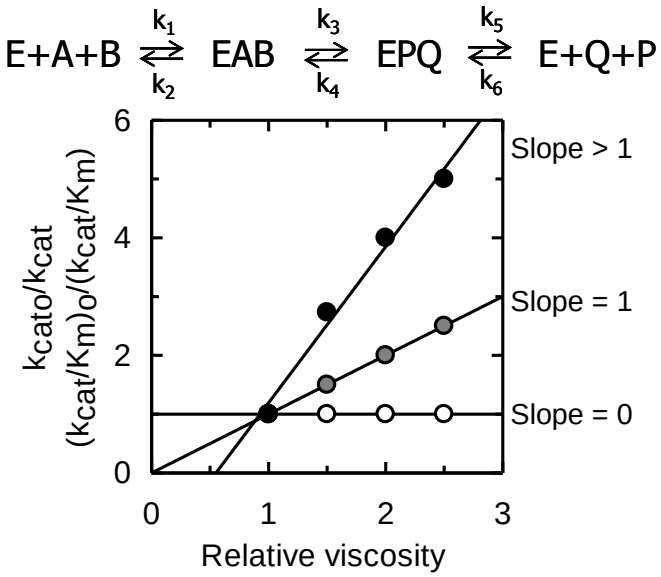

Figure 6.8. Solvent viscosity effect on the kinetic parameters k_{cat} and k_{cat}/K_m for a generic enzymatic reaction. Slope = 0, the value of parameter is determined by chemical steps (k_3, k_4); Slope = 1, diffusion-controlled events determine the value of the parameter (k_1, k_2, k_5, k_6); Slope >1, conformational changes determine the value of the parameter.

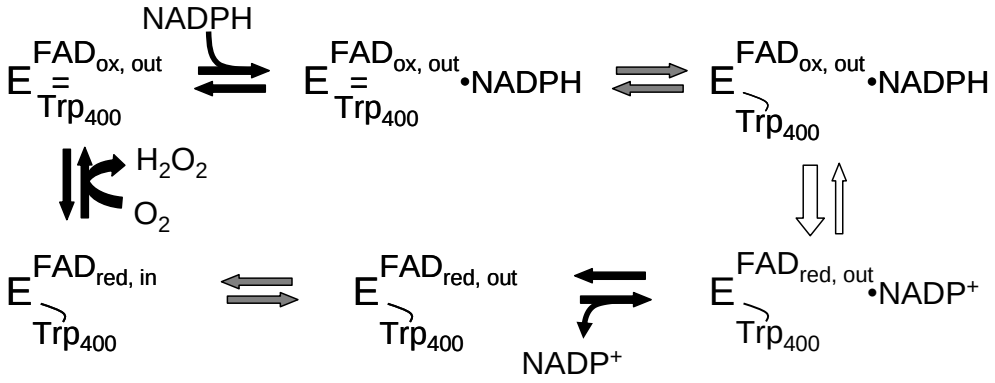

Scheme 6.3 Reaction steps of the NADPH oxidase activity of MICAL and possible conformational changes occurring during the catalytic cycle. On the basis of the 3D-structure of the MO domain of mouse MICAL1 (PDB ID, 2C4C, 2BRY; Nadella et al., 2005; Siebold et al., 2005) conformational changes predicted to take place are the following: movement of Trp400 and transition between "flavin in" and "flavin out" conformations. White arrow, the reaction steps dependent on the chemistry of the reaction; Grey, diffusion limited steps and black, step in which conformational changes can occur.

6.2. Determination of the steady-state kinetic parameters k_{cat} and $K_{m,\ NADPH}$ of the NADPH oxidase activity of MICAL forms

With the newly produced full-length MICAL and the truncated MOCH and MOCHLIM forms we characterized their NADPH oxidase reaction under steady-state kinetic conditions. These studies are important to determine if and to what extent some or all of the biological functions of MICAL are due to its H_2O_2-producing NADPH oxidase activity and to determine how the presence of the CH, LIM and C-terminal domains affect the activity of the MO domain.

To test the effect of the CH and LIM domains and of the C-terminal region on the NADPH oxidase activity of the MO domain, the apparent steady-state kinetic parameters k_{cat} and K_m for NADPH (K_{NADPH}) of MICAL, MOCH and MOCHLIM forms were first determined in 20 mM Hepes/KOH buffer, pH 7, varying NADPH concentration.

The measured v/[E] values, expressed in s^{-1}, were fitted to the Michaelis-Menten equation (Eq 2) to determine the kinetic parameters of the reaction. The calculated k_{cat} values of MOCH and MOCHLIM forms were similar to those of the isolated MO domain, while MICAL showed a 10-fold drop (Table 6.5, Figure 6.7). Instead, the value of K_{NADPH} progressively increased from ~20 μM (MO), to ~130 μM (MOCH), ~230 μM (MOCHLIM) and ~370 μM (MICAL), (Table 6.5, Figure 6.9).

The increase of K_m for NADPH due to the presence of the CH, LIM and the C-terminal domains apparently correlates with the change of the overall charge of the protein starting from a positive value (MO pI 9, Figure 10.4) to progressively less positive and negative values at pH 7: 10.4, 2.6, -4.8 and -12.7 for MO, MOCH (pI, 7.7), MOCHLIM (pI, 6.7) and MICAL (pI, 6.2), respectively (Figure 6.10) due to the addition of the acidic CH, LIM and C-terminal region (Figure 3.6). The effect exerted by the C-terminal region on k_{cat}, which is 10-fold lower than that of MO (0.28 s^{-1} *vs* 3 s^{-1}) is in agreement with the proposal that the C-terminal region has an autoihnibitory function in MICAL and that MICAL activation takes place following the interaction between semaphorin and plexin (Schmidt et al., 2008; Giridharan et al., 2012; Figure 1.8). However, these data are not sufficient to clarify the effect of the CH and LIM domains and C-terminal region on the MO domain. The higher K_m for NADPH and lower k_{cat} of MICAL may depend on a different pH optimum of the reaction that might be linked to changes in the pK_a of some key residues and/or to changes in the rate limiting steps of the reaction resulting from conformational changes induced by the CH, LIM and C-terminal domains. Thus the NADPH oxidase activity was studied as a function of pH and solvent viscosity. Prior to these experiments, we wished to test the sensitivity to ionic strength and type of ions on the NADPH oxidase activity of MOCH and MOCHLIM. Due to the high K_m for NADPH (MOCHLIM and MICAL) and the low k_{cat} (MICAL) only MOCH could be analyzed in detail.

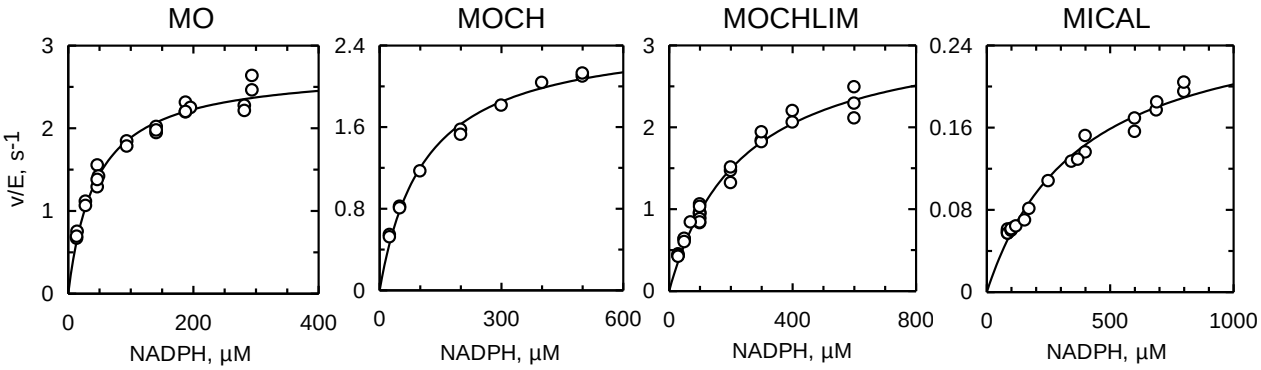

Figure 6.9. Determination of the kinetic parameters k_{cat} and K_m for NADPH of the NADPH oxidase activity of MICAL forms. The initial velocity (v/[E], s^{-1}) of the NADPH oxidation reaction catalyzed by MO (20 nM), MOCH (60 nM), MOCHLIM (60 nM) and MICAL (690 nM) was measured in 20 mM Hepes/KOH buffer, pH 7 varying NADPH concentrations at 25°C. The apparent k_{cat} and K_{NADPH} values and their associated errors were determined by fitting the data to the Michaelis-Menten equation (Eq.2) and are in Table 6.5.

Table 6.5. Steady-state kinetic parameters of the NADPH oxidase activity of MICAL forms. Assays were carried out in 20 mM Hepes/KOH buffer, pH 7, in the presence of the indicated NADPH concentration ranges at 25°C. Apparent k_{cat} and K_{NADPH} values and their associated errors were determined by fitting the data to the Michaelis-Menten equation.

Protein, nM	*NADPH, µM*	k_{cat}, s^{-1}	K_m, µM	k_{cat}/K_m, $s^{-1}mM^{-1}$
MO, 20	10-300	3.1 ± 0.1	19 ± 2	163 ± 18
MOCH, 60	10-600	2.5 ± 0.1	134 ± 5	18.5 ± 1
MOCHLIM, 60	30-1000	3.5 ± 0.1	230 ± 16	15.3 ± 1.2
MICAL, 690	100-800	0.28 ± 0.01	375 ± 33	0.75 ± 0.07

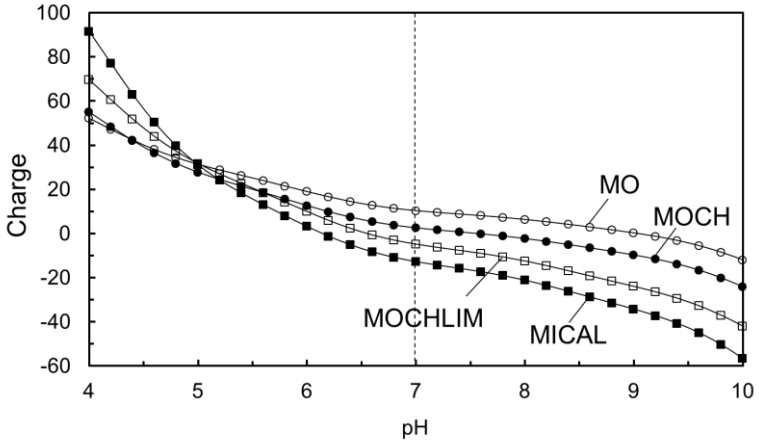

Figure 6.10. Calculated charge of MICAL forms as a function of pH. The total charge of each protein form as a function of pH was computed using the amino acyl composition of the proteins and the pK_a values reported in Voet, D. and Voet, J. (2012), *Biochemistry*, 4th edn, Wiley, New York.

6.3. Effect of the ionic strength on the NADPH oxidase activity.

The isolated MO domain of human MICAL was sensitive to ionic strength and anionic composition of the medium (Zucchini et al., 2011). As discussed previously this effect is mainly due to a competition between anions and NADPH for some of the positively charged residues of the NADPH binding site. However, with some anions the effect could be attributed to the overall charge of the protein. Since the CH, LIM and C-terminal domains of MICAL lower the total charge of the protein, the strong positive charge of MO may be attenuated. As a result also the sensitivity to ionic strength and anions could decrease. This properties would make it easier to carry out some experiments due to a less stringent need to maintain ionic strength at a low, and, especially, rigorously constant value.

The kinetic parameters of the NADPH oxidase reaction catalyzed by MOCH were determined by varying the NADPH concentration in 20 mM Hepes/KOH buffer, pH 7 supplemented with NaCl (0-100 mM; I, 4.4-104.4 mM) or Na-acetate (0-250 mM; I, 4.4-254.4 mM); in Tris-acetate buffer, pH 7 (50-250 mM; I, 45-180 mM) or in imidazole-acetate buffer, pH 7 (50-150 mM; I, 24-72 mM).

In all cases the plots of the reciprocal initial velocities as a function of the reciprocal of NADPH concentration were linear and converging on the Y axis, indicating that the various salts have an effect on k_{cat}/K_{NADPH} due to an increase of K_m for NADPH. This effect is lower than that measured for MO (Figure 6.11). The effect was exerted by NaCl was stronger than that of Na-acetate, imidazole-acetate buffer and Na-acetate (Figure 6.11). k_{cat}/K_{NADPH} decreased linearly as the concentration of NaCl, Na-acetate and Tris-acetate buffer increased (Figure 6.11, panels A and B). On the contrary, as observed for MO (Zucchini et al., 2011) the effect of imidazole-acetate buffer on k_{cat}/K_{NADPH} (expressed as $(k_{cat}/K_{NADPH})/(k_{cat}/K_{NADPH})_0$) as a function of ionic strength was well fitted to the equation describing a limiting case of the Debye-Hückel equation (Norby et al., 1997; Eq 3), where the (k_{cat}/K_{NADPH}) is the parameter value obtained in the presence of a given value of ionic strength (I) and $(k_{cat}/K_{NADPH})_0$ is the value of the parameter calculated at zero ionic strength (Figure 6.11, panel C). The equation allows to calculate the ionic strength-independent value of the parameter and the charge of the NADPH binding site. Since at pH 7 NADPH should carry 3-4 negative charges the active site of MOCH should have a charge of 0.031-0.041 (Table 6.6), which is 3-fold lower than that calculated for MO (0.1-0.13; Table 6.6).

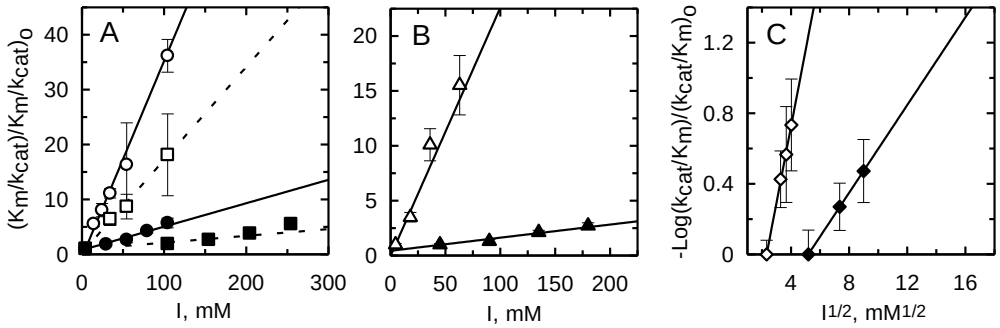

Figure 6.11. Comparison of the sensitivity to ionic strength and ions of the NADPH oxidase activity of MO and MOCH forms. The values of slopes ratio $(K_{NADPH}/k_{cat})/(K_{NADPH}/k_{cat})_0$ are obtained by measuring initial velocities reaction of MO (empty symbols) and MOCH (full symbols) in the presence of varying NADPH and different concentration of salts or buffers are plotted as a function of ionic strength (I) of the assay mixture. Panel A: Salts: NaCl (○, ●) and Na-acetate (□, ■) were added to the standard assay buffer (20 mM Hepes/KOH, pH 7); The continuous lines are the fit of the data obtained with NaCl, the dotted lines are the the fit of the data obtained with Na-acetate. Panel B: assays were carried out in the presence of different concentrations of Tris-acetate buffer (Δ, ▲). The continuous lines are the fit of the data obtained for MICAL-MO and MICAL-MOCH with different concentration of Tris-acetate buffer. Panel C: assays were carried out in the presence of different concentrations of Imidazole-acetate buffer (◊, ♦), the lines are the fit of data to Eq 3. The values of the slope and intercepts of the lines are in Table 6.6.

Table 6.6. Determination of the charge (z_e) of MO and MOCH forms. The slope of the lines show in Figure 6.14 correspond to z_e*z_s, the intercept corresponds to $-Log(k_{cat}/K_m)/(k_{cat}/K_m)_0$ at zero ionic strength thus $(k_{cat}/K_m)_0$ can be calculated. [a]Data from Zucchini et al., 2011.

Protein, nM	*buffer*	*slope*	*intercept*	z_e*z_s	z_{NADPH}, -3	z_{NADPH}, -4	$(k_{cat}/K_m)_0$
MO, 20[a]	Imidazole-acetate	0.430±0.016	-1.004±0.061	- 0.43	0.143	0.107	3.38
MOCH, 60 nM	Imidazole-acetate	0.124±0.001	-0.645±0.0055	-0.124	0.041	0.031	0.041

The high K_m for NADPH of MOCHLIM limited the analysis of the sensitivity of its reaction to ionic strength. Thus, the NADPH oxidase activity of MOCHLIM was studied only in selected buffers, namely: 20 mM Hepes/KOH buffer, pH 6.5 (I, 1.35 mM); 12.5 mM formate, 5 mM imidazole, pH 7 (I, 12.5 mM); 50 mM Na-phosphate buffer, pH 7.5 (I, 48 mM) and F-buffer (9.5 mM Tris/HCl, pH 7.7, 45 mM KCl, 0.18 mM $CaCl_2$, 1.18 mM $MgCl_2$, 1.1 mM ATP, 1.33 mM DTT; I, 60 mM).

The steady-state kinetic parameters obtained for MOCHLIM in such buffers are summarized in Table 6.7. By taking into account the differences in pH, which will be later analyzed in greater detail, it appears that with MOCHLIM k_{cat}/K_{NADPH} is little sensitive to the ionic strength of the buffer. The value of the parameter decreases only 4-fold when F-buffer substitutes the standard 20 mM Hepes/KOH buffer, pH 7. As observed for MO, phosphates appear to have a strong effect in lowering the affinity for NADPH.

Also MICAL was sensitive to buffer composition. The low k_{cat} and the high K_{NADPH} prevented detailed analyses. An example is given in Table 6.7 (last two rows), in which it is clear that switching from Hepes buffer to F-buffer leads to an increase of K_{NADPH} such that its value and, as a consequence, those that of k_{cat} and k_{cat}/K_{NADPH} become undetermined.

Overall, although MOCH and MOCHLIM seem to be less sensitive than MO to ionic strength and certain anions, these experiments clearly show that these parameters need to be carefully controlled in our experiments to avoid misleading results.

The high sensitivity of the K_m for NADPH of the NADPH oxidase activity of MICAL to ionic strength and anions, especially phosphate, which also influenced by the overall charge of the protein, may have consequences for the biological function of MICAL. In the cell, the H_2O_2-producing NADPH oxidase activity of its N-terminal flavoprotein domain may be low due to the predicted high ionic strength and the presence of phosphate anions that lead to a high K_{NADPH}.

However, local increases in NADPH concentration or interaction with specific proteins may increase the NADPH oxidase activity of MICAL. The changes of H_2O_2-production by MICAL may be responsible for some of its reported functions in cell.

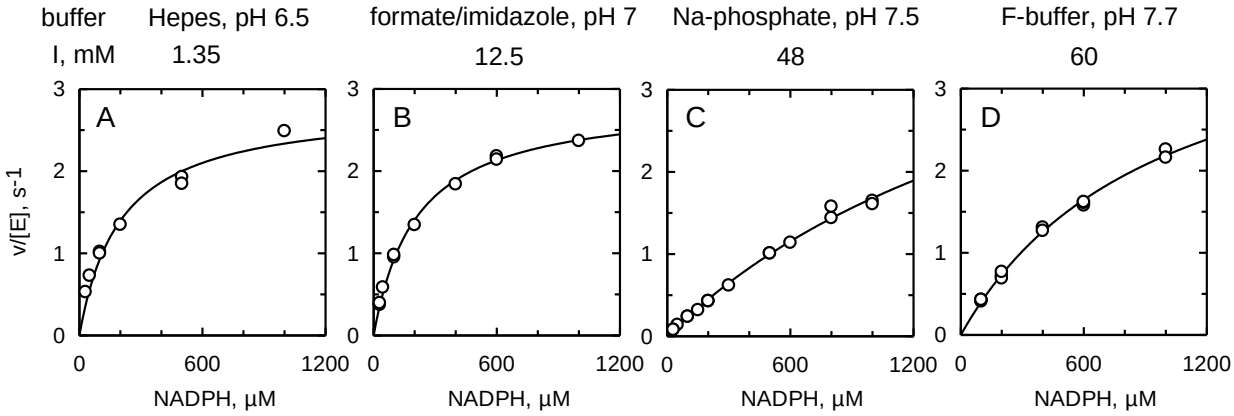

Figure 6.12 Effect of the ionic strength and buffer composition on the kinetic parameters k_{cat} and K_{NADPH} of the NADPH oxidase activity of MOCHLIM form. The initial velocities of the NADPH oxidation reaction catalyzed by MOCHLIM form were measured by varying NADPH concentration in 20 mM Hepes/KOH buffer, pH 6.5 (panel A); 12.5 mM formate, 5 mM imidazole, pH 7 (panel B); in 50 mM Na-phosphate buffer, pH 7.5 (panel C); in F-buffer (9.5 mM Tris/HCl, pH 7.7, 45 mM KCl, 0.18 mM $CaCl_2$, 1.18 mM $MgCl_2$, 1.1 mM ATP, 1.33 mM DTT); the ionic strength of the buffers is indicated in the Figure. The values of the initial velocity were fitted to Eq 2 and the resulting kinetic parameters are reported in Table 6.7.

Table 6.7. Effect of the ionic strength on the steady-state kinetic parameters of the NADPH oxidase reaction of MOCHLIM form and MICAL.

Protein, nM	*Buffer*	*pH*	*I, mM*	*NADPH, µM*	k_{cat}, s^{-1}	K_{NADPH}, *µM*	k_{cat}/K_{NADPH}, s^{-1} mM^{-1}
MOCHLIM, 60	20 mM Hepes/KOH	7	4.4	30-1000	3.5 ± 0.1	230 ± 16	15.3 ± 1.2
MOCHLIM, 60	20 mM Hepes/KOH	6.5	1.35	30-1000	2.81 ± 0.17	202 ± 40	13.92 ± 2.9
MOCHLIM, 60	12.5mM formate 5 mM imidazole	7	12.5	30-1000	2.87 ± 0.07	208 ± 15	13.78 ± 1.04
MOCHLIM, 300	50 mM Na-phosphate	7.5	48	30-800	5.27 ± 0.65	2137 ± 350	2.47 ± 0.5
MOCHLIM, 125	F buffer	7.7	60	30-800	4.3 ± 0.19	966 ± 69	4.45 ± 0.37
MICAL, 690	20 mM Hepes/KOH	7	4.4		0.28 ± 0.01	375 ± 33	0.75 ± 0.07
MICAL, 1250	F buffer	7.7	60		0.77 ± 0.47	4652 ±3202	0.17 ± 0.15

6.4. pH dependence of the kinetic parameters k_{cat}, K_m and k_{cat}/K_m of the NADPH oxidase activity of MICAL forms.

The effect of pH on the kinetic parameters of the NADPH oxidase activity of MICAL forms was studied under carefully controlled buffer conditions. As done during the study of the pH dependence of the NADPH oxidase activity of MO, the ionic strength of the buffer needed to be kept low and constant throughout the explored pH range (Zucchini et al., 2011).

In this present work, we used both mixed buffer A (10 mM acetate, 5 mM imidazole, 5 mM Tris) and mixed buffer B (12.5 mM formate, 5 mM imidazole, 5 mM Tris) at similar ionic strength (10 and 12.5 mM for mixed buffer A and B, respectively). The pH dependence of the kinetic parameters of the NADPH oxidase reaction catalyzed by MO and MOCH was studied both in mixed buffer A and mixed buffer B, while for MOCHLIM and MICAL only mixed buffer B was used. The pH range investigated varied from 5 to 10 for MO and MOCH, but only from 5 to 9 for MOCHLIM and from 5 to 8 for MICAL, by taking into the account the stabilities of NADPH and of the enzymes, as well as the k_{cat} and K_{NADPH} values we measured.

The initial velocity of the NADPH oxidase activity of the MICAL forms was measured in the mixed buffers at varying pH and varying the NADPH concentration. The standard NADPH oxidase activity of the enzymes was also measured every 1-1.5 h to check enzyme stability. Since values were constant during the experiment and similar to those measured at the end of the protein preparations, no correction of the v/[E] values was applied. Figure 6.13 shows that the pH profiles of k_{cat}, k_{cat}/K_{NADPH} and $1/K_{NADPH}$ of MICAL forms are complex. For MOCH no difference was observed depending on the mixed buffer used, while for MO differences were observed highlighting the sensitivity of MO to ionic strength and ionic composition of the medium (Figure 6.13). For MO and MOCH the k_{cat} values increased from non-zero limits at low and high pH to a maximum around pH 7-8. The calculated pK_a values (Table 6.8) were similar for MO and MOCH and may reflect changes of the overall charge of the protein, rather the ionization state of specific residues. The k_{cat} of MOCHLIM was constant in the pH range 6-9 and similar to the maximum value of k_{cat} measured for MO and MOCH. It decreases at lower pH to k_{cat} values similar to those of MO and MOCH at the same pH (Figure 6.13, panel C). On the contrary, the k_{cat} of MICAL increased from a non-zero value at pH 6-8 as pH lowered (Figure 6.13, panel D). This observation could be consistent with the hypothesis that the C-terminal region of MICAL inhibits the MO domain by forming a complex through electrostatic interactions. At pH < 6 the C-terminal domain (pI 5.2) would become less negatively charged, thus the interaction with the MO domain would weaken and the inhibition exerted by the C-terminal region on the MO domain would be (in part) decreased.

The pH dependence of k_{cat}/K_{NADPH} and $1/K_{NADPH}$ is similar in shape for all MICAL forms. It is also complex and similar to that previously reported for MO (Zucchini et al., 2011) and similar to the pH dependence of the K_d for NADPH observed with PHBH (Palfey et al., 1999). The pH profiles seem to reflect the fact that binding of NADPH is mainly determined by the overall charge of the protein. In support to this conclusion is the similarity of the shape of the k_{cat}/K_{NADPH} and $1/K_{NADPH}$ profiles to that describing the protein charge as a function of pH (Figures 6.13 and 6.10).

Overall, these experiments also show that the differences in k_{cat} and K_{NADPH} among the various MICAL forms we initially determined at pH 7 (Table 6.5) are intrinsic properties of the proteins rather than caused by changes in the pH optimum of the reaction.

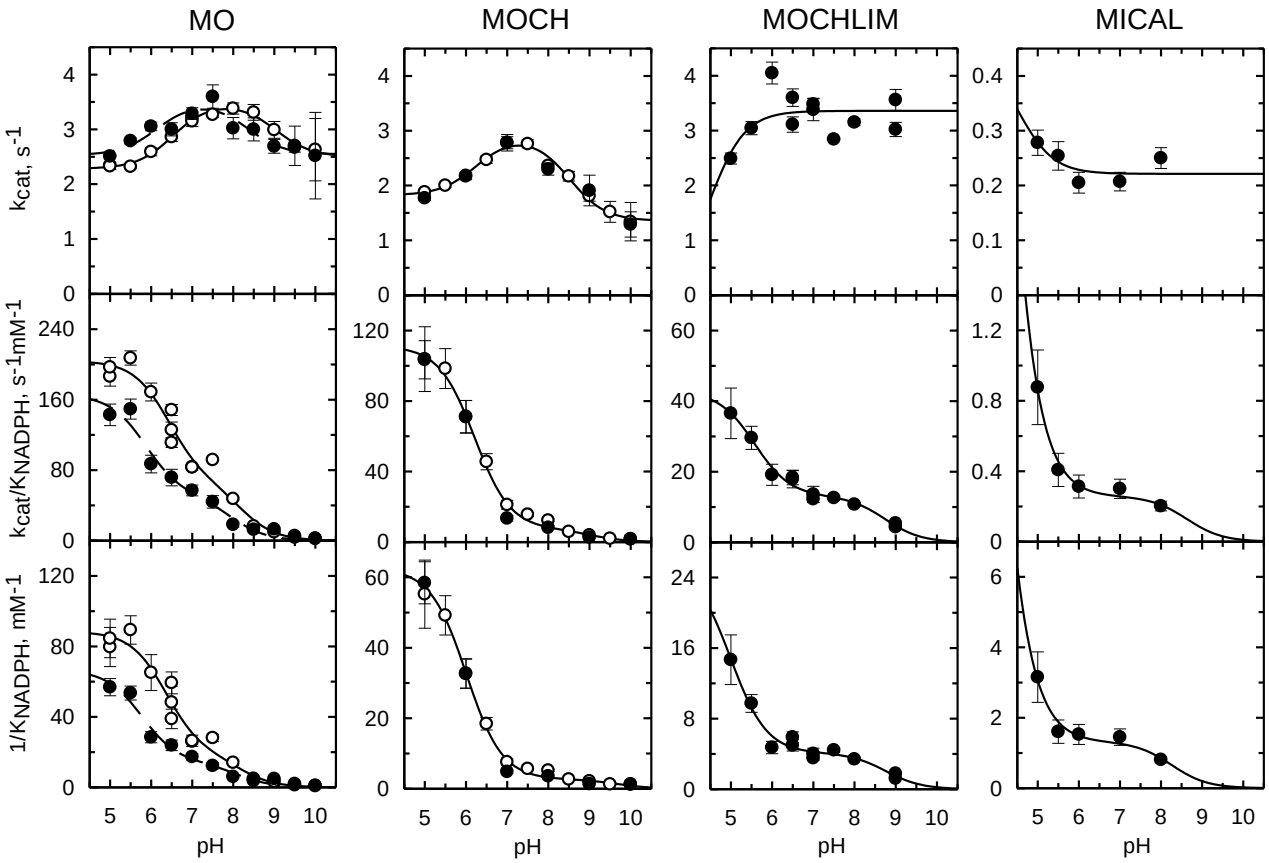

Figure 6.13. pH dependence of k_{cat}, k_{cat}/K_{NADPH} and $1/K_{NADPH}$ of MICAL forms. The steady-state kinetic parameters k_{cat}, k_{cat}/K_{NADPH} and K_{NADPH} for the NADPH oxidase activity of the MO, MOCH, MOCHLIM truncated forms and the full-length protein (MICAL) were determined spectrophotometrically at 25°C by varying NADPH concentration in a mixed buffer composed of 10 mM acetate, 5 imidazole, 5 mM Tris, (○, mixed buffer A, ionic strength 10 mM , Zucchini et al., 2011) or of 12.5 mM formate, 5 mM imidazole, 5 mM Tris (●, mixed buffer B, ionic strength 12.5 mM).The curves were drawn with the equations and parameters values reported in Table 6.7.

Table 6.8. pH dependence of the kinetic parameters k_{cat}, k_{cat}/K_{NADPH} and $1/K_{NADPH}$ of the NADPH oxidase activity of MICAL forms. Initial velocity measurements were carried out by varying NADPH concentration in the presence of 10 mM acetic acid, 5 mM imidazole, 5 mM Tris (Ionic strength, 10 mM, mixed buffer A) or 12.5 mM formic acid, 5 mM imidazole, 5 mM Tris (Ionic strength, 12.5 mM, mixed buffer B). The calculated parameters were used to draw the curves in Figure 6.13. [a]Data obtained with mixed buffer A and B were fitted together; [b]The parameters were poorly determined due to a combination of low k_{cat} and high K_m for NADPH.

Protein	*Buffer*	*Parameter*	*Equation*	A_1	A_2	A_3	pKa_1	pKa_2
MO	1	k_{cat}, s^{-1}	2	2.2 ± 0.04	3.5 ± 0.1	2.5 ± 0.1	6.5 ± 0.1	9.0 ± 0.1
		k_{cat}/K_m, $s^{-1}mM^{-1}$	5	136 ± 25	68 ± 27		6.4 ± 0.3	8.2 ± 0.3
		$1/K_m$, mM^{-1}	5	69 ± 9	20 ± 10		6.4 ± 0.2	8.2 ± 0.6
MO	2	k_{cat}, s^{-1}	2	2.5 ± 0.2	3.5 ± 0.2	2.5 ± 0.1	6.1 ± 0.5	8.4 ± 0.4
		k_{cat}/K_m, $s^{-1}mM^{-1}$	5	114 ± 17	52 ± 16		5.9 ± 0.3	8.0 ± 0.4
		$1/K_m$, mM^{-1}	5	52 ± 6	14 ± 4		5.8 ± 0.2	8.1 ± 0.4
MOCH	1+2[a]	k_{cat}, s^{-1}	2	1.8 ± 0.1	2.9 ± 0.1	1.4 ± 0.1	6.3 ± 0.2	8.5 ± 0.1
		k_{cat}/K_m, $s^{-1}mM^{-1}$	5	104 ± 3	7.3 ± 2.9		6.2 ± 0.1	9.1 ± 0.5
		$1/K_m$, mM^{-1}	5	60 ± 1	2.7 ± 0.7		6.0 ± 0.04	9.7 ± 0.6
MOCHLIM	2	k_{cat}, s^{-1}	3	3.3 ± 0.1			4.4 ± 0.3	
		k_{cat}/K_m, $s^{-1}mM^{-1}$	5	30 ± 3	13 ± 0.9		5.6 ± 0.2	8.8 ± 0.2
		$1/K_m$, mM^{-1}	5	21 ± 7	4.1 ± 0.4		5.0 ± 0.3	8.8 ± 0.3
MICAL	2	k_{cat}, s^{-1}	4	0.5 ± 0.6[b]	0.2 ± 0.02		4.5 ± 1.8	
		k_{cat}/K_m, $s^{-1}mM^{-1}$	5	10 ± 7[b]	0.3 ± 0.05		3.8 ± 0.4	8.6 ± 0.9
		$1/K_m$, mM^{-1}	5	33 ± 41[b]	1.3 ± 0.3		3.8 ± 0.6	8.3 ± 0.6

6.5. Effect of solvent viscosity on the NADPH oxidase activity of MICAL forms

To obtain information on the effect of the CH, LIM and C-terminal domains on catalytically relevant conformational changes as well as possible changes of the rate determining steps of the reaction, the effect of solvent viscosity on the kinetic parameters k_{cat} and K_m for NADPH of the NADPH oxidase activity of MOCH, MOCHLIM and MICAL was studied in 20 mM Hepes/KOH buffer, pH 7, supplemented with fixed concentrations of glycerol and varying NADPH concentration (upper panels of Figure 6.14).

Both k_{cat} and k_{cat}/K_{NADPH} were lowered in the presence of glycerol. Data analysis ruled out that glycerol was an inhibitor of the NADPH oxidase reaction. Rather, the data were well fitted to Eq.8 that correlates the effect of viscosity on k_{cat}/K_{NADPH} (i.e.: $(k_{cat}/K_{NADPH})_0/(k_{cat}/K_{NADPH})_\eta$) and k_{cat} (i.e.: $k_{cat,0}/k_{cat,\eta}$) to the relative viscosity of the solvent (Sampson et al., 1992; Simpoulos et al., 1994; Eser et al., 2010). The effect of solvent viscosity on k_{cat}/K_{NADPH} linearly increased with solvent viscosity with a slope of 2.7 ± 0.4, 2.3 ± 0.3, 1.8 ± 0.2, and 1.7 ± 0.3 for MO, MOCH, MOCHLIM and MICAL, respectively (lower panels in Figure 6.14, Table 6.9). The slope calculated for the effect on k_{cat} was ≈1 for all forms (namely: 0.9 ± 0.1, 1.4 ± 0.1, 1.1 ± 0.1 and 0.9 ± 0.2 for MO, MOCH, MOCHLIM and MICAL respectively, lower panels in Figure 6.14, Table 6.9). The slope >1 of the dependence of the viscosity effect on k_{cat}/K_{NADPH} reveals the presence of conformational changes that contribute to the determination of the value of k_{cat}/K_{NADPH} (2011; McKay et al., 1996; Sampson et al., 1992; Eser et al., 2010). For the reaction, k_{cat}/K_{NADPH} includes steps from NADPH binding up to FAD reduction or $NADP^+$ release (Zucchini et al., 2011). The importance of such conformational change is maximal in MO and progressively decreases in MOCH, MOCHLIM and MICAL (Figure 6.14; Table 6.9). This observation can be explained by taking into account the increase of the K_m for NADPH observed for the species (Figure 6.9; Table 6.5). As binding of NADPH becomes less efficient, the importance of the conformational change following NADPH binding in determining the value of k_{cat}/K_{NADPH} would decrease. Should the rate of binding of NADPH to the enzyme (a diffusion sensitive process) become fully rate limiting, the slope of the plot would become 1. By borrowing the terminology developed to describe kinetic isotope effect, we could say that the viscosity effect observed in k_{cat}/K_{NADPH} due to the conformational change is partially "suppressed" by less efficient binding of NADPH.

The similarity of the solvent viscosity effect on k_{cat} for all MICAL forms indicates that the CH, LIM and C-terminal domains do not alter the relative rates of the conformational change taking place after NADPH binding and of the chemical step of the reaction that contributes to the value of k_{cat}.

This observation is a further proof that the CH, LIM and C-terminal regions of MICAL have little effects on the mechanism of the reaction that takes place within the MO domain. Importantly, these results show that the low k_{cat} of MICAL is unlikely to be due to a decrease of the rate of hydride transfer from NADPH to FAD or to slowing down other chemical steps. If such chemical step (or another chemical step beyond hydride transfer) had become fully determining, the k_{cat} value would have become independent from

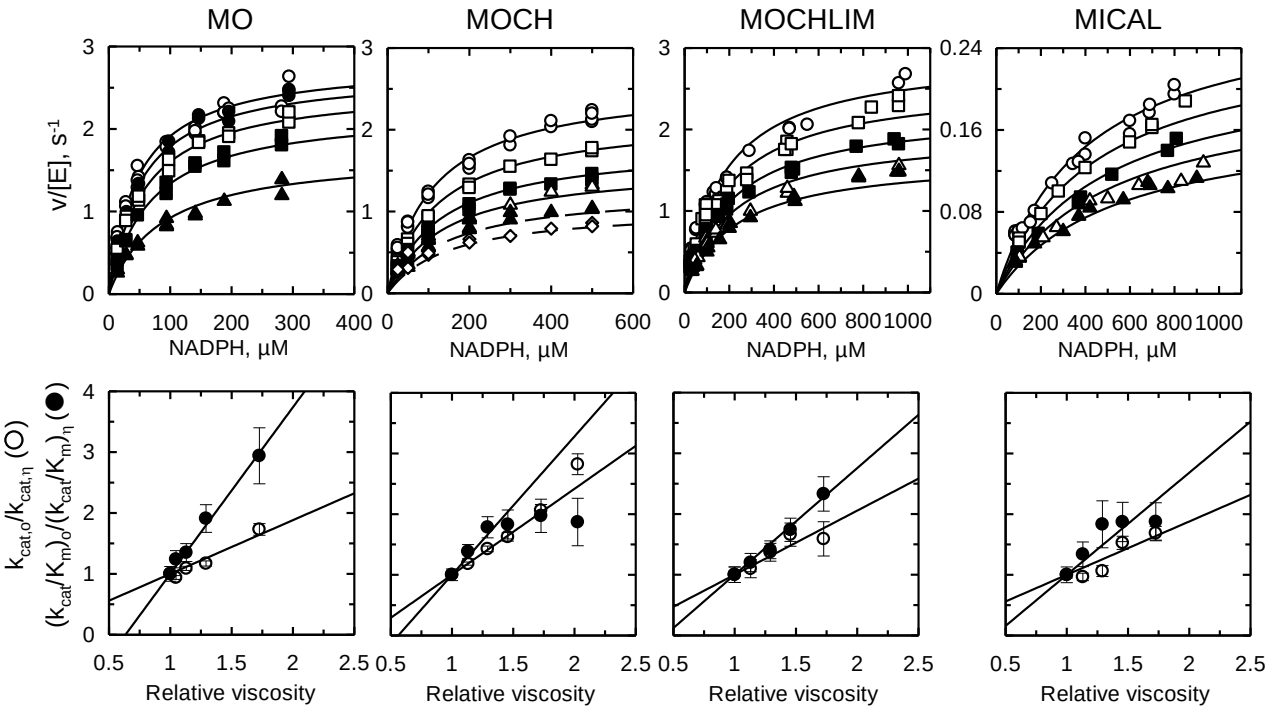

Figure 6.14. Viscosity effects on kcat and kcat/KNADPH of the NADPH oxidase activity of human MICAL1forms. NADPH oxidase reaction of MICAL forms were determined in the presence of varying NADPH concentrations in the presence of different glycerol concentrations expressed in % (w/w): ○, 0 %, η_{rel}, 1; ●: 2.5 %, η_{rel}, 1.04; □, 5%, η_{rel}, 1.13; ■, 10%, η_{rel}, 1.291, Δ, 15%, η_{rel}, 1.456; ▲, 20%, η_{rel}, 1.726; ◊, 25%, η_{rel}, 2.027. The curves correspond to the best fit of the entire datasets to Eq. 8, which provides the estimate of the slopes of the plots of the effect of viscosity on k_{cat} (n value, $k_{cat,0}/k_{cat,\eta}$) and on k_{cat}/K_{NADPH} (m value, $(k_{cat}/K_{NADPH})_0/(k_{cat}/K_{NADPH})_\eta$) as a function of relative viscosity (η_{rel}, Table 6.8). For MOCH only the data up to 15% glycerol were fitted to Eq. 7 due to deviation from linearity of the $k_{cat,0}/k_{cat,\eta}$ and $(k_{cat}/K_{NADPH})_0/(k_{cat}/K_{NADPH})_\eta$) values calculated by individually fitting the initial velocity data obtained at a given glycerol concentration to the Michaelis-Menten equation (Eq. 2, see lower panel). The dashed lines indicate the calculated curves at 20 and 25% glycerol using the parameters shown in Table 6.8. The lower panels compare the values of the effects of viscosity on k_{cat} and on k_{cat}/K_{NADPH} calculated by fitting independently the individual series of data to the Michaelis-Menten equation (Eq.2) with the lines calculated by fitting the whole set of data to Eq. 8. For MO the data are taken from Zucchini et al., 2011 and reanalyzed.

Table 6.9. Summary of the effects of viscosity on k_{cat} and k_{cat}/K_{NADPH} of the NADPH oxidase activity of MICAL1 forms. The initial velocity values (v/E) obtained by varying NADPH in the presence of different glycerol concentrations in 20 mM Hepes/KOH buffer, pH 7.0 at 25°C (Figure 5) were fitted to Eq. 8, in which the m and n values correspond to the slopes of the plots of $(k_{cat}/K_m)_0/(k_{cat}/K_m)_\eta$ and of $k_{cat,0}/k_{cat,\eta}$ as a function of the relative viscosity of the solvent.

				Slope	
Protein	k_{cat}, s^{-1}	K_{NADPH}, μM	k_{cat}/K_{NADPH} , $mM^{-1}s^{-1}$	$(k_{cat}/K_m)_0/(k_{cat}/K_m)_\eta$	$k_{cat,0}/k_{cat,\eta}$
MO	2.8 ± 0.04	47 ± 3	59.5 ± 3.3	2.7 ± 0.4	0.9 ± 0.1
MOCH	2.6 ± 0.05	111± 6	23.2 ± 1.3	2.3 ± 0.3	1.4 ± 0.1
MOCHLIM	2.9 ± 0.07	178 ± 10	16.5 ± 1.0	1.8 ± 0.2	1.1 ± 0.1
MICAL	0.3 ± 0.01	398 ± 31	0.73 ± 0.06	1.7 ± 0.3	0.9 ± 0.2

7. MICAL and F-actin

7.1. Introduction

The cytoskeleton of eukaryotic cells is composed of actin microfilaments, microtubules and intermediate filaments. The cytoskeleton is dynamic and strong, ever ready to adapt to the demands of the cells (Dominguez and Holmes 2011). Actin is the most abundant protein in eukaryotic cells and plays a critical role in fundamental cell processes ranging from cell motility and maintenance of cell shape, to polarity and regulation of transcription thanks to its ability to transition between monomeric (G-actin) and filamentous state (F-actin) under the control of nucleotide hydrolysis, ions and a large number of actin binding proteins (ABP) that control the organization of its polymerization and disassembly (Dominguez and Holmes 2011). Vertebrates express three main actin isoforms: α-actin of skeleton, cardiac and smooth muscles and β- and γ-actin expressed in non-muscle and muscle cells, respectively, differing by few amino acids at their N-terminus (Figure 7.1). Actin also undergoes various post-traslational modifications, such as, e.g., methylations and acetylations (Dominguez and Holmes 2011). The discovery of bacterial homologs of eukaryotic actin is relatively recent. MreB was first identified as a protein involved in cell shape regulation in *E.coli* in the late 1980s (Doi et al. 1988), but only in 2001 it was demonstrated that *Bacillus subtilis* MreB forms cytoskeletal filaments *in vivo* (Shaevitz and Gitai 2010). Actin and its bacterial homologs, with sugar kinases and Hsp90 proteins, belong to a structural superfamily. Common to these proteins is that the polypeptide folds into two major α/β-domains (Dominguez and Holmes 2011). Actin is formed by a small domain composed of subdomains 1 and 2, and a large domain composed of subdomains 3 and 4, leading to the formation of a cleft where ATP binds (Figure 7.2). G-actin can be found in "open" and "closed" conformations depending on the position of the D loop (Figure 7.2). The latter probably oscillates in solution between the conformations in order to exchange the bound nucleotide (Figure 7.2; Aguda et al., 2005).

The phases of the process through which actin monomers self-assemble into filaments and higher order assemblies are: (1) a slow association of monomers to yield the actin dimer; (2) formation of a stable trimer, defined as the "nucleus of polymerization" and (3) the elongation phase. The polymerization of actin is promoted by high ionic strength (≈50 mM KCl) at neutral pH, high concentration of Mg^{++} rather than Ca^{++} and elevated temperatures. All these conditions are normally found within the cells, so that actin would all be present in the filamentous state. Polymerization is also coupled with the hydrolysis of ATP. Actin is endowed with an ATPase activity only in the polymeric state, so that along the filament there are ATP•Actin, ADP•Pi•Actin and ADP•Actin complexes (Figure 7.3; Bamburg et al., 2008). The ADP•Actin monomer is released from the filament that is in a continuous state of assembly and disassembly, defined as treadmilling (Figure 7.3). As a consequence, in the steady-state a small concentration of G-actin will be present in dynamic equilibrium with F-actin at the so called critical concentration (Cc). The elongation of actin filaments has a precise and distinguishable direction of growth due to the position of two monomers of actin leading to the formation of barbed- and pointed-ends of the filament (Figure 7.3). The barbed-end of

the filament has a lower Cc compared to that of the pointed-end. As a consequence at the barbed-end polymerization occurs faster than depolymerization.

```
betaACTIN_mouse         --MDDDIAALVVDNGSGMCKAGFAGDDAPRAVFPSIVGRPRHQGVMVGMGQKDSYVGDEA 58
betaACTIN_rabbit        --MDDDIAALVVDNGSGMCKAGFAGDDAPRAVFPSIVGRPRHQGVMVGMGQKDSYVGDEA 58
betaACTIN_human         --MDDDIAALVVDNGSGMCKAGFAGDDAPRAVFPSIVGRPRHQGVMVGMGQKDSYVGDEA 58
gammaACTIN_mouse        --MEEEIAALVIDNGSGMCKAGFAGDDAPRAVFPSIVGRPRHQGVMVGMGQKDSYVGDEA 58
gammaACTIN_human        --MEEEIAALVIDNGSGMCKAGFAGDDAPRAVFPSIVGRPRHQGVMVGMGQKDSYVGDEA 58
alphaACTIN_rabbit       MCDEDETTALVCDNGSGLVKAGFAGDDAPRAVFPSIVGRPRHQGVMVGMGQKDSYVGDEA 60
alphaACTIN_mouse        MCDEDETTALVCDNGSGLVKAGFAGDDAPRAVFPSIVGRPRHQGVMVGMGQKDSYVGDEA 60
alphaACTIN_human        MCDEDETTALVCDNGSGLVKAGFAGDDAPRAVFPSIVGRPRHQGVMVGMGQKDSYVGDEA 60
                           ::: :*** *****: ****************************************

betaACTIN_mouse         QSKRGILTLKYPIEHGIVTNWDDMEKIWHHTFYNELRVAPEEHPVLLTEAPLNPKANREK 118
betaACTIN_rabbit        QSKRGILTLKYPIEHGIVTNWDDMEKIWHHTFYNELRVAPEERPVLLTEAPLNPKANREK 118
betaACTIN_human         QSKRGILTLKYPIEHGIVTNWDDMEKIWHHTFYNELRVAPEEHPVLLTEAPLNPKANREK 118
gammaACTIN_mouse        QSKRGILTLKYPIEHGIVTNWDDMEKIWHHTFYNELRVAPEEHPVLLTEAPLNPKANREK 118
gammaACTIN_human        QSKRGILTLKYPIEHGIVTNWDDMEKIWHHTFYNELRVAPEEHPVLLTEAPLNPKANREK 118
alphaACTIN_rabbit       QSKRGILTLKYPIEHGIITNWDDMEKIWHHTFYNELRVAPEEHPTLLTEAPLNPKANREK 120
alphaACTIN_mouse        QSKRGILTLKYPIEHGIITNWDDMEKIWHHTFYNELRVAPEEHPTLLTEAPLNPKANREK 120
alphaACTIN_human        QSKRGILTLKYPIEHGIITNWDDMEKIWHHTFYNELRVAPEEHPTLLTEAPLNPKANREK 120
                        **********************:************************:*.***************

betaACTIN_mouse         MTQIMFETFNTPAMYVAIQAVLSLYASGRTTGIVMDSGDGVTHTVPIYEGYALPHAILRL 178
betaACTIN_rabbit        MTQIMFETFNTPAMYVAIQAVLSLYASGRTTGIVMDSGDGVTHTVPIYEGYALPHAILRL 178
betaACTIN_human         MTQIMFETFNTPAMYVAIQAVLSLYASGRTTGIVMDSGDGVTHTVPIYEGYALPHAILRL 178
gammaACTIN_mouse        MTQIMFETFNTPAMYVAIQAVLSLYASGRTTGIVMDSGDGVTHTVPIYEGYALPHAILRL 178
gammaACTIN_human        MTQIMFETFNTPAMYVAIQAVLSLYASGRTTGIVMDSGDGVTHTVPIYEGYALPHAILRL 178
alphaACTIN_rabbit       MTQIMFETFNVPAMYVAIQAVLSLYASGRTTGIVLDSGDGVTHNVPIYEGYALPHAIMRL 180
alphaACTIN_mouse        MTQIMFETFNVPAMYVAIQAVLSLYASGRTTGIVLDSGDGVTHNVPIYEGYALPHAIMRL 180
alphaACTIN_human        MTQIMFETFNVPAMYVAIQAVLSLYASGRTTGIVLDSGDGVTHNVPIYEGYALPHAIMRL 180
                        **********.**********************:********.*************:**

betaACTIN_mouse         DLAGRDLTDYLMKILTERGYSFTTTAEREIVRDIKEKLCYVALDFEQEMATAASSSSLEK 238
betaACTIN_rabbit        DLAGRDLTDYLMKILTERGYSFTTTAEREIVRDIKEKLCYVALDFEQEMATAASSSSLEK 238
betaACTIN_human         DLAGRDLTDYLMKILTERGYSFTTTAEREIVRDIKEKLCYVALDFEQEMATAASSSSLEK 238
gammaACTIN_mouse        DLAGRDLTDYLMKILTERGYSFTTTAEREIVRDIKEKLCYVALDFEQEMATAASSSSLEK 238
gammaACTIN_human        DLAGRDLTDYLMKILTERGYSFTTTAEREIVRDIKEKLCYVALDFEQEMATAASSSSLEK 238
alphaACTIN_rabbit       DLAGRDLTDYLMKILTERGYSFVTTAEREIVRDIKEKLCYVALDFENEMATAASSSSLEK 240
alphaACTIN_mouse        DLAGRDLTDYLMKILTERGYSFVTTAEREIVRDIKEKLCYVALDFENEMATAASSSSLEK 240
alphaACTIN_human        DLAGRDLTDYLMKILTERGYSFVTTAEREIVRDIKEKLCYVALDFENEMATAASSSSLEK 240
                        **********************.**********************:*************

betaACTIN_mouse         SYELPDGQVITIGNERFRCPEALFQPSFLGMESCGIHETTFNSIMKCDVDIRKDLYANTV 298
betaACTIN_rabbit        SYELPDGQVITIGNERFRCPEALFQPSFLGMESCGIHETTFNSIMKCDVDIRKDLYANTV 298
betaACTIN_human         SYELPDGQVITIGNERFRCPEALFQPSFLGMESCGIHETTFNSIMKCDVDIRKDLYANTV 298
gammaACTIN_mouse        SYELPDGQVITIGNERFRCPEALFQPSFLGMESCGIHETTFNSIMKCDVDIRKDLYANTV 298
gammaACTIN_human        SYELPDGQVITIGNERFRCPEALFQPSFLGMESCGIHETTFNSIMKCDVDIRKDLYANTV 298
alphaACTIN_rabbit       SYELPDGQVITIGNERFRCPETLFQPSFIGMESAGIHETTYNSIMKCDIDIRKDLYANNV 300
alphaACTIN_mouse        SYELPDGQVITIGNERFRCPETLFQPSFIGMESAGIHETTYNSIMKCDIDIRKDLYANNV 300
alphaACTIN_human        SYELPDGQVITIGNERFRCPETLFQPSFIGMESAGIHETTYNSIMKCDIDIRKDLYANNV 300
                        **********************:******:****.******:*******:*********.*

betaACTIN_mouse         LSGGTTMYPGIADRMQKEITALAPSTMKIKIIAPPERKYSVWIGGSILASLSTFQQMWIS 358
betaACTIN_rabbit        LSGGTTMYPGIADRMQKEITALAPSTMKIKIIAPPERKYSVWIGGSILASLSTFQQMWIS 358
betaACTIN_human         LSGGTTMYPGIADRMQKEITALAPSTMKIKIIAPPERKYSVWIGGSILASLSTFQQMWIS 358
gammaACTIN_mouse        LSGGTTMYPGIADRMQKEITALAPSTMKIKIIAPPERKYSVWIGGSILASLSTFQQMWIS 358
gammaACTIN_human        LSGGTTMYPGIADRMQKEITALAPSTMKIKIIAPPERKYSVWIGGSILASLSTFQQMWIS 358
alphaACTIN_rabbit       MSGGTTMYPGIADRMQKEITALAPSTMKIKIIAPPERKYSVWIGGSILASLSTFQQMWIT 360
alphaACTIN_mouse        MSGGTTMYPGIADRMQKEITALAPSTMKIKIIAPPERKYSVWIGGSILASLSTFQQMWIT 360
alphaACTIN_human        MSGGTTMYPGIADRMQKEITALAPSTMKIKIIAPPERKYSVWIGGSILASLSTFQQMWIT 360
                        :************************************************************:

betaACTIN_mouse         KQEYDESGPSIVHRKCF 375
betaACTIN_rabbit        KQEYDESGPSIVHRKCF 375
betaACTIN_human         KQEYDESGPSIVHRKCF 375
gammaACTIN_mouse        KQEYDESGPSIVHRKCF 375
gammaACTIN_human        KQEYDESGPSIVHRKCF 375
alphaACTIN_rabbit       KQEYDEAGPSIVHRKCF 377
alphaACTIN_mouse        KQEYDEAGPSIVHRKCF 377
alphaACTIN_human        KQEYDEAGPSIVHRKCF 377
                        ******:**********
```

Figure 7.1. Sequence comparison of human, rabbit and mouse α-, β- and γ-actin. Highlighted in yellow are the residues that are responsible for longitudinal contacts in F-actin and stabilize the filament (Galkin et al., 2015). α-actin from mouse (Uniprot P68134), rabbit (P68135), human (P68133); β-actin from mouse (AAI38615.1), rabbit (P29751.1), human (P60709.1); γ-actin from rabbit (P63260.1), human (P63261).

Thus, it is the site of filament growth often indicated as + end of the filament. The Cc depends on solvent conditions and, particularly, on the presence of ABP, which play a major role in determining the structure and dynamics of filamentous actin (Bamburg et al., 2008).

ABP proteins regulate actin dynamics primarily by varying the critical concentration of actin. There are three main classes of ABP: (1) monomer binding proteins, (2) severing, capping and uncapping proteins and (3) crosslinking proteins (Puius et al., 1998).

The monomer binding proteins, among which profilin is the most studied, bind to free monomeric ADP•actin promoting the nucleotide exchange with ATP and polymerization of the ATP-actin monomer to the filament (Puius et al., 1998). Severing, capping and uncapping proteins are divided in two families represented by gelsolin and cofilin. These proteins are able to bind both G- and F-actin and to sever actin filaments. Members of the gelsolin family are activated in a Ca^{++}-dependent manner. Ca^{++} binding fully exposes the actin binding site allowing the interaction with actin monomers of two different strands of the filament and leading to its severing. In addition they can also cap the barbed-end of the filament preventing its elongation. Cofilin and the homologous Actin Depolymerizing Factor (ADF) bind F-actin in a cooperative fashion causing partial depolymerization and weak severing of the filaments in a pH-dependent manner (Carlier et al., 1999; Bamburg et al., 2010).

Crosslinking or bundling proteins are characterized by the presence of several actin binding regions, such as tandem CH and LIM domains, and are responsible for the assembly of complex structures like Y-junctions between actin filaments in lamellopodia (Borisy and Svitkina 2000).

All ABP exert their activity by sequestering free monomers or by twisting and destabilizing the filaments for their depolymerization only through protein-protein interaction upon their activation and recruitment in response to cell demand. The main mechanism by which the ABP are regulated is represented by their phosphorylation/dephosphorylation state through kinase and phosphatase activities that determine the interactions and their specificity and thus their function (Bamburg 1999).

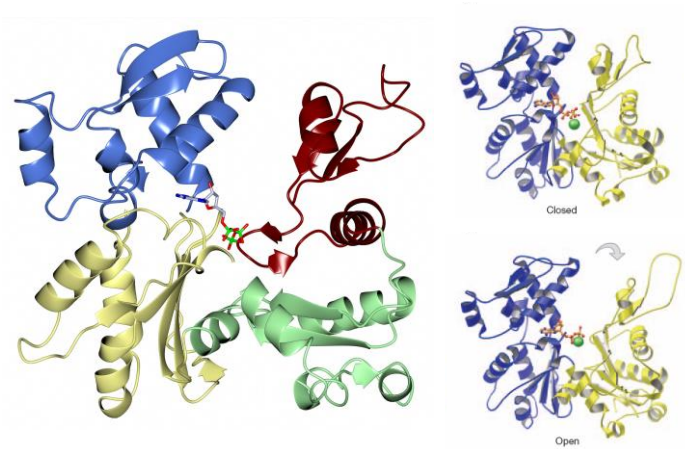

Figure 7.2. Three-dimensional structures of G-actin. The three dimensional structure of rabbit α-actin (PDB ID 3DAW) is shown. Colour code: green, subdomain 1 (residues 1-33, 96-145, 339-374); dark red, subdomain 2 (residues 34-95); yellow, subdomain 3 (residues 146-180, 270-338); blue, subdomain 4 (residues 181-269). ATP is shown in sticks with carbon in light grey, nitrogen in blue, oxygen atom in red and phosphorus group in red. The CCP4 program was used to generate the figure (left panel) (McNicholas et al., 2011). The open and closed conformations are also shown (Aguda et al., 2005).

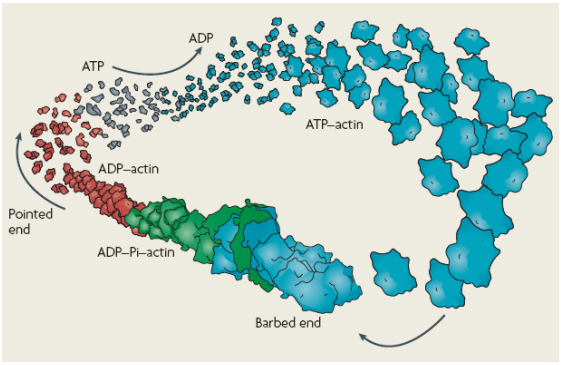

*Figure 7.3. Dynamic equlibrium of the actin filament.*The polymerization of actin into filaments is coupled to ATP hydrolysis. As a result the actin filament is composed by ATP●Actin (light blue), ADP●P_i●Actin (green) and ADP●Actin (red) complexes. At the steady-state the ATP●Actin molecules are added to the barbed-end of the filament for its elongation and the ADP●Actin complexes dissociate (grey) from the pointed-end of the filament. This process is defined as treadmilling (Bamburg et al., 2010).

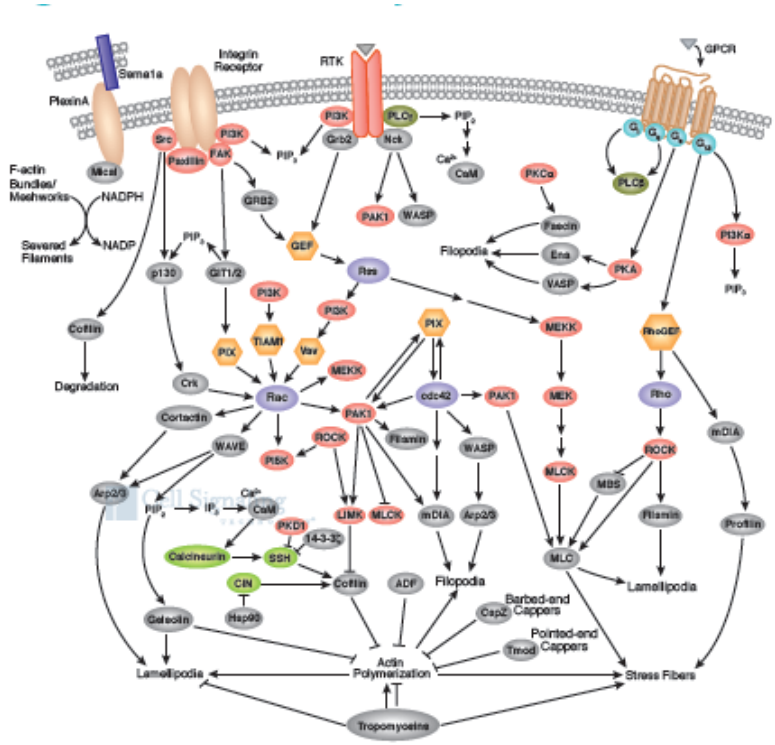

Figure 7.4 Regulatory pathways controlling actin dynamics in cell. (Cell Signaling)

The interaction of semaphorins with their plexin receptors is one of the signaling pathways that leads to reorganization of the cytoskeleton (Figure 7.4). As discussed in the Introduction (Chapter 1), the activity of the N-terminal flavoprotein domain of MICAL is essential for the correct transduction of semaphorin signaling resulting in local F-actin depolymerization. Several hypotheses have been made about MICAL's mechanism of action. The essentiality of the MO domain for MICAL's function in actin depolymerization led to propose that it either acted by oxidizing a small molecule or a protein side chain through a NADPH oxidase (H_2O_2-producing) or NADPH-dependent hydroxylase activity as part of its signal transduction mechanism (Terman et al., 2002). Using genetic approches, Drosophila MICAL (D-MICAL) was shown to mediate growth and directionality of axons (Figure 7.5, panels a and b), but also that MICAL is required for pruning developing neuronal dendrites (Figure 7.5 panel c), muscle organization (Figure 7.5 panel d), larval movements and flight (Figure 7.5 panels d-h) (Hung and Terman 2011). The MO and MOCH regions of D-MICAL were also expressed and purified (Hung et al., 2010, 2011). Although, no information on the quality of these preparations has been given, the proteins were found to catalyze irreversible F-actin depolymerization in a NADPH-dependent fashion indicating that the CH domain is not essential for MICAL function (Figure 7.6, panel A).

The interaction between MICAL and F-actin appeared to take place along the filament rather than at one of the ends of the filament as demonstrated by the analysis of the site of cleavage of filament actin incubated with D-MICAL and NADPH using electron microscopy (Hung et al., 2011; Figure 7.6, panel B). Accordingly, the addition of latrunculin, a capping protein, had no effect on the depolymerizing activity of MICAL (Hung et al., 2011). Analysis of actin treated with the MOCH region of D-MICAL and NADPH revealed that Met44 and Met47 were converted to methionine sulfoxide. Actin Met44Leu and Met47Leu variants were both able to polymerize, but only the actin Met44Leu variant could not be depolymerized by MICAL (Hung et al., 2011; Figure 7.6, panel C). This result led to the proposal that actin Met44 is the substrate of the hydroxylase/monooxygenase activity of MICAL and that its oxidation causes the depolymerization of the filament (Hung et al., 2011). Further work led to identify a Drosophila-specific methionine sulfoxide reductase SelR, similar to mammalian MrsB, which opposes MICAL effect on actin by reverting the methionine-R-sulfoxide residue to methionine, so that G-actin is now able to repolymerize (Figure 7.6, panels D and E; Hung et al., 2013). Similar results were obtained with the MOCH form of mouse MICAL1 and MICAL2 (Lee et al., 2013).

Recently, it has also been demonstrated that MICAL2 mediates serum response factor (SFR)/myocardin-related transcription factor-A (MRTF-A)-dependent gene transcription through its depolymerizing redox activity on nuclear F-actin (Lundquist et al., 2014). Gene transcription is activated when nuclear MRTF-A levels increase leading to the formation of active SFR/MRTF-A complex. The level of nuclear MRTF-A is regulated by nuclear levels of G-actin, since the interaction between the proteins promotes MRTF-A nuclear export. MICAL2 activity would decrease nuclear G-actin and thus increase MRTF-A concentration in the nucleus, resulting in transcription of genes involved in diverse cellular processes such as cell migration, cancer cell metastasis, mammary myoepithelium development and neurite formation (Lundquist et al., 2014).

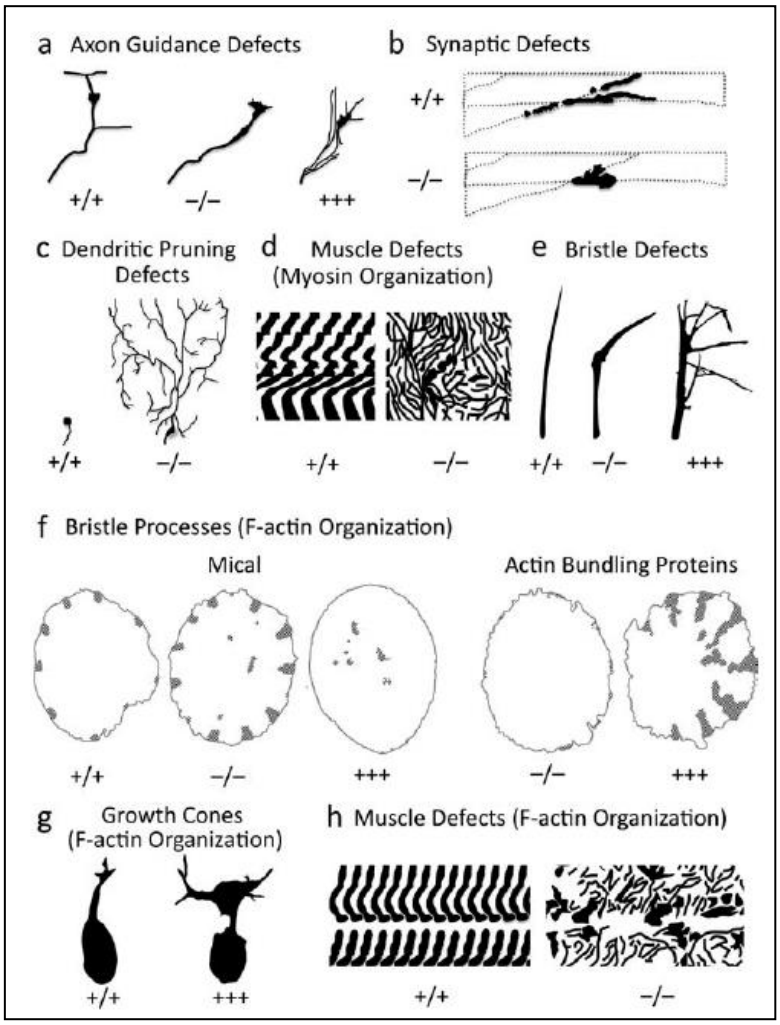

Figure 7.5. In vivo organization of F-actin by MICAL from. Function of Drosophila MICAL during axon guidance (a and g), neuronal synapse formation (b), dendrite pruning (c), muscle formation (d and h), and bristle shape (e-f); -/- mutant loss of function (G-to-W substitution in the FAD-binding region); +/+ mutant gain of function (overexpression of MICAL) (Hung et al., 2010).

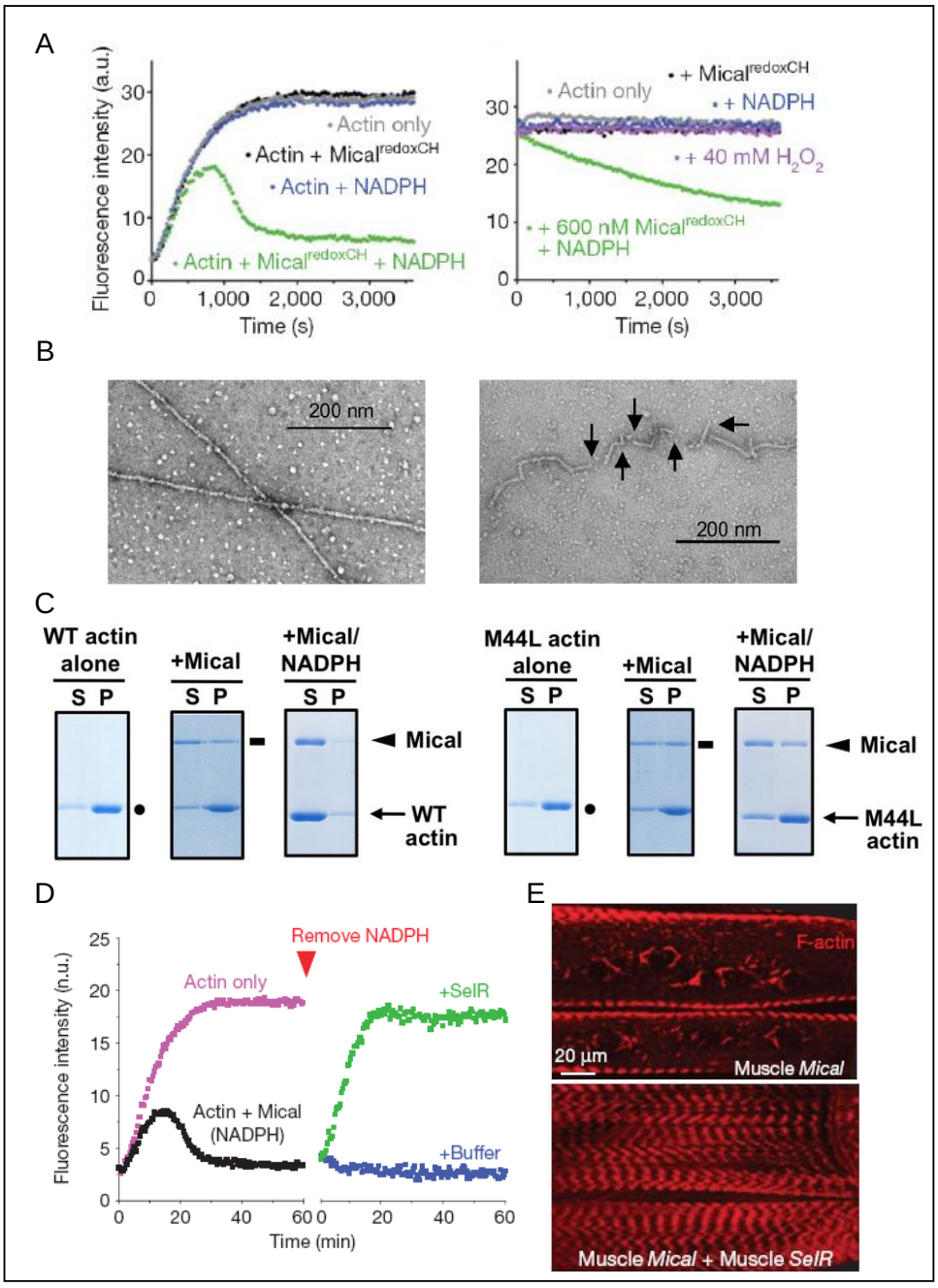

Figure 7.6. Effect of Drosophila MICAL forms and NADPH on the actin polymerization state. Panel A: Pyrene-labelled G-actin (1.1 µM final concentration) was incubated with Drosophila MICAL-MOCH (Mical^{redoxCH} , 600 nM) and/or NADPH (100 µM) in G buffer. Polymerization of actin was induced and fluorescence intensity was immediately monitored; Drosophila MICAL-MOCH, NADPH, and/or hydrogen peroxide were added to pre-polymerized pyrene-labelled F-actin (1.1 µM) (Hung et al., 2010). Panel B: Electron microscopy analysis of F-actin filaments (left panel) and after incubation with Mical^{redoxCH} , 600 nM) and NADPH (100 µM) (right panel), the arrows indicate the cut due to MICAL activity along the filament. Panel C: cosedimentation assays of wild-type (WT) and M44L F-actin mutant incubated with MOCH form (Mical, 600 nM) in the absence and presence of NADPH (100 µM) (Hung et al., 2010, 2011). Panel D:Fluorescence increase was monitor for 1.1 µM Pyrenyl-actin alone (purple dots) and in the presence of 600 nM D-MOCH and 100 µM NADPH (black dots). Polymerization of MICAL-treated actin was followed after addition of 2.4 µM SelR (green dots) and buffer (blue dots). Panel E: actin organization in muscles cells overexpressing MICAL (Muscle Mical) and co-expressing MICAL and SelR (Muscle Mical+Muscle SelR) (Hung et al., 2013).

The human MICAL-MO was also found to exhibit an F-actin depolymerizing activity (Zucchini et al., 2011). The reaction was monitored fluorimetrically, by exploiting the different fluorescence intensity of pyrene-labeled G- and F-actin (Figure 7.7 panels A and B), by sedimentation assays and by monitoring changes of the size of particles in solution by dynamic light scattering (Figure 7.7, panel C; Zucchini et al., 2011). Addition of human MICAL-MO to pre-polymerized pyrenyl-actin, in a buffer stabilizing F-actin (F-buffer), after NADPH, led to a decrease of fluorescence, which was dependent on MICAL and NADPH concentration and much faster than that reported for D-MICAL. Moreover, catalytic amounts of human MO (10-30 nM) were sufficient to cause F-actin depolymerization compared to the stoichiometric amounts used in the experiments carried out with D-MICAL (Hung et al., 2010, 2011, 2013). Dynamic light scattering (DLS) was also used to monitor the decrease in size of actin filaments, which was partial, suggesting that MICAL caused fragmentation of filaments and/or aggregation (Figure 7.7, panel C; Zucchini et al., 2001). F-actin, but not G-actin, significantly stimulated NADPH oxidation (Figure 7.7 panel D) by lowering the K_m value for NADPH (50-fold) and increasing k_{cat} (3- or 6-fold at 2.4 μM actin or extrapolated at infinite actin concentration, respectively) when compared to the values measured in the absence of actin (Table 7.1), resulting in a ~500-800-fold k_{cat}/K_{NADPH} increase (Zucchini et al., 2011). More importantly, assuming that MICAL-MO catalyzes the hydroxylation of one specific actin residue, with a 1:1 stoichiometry of NADPH being oxidized per actin monomer being modified, one would have predicted biphasic traces. Initially, MICAL would behave as expected for a monooxygenase in the presence of its substrate. The rate of NADPH consumption would be fast and the amount of NADPH consumed in this phase should be lower or equal to the total actin monomer concentration. A second slower phase of NADPH oxidation should follow due to the MICAL NADPH oxidase reaction with residual oxygen. On the contrary, although traces showed some biphasicity, which could not be clearly correlated with the total actin concentration present, the second phase was much faster than that measured in the NADPH oxidase activity under the same conditions and fast oxidation of all NADPH present was obtained (Figure 7.7 panel D; Zucchini et al., 2011). The observed extent and time-course of NADPH consumption are consistent with either a case of substrate recycling suggesting that the effect of MICAL (and NADPH) on F-actin may be reversible or with the fact that the depolymerization of F-actin is due to *in situ* H_2O_2 release. In this respect, that F-actin is sufficient to enhance the rate of FAD reduction by NADPH has been demonstrated in a stopped-flow experiment with the isolated MO domain of mouse MICAL2 (McDonald et al., 2013).

Although the MO domain is sufficient to catalyze the NADPH-dependent F-actin depolymerization reaction, it was important to determine the effect of CH, LIM and C-terminal domains of MICAL on this activity. The CH and LIM domains are typical of cytoskeleton proteins and mediate protein-protein interactions and both can bind actin for its regulation in response to cell signaling (Puius et al., 1998). Thus, they may alter the affinity for actin and also modify the time-course and extent of NADPH oxidation observed with the isolated MO domain, which is in contrast with the specific Met hydroxylase activity proposed for Drosophila and mouse MICAL (Hung et al., 2013; Lee et al., 2013).

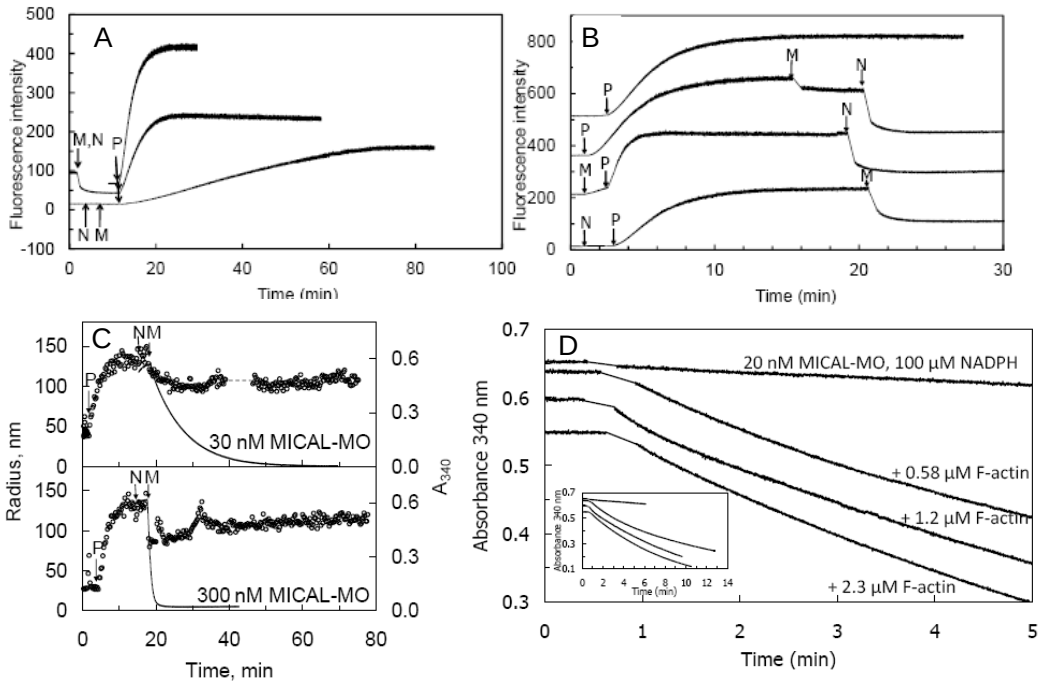

Figure 7.7. Effect of human MO domain on actin polymerization state and effect of F-actin on its NADPH oxidation reaction. Panel A: the polymerization state of pyrene-labelled G-actin (4.1 µM) in the presence or absence of NADPH (N, 100 µM) and human MICAL-MO (M, 660 nM) was monitored fluorimetrically in a Cary Eclipse (Varian) fluorimeter. The polymerization was induced by addition of 1/10 volume of polymerization buffer (P) to the solution in G-buffer; Panel B: Fluorescence-monitored polymerization and depolymerization of actin (2.3 µM) in the presence of NADPH (N, 100 µM) and human MICAL-MO (660 nM, M) added at the indicated times. In the panels the traces have been offset for graphical purposes. Panel C: polymerization of G-actin (5 µM) and the effect of the addition of MO (M, 30 and 300 nM) and NADPH (N, 100 µM) were monitored by dynamic light scattering. Solid lines: oxidation of NADPH (100 µM) monitored at 340 nm under identical conditions. The A_{340} traces are offset to match the time of enzyme addition to the solution containing F-actin and NADPH in the DLS experiment. Panel D: time-course and extent of NADPH oxidation catalyzed by MO (M, 20 nM) in the absence and presence of F-actin; the insert shows the same traces but on a different time-scale (Zucchini et al., 2011; Vanoni et al., 2012).

Table 7.1. Effect of G- and F-actin on the steady-state kinetic parameters of the reaction of human MICAL-MO. The steady-state kinetic parameters of the reaction catalyzed by human MICAL-MO in the absence and presence of G- and F-actin were measured at 25 °C in 20 mM Hepes/KOH buffer, pH 7.0 (Hepes), G-buffer (5 mM Tris/HCl, pH 8.0, 0.2 mM $CaCl_2$, 0.2 mM ATP, 1 mM DTT) or and F-buffer (9.5 mM Tris/HCl, pH 7.7, 0.18 mM $CaCl_2$, 1.1 mM ATP, 1.3 mM DTT, 45 mM KCl, 1.8 mM $MgCl_2$). The substrates concentrations or concentration ranges are indicated. The KM is that calculated for the varied substrate. Data are from Zucchini et al., 2011.

NADPH, µM	MICAL, nM	Buffer	Actin, µM	K_M, µM	k_{cat}, s^{-1}	k_{cat}/K_m, s^{-1} μM^{-1}
10–300	30	Hepes	-	19 ± 2	3.1 ± 0.1	0.163 ± 0.018
10–300	30	G-buffer	-	102 ± 8	3.4 ± 0.1	0.034 ± 0.003
10–300	75	G-buffer	G, 3.3	96 ± 28	4.5 ± 0.6	0.047 ± 0.015
10–300	120	F-buffer	-	555 ± 118	2.6 ± 0.4	0.005 ± 0.001
10–300	20	F-buffer	F, 2.4	11 ± 3	12.3 ± 0.5	1.12 ± 0.31
300	20	F-buffer	F, 7–85	4.7 ± 1	19.5 ± 1	4.2 ± 0.9

7.2. NADPH dependent F-actin depolymerizing activity of MICAL forms

The effect of MOCH, MOCHLIM and MICAL on the oligomeric state of F-actin was studied by monitoring fluorescence changes using pyrenyl-actin and by DLS.

G-pyrenyl-actin solutions (0.12 mg/ml, 2.8 μM) were prepared as described in Materials and Methods (Chapter 10). The actin polymerization, after the addition of 1/10 volume of the polymerization buffer (P), was followed by monitoring the increase of emission fluorescence at 407 nm (λ_{ex} 365 nm) (Figure 7.8). The addition of NADPH (N, 50 μM) partially quenched the fluorescence intensity due to absorbance of the exciting light (Figure 7.8). The addition of MOCH (120 nM, Figure 7.8, panel A), MOCHLIM (120 nM, Figure 7.8, panel B) and MICAL (120 nM, Figure 7.8, panel C) caused a drop of the fluorescence intensity, indicating that they are all able to catalyzed the F-actin depolymerizing activity. Control experiments showed that this process is NADPH-dependent (Figure 7.8, panels D and E).

As an alternative to fluorescence spectroscopy, the aggregation state of actin can be monitored by DLS that measures the mean radius of particles in solution as a function of time. In parallel experiments, the NADPH oxidation could be monitored spectrophotometrically at 340 nm. The polymerization of the G-actin solution (0.19 mg/ml, 4.6 μM) was followed by measuring the increase of the mean radius in solution after the addition of 1/10 volume of the polymerization buffer (P). It should be noted that the starting G-actin solution showed a average radius of ≈ 20 nm (Figure 7.9, panel A), but data analysis demonstrated the presence of a protein species with a radius of 3.2 nm, 51 kDa (Figure 7.9, panel B) corresponding to G-actin, and a small fraction of aggregated protein (Figure 7.9, panel B) even after centrifugation at 100000xg for 1 h at 4°C. After the addition of polymerization buffer the mean radius reached a maximum value within 20-25 min. Analysis of the data collected 50-60 min after the addition of the polymerization buffer (Figure 7.9, panel C) confirmed the complete conversion of G-actin to F-actin (Figure 7.9, panel E) showing the presence of species with large molecular mass (R, 232 nm) along with smaller species (R ≈8.5 nm, 476 kDa; Figure 7.10, panel A). When NADPH (N, 100 μM) was added the average radius of particles in solution did not change (Figure 7.9, panels C, D and E). Instead, after the addition of MOCH (130 nM or 30 nM) the average radius of particles in solution decreased from 110 to 70 nm within 5 min, a time similar to that required for the consumption of all the NADPH present (Figure 7.9, panels C and D). The plateau value of the mean radius was higher than that observed for the starting G-actin indicating a partial depolymerization of F-actin and/or the presence of aggregates. In fact, by analyzing the data collected ≈ 30 min after MOCH addition two protein species were present with an apparent radius of 6.2 (252 kDa) and 177 nm (Figure 7.9, panel E), that were lower than those observed for F-actin incubated with NADPH (Figure 7.9, panel E). To remove large aggregates, which may be formed in solution, the sample was centrifuged at 14900xg for 15 min at 4°C. Now the average radius was 15 nm similar to that observed with the starting G-actin solution (Figure 7.9, panels A, C and D). The supernatant contained ≈75% of the total protein of the sample before centrifugation and analysis of the DLS signals showed the presence of protein species with a radius of 3.3 or 3.5 nm (55 or 63 kDa) (Figure 7.9, panel E), similar to that measured for the starting G-actin solution. A second peak of ≈14 nm (156000 kDa; Figure 7.9, panel E) for the actin sample incubated with 130 nM MOCH and of 140 nm,

when 30 nM MOCH was added was observed. These species can correspond to shorter actin filaments and/or aggregates. Centrifugation was not sufficient to remove all the aggregates present (third peak in Figure 7.9, panel E). When MOCHLIM (120 nM or 47 nM) was added to F-actin (4.2 μM) in the presence of NADPH (100 μM) the mean radius decreased from 170 to 130 nm, but then increased suggesting the formation of aggregates (Figure 7.10, panel A). After centrifugation at 14900xg for 15 min at 4°C the mean radius of the supernatant, that contained ≈80% of the total protein content, was 90 nm (Figure 7.10, panel B) that was higher than that of G-actin solution. The higher value of the radius could be due to the presence of some aggregates that can not be removed at low speed or the presence of shorter actin filaments. In fact, in the supernatant protein species with a radius of 6.6 or 6.1 nm (280 or 232 kDa, Figure 7.10, panel B) and of 168 or 124 nm were detected (Figure 7.10, panel B), which can correspond to shortened actin filaments and/or aggregates.

Interestingly, the addition of MICAL (1.57 μM) that has been proposed to be inactive with absence of plexin (Schmidt et al., 2008), in the presence of NADPH caused an instantaneous decrease of the average particles radius from 240 to 170 nm (Figure 7.10, panel C) and reached a final value of 70 nm in 10 min. The same time was required to the enzyme to completely oxidize all NADPH present (Figure 7.10, panel C). The supernatant of centrifugation at 14900xg for 15 min at 4°C showed an average radius of 40 nm indicating, also in this case, the removal of some aggregates (Figure 7.10, panels C and D). Species with a 6.5 nm radius were observed as for MOCHLIM. To ensure that the drop of the mean radius was not due to the addition of the enzyme, F-actin was incubated with MICAL and the mean radius of the solution remained constant with a value similar to that of F-actin (Figure 7.10, panel E). The addition of NADPH (100 μM) to F-actin led to a decrease of the radius with a similar kinetic of the experiment just described (Figure 7.10, panel C) indicating that the depolymerization and or aggregation observed were dependent on the NADPH oxidation reaction catalyzed by the enzyme. The data obtained after centrifugation of the samples were similar to those observed for MOCHLIM (Figure 7.10, panels D and F). F-actin control sample indicated that the disappearance of the protein species with a radius >230 nm was not due to centrifugation and that F-actin solution was stable and no aggregates were detected in the supernatant (Figure 7.10, panels G and H).

These experiments qualitatively show that all MICAL forms catalyze a NADPH-dependent reaction, in which F-actin filaments are disassembled to yield free monomers in the case of MO and MOCH, but larger fragments for MOCHLIM and full-length MICAL and aggregated forms are also present for all proteins . In order to obtain quantitative data on the kinetics of the process and on the affinity for NADPH and F-actin, the steady-state kinetic parameters of the reaction of MICAL forms with NADPH and F-actin were studied.

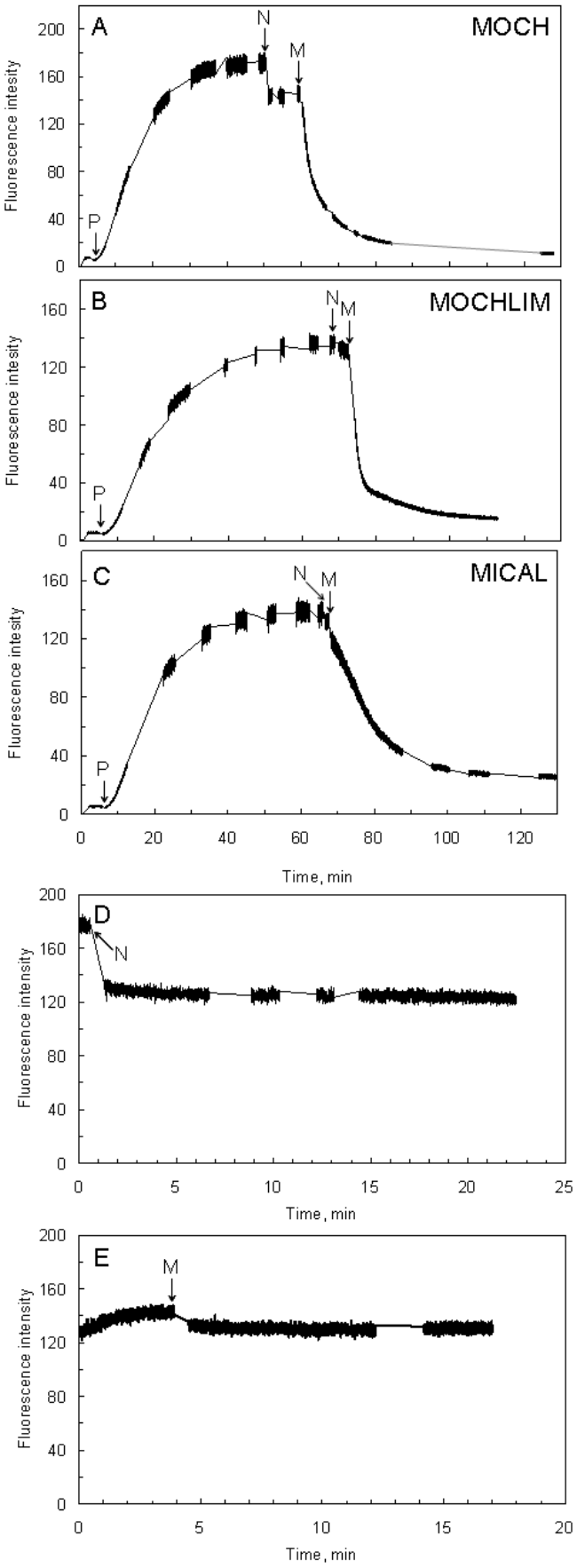

Figure 7.8. Time-course of F-actin depolymerization catalyzed by MICAL1 forms. Pyrenyl-actin (2.6 µM) in G-buffer was polymerized at room temperature upon addition of one tenth volume of polymerization buffer (P) NADPH (50 µM, N) and the indicated MICAL forms (120 nM, panles A-C) were added at times indicated by arrow. Panels D and E show that NADPH or MOCH alone are not sufficient to alter F-actin polymerization state. The reactions were monitored by measuring the fluorescence emission at 407 nm with excitation light at 360 nm in a Cary Eclipse spectrophotofluorimeter. To avoid potential artifacts, irradiation was interrupted for several intervals of time (continuous lines).

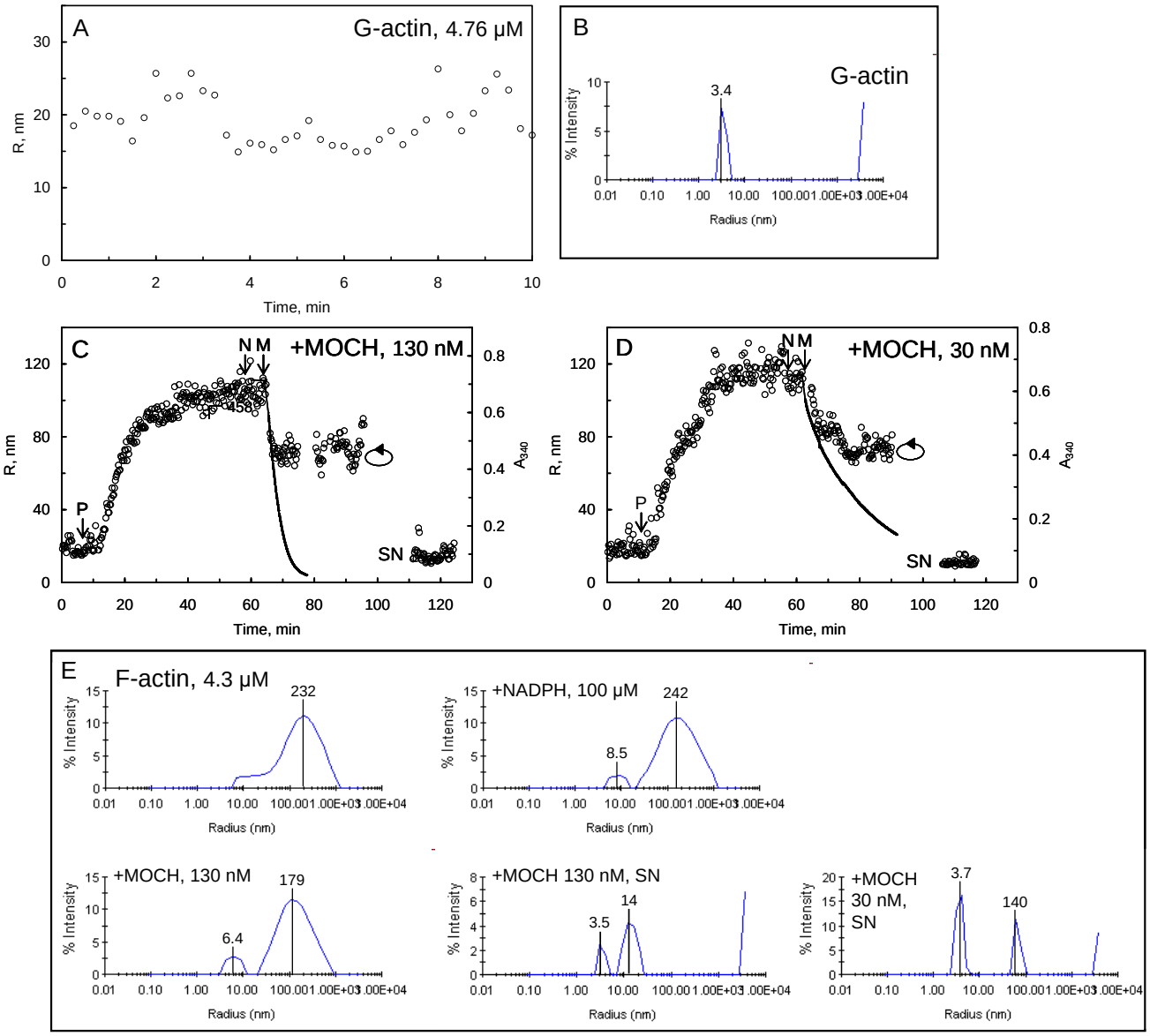

Figure 7.9. Analysis of G- and F-actin solutions treated with NADPH and MOCH by DLS. The average radius of G-actin solution (4.76 µM) was monitored by DLS for 10 min (panel A), which contains protein species corresponding to monomeric actin (3.4 nm) and aggregated forms (panel B). Panels C and D: Polymerization of G-actin was followed after addition of 1/10 volume of polymerization buffer (P). When G-actin was completely converted to F-actin NADPH (100 µM, N) and MOCH (130 nM and 30 nM) were added. At ≈90 min the sample was centrifuged at 14900xg for 15 min at 4°C and the supernatants (SN) were analyzed. Panel E: Determination of the protein species present in the F-actin, after the addition of NADPH, ≈30 min after the addition of MOCH and in the supernatants obtained by centrifugation.

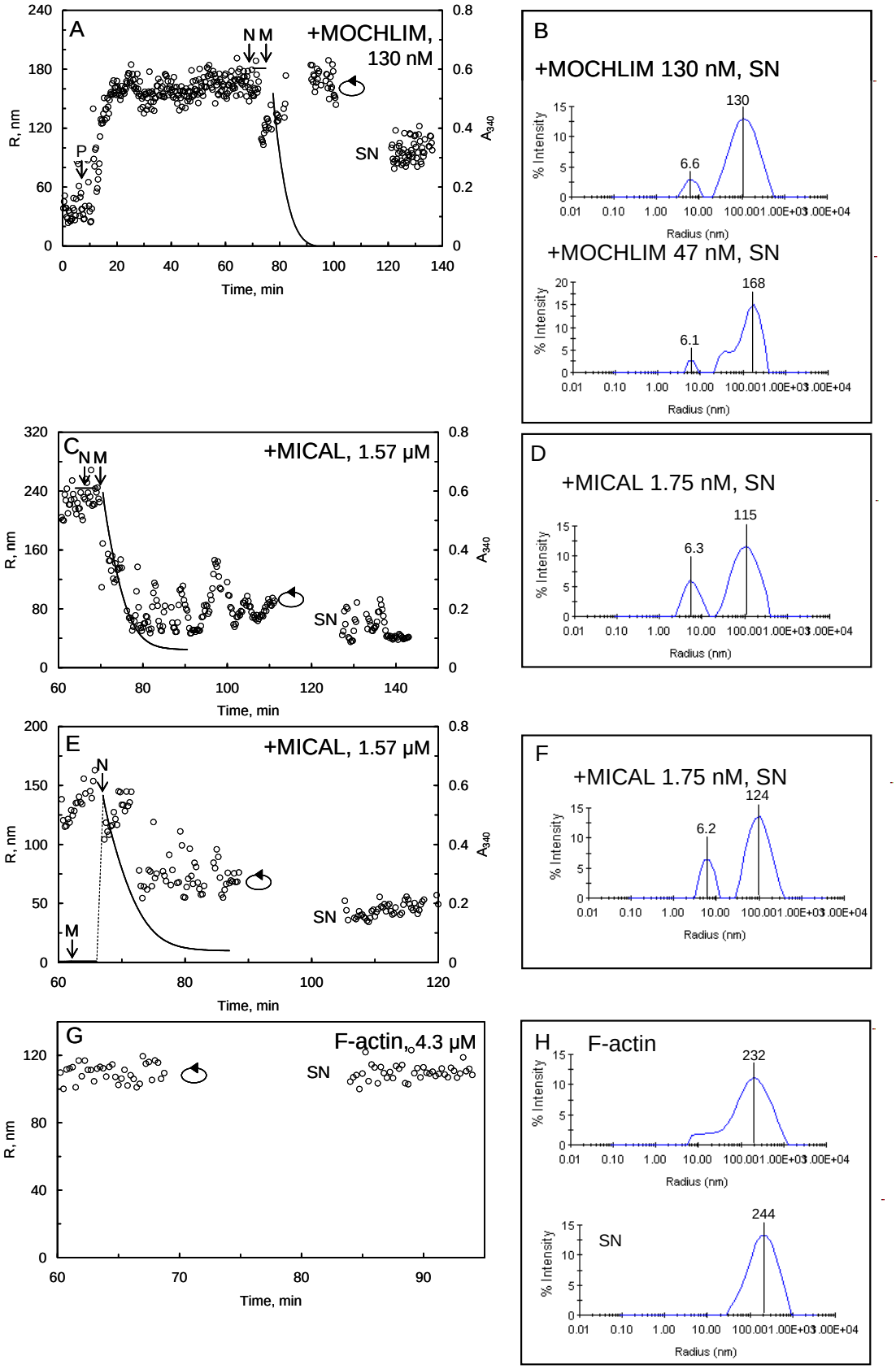

Figure 7.10. Analysis of G- and F-actin solutions treated with NADPH and MOCHLIM and MICAL by DLS Panels A, C, E,: Polymerization of G-actin was followed after addition of 1/10 volume of polymerization buffer (P). When G-actin was completely converted to F-actin NADPH (100 µM, N) and MOCHLIM (130 nM and 47 nM) and MICAL (1.7 µM) were added. At ≈90 min the sample was centrifuged at 14900xg for 15 min at 4°C and the supernatants (SN) were analyzed. Panel B, D, F: Determination of the protein species present in the F-actin, after the addition of NADPH, ≈30 min after the addition of MOCH and in the supernatants obtained by centrifugation. Analysis of F-actin control sample is shown in panels G and H.

7.3. Effect of F-actin on the NADPH oxidation reaction of MICAL forms

F-actin, but not G-actin, stimulates the rate of NADPH oxidation reaction catalyzed by the isolated MO domain of human MICAL1 (Zucchini et al., 2011). The effect of F-actin on the reaction catalyzed by MOCH, MOCHLIM and MICAL was studied.

In preliminary experiments, F-actin solutions (0.2 mg/ml, 5 μM) were incubated with NADPH (100 μM) for 3 min at 25°C, then MOCH (150 nM), MOCHLIM (115 nM) or MICAL (1.57 μM) was added. The NADPH oxidation was monitored by recording the absorption spectrum every 10 s in a diode array spectrophotometer. In this way, we could detect the contribution of absorbance of F-actin and possible absorbance changes due to aggregation/denaturation. For comparison oxidation was measured in F-buffer in the absence of F-actin.

For all MICAL forms F-actin enhanced the rate of NADPH consumption, so that the initial velocity, expressed as v/[E] to compensate for the different mass of the enzymes, increased ≈10-fold: from 0.3 s^{-1} in F-buffer to 2.9 s^{-1} for MOCH (Figure 7.11, panel A), from 0.2 s^{-1} to 2.15 s^{-1} for MOCHLIM (Figure 7.11, panel B) and from 0.02 s^{-1} to 0.2 s^{-1} for MICAL (Figure 7.11, panel C).

As observed for MO, F-actin greatly stimulates NADPH consumption by MOCH, MOCHLIM and MICAL as expected for a monooxygenase in the presence of its substrate. However, in contrast with the hypothesis of a specific actin monooxygenase reaction, the amount of NADPH being oxidized always exceeded that of F-actin present. This result is in contrast with the specific modification of Met44 or Met47 of actin monomers that would have predicted fast oxidation of 2 molecules of NADPH per actin monomer present (Hung et al., 2014; Lee et al., 2014). Rather the observed time-course and extent of NADPH consumption could be explained, as done before, as due to: (i) a case of substrate recycling (i.e.: the effect of MICAL on F-actin is reversible); (ii) an enhanced rate of the NADPH oxidation upon interaction with F-actin leading to both Met hydroxylation (monooxygenase activity) and NADPH oxidase (H_2O_2-production) activity occurring at the same rate or (iii) enhanced NADPH oxidase activity. In the latter case, actin chemical modification would be due to *in situ* enhanced production of H_2O_2 rather than to a hydroxylation reaction.

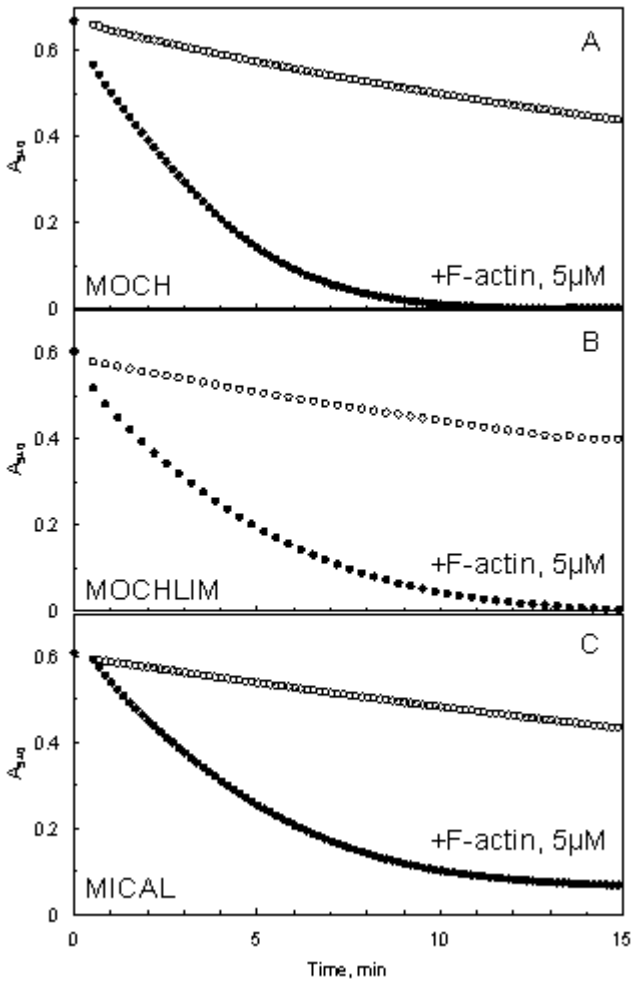

Figure 7.11. Time-course of NADPH oxidation catalyzed by MICAL and the truncated MOCH and MOCHLIM forms in the absence (open circles) or in the presence of F-actin (5 μM, closed circles) in F-buffer. MOCH (150 nM), MOCHLIM (115 nM), and full-length MICAL (1.5 μM) were incubated with NADPH (100 μM) in the absence (open circles) or in the presence of F-actin (5 μM, closed circles) in F-buffer at 25 °C. The time-course of NADPH oxidation was monitored by absorption spectroscopy at 340 nm.

7.4. Determination of the steady-state kinetic parameters of the NADPH oxidation reaction of MICAL forms in the presence of F-actin

The apparent steady-state kinetic parameters k_{cat}, K_{NADPH} and apparent K_m for F-actin of MOCH, MOCHLIM and MICAL forms were determined by measuring the initial velocity of NADPH consumption monitored at 340 nm and 25°C.

The kinetic parameters k_{cat} and K_{NADPH} were determined in the absence and in the presence of fixed F-actin concentration (≈0.17 mg/ml, 4 μM) in F-buffer and varying the NADPH concentration (10 - 400 μM).

Double reciprocal plots were linear so that the k_{cat} and K_{NADPH} could be calculated by fitting the data to the Michaelis-Menten equation (Eq.2; Figure 7.12, upper and middle panels; Table 7.2).

The k_{cat} and apparent K_m for F-actin parameters were determined in the presence of a fixed NADPH concentration (200 μM) and varying F-actin concentration (1-26 μM).

Again, a hyperbolic dependence of v/[E] upon F-actin concentration was observed (Figure 7.12, lower panels; Table 7.2). The calculated k_{cat} and K_m for F-actin are in Table 7.2.

F-actin stimulates the NADPH oxidation reaction by increasing k_{cat} and lowering K_m for NADPH leading to values that vary within a factor of 2 for MO, MOCH and MOCHLIM (Table 7.1 and 7.2). Also the apparent K_m for F-actin of the three truncated MICAL forms was similar (≈4 μM). These results indicated that the presence of the CH and LIM domains, which are found in proteins that interact with actin do not apparentely alter the affinity of MICAL for filamentous actin and the flavoprotein domain seem to be the main site where the interaction with F-actin takes place.

Full-length MICAL showed an apparent K_m for F-actin 10-fold higher than that of the other forms (Table 7.2) indicating that the C-terminal region of MICAL lowered the apparent affinity of the MO domain for F-actin. Instead, the apparent values of k_{cat} and K_{NADPH} (extrapolated at infinite actin concentration and at 200 μM NADPH) were similar to those of the other forms (K_{NADPH}) and only 2-3-fold lower (k_{cat}) (Table 7.2).

Overall, contrary to early proposals, these results indicate that the CH and LIM domains do not alter the affinity for F-actin and have no effect on the rate at which the MO domain oxidizes NADPH in the presence of F-actin. Interaction between all MICAL forms and F-actin, presumably mainly through the MO domain, causes an increase of k_{cat} to similar values, as well as a drop of K_{NADPH} also to similar values for the four proteins forms. The C-terminal region of MICAL causes only a 10-fold increase of the apparent K_m for F-actin, which makes this species able to bind to F-actin and depolymerize it also in the free form; i.e., in the absence of the activating interaction with plexin in response to semaphorins or other interactors.

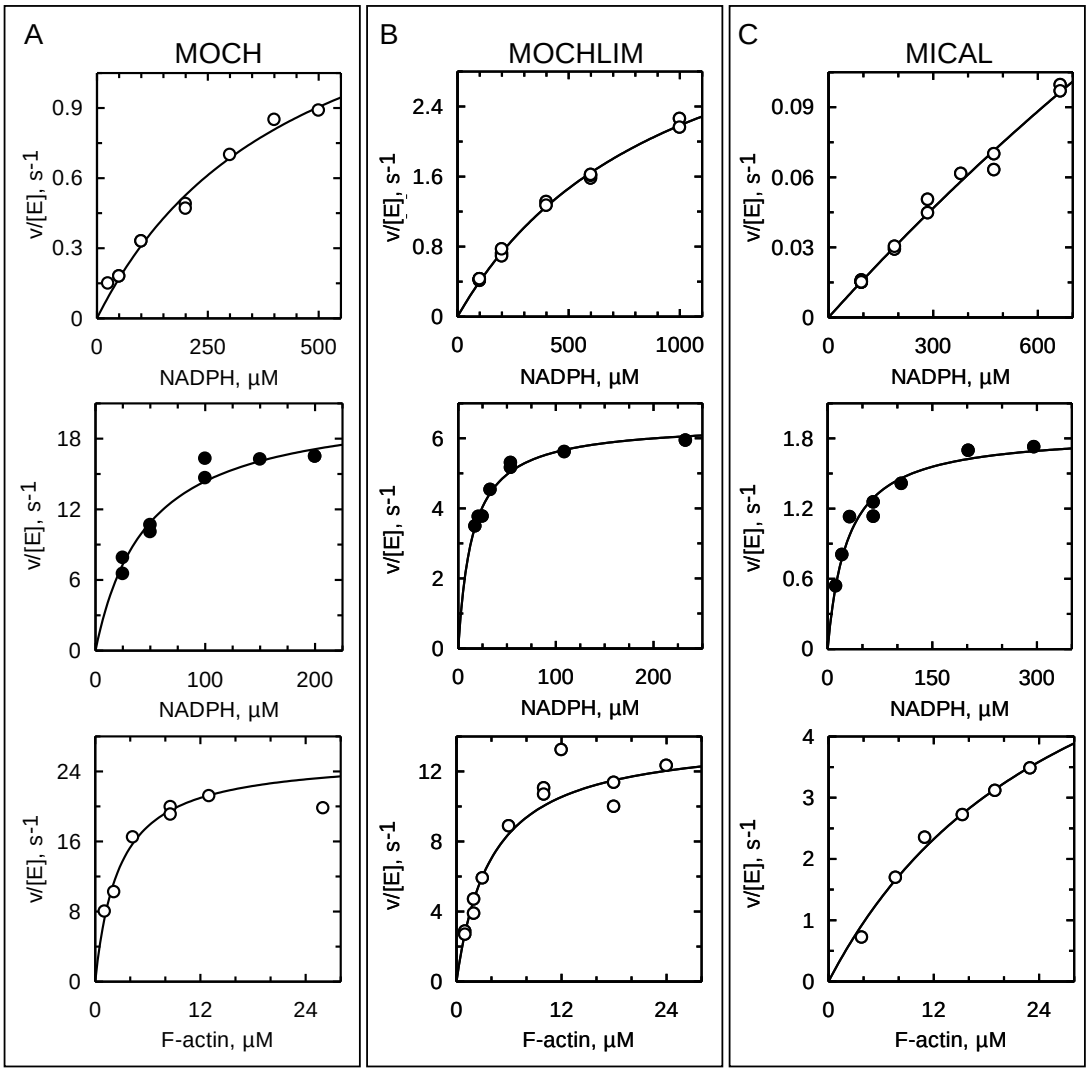

Figure 7.12. Determination of the steady-state kinetic parameters of the NADPH oxidation reaction catalyzed by human MICAL1 forms in the absence and presence of F-actin. The initial velocity of the NADPH oxidation catalyzed by MOCH (panel A), MOCHLIM (panel B) and full-length MICAL (panel C) was measured in F-buffer in the absence (upper panels) and in the presence of 4 µM F-actin (middle panels) by varying NADPH concentration. The v/E values were also measured in the presence of 200 µM NADPH and by varying F-actin concentration (lower panels). The curves are the best fit of the data to the Michaelis-Menten equation (Eq 2). The calculated values of the kinetic parameters are indicated in Table 7.2.

Table 7.2. Steady-state kinetic parameters of the NADPH oxidative reaction in the presence of F-actin catalyzed by MICAL1 forms. Assays were carried out at 25°C in F-buffer in the absence or presence of the indicated concentrations or concentration ranges of F-actin and NADPH. The apparent k_{cat} and K_m values for the varied substrate and their associated errors were determined by fitting the data to the Michaelis-Menten equation (Eq. 1). The error associated with the calculated k_{cat}/K_m values was calculated according to Bevington et al., 1969.

Protein, nM	*NADPH, μM*	*F-actin, μM*	k_{cat}, s^{-1}	K_m, μM	k_{cat}/K_m, $s^{-1}mM^{-1}$
MO, 120[a]	10-300	-	2.6 ± 0.4	555 ± 118	4.6 ± 1.2
MO, 20[a]	10-300	2.4	12 ± 0.5	11.3 ± 2.7	1090 ± 260
MO, 20[a]	300	7 - 35	20 ± 1.0	4.7 ± 1.0	4149 ± 908
MOCH, 190	10-500	-	1.7 ± 0.1	459 ± 66	3.8 ± 0.6
MOCH, 3	10-200	4.2	21 ± 1.2	50 ± 8	423 ± 72
MOCH, 3	200	1 - 26	26 ± 1.2	2.7 ± 0.4	9487 ± 1468
MOCHLIM, 125	25-1000	-	4.3 ± 0.2	966 ± 66	4.5 ± 0.4
MOCHLIM, 12	20-200	4.4	6.4 ± 0.2	14 ± 1.6	448 ± 52
MOCHLIM, 12	200	2-24	15 ± 0.6	4.4 ± 0.5	3390 ± 378
MICAL, 1250	100-700	-	0.8 ± 0.5[b]	4652 ± 3202[b]	0.17 ± 0.15[b]
MICAL, 91	10-400	4.3	1.9 ± 0.1	29 ± 5	64.8 ± 12.2
MICAL, 91	200	3.8-23	7.8 ± 1.2	29 ± 7	276 ± 87

[a]Data from Zucchini et al., 2011; [b]the parameters are poorly defined due to the high K_m value for NADPH.

7.5. Determination of the chemical modifications of actin introduced by the NADPH oxidation reaction catalyzed by human MICAL1 forms

In the presence of F-actin all MICAL forms consumed all the NADPH present at a rate that was higher than that measured in the absence of F-actin. This result was in contrast with the proposal of a specific modification of Met44 and/or Met47 residue through hydroxylation (Hung et al., 2014; Lee et al., 2014); that predicted a fast consumption of 2 molecules of NADPH per mol of actin present. Thus, it was important to determine the extent of actin oxidation during this reaction with each one of the proteins. Toward this goal, actin samples treated with human MICAL forms were prepared to determine (i) the mass of the actin monomer and (ii) the modified residues, in comparison with control actin samples. The mass spectrometry analyses were carried out in the laboratory of Prof. Tedeschi (Dipartimento di Scienze Veterinarie e Sanità Publica, Università degli Studi di Milano).

To prevent non-specific modifications of actin residues due to H_2O_2 production by the NADPH oxidase activity of free MICAL forms, catalase (0.83 μg/ml) was added in the reaction mixture in addition to DTT already present in F-buffer. Aliquots of F-actin solution that had been incubated with NADPH and MICAL forms at concentration suitable to bring the reaction to completion in less than 1 h were additionated with 10 volumes of cold acetone:methanol (8:1) to precipitate the proteins. The dried protein pellets were kept at -20°C until analyses. We also prepared several control samples of G- and F-actin that had been incubated on ice or at 25°C in the presence/absence of NADPH for times similar to those of the samples incubated with NADPH and MICAL forms.

Actin samples and samples of actin treated with MICAL forms in the presence of NADPH, were analyzed by MALDI-TOF (at least two independent measurements per sample) to determine the mass of the protein.

G-actin sample treated with MOCH (600 nM; Figure 7.13, panel A) showed an increase of mass (Δmass) of 16 Da with respect to the untreated sample (Table 7.3, Figure 7.14 panel A) consistently with the introduction of one atom of oxygen in each actin monomer that, in this case, was due only to the NADPH oxidase H_2O_2-producing activity of MOCH. Instead, F-actin samples incubated with 100 or 200 μM NADPH and MO, MOCH, MOCHLIM and MICAL (Figure 7.13, panels B-H) until >90% of the NADPH had been oxidized, showed a similar Δmass of 30-48 Da compared to the control actin sample indicating the addition of 2-3 atoms of oxygen per actin monomer (Table 7.3, Figure 7.14, panels B-D). Interestingly, F-actin sample that had been incubated with NADPH and MOCH for a time corresponding to only 20-30 μM NADPH oxidation showed modification levels below detection. This observation would rule out that in the early reaction phase the enzyme acts as a Met monooxygenase and later as an oxidase. Analysis of peptides obtained by tryptic digestion follwed by mass spectrometry showed tha actin Met44 and Met47 were modified along several other Met and Trp residues (Table 7.4). Although aromatic residues could be substrates of a monooxygenase reaction of MICAL-MO, especially in the light of similarity with PHBH, it seems unlikely that the enzyme is equally able to modify Met and Trp residues. Rather, the modification of several residues would suggest that actin modification by MICAL is indirect and depends on *in situ* NADPH-dependent H_2O_2-production.

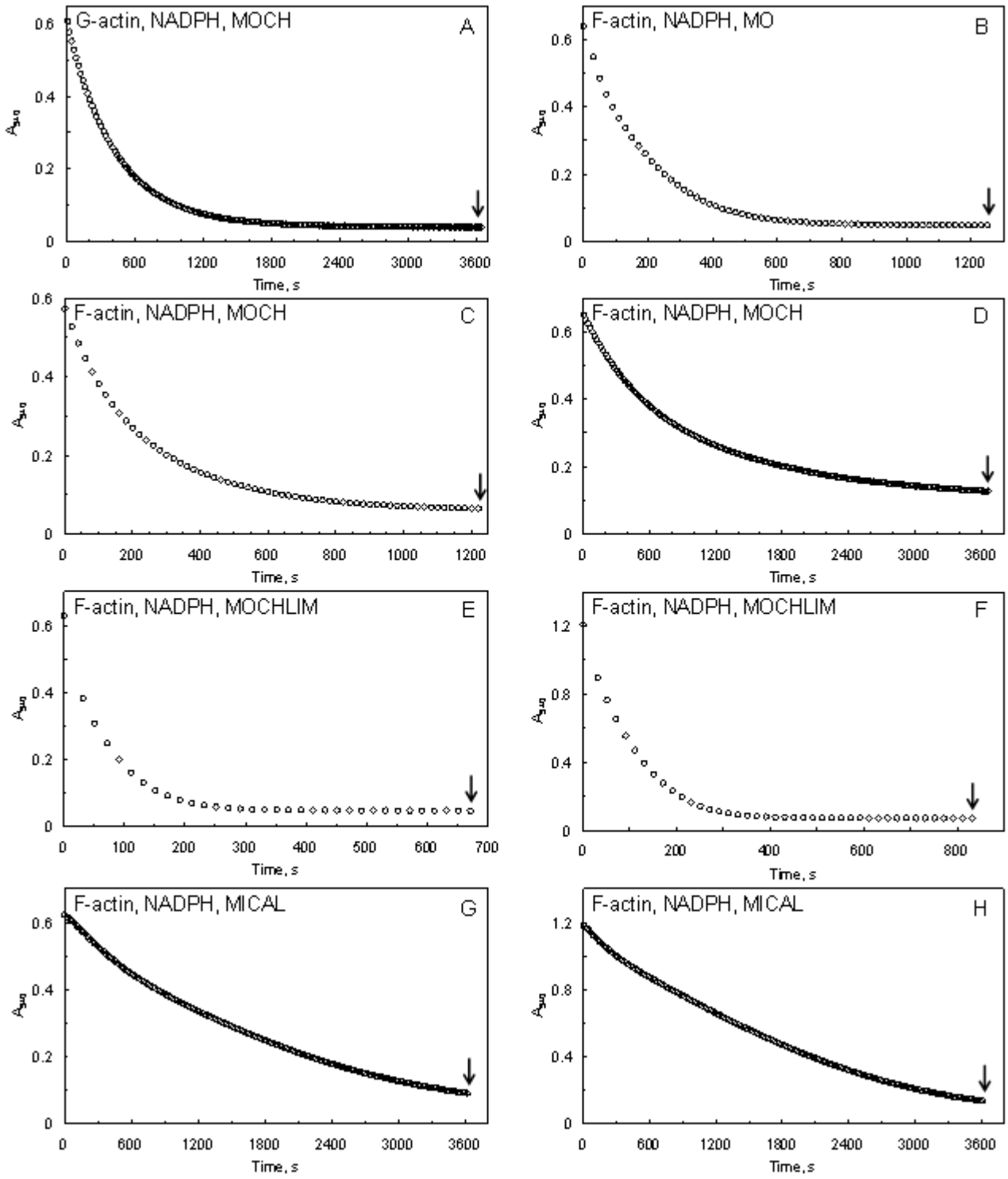

Figure 7.13. Time-course inspection of the NADPH oxidation of F-actin samples treated with human MICAL1 forms form their analysis by mass spectrometry. G-actin solution (23 μM) was incubated with NADPH (100 μM) and MOCH (panel A). F-actin (23 μM) was incubated with 100 μM NADPH and MO (30 nM, panel B), MOCH (30 nM or 10 nM, panels C, D), MOCHLIM (115 nM, panel E) and MICAL (115 nM, panel G) or with 200 μM NADPH and MOCHLIM (115 nM, panel F) and MICAL (115 nM, panel H). The arrow indicates the time at which the reaction was blocked by adding acetone-methanol. F-actin samples treated with MICAL forms were used to determine the whole mass of actin by MALDI-TOF to compare with that of control actin sample. The results are indicated in Table 7.3.

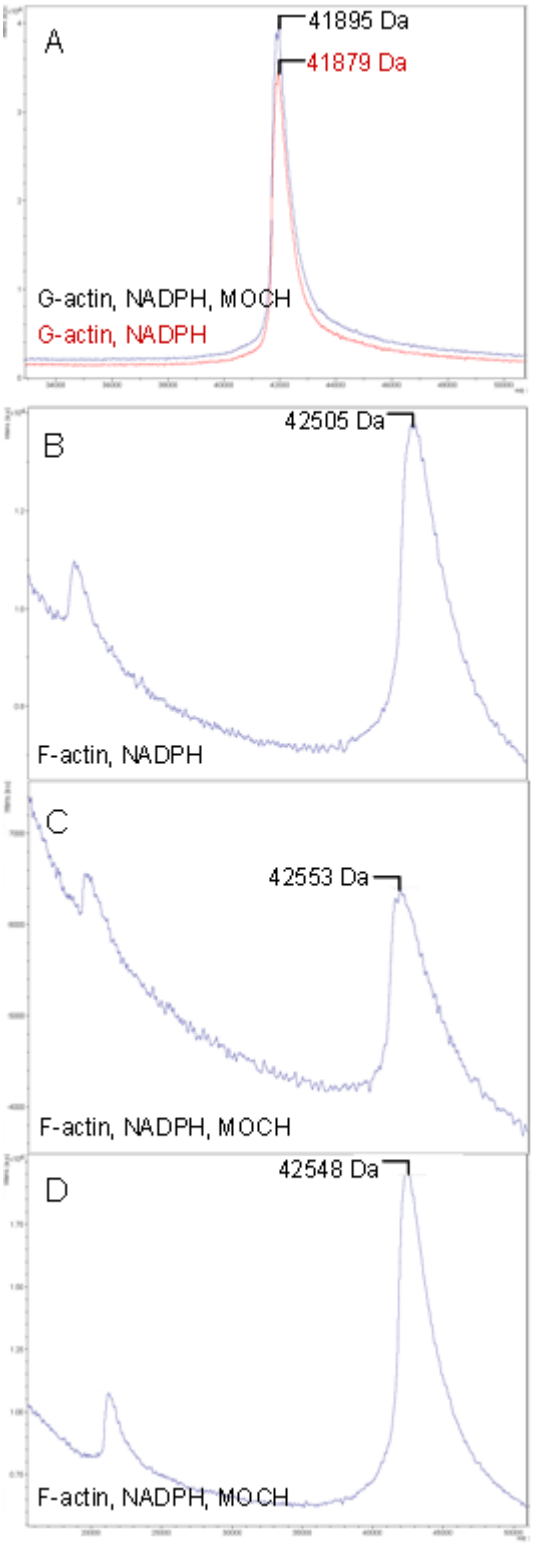

Figure 7.14. Mass spectra of G- and F-actin after incubation with NADPH and MOCH form of human MICAL1. Panel A: mass spectra of G-actin (red line) solution and that after incubation with MOCH (600 nM) and NADPH (100 μM; A_{340} changes are shown in Figure 7.13, panel A) are shown. The mass spectra of F-actin (20 μM) incubated with NADPH (100 μM) in the absence (panel B) and presence of MOCH (30 nM, panel C; 10 nM, panel D) are shown. The corresponding time-course of NADPH oxidation catalyzed by MOCH are shown in Figure 7.13, panels C and D. The observed mass of actin samples is indicated in Table 7.3.

Table 7.3. Summary of the mass of actin samples that had been treated with human MICAL1 forms, as determined by MALDI-TOF. F-actin samples that has been incubated with MICAL forms and NADPH in F-buffer additioned with catalase (1 mg/ml) for the indicated amounts of time were precipitated with cold methanol/acetone and subjected to mass determination by MALDI-TOF (at least two independent measurement per sample). The mass change (ΔMass) was calculated with respect to the mass of F-actin samples that had been incubated in the absence of MICAL forms (in bold). Note that the actin batch used for Experiment 1 is different from that used for the other two experiments.

Experiment	*Protein nM*	*Actin µM*	*NADPH µM*	*Time min*	*Reaction %*	*Mass Da*	*ΔMass Da*	*Oxidations*
1	-	(G-) 23	100	-	N/A	41879	-	
	MOCH, 600	(G-) 23	100	60	95	41894	15	1
1	-	**(F-)23**	**100**	**20**	**N/A**	**42505**	**-**	**-**
	MOCH, 30	(F-) 23	98	20	90	42553	48	3
	MOCH, 10	(F-) 23	97	60	85	42548	43	3
2	-	**(F-) 23**	**100**	**10**	**N/A**	**41847**	**-**	**-**
	MO, 30	(F-) 23	100	20	96	41887	40	3
	MOCHLIM,120	(F-) 23	100	10	96	41889	42	3
	MICAL,120	(F-) 23	100	60	86	41887	40	3
3	-	**(F-) 23**	**190**	**13**	**N/A**	**41847**	-	-
	MOCHLIM, 120	(F-) 23	190	13	96	41879	32	2
	MICAL,240	(F-) 23	190	60	96	41880	33	2

Table 7.4. Identification of actin residues modified upon incubation with MICAL MO and MOCH forms. Aliquots of F-actin (25 µM) samples that had been incubated at 25°C with NADPH (85-200 µM) and MICAL MO (30 nM) or MOCH (10-20 nM) in F-buffer supplemented with catalase (1 mg/ml) for 10-60 min to reach 90-95% oxidation of NADPH were precipitated with methanol/acetone, digested with trypsin and analyzed by MALDI-TOF (at least two duplicates per sample). The peptide maps were independent from the protein form, NADPH concentration and incubation time and led to identify the indicated residues. The numbering is that of rabbit skeletal α-actin (UniProt code P68135, ACTS_RABIT, see below), so that Met46 and Met49 correspond to Met44 and Met47 discussed in the main text and in (Hung et al., 2011, 2013; Galkin et al., 2015).

Peptide sequence	*Residue*	*Δ mass*
$_{21}$AGFAGDDAPRAVFPSIVGRPRHQGV**M**VG**M**GQK$_{52}$	M46, M49	+32 (2ox)
$_{42}$HQGV**M**VG**M**GQK$_{52}$	M46,M49	+32 (2ox)
$_{259}$CPETLFQPSFIG**M**ESAGIHETTYNSI**M**K$_{286}$	M271 or M285	+16 (1ox)
$_{331}$IIAPPERKYSV**W**IGGSILASLSTFQQ**M**W ITK$_{361}$	M357 or W342 or W358	+16 (1ox)
$_{71}$YPIEHGIITN**W**DD**M**EKI**W**HHTFYNELR$_{97}$	M84 or W81 orW88	+32 (2ox)

Inspection of the location of the modified residues on actin filaments reveals how their modification may take place through such *in situ* H_2O_2 production with some (stereo)specificity.

F-actin consists of two interacting strands containing two-six subunits per turn. Thus it cannot be crystallized preventing its structural determination at the atomic level. Techniques such as cryo-electron microscopy (cryo-EM) and X-ray fiber diffraction have been the main tools available to study the structure of protein polymers like F-actin of which multiplicity of structural states and models have been proposed (Galkin et al., 2015). Recently, the development of direct electron detectors allows cryo-EM to reach near-atomic resolution (4.5 Å); such technique has been used to study the details of intra- and inter-molecular interactions of the actin filament (Galkin et al., 2015). *In vitro* polymorphism was observed in actin filaments, in agreement with the dynamic nature of the molecule and demonstrating that a unique model of its structure is not possible (Figure 7.15). Each actin strand in the filament is stabilized by longitudinal contacts between subdomains (SD) 3-4 and 2-1 of adjacent monomers; Asp241, Glu245, and Asp244 of the actin molecule interact with Thr324, Pro322, and Met325 of the monomer just above it, along the filament (Figure 7.16). The interface between SD2 of the lower subunit and SD1/3 of the upper subunit includes contacts between residues Met44:Tyr143, Met47:Phe352, Lys61:Ile167, Arg62:Asp288, and Ile64:Tyr166 (Figure 7.16). Lateral contacts between the strands involve two pairs of interacting residues in SD1 and SD4, namely: residues Lys113:Asp195 and Arg111:Thr194 (Figure 7.16). Met44 interacts with Tyr143 and the backbone of nitrogen of Met44 makes a hydrogen bond with Gly168 indicating that this residue is crucial for the stabilization of the filament. In addition, Met47 interacts with Phe352 stabilizing the D loop that is a highly flexible region of actin and its position and stabilization is critical for the maintenance of the integrity of the filament. Met44 and Met47 are in the proximity of Lys61, Arg62, Ile64, Lys113 residues that stabilize lateral interactions in the filament. The role and the position of Met44 and Met47 explain why F-actin depolymerization occurs upon their modification by MICAL. The other residues that have been found to be modified in F-actin treated with NADPH and MO and MOCH (Table 7.4) are located close or at the interface between actin monomers. Met283 and Met269 are in the proximity of residues Glu241, Asp244, Asp288, Thr324, Met325, which are involved in the stabilization of dimer units of filament actin through interactions with upper-lower monomer; Trp356 and Met355 are in the proximity of Phe352 that stabilizes D-loop (Figures 7.17 and 7.18).

The data are consistent with the work done with the Drosophila and mouse MICAL, for which the modification of Met44 and Met47 of actin that of several other residues was reported (Hung et al., Lee et al., 2013). We can speculate that MICAL may bind to F-actin with the MO domain at the interface between actin monomers. The interaction may activate the NADPH oxidase activity so that *in situ* release of H_2O_2 may lead to the modification of a limited number of residues. Met44 and Met47 may be located at a site that makes them especially vulnerable to H_2O_2 attack. The precise geometry of MICAL-MO/actin interaction may render the H_2O_2-mediated oxidation of these Met residues stereospecific to yield an enantiomeric excess of the R isomer. In this respect, experiments to test the interaction between MICAL forms and F-actin in the absence of NADPH are in progress to set the basis to determine precisely where the interaction between MICAL forms and F-actin takes place, e.g., by cryo-electron microscopy.

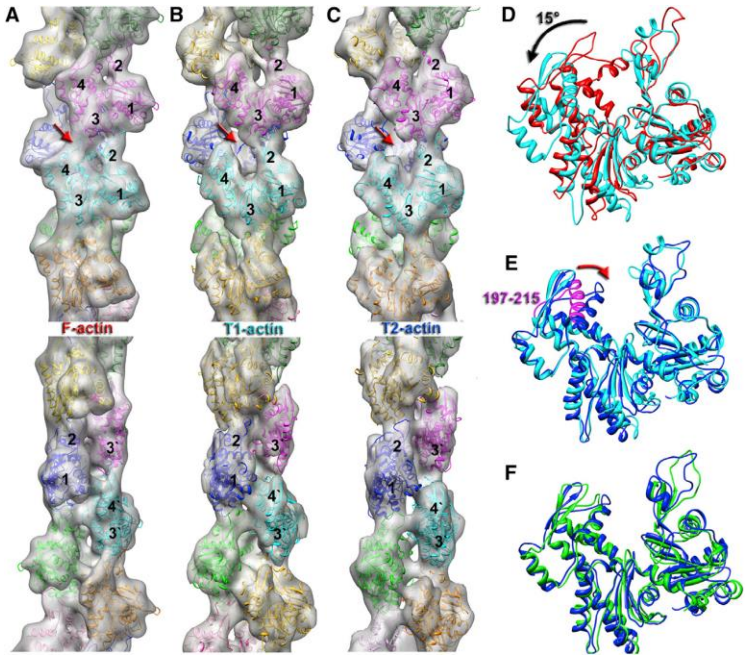

Figure 7.15. Comparison of Canonical F-Actin with T1-Actin and T2-Actin. Panels A-C: SD1–SD4 are labeled 1–4. The bottom are the same 3D reconstructions rotated by 90 degrees. Actin protomers are shown in different colors. All 3D reconstructions are filtered to 12 A ° resolution. Panel D: Transition from canonical actin (red) to T1-actin (cyan) involves a rotation of SD4/SD3 by 15° around the hinge region (black arrow). Panel E: Transition from T1-actin (cyan) to T2-actin (blue) mainly involves transition of the 197–215 region of SD4 (magenta) toward SD2 (red arrow).Panel F) Alignment of T2-protomer (blue) with the crystal structure of actin in the open state (Galkin et al., 2015).

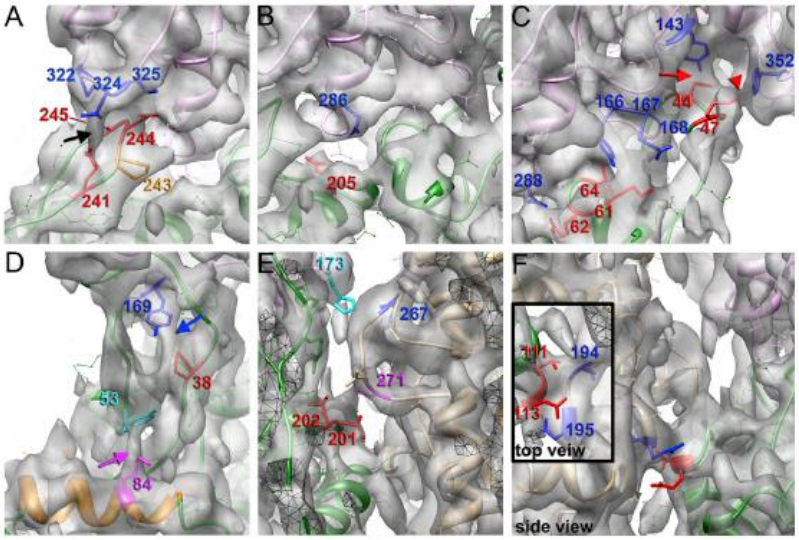

Figure 7.16. Interface between Actin Protomers in the Canonical Structural State of F-Actin .(A) Interface between SD3 and SD4. Residues in SD4 of the lower protomer are in red, while residues in SD3 of the upper protomer are in blue. Black arrow indicates a bridge of density between residues 241 and 324. Pro243 forms a kink in the top of the loop and is believed to position Asp241, and Asp244 is shown in orange. (B) Side chains of residues 205 (in red) and 286 (in blue) are seen in the map and are not involved in the SD3/SD4interactions. (C) Interface between SD2 of the lower protomer (red residues) and SD1/3 of the upper protomer (blue residues). Red arrow indicates a contact between residues 44:143, while the red arrowhead marks a contact between residues 47:352. (D) Pro38 (red) makes a bridge of density with Tyr169 in blue (blue arrow), while Tyr53 (cyan) makes an interaction with Lys84, which is in magenta (magenta arrow). (E) Hydrophobic plug does not make any strong specific interactions with protomers in the opposite strand. There are hydrogen bonds between Val201/Thr202 (in red) and Ser271 (in magenta), along with a hydrophobic interaction between His173 (in cyan) and Ile267 (in blue). (F) Lateral contacts between the two strands contain two pairs of interacting residues in SD1 are in blue, while residues in SD4 are in red (Galkin et al., 2015).

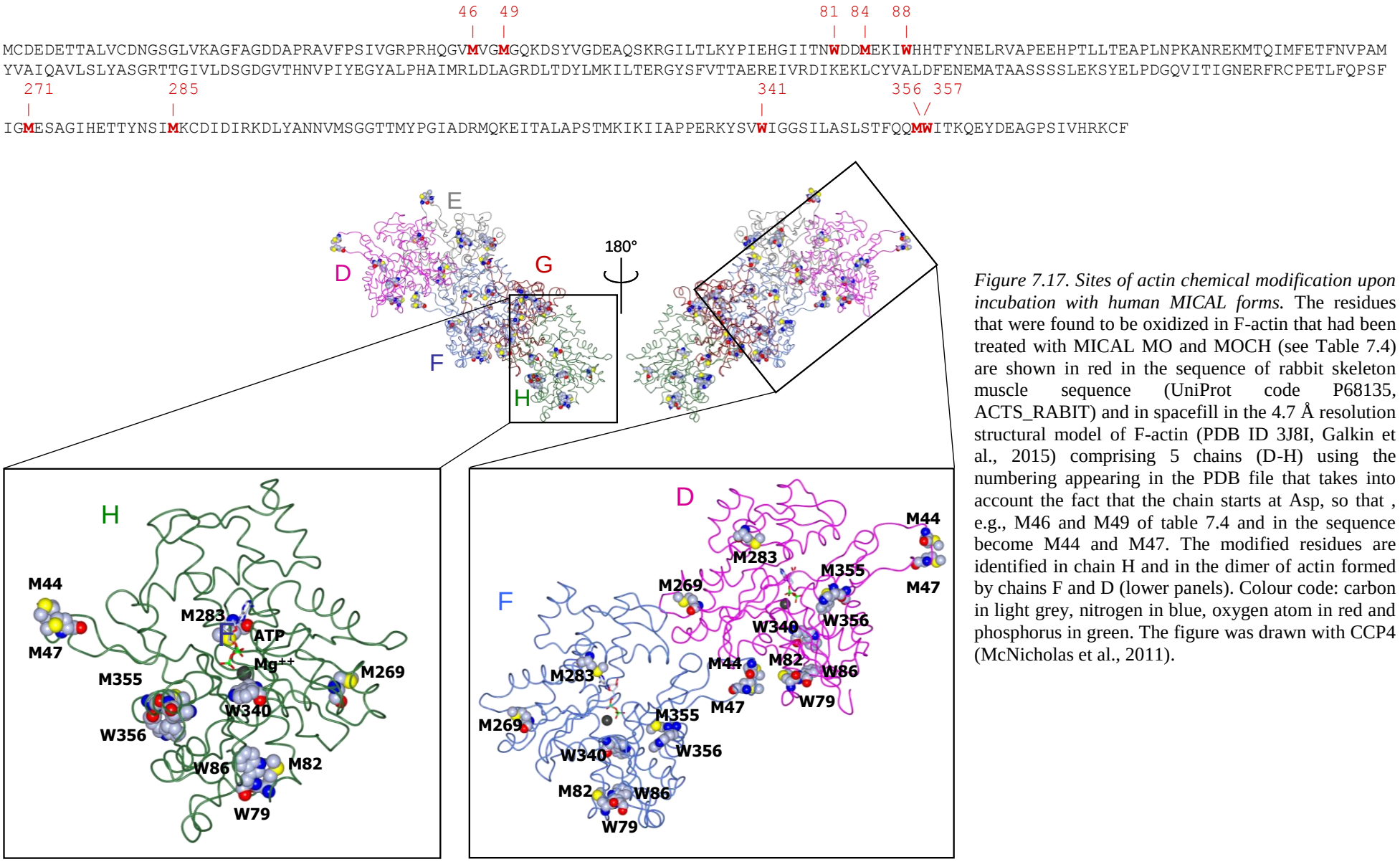

Figure 7.17. Sites of actin chemical modification upon incubation with human MICAL forms. The residues that were found to be oxidized in F-actin that had been treated with MICAL MO and MOCH (see Table 7.4) are shown in red in the sequence of rabbit skeleton muscle sequence (UniProt code P68135, ACTS_RABIT) and in spacefill in the 4.7 Å resolution structural model of F-actin (PDB ID 3J8I, Galkin et al., 2015) comprising 5 chains (D-H) using the numbering appearing in the PDB file that takes into account the fact that the chain starts at Asp, so that , e.g., M46 and M49 of table 7.4 and in the sequence become M44 and M47. The modified residues are identified in chain H and in the dimer of actin formed by chains F and D (lower panels). Colour code: carbon in light grey, nitrogen in blue, oxygen atom in red and phosphorus in green. The figure was drawn with CCP4 (McNicholas et al., 2011).

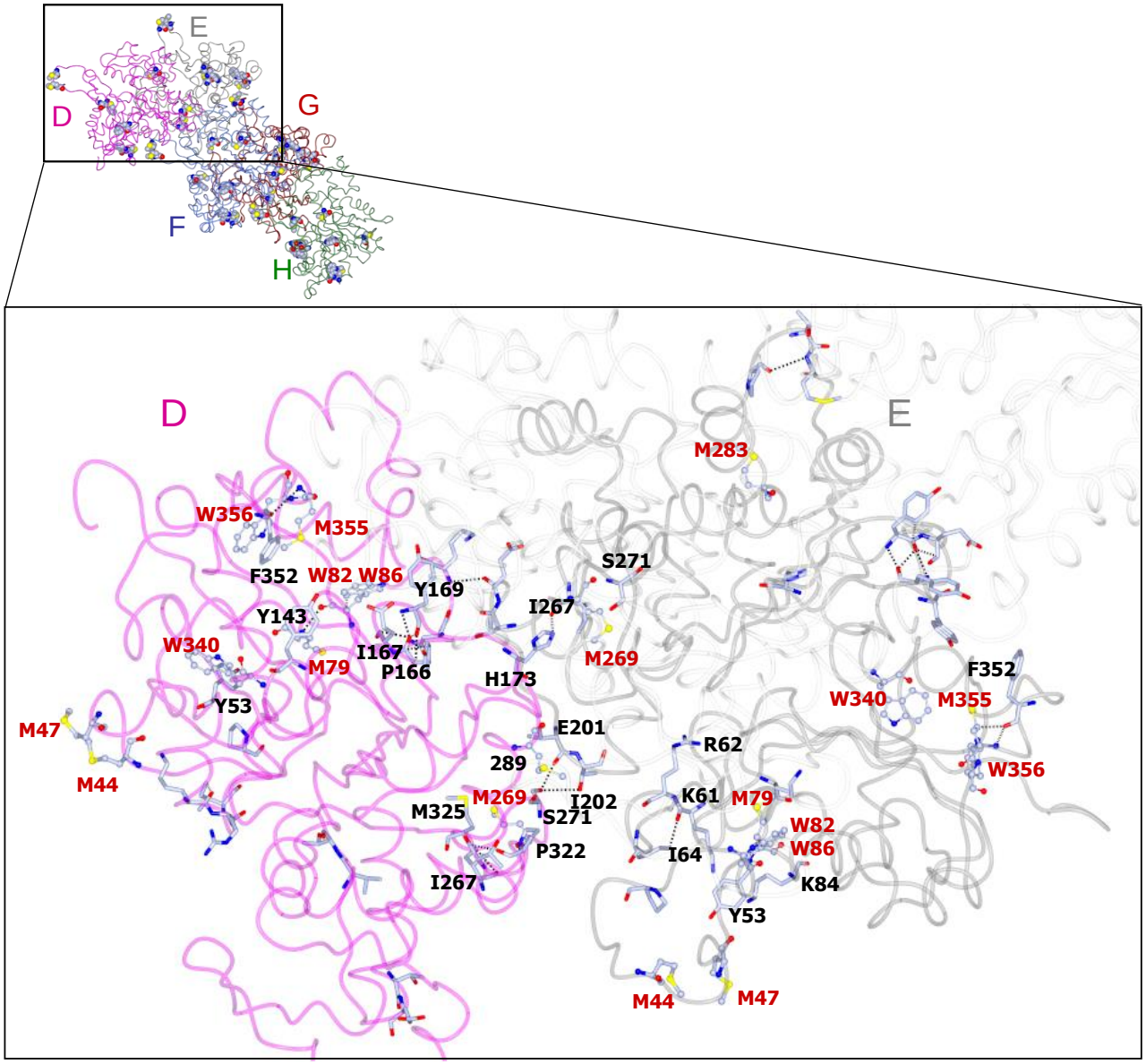

Figure 7.18. Sites of actin chemical modification upon incubation with human MICAL forms. The residues that were found to be oxidized in F-actin that had been treated with MICAL MO and MOCH (see Table 7.4) are in ball and sticks (red labels in lower panel) and residues important to the stabilization of the actin filaments (black labels) according to Galkin et al., 2015 are in sticks in the 4.7 Å resolution structural model of F-actin (PDB ID 3J8I, Galkin et al., 2015) comprising chains A and E using the numbering appearing in the PDB file that takes into account the fact that the chain starts at Asp, so that , e.g., M46 and M49 of table 7.4 and in the sequence become M44 and M47. The modified residues are identified in chain H and in the dimer of actin formed by chains F and D (lower panels). Colour code: carbon in light grey, nitrogen in blue, oxygen atom in red and phosphorus in green. The figure was drawn with CCP4 (McNicholas et al., 2011).

.

8. MICAL and CRMP

Collapsin Response Mediator Proteins (CRMP) form a family of cytoplasmic proteins, which participate in cytoskeleton dynamics by controlling the assembly of microtubules and actin filaments. It has been recently proposed that MICAL and CRMP proteins interact, and that such interactions link actin and microtubules dynamics in the cell (Schmidt et al., 2008).

In this chapter an overview of CRMP properties and functions is followed by a summary of the experimental evidence of MICAL-CRMP interactions and how these interactions may link the actin and microtubules cytoskeleton components. Then, the results of a series of preliminary experiments aimed to study the interaction of CRMP1 with human MICAL1 MO and MOCH and its effect on the catalytic properties of MICAL, will be presented.

8.1. Collapsin Response Mediator Proteins (CRMP)

CRMPs form a family of cytosolic phosphoproteins that are expressed mainly in the central nervous system, with some isoforms also expressed in peripheral nervous system (Schimdt et al., 2007). Chick CRMP-62 protein was isolated as a factor required for collapsin1-mediated signaling leading to growth cone collapse in dorsal ganglion neurons (Wang et al., 1997). Independently, and at approximately the same time, a number of CRMP genes were indentified in different species and they were named according to their method of discovery. CRMP proteins are also known as TOAD-64 (turned on after division), DRP (dihydopyirimidinase related protein), Ulip (unc33 like protein) and TUC (TOAD64/Ulip/CRMP) (Schimdt et al., 2007). In vertebrates 4 genes encode CRMP1, 2, 4 and 5 proteins, with CRMP4 sometimes called CRMP3 and CRMP5 also named "CRMP3-associated molecule" (Table 8.1). Drosophila has only one gene coding for CRMP. CRMP1-5 proteins show high protein sequence identity with each other (Figure 8.1, Table 8.1) and some isoforms of CRMP1, 2 and 4 have been found to derive from alternative splicing (Leung et al., 2002; Quinn et al., 2003). CRMP1-5 proteins show high sequence homology and structural similarity to dihydropyrimidinase (DHPase), which belongs to the family of metal-dependent aminohydrolases (Wang et al., 1997; Deo et al., 2004). However, CRMPs have no enzymatic activity, likely due to the absence of the crucial catalytic His residues of DHPase that coordinate the zinc ion in the active site (Deo et al., 2004).

A form of mouse CRMP1 lacking the first 7 residues was produced in *E.coli* cells and purified in order to subject it to crystallization experiments. During purification the protein underwent proteolytic removal of the last 60 residues so that crystals of CRMP1 8-490 form were obtained (Deo et al., 2004). In the crystal, each polypeptide chain folds in two domains and oligomerizes to yield a tetramer. The three-dimensional structure of full-length human CRMP2 and CRMP5 showed the same fold (Stenmark et al., 2007; Ponnusamy et al., 2013) as that of mouse CRMP1 (Figure 8.2). The asymmetric crystallographic unit of CRMP2 consisted of a homotetramer. However, the protein eluted from gel filtration with a mass of 150 kDa that corresponds to a trimer of 55 kDa monomers, indicating the presence of various oligomeric states (Stenmark et al., 2007). In both CRMP 2 and CRMP5 structures the C-terminal region was not visible, in the structure of CRMP5 10 extra residues were observed compared to CRMP1 and 2. Their

location indicated that the C-terminal region of CRMP does not have a secondary structure and is far away from the core of the protein supporting its role in stabilizing interactions among monomeric units rather than intramolecular interactions (Figure 8.2; Ponnusamy et al., 2013).

CRMP proteins are able to interact with each other to form heterotetramers when purified from brain (Wang et al., 1996). It has been proposed that the specificity of the hetero-oligomerization is driven by the different tendency of CRMP proteins to interact with each other, but *in vivo*, also by the spatio-temporal expression of CRMP1-5 protein. The formation of heterotetramers was also confirmed by co-immunoprecipitation of lysate of HEK293T cells expressing CRMP2 and CRMP3 (actually CRMP4) (Wang et al., 1997). CRMPs are most highly expressed during the neurogenic period of brain development and expression levels increased during axon cone growth. CRMP proteins are mainly found in the cytoplasm, but a significant fraction has been found associated with the cell membrane at the leading edge of the growth cone, in lamellipodia and filopodia, supporting a role in axon outgrowth and guidance, as well as cell migration and cell-cell contacts. Moreover, CRMP expression is induced after injury in both the central and peripheral nervous system (Schimdt et al., 2007). In this respect, it has been demonstrated that also CRMPs are involved in the control of cytoskeleton dynamics in response to the semaphorins signaling (Deo et al., 2004). COS7 cells expressing PlexA1 and NP1 (neuropilin 1) alone or in the presence of CRMP1-5 were incubated with Sema3A. The cells area of COS7 cells co-expressing PlexA1-NP1 and CRMPs decreased 10 min after of the addition of Sema3A, while 60 min were required when only PlexA1-NP1 were expressed (Deo et al., 2004). An interaction between PlexA1 and CRMP1-5 was observed in co-immunoprecipitation experiments, but direct complex formation between the purified proteins expressed in *E.coli* cells was not detected (Deo et al., 2004). Mutation of residues 49-56, which form the "activation loop" (shown in red in Figure 8.1 and 8.2) of the mouse CRMP1 resulted in a constitutively active protein that leads to cell contraction also in the absence of PlexA and/or Sema3A (Deo et al., 2004).

The activation of CRMP is also regulated by their phosphorylation state. It has been demonstrated that the phosphorylation of Ser522 by Cdk5 allows for the subsequent phosphorylation of CRMP2 and CRMP4 at Ser518, Thr509 and Thr514 by the serine/threonine kinase GSK3β (Glycogen sintase kinase 3-beta) (Zhang et al., 2008; Figure 8.1). The contractile effect exerted by CRMP in cells indicates that also CRMP has a functional role in the control of cytoskeleton dynamics in the semaphorin signaling pathway. In fact, CRMP2 induces microtubule assembly by binding to α- and β-tubulin heterodimers through residues 500-570 (double underlined sequence in Figure 8.1; Figure 8.3; Gu et al., 2000; Lin et al., 2008). However, this activity is abolished when Thr514 is phosphorylated by GSK3β kinase and also by Rho kinase suggesting that also other guidance cues may converge on this pathway (Lin et al., 2008). Other studies have shown that a pool of CRMP proteins colocalize with actin in growth cones (Khazaei et al., 2014). It is therefore possible that CRMP modulates changes in actin dynamics as well. However, CRMP may be linked to actin cytoskeleton by other proteins, like MICAL.

Table 8.1. Summary of CRMP sequences retrieved from databanks. The identification was done by taking into account annotations and direct sequence comparison. When several isoforms were present the putative full-length protein was selected. The comparison of the following sequences is shown in Figure 8.1 and was done using ClustalW (Goujon et al., 2010).

Protein	*Chromosome location*	*Organism*	*Protein synonym*	*Accession number*
CRMP1	4p16.1	*Homo sapiens*	dihydropyrimidinase-related protein 1 dihydropyrimidinase-like 1 unc-33-like phosphoprotein 3	NP_001304.1
CRMP1	5 B3; 5 19.96 cM	*Mus musculus*		NP_031791.3
CRMP1	14	*Rattus norvegicus*		Q62950.1
CRMP1	1	*Danio rerio*		NP_001018561.1
CRMP1	5	*Macaca mulatta*		NP_001253004.1
CRMP2	8p22-p21	*Homo sapiens*	dihydropyrimidinase-related protein 2 unc-33-like phosphoprotein 2	NP_001377.1
CRMP2	14 D1; 14 34.6 cM	*Mus musculus*	DRP-2 ULIP-2	NP_034085.2
CRMP2	15p12	*Rattus norvegicus*		NP_001099187.1
CRMP2	10	*Danio rerio*		NP_001018353.1
CRMP2	8	*Macaca mulatta*		EHH28366.1
CRMP4	10q26	*Homo sapiens*	dihydropyrimidinase-related protein 4 unc-33-like phosphoprotein 4 CRMP3 DRP-4 ULIP-4	NP_006417.2
CRMP4	7 (F4)	*Mus musculus*		NP_036123.3
CRMP4	1q41	*Rattus norvegicus*		NP_037065.1
CRMP4	21	*Danio rerio*		NP_001018348.1
CRMP5	2p23.3	*Homo sapiens*	dihydropyrimidinase-related protein 5 unc-33-like phosphoprotein 6 DRP-5 ULIP-6 CRMP3-associated molecule	NP_001240653.1
CRMP5	5 (B5)	*Mus musculus*		NP_075534.1
CRMP5	6q14	*Rattus norvegicus*		NP_075412.1
CRMP5	4	*Danio rerio*		AAX86822.1

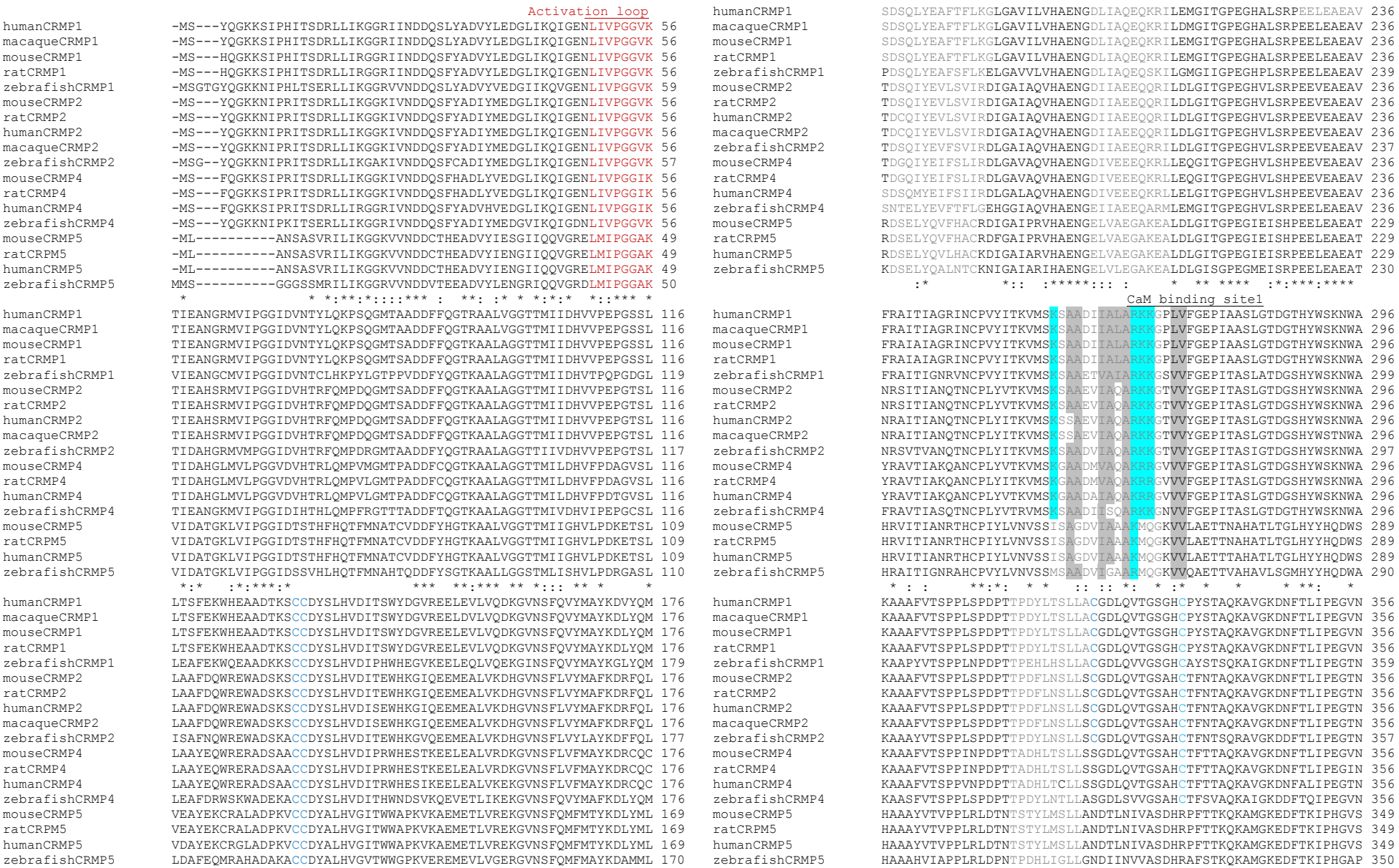
Activation loop
CaM binding site1
humanCRMP1
macaqueCRMP1
mouseCRMP1
ratCRMP1
zebrafishCRMP1
mouseCRMP2
ratCRMP2
humanCRMP2
macaqueCRMP2
zebrafishCRMP2
mouseCRMP4
ratCRMP4
humanCRMP4
zebrafishCRMP4
mouseCRMP5
ratCRPM5
humanCRMP5
zebrafishCRMP5

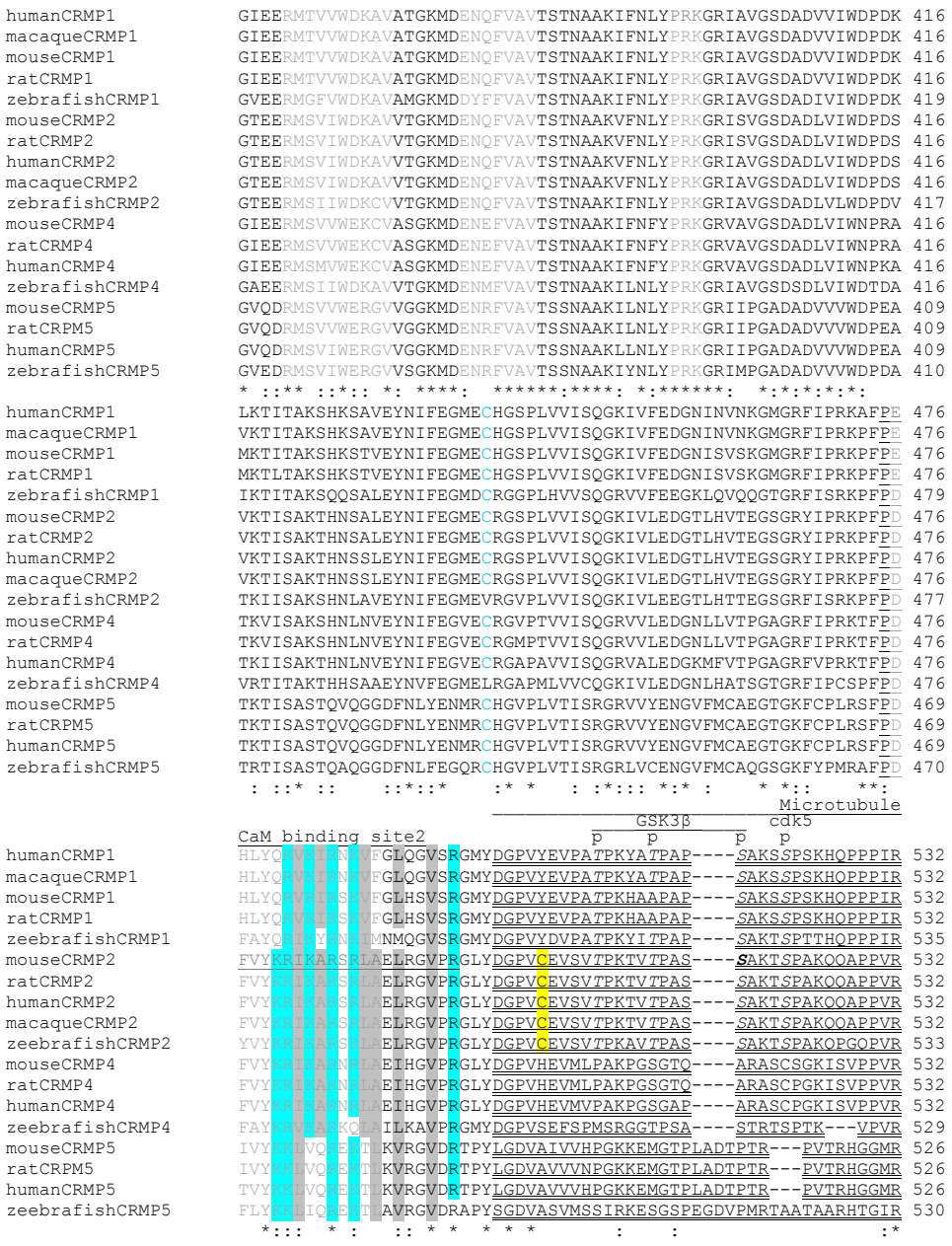

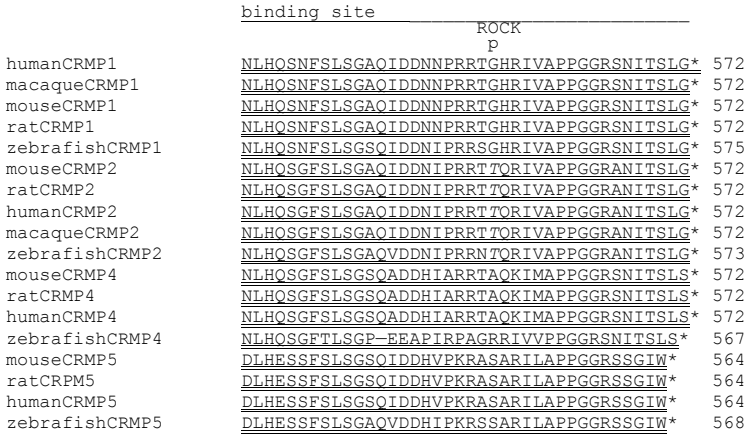

*Figure 8.1 Sequence comparison of CRMP1-5 forms.*The output reflects the degree of sequence similarity among the proteins. Sequence in red: activation loop (49-56 aa, Strittmatter et al., 2007); underlined sequence: putative CaM binding site: region rich in basic, (highlighted blue) and hydrophobic residues, (highlighted grey; 475-493 aa, Zhang et al., 2008); in bold and italic: residues undergoing phosphorylation (p, Thr509, 514, 555; Ser518, 522) with the specific GSK3ß,Cdk5 and ROCK kinases indicated (Zhang et al., 2008 and Lin et al.; 2011); double underlined sequence: Microtubule interaction domain (500-570 aa, Lin et al.,2011); in bold and grey are regions important to stabilize the tetramer (Deo et al., 2004); in bold and dark blue are Cys 132 and 133 exposed to solvent, in bold and blue are Cys 248, 323 and 439 at the interface region involved in tetramer stabilisation, in bold and light blue are Cys 334 and 439 not accessible to solvent; highlighted yellow Cys 504 in CRMP2, the putative Cys involved in thioredoxin interaction (Morinaka et al., 2011) that is absent in all the other CRMP isoforms. *, identical residues; :, conserved residues.

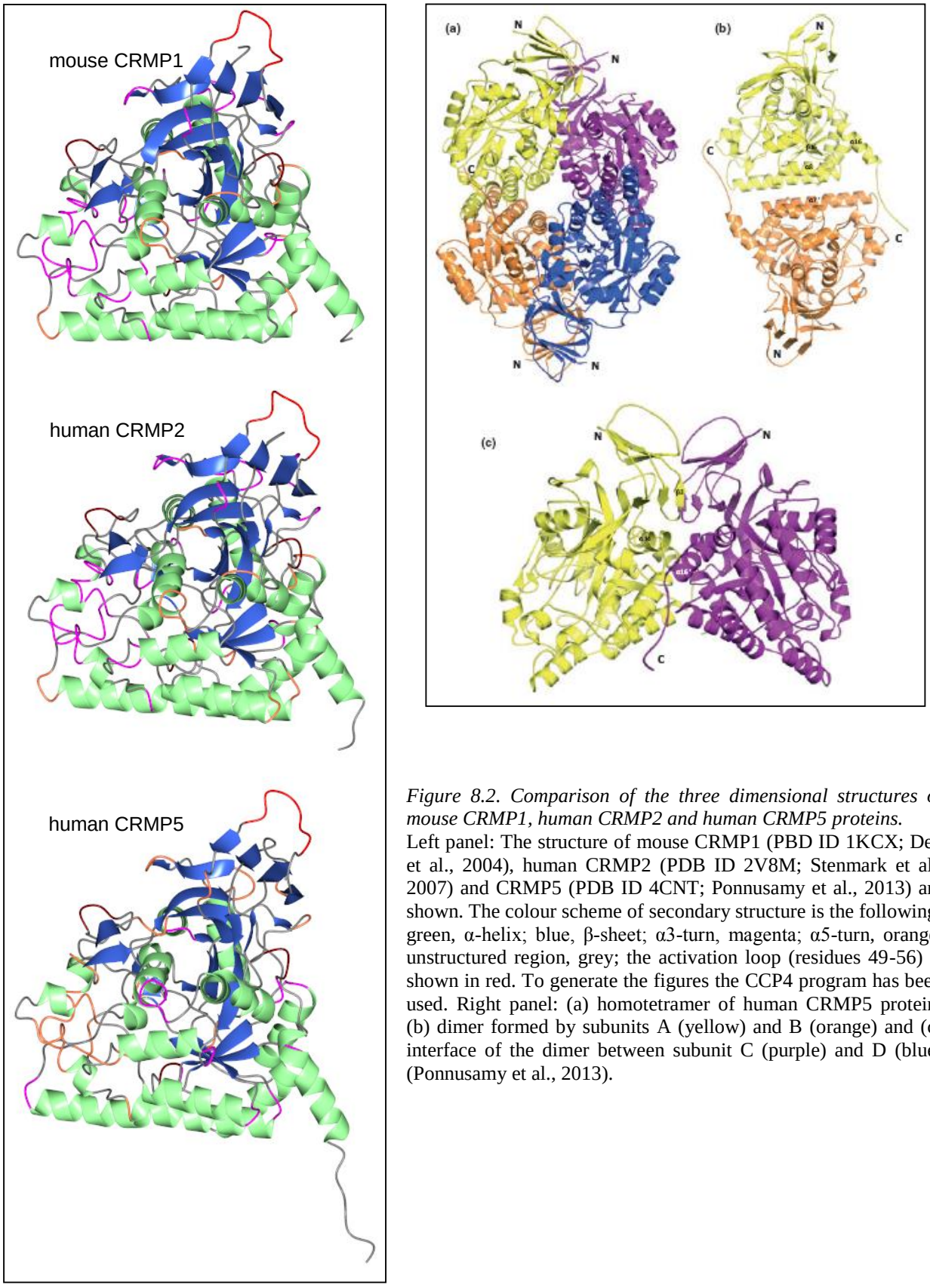

Figure 8.2. Comparison of the three dimensional structures of mouse CRMP1, human CRMP2 and human CRMP5 proteins.
Left panel: The structure of mouse CRMP1 (PBD ID 1KCX; Deo et al., 2004), human CRMP2 (PDB ID 2V8M; Stenmark et al., 2007) and CRMP5 (PDB ID 4CNT; Ponnusamy et al., 2013) are shown. The colour scheme of secondary structure is the following: green, α-helix; blue, β-sheet; α3-turn, magenta; α5-turn, orange; unstructured region, grey; the activation loop (residues 49-56) is shown in red. To generate the figures the CCP4 program has been used. Right panel: (a) homotetramer of human CRMP5 protein; (b) dimer formed by subunits A (yellow) and B (orange) and (c) interface of the dimer between subunit C (purple) and D (blue) (Ponnusamy et al., 2013).

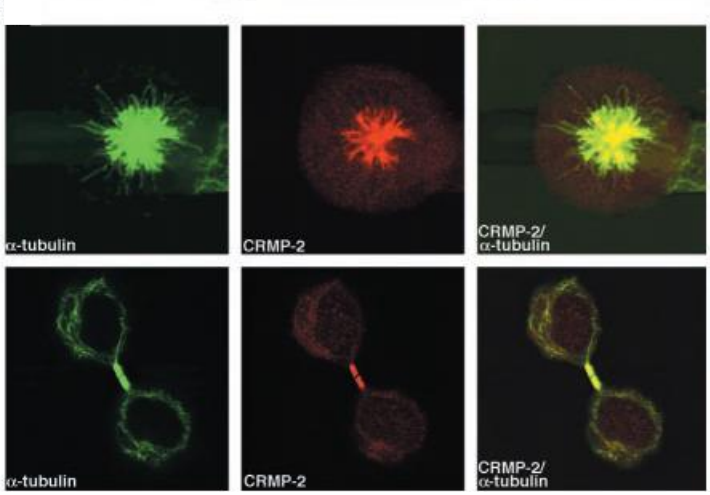

Figure 8.3 Distribution of CRMP-2 and cytoskeleton in N2a cells. Colocalization of CRMP-2 with microtubule bundles in the spindle at the metaphase (upper panel) and in the midbody at the late telophase (lower panel) in mitotic cells. Double labeling was performed with a monoclonal antibody to α-tubulin and a polyclonal antibody to CRMP-2, A667; the primary antibodies were detected with FITC-conjugated goat anti-mouse IgG (green) or rhodamine-conjugated donkey anti-rabbit IgG (red), respectively. Yellow indicates colocalization of CRMP-2 with α-tubulin (Gu et al., 2000).

As mentioned before, interaction between mouse MICAL1 and mouse CRMP1-5 was detected in HEK293T cell lysates coexpressing V5-CRMP and Myc-tagged MICAL1 (Schimdt et al., 2008; Figure 8.4, panel A). Lysates of HEK293T cells transfected with truncated forms of mouse MICAL1 were used to try to identify the region of MICAL responsible for the interaction with mouse CRMP1. In these experiments CRMP1 was found to interact only with the full-length MICAL and with the form comprising the MO, CH and LIM domain (MOCHLIM), although to a lesser extent (Figure 8.4, panel B; Schmidt et al., 2008). However, MICAL forms were expressed at different levels in COS7 cells either in the absence or presence of CRMP, as shown in Figure 8.4 (panel B). In particular, no production of the isolated MO domain was observed. These observations may explain the reason why the interaction with CRMP was observed only in lysates of cells expressing full-length MICAL and MOCHLIM form.

COS7 cells transfected with mouse CRMP1 and mouse MICAL1 showed a decrease of H_2O_2 production compared to the cells transfected only with MICAL1 (Figure 8.4, panel C). An increase of cell contraction was observed in COS7 cells containing MO, MOCH and MOCHLIM forms of MICAL1 and CRMP1/8-525 form compared to that of cells expressing only MICAL forms or CRMP1 (Figure 8.4, panel D and Figure 8.5, panels A and B; Schmidt et al., 2008). These results suggested that the coexpression of MICAL1 and CRMP1 leads to local cytoskeleton disassembly even in the absence of semaphorin-plexin interaction. Two mechanisms were proposed: (i) CRMP positively modulates the enzymatic activity of MICAL1 mimicking Sema/PlexA-dependent activation of MICAL1 or (ii) MICAL modifies CRMP through its activity promoting its phosphorylation and, therefore, microtubules disassembly (Schmidt et al., 2008). To distinguish between these hypotheses the H_2O_2 produced by the NADPH-dependent activity of MICAL was measured in lysates of cells that had expressed MICAL and or CRMP. Coexpression of mouse CRMP1 (residues 8-525) did not alter the activity of the mouse full-length MICAL1, while it decreased the activity of the MICAL form lacking the C-terminal region (MOCHLIM) (Figure 8.5, panel C). To independently verify these results, wild-type GST-CRMP (8-525) and the constitutively active form (mutated in the activation loop, CA CRMP) were added to lysates of cell expressing MICAL or MOCHLIM. A reduction of H_2O_2 production was observed for MOCHLIM in the presence of both wild-type and mutant forms of GST-CRMP (8-525) (Figure 8.5, panels D and E). These data would rule out that CRMP activates the NADPH oxidase activity of MICAL by producing H_2O_2 as a second messenger. The experimental observations could be explained by assuming that CRMP is a substrate of the monooxygenase reaction of MICAL1. In this case, the reaction would be the hydroxylation of CRMP and H_2O production rather than H_2O_2 production (Scheme 6.2).

These experiments also revealed a possible autoihnibitory function of the C-terminal region of MICAL (Schimdt et al., 2008). H_2O_2 was not detected in the lysates of HEK293T cells expressing full-length MICAL and MICAL form lacking the MO domain. On the contrary, MOCH and MOCHLIM forms incubated with NADPH were active (Schmidt et al., 2008), leading to the proposal that the C-terminal region inhibits the N-terminal MO domain of MICAL. To test this hypothesis, purified GST-fusion MICAL1 form comprising residues 761-1048 was added to lysates of cells expressing MOCH and MOCHLIM. The addition of the C-terminal region (1 μM) led to up to 75% decrease of the activity

(Schmidt et al., 2008) (Figure 8.6). The autoihnibitory function of the C-terminal region of MICAL1 was later confirmed also for the human protein (Giridharan et al., 2012; Chapter 1).

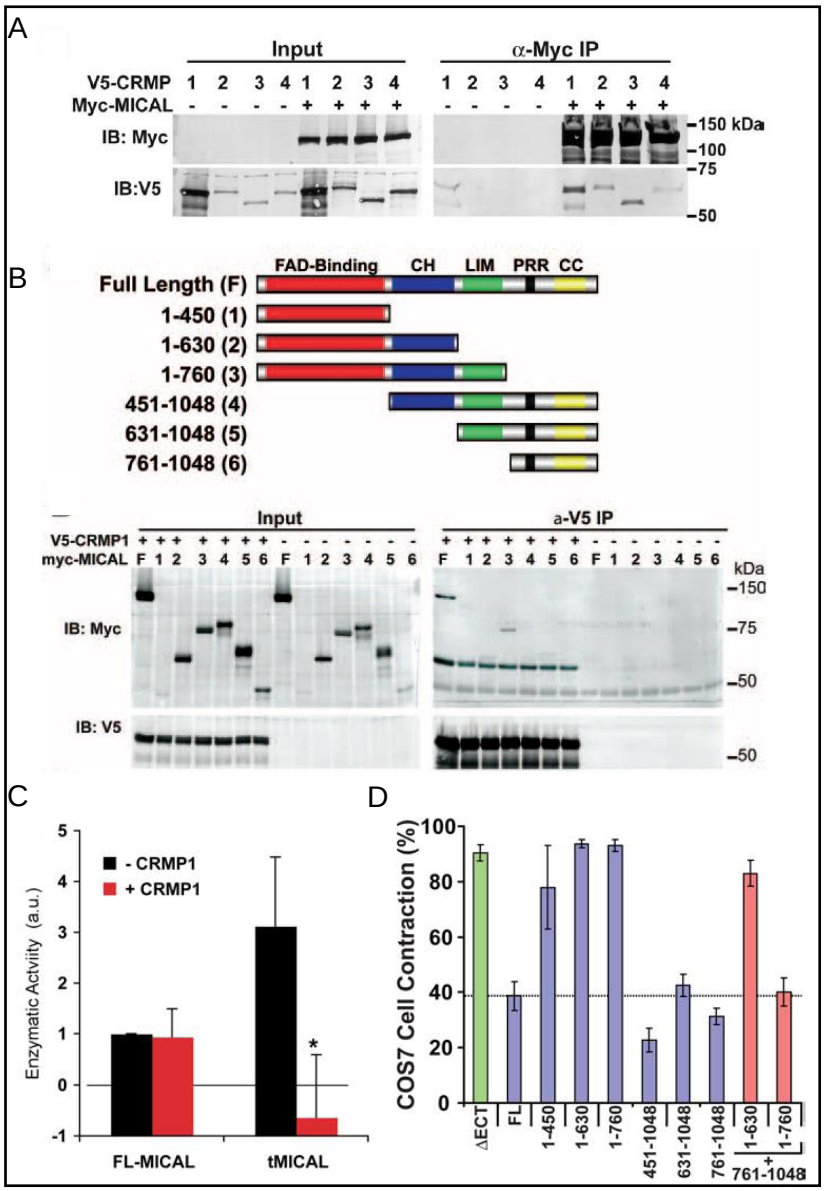

Figure 8.4. Interaction between human MICAL1 forms and CRMP proteins in HEK293T and COS7 cells. Panel A: HEK293T cells were co-transfected with plasmids encoding mouse Myc-MICAL1 and V5-CRMP1-4 proteins. Cell lysates were immunoprecipitated (IP) with anti-Myc antibodies, and Western blots were probed for Myc or V5 immunoreactivity. Panel B: Scheme of MICAL1 truncation mutants (tMICALs) with domains indicated. Lysates of HEK293T cells transfected with V5-CRMP1 and Myc-tagged full-length or truncated MICAL1 were immunoprecipitated (IP) with anti-V5 and after western blotting they were tested for anti-V5 or anti-Myc immunoreactivity. Panel C: H_2O_2 production from lysates of HEK293T cells cotransfected with indicated FL-MICAL, tMICAL 1–760, and CRMP1 expression vectors in the presence of 200 μM NADPH. Panel D: Quantification of contraction of COS7 cells transfected with the indicated truncated MICAL forms and constitutively active PlexA (ΔECT) (Schmidt et al., 2008).

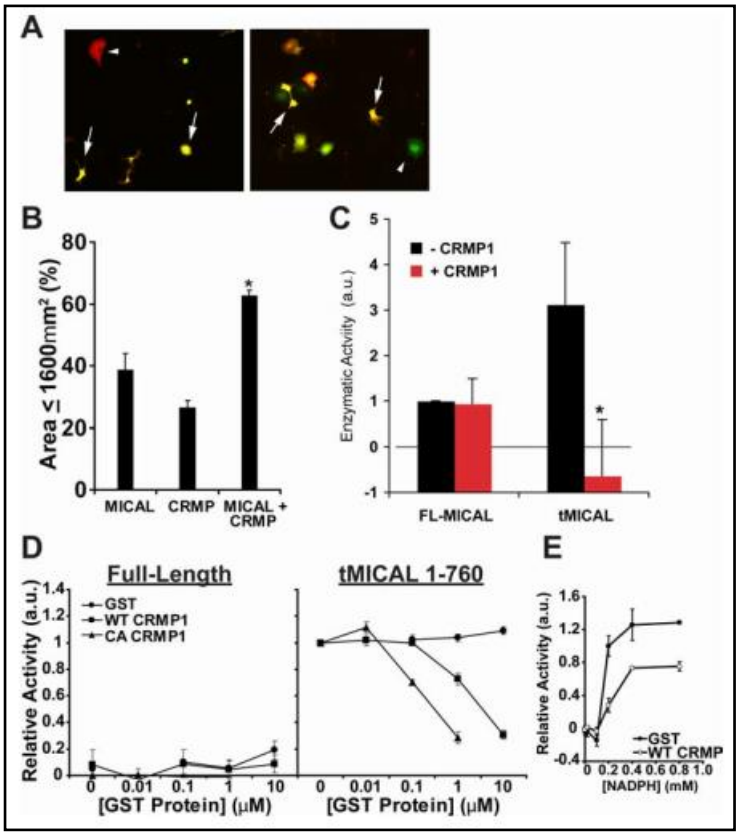

Figure 8.5. Effect of CRMP1-MICAL1 interaction. Panel A: COS7 cells cotransfected with V5-CRMP1 (green) and Myc-MICAL1 (red). Cells expressing either MICAL1 alone or CRMP1 alone appeared spread (arrowheads), whereas many of the cells expressing both proteins were contracted (arrows). Panel B: Quantification of contraction of cells from panel A. Sixty-one percent of the cells expressing both proteins were contracted. Panel C: H_2O_2 production from lysates of HEK293T cells cotransfected with the indicated FL-MICAL, tMICAL 1–760, and CRMP1 expression vectors in the presence of 200 μM NADPH (data are from 3 experiments; comparing with and without CRMP1). Panel D: Quantitation of the rate of H_2O_2 production by full-length and truncated 1-760 forms of MICAL in HEK293T lysates after the addition of purified wilde-type CRMP (WT CRMP1) or of the form mutated in the activation loop (CA CRMP1), which were added as GST-fusion proteins. Panel E: MICAL activity was measured in the presence of 1 μM GST or 1μ M mouse GST-WT CRMP1 at various NADPH concentrations (Schmidt et al., 2008).

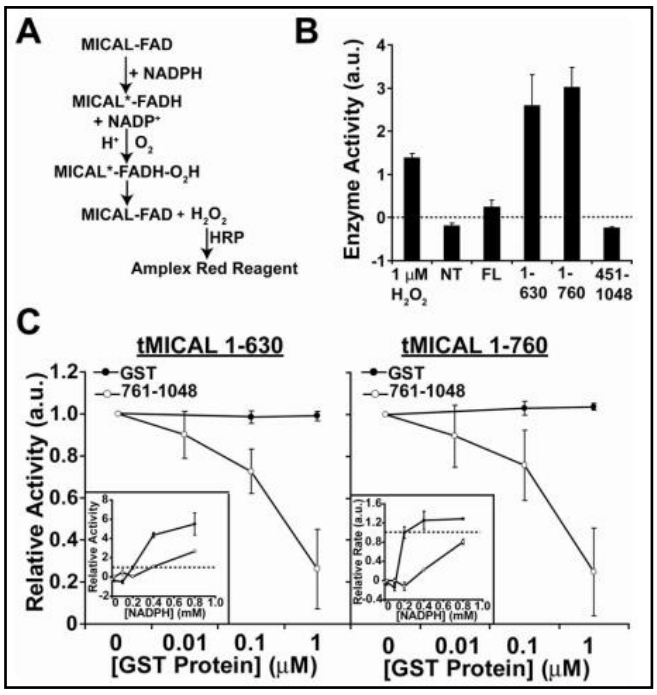

Figure 8.6. Activity of MICAL1 forms expressed in HEK293T cells. Panel A: flow chart depicting the assay used by Schmidt et al., (2008). H_2O_2 production is measured by the Amplex Red Peroxidase assay (Nadella et al., 2005). Panel B: Measurement of H_2O_2 production from lysates of HEK293T cells untransfected (NT) or transfected with the indicated MICAL constructs in the presence of 200 μM NADPH. H_2O_2 (1 μM) in reaction buffer was used to show the sensitivity of the assay. Panel C: Quantitation of the NADPH oxidase activity in cell lysates that had expressed tMICAL 1– 630 and 1–760 when increasing concentrations of GST-761–1048 form of MICAL1 were added. The addition of the MICAL C-terminal domain decreased the constitutive activity and shifted the concentration dependence for NADPH (insets) (Schmidt et al., 2008).

Independent experiments confirm a modulatory role of MICAL-CRMP interaction, linked to the H_2O_2-producing NADPH oxidase activity of MICAL1 (Morinaka et al., 2011). Morinaka and coworkers isolated a covalent CRMP2-TRX (thioredoxin) adduct due to the formation of a disulfide bond between TRX-Cys32 and CRMP-Cys504.

Starting from the observation that silencing CRMP2 in dorsal root ganglion neurons abolished growth cone collapse induced by Sema3A (Goshima et al., 1995), Morinaka et al. compared the effect of overexpressing the wilde-type and the C504S mutant of CRMP2 in COS7 cells. They concluded that Cys504 is required for the transduction of the signal upon semaphorin/plexin interaction, because the overexpression of CRMP2 C504S form suppressed the Sema3A-induced cone growth collapse (Morinaka et al., 2011). Cys504 is conserved in CRMP2 proteins, which is absent in the other CRMP forms (Figure 8.1). This is responsible for the stabilization of a disulfide-linked homodimer of CRMP2 and for the interaction with TRX. In fact, incubation of COS7 cells expressing CRMP2 with H_2O_2 led to the formation and stabilization of dimeric CRMP2. From the same cells CRMP2 was isolated by immunopurification and its incubation with TRX led to the disappearance of dimeric CRMP2 with the stabilization of the monomer (Morinaka et al., 2011). The homodimeric CRMP2 is the form that can be phosphorylated by serine/threonine kinase GSK3β preventing the interaction of CRMP2 with tubulin dimers and, thus, leading to microtubules disassembly. Morever, CRMP2 did not form the disulfide-linked homodimer in MICAL knockdown neurons in response to Sema3A stimulation (Morinaka et al., 2012). These observations led to the proposal that CRMP2 can be regulated by the H_2O_2-producing activity of MICAL stimulated by Sema3A leading to the activation of CRMP by phoshorylation (Figure 8.7; Morinaka et al., 2011). As a result CRMP2 would not longer promote microtubules assembly and thus, axon cone growth collapse would occur (Morinaka et al., 2011).

In a recent review that discusses the redox regulation of cytoskeleton dynamics (Gellert et al., 2014) the authors state that the proposed mechanism of control of the oxidation state of CRMP2 by the MICAL/TRX system is unlikely since they demonstrated that the transient mixed disulfide of TRX is not stable enough to serve as a signal due to the different pK_a values of Cys in the active site of the proteins (Gellert et al., 2013). Rather, they identified Grx2c (Glutaredoxin 2c) protein, which is necessary for axon outgrowth and embryonic development, as a CRMP2 partner.

Glutaredoxins are glutathione-dependent reductases, which reduce protein disulfides and can form reversible protein-GSH mixed disulfide. Neuroblastoma cells overexpressing Grx2c during differentiation showed 2-fold longer axons (Gellert et al., 2013). This observation indicated that Grx2c is essential for neuronal differentiation by controlling axonal outgrowth. In this process the dithiol reaction mechanism is required, in which at last one specific protein disulfide is reduced (Bräutigam et al., 2011). It has been also demonstrated that Grx2c controls axonal outgrowth via thiol redox regulation of CRMP2. In fact, knockdown of Grx2 in zebrafish led to a phenotype similar to that observed for a knockdown of CRMP2. However, a stable complex between Grx2c and CRMP2 was not detected leading to the proposal that redox regulation of CRMP2 could induce conformational changes with the consequent exposure of

phosphorylation sites of CRMP2 for its activation in response to semaphorins (Figure 8.8; Gellert et al., 2013).

All together these studies indicated that MICAL-CRMP interaction is important for the transduction of the signal initiated by the interaction between semaphorins and plexins to the control of cytoskeleton dynamics. However, the molecular mechanism that leads to the re-organization of cytoskeleton by MICAL-CRMP complex remains unclear.

Cellular studies carried out with CRMP1 demonstrated that MICAL1 and CRMP interacted and such interaction led to a decrease of the H_2O_2 produced by MICAL1 coupled to an increase of cell contraction (Schmidt et al., 2008). These observations led the proposal that CRMP could be the substrate of the monooxygenase activity of MICAL1 and this interaction mutually modulates the activity of MICAL1 and CRMP1. Thus, in this case MICAL1 exerts its function through a monooxygenase activity (Schmidt et al., 2008).

On the other hand, for CRMP2 it has been proposed that MICAL1 stabilizes the formation of disulfide-dimeric CRMP2, which can be phosphorylated preventing the assembly of microtubules (Morinaka et al., 2011). In this case it is the H_2O_2 produced by MICAL1 in response to semaphorin that modulates the CRMP2 activity. Thus, here MICAL1 would function as a NADPH oxidase (Morinaka et al., 2011).

It is evident that it was not clear if MICAL1 functions as a monooxygenase or as a oxidase to modulate the activity of CRMP proteins or if CRMP modulates MICAL1 activity in response to semaphorin/plexin interaction. Thus, in the effort to clarify and better understand the relation between MICAL and CRMP, we initiated a series of *in vitro* experiments with purified mouse CRMP1 and MO and MOCH forms of human MICAL1. In these experiments we first investigated the interaction between MO and CRMP1/8-525 form by Ni-NTA affinity chromatography. Then we studied the effect of CRMP on the rate of NADPH oxidation reaction catalyzed by MO and MOCH under several conditions. Finally, we also tested the effect of CRMP on the activity of MOCH when F-actin was present.

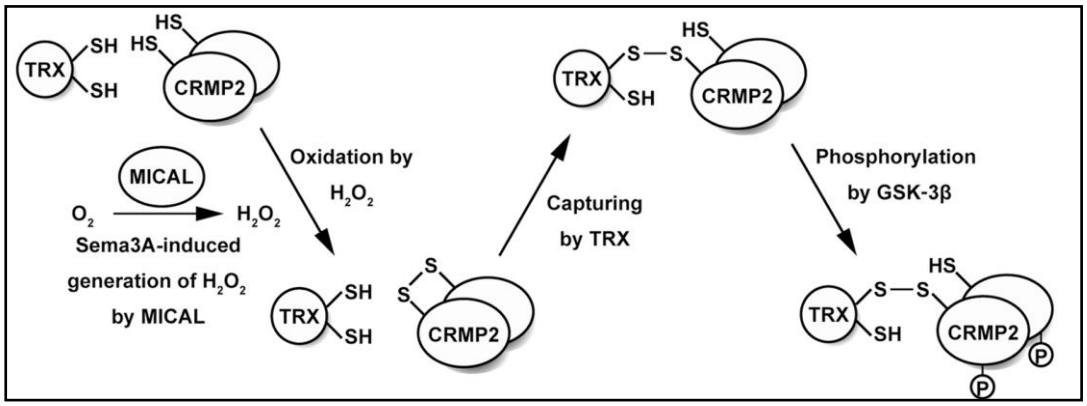

Figure 8.7 Model of thioredoxin(TRX)-mediated CRMP2 phosphorylation. After Sema3A stimulation, MICAL generates H_2O_2 at growth cones and oxidizes CRMP2 to form a disulfide-linked homodimer through Cys504. In turn, oxidized CRMP2 forms a disulfide complex with thioredoxin (capturing by TRX) and becomes preferentially phosphorylated by GSK-3, resulting in growth cone collapse (Morinaka et al., 2012)

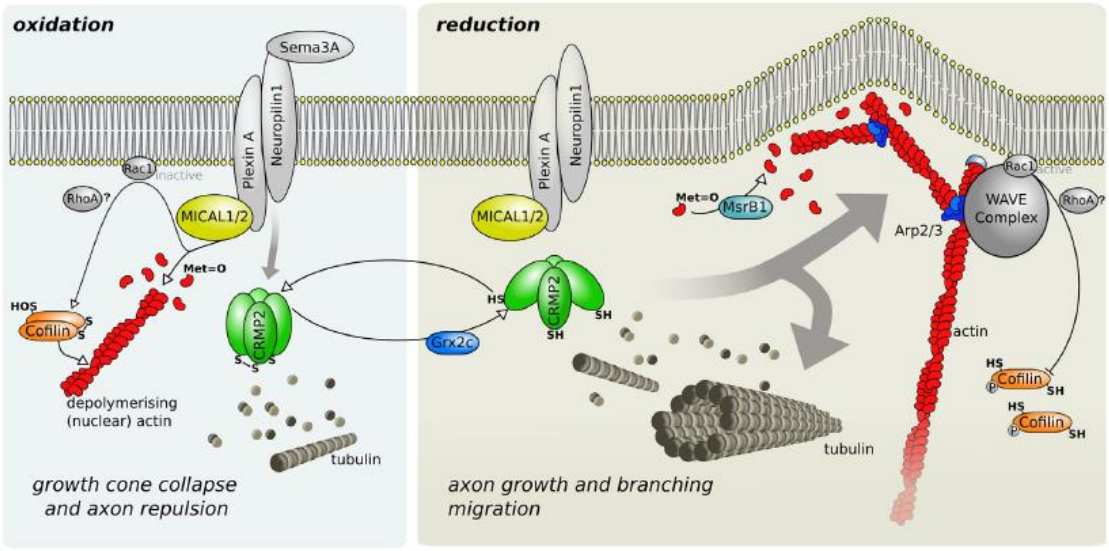

Figure 8.8 Redox switches in semaphorin signaling, cofilin, and actin dynamics. Sema3A binding to NP1 activates PlexA and the semaphorin signaling cascade. Activated PlexA interacts with MICAL1/2 that then leads to direct actin depolymerization or through cofilin activation. CRMP2 is another mediator of the Sema3A signalling cascade that induces growth cone collapse and axon repulsion (left side: 'oxidation').Without Sema3A binding, MICALs are not activated by the NP1/PlexA receptor. The reduction of CRMP2 by cytosolic Grx2 leads to a conformational change of the homo-tetramer. This conformational change causes (directly or indirectly) the polymerisation of actin and tubulin. MsrB1 is able to reduce the sulfoxides of methionyl residues of β-actin, allowing polymerisation. The WAVE complex is activated close to the membrane by active Rac1 and binds Arp2/3which leads to actin polymerisation and branching. Activated Rac1 also leads to the phosphorylation and therefore inactivation of cofilin. The absence of Sema3A and the resulting changes of the cytoskeletal dynamics lead to axon outgrowth and branching as well as enabling active migration (right side: 'reduction') (Gellert et al., 2014).

8.2. Expression and small- scale purification of mouse CRMP1 forms

The plasmids encoding various mouse CRMP1 forms have been received from Prof. S.M Strittmatter (Yale University, CN, USA); the constructs have been designed to generate mouse CRMP1 forms that differed for the presence or absence of the C-terminal 50 residues (disordered) region and the presence or absence of mutations in the "activation loop" at position 49-56 introducing the AAGAAGAA sequence leading to a constitutively active CRMP (CA-CRMP; Table 8.2). The plasmids were pGEX-derivatives for the expression of CRMP forms as GST-fusion proteins, with a prescission protease site to release CRMP from GST. The plasmids we received from Yale were transformed in *E.coli* DH5α cells, purified, analyzed by restriction digestion (not shown) and sequenced.

Table 8.2 . Summary of plasmid for the expression of mouse CRMP1 forms. The theoretical mass and pI values of the proteins was calculated with Mw/pI at www.expasy.ch

Plasmid	*Protein, residues*	*Theoretical mass, Da*	*pI*
EFS10	GST-mCRMP1 8-572 wt	88580	6.09
	mCRMP1 8-572 wt	62167	6.27
EFS11	GST-mCRMP1 8-572 mut 49-56 (CA-CRMP)	88357	6.03
	mCRMP1 8-572 mut 49-56 (CA-CRMP)	61944	6.17
EFS12	GST-mCRMP1 8-525 wt	84193	5.87
	mCRMP1 8-525 wt	57780	5.95
EFS13	GST-mCRMP1 8-525 mut 49-56 (CA-CRMP)	83281	5.76
	mCRMP1 8-525 mut 49-56 (CA-CRMP)	56868	5.77

They were used to transform *E.coli* BL21(DE3) cells for protein production by following the protocol received from Prof. Strittmatter with some modifications (see Materials and Methods, Chapter 10).

The SDS-PAGE analysis of extracts of cells harvested at different times after the addition of IPTG showed the expression of the proteins (Figure 8.9, panel A), but their apparent mass were lower than those expected for the different GST-fusion proteins (Table 8.2). The wild-type form lacking the C-terminal region (CRMP1/8-525) was produced at higher levels compared to the other forms (Figure 8.9, panel A).

To determine the integrity and quality of the expressed CRMP forms, their purification by affinity chromatography on a glutathione(GSH)-Sepharose resin was done on a small-scale from ≈2 g of these cells (Figure 8.9, panel B; Table 8.3) was set-up.

The protein bands that accumulated after IPTG induction (Figure 8.9, panel A), probably the GST-CRMP fusion proteins, bound to the resin and were found in the fractions eluted with 15 mM GSH (E1-3, Figure 8.9, panel B). However, their amounts and quality varied for the different CRMP forms. SDS-PAGE analysis of the fractions derived from cells that had expressed the longer wild-type form (8-575) showed the presence of two main bands of ≈75 kDa and ≈72 kDa (Figure 8.9, panel B) both lower than the expected value of 88.9 kDa (Table 8.2). Also the corresponding constitutively active mutant forms of

CRMP showed two bands with a mass lower than that expected for the intact fusion protein (Figure 8.9, panel B), suggesting a proteolytic degradation of the proteins that probably occurred at their C-terminal. Instead, the wild-type form lacking the C-terminal region (8-525) did not seem to be proteolitically degraded, although its mass was lower than the expected one (≈74 *vs* 84 kDa; Table 8.2). However, this form of CRMP was present in the highest amounts in the starting cells (Figure 8.9, panel B). The corresponding mutant form also seemed to be proteolytically degraded after purification and it was the form that could be purified at the lowest levels (Figure 8.9, panel B).

The fractions containing the full-length (8-575) and truncated wild-type CRMP (8-525) forms were pooled (fractions E1-3, Table 8.3), dialyzed overnight against 20 mM Hepes/NaOH buffer, pH 7.5, 100 mM NaCl (Schimdt et al., 2008) to remove GSH, and concentrated. At this stage, the full-length (8-575) form of CRMP was very sensitive to proteolysis as shown by SDS-PAGE of the sample after concentration, in which the bands of ≈75 kDa and ≈72 kDa had disappeared with the formation of species of ≈54 kDa and ≈26 kDa. On the contrary, the form comprising residues 8-525 was stable both during dialysis and concentration (Figure 8.9, panel C).

Thus, these preliminary results indicated that the C-terminal region of CRMP is sensitive to proteolysis leading to destabilization of the whole protein that undergoes further degradation. However, the removal of the last 50 residues is sufficient to obtain a stable form of CRMP fused with GST protein. The mutations leading to the constitutively active forms seem to make the protein very sensitive to proteolysis regardless of the presence of the C-terminal fragment. On the basis of these results we decided to focus on the most abundant 8-525 CRMP1 form, which is the form used to show quenching of H_2O_2 production by MOCH and MOCHLIM forms of mouse MICAL1 in cell extracts (Schmidt et al., 2008). An aliquot of the wild-type CRMP1/8-525 after GSH-Sepharose chromatography was incubated with prescission protease, which specifically cleaved the protein in the linker region between the protein of interest and GST, to release CRMP. In a preliminary experiment aliquots of the reaction mixture were withdrawn at different incubation times with the proteases, to monitor the extent of GST release by SDS-PAGE. As shown in Figure 8.10 the ≈75 kDa band of progressively disappeared with the accumulation of protein bands of ≈55 kDa and ≈27 kDa. Now the observed mass matched those expected for CRMP and GST. In particular, no bands with a lower mass were observed indicating the stability of the released GST and CRMP proteins (Figure 8.10). Interestingly, the calculated mass of CRMP (55.3 kDa) and GST (27.26 kDa) were now similar to the expected ones (57.7 and 26.4 kDa, respectively) (Figure 8.10). The sum of the molecular mass of the two proteins is 82.56 kDa, greater than the 75 kDa observed for the GST-CRMP before the cleavage of GST but similar to the expected mass of 84.19 kDa for GST-CRMP1/8-525 protein. Therefore the GST-CRMP1/8-525 protein had an anomalous electrophoretic behavior and the same may apply to the other CRMP forms.

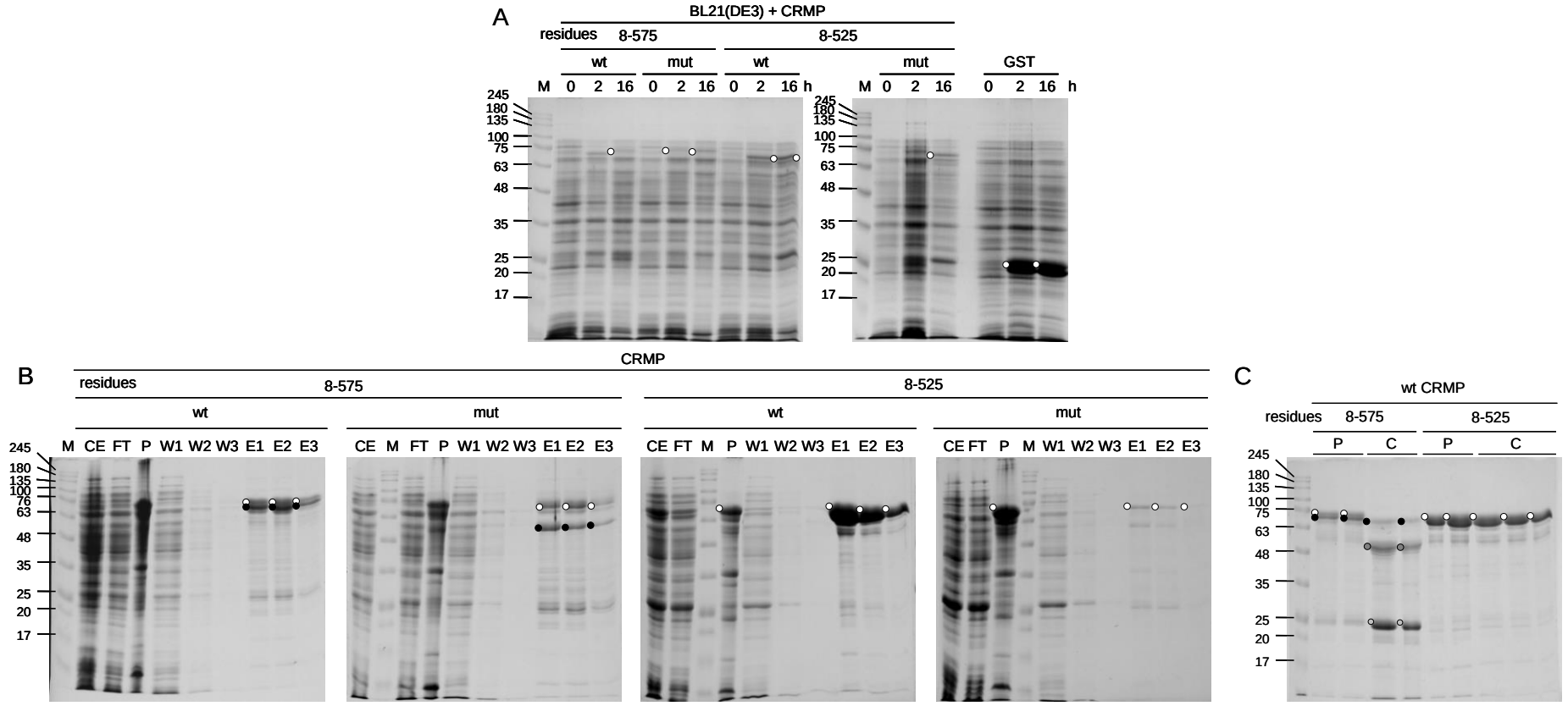

Figure 8.9. SDS-PAGE analysis of mouse CRMP1 forms expressed in E.coli BL21(DE3) cells and purified by glutathione-affinity chromatography. Panel A: Total cell extracts before (0 h) and after the addition of 1 mM IPTG (2, 16 h) to *E.coli* BL21(DE3) cells transformed with pGEX derivatives for the expression of GST-CRMP proteins. Panel B: GST-CRMP proteins were purified on GSH-Sepharose resin and eluted with 15 mM GSH; CE, crude extract; FT, unbound proteins; W1-3, weakly bound proteins removed by flowing lysis buffer; E1-3; fractions eluted with 15 mM GSH. Panel C: Fractions enriched in wild-type GST-CRMP (8-575 and 8-525) were pooled (P) and concentrated (C). ○, full-length GST-CRMP proteins; ●, truncated GST-CRMP proteins.

Table 8.3. Purification of the different mCRMP1 forms from 2 g of BL21(DE3) E.coli cells containing the different protein forms on Glutathione Sepharose4B affinity chromatography. Protein concentration was determined with the Bradford method.

Protein	*Sample*	*mg/ml*	*ml*	*mg*	*yield, %*
mCRMP1, 8-575 aa	Crude Extract	11.58	7.00	81.06	100.00
	E1	0.65	1.00	0.65	0.80
	E2	0.67	1.00	0.67	0.83
	E3	0.36	1.00	0.36	0.44
	Pool E1-E3	0.49	2.50	1.23	1.51
	After concentration	1.17	0.40	0.47	0.58
mCRMP1, 8-575 aa mut 49-56	Crude Extract	11.02	7.00	77.14	100.00
	E1	0.73	1.00	0.73	0.95
	E2	0.55	1.00	0.55	0.71
	E3	0.27	1.00	0.27	0.35
mCRMP1, 8-525 aa	Crude Extract	10.38	7.00	72.66	100.00
	E1	2.22	1.00	2.22	3.06
	E2	1.11	1.00	1.11	1.53
	E3	0.40	1.00	0.40	0.55
	Pool E1-E3	1.24	2.60	3.22	4.44
	After concentration	3.06	0.46	1.41	1.94
mCRMP1, 8-525 aa mut 49-56	Crude Extract	11.32	7.00	79.24	100.00
	E1	0.18	1.00	0.18	0.23
	E2	0.09	1.00	0.09	0.11
	E3	0.10	1.00	0.10	0.13

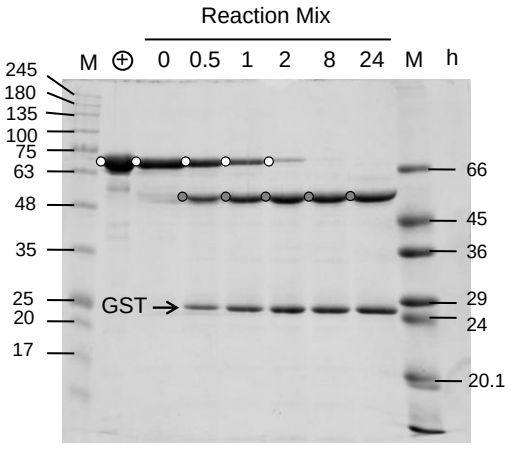

Figure 8.10. SDS-PAGE analysis of proteolytic cleavage of the GST-tag from the GST-CRMP1/8-525 protein. The GST-CRMP (8-525, ○, Figure 8.9, panel C) form was incubated with prescission protease at 4°C to separate GST (●) from CRMP (○); the reaction was monitored by SDS-PAGE of aliquots withdrawn at different times (0.5, 1, 2, 8 and 24 h).

8.3. Large-scale purification of the mouse CRMP1/8-525 form

In order to obtain amounts of CRMP1/8-525 sufficient for our planned experiments, 4 l cell cultures were set up.

The crude extract from 20-30 g of *E.coli* BL21(DE3) cells that had produced the GST-CRMP1/8-525 fusion protein was subjected to GSH-Sepharose affinity chromatography (Table 8.4) (Materials and Methods, Chapter 10).

The fractions were analyzed by SDS-PAGE (Figure 8.11, panel A) and determining the protein concentration with the Bradford method (Table 8.4). Fractions containing most of GST-CRMP (E1-E5) were pooled (Table 8.4) and dialyzed against Cleavage buffer (50 mM Tris/HCl, pH 7, 150 mM NaCl, 1 mM EDTA, 1 mM DTT) for 16-18 h at 4°C. At the end of the dialysis the sample (Table 8.4; Figure 8.11) was incubated overnight at 4°C with prescission protease (2 U/µl; 10 µl/mg of protein) to remove the GST protein. The reaction mixture was incubated with GSH-Sepharose to allow the binding to the resin of the released GST and residual uncleaved GST-CRMP. The cleavage and removal of GST from CRMP was complete (Figure 8.11, panel B). The fractions containing most of CRMP (fractions 1-2) were pooled, concentrated (Table 8.4) and dialyzed against 20 mM Hepes/KOH, pH 7.5, 300 mM NaCl, 10 % glycerol, 1 mM DTT (Stenmark et al., 2007). This buffer was used instead of 20 mM Hepes/NaOH, pH 7.5, 100 mM NaCl as indicated in Deo et al., 2004 because we observed that it leads to protein aggregation after dialysis and instability of CRMP preparations after freezing and thawing. The final CRMP solution (≈10 mg/ml) was stored in 0.25-0.5 ml aliquots at -80°C after flash freezing in liquid nitrogen. At this stage the CRMP preparation showed small amounts of contaminants as well as a fraction of aggregated protein that could be both removed by gel filtration on a Superose12 column.

Table 8.4. Large-scale purification of CRMP 8-525 form (CRMP) by glutathione affinity chromatography from 20 g of E.coli BL21(DE3) cells that had overexpressed the GST-CRMP fusion protein. The protein concentration was determined with the Bradford method.

Sample	*mg/ml*	*ml*	*mg*	*yield, %*
Crude extract	15.5	100	1550	100
E1	1.38	10.00	13.78	0.89
E2	1.16	10.00	11.63	0.75
E3	0.63	10.00	6.27	0.40
E4	0.66	1.00	0.66	0.04
E5	0.63	1.00	0.63	0.04
Pool E1-E5	1.15	30.00	34.38	2.22
After dialysis	1.02	30.00	30.69	1.98
After incubation with Prescission Protease				
Fractions 1-2 from GSH-Sepharose	0.51	40	20.5	1.32
After concentration	13.59	1.23	16.71	1.08
After dialysis	12.21	1.30	15.87	1.02

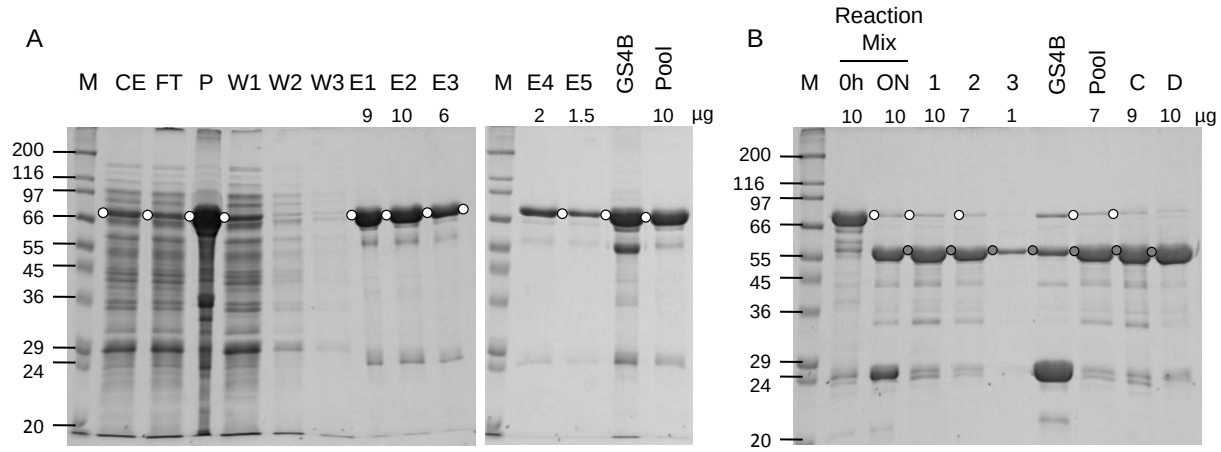

Figure 8.11. SDS-PAGE analysis of the large-scale purification of CRMP1/8-525 form by glutathione affinity chromatography. The crude extract from 20 g of *E.coli* BL21(DE3) cells containing GST-CRMP1/8-525 (GST-CRMP) was incubated with GSH-Sepharose resin and GST-CRMP was eluted 15 mM GSH. Panel A: CE, crude extract; FT, unbound proteins; P, pellet; W1-W3, proteins removed by flowing lysis buffer; E1-4, proteins eluted with 15 mM GSH; Pool, fractions E1-4 were pooled. Panel B: analysis of the proteolytic cleavage of the purified GST-CRMP before (0 h) and after incubation with prescission protease for 15 h (ON) at 4°C. At the end of the reaction, the sample was loaded on a GSH-Sepharose column. CRMP (○) was found in the initial wash (fractions 1-3), while GST (●) remained bound to the resin (GS4B). Fractions 1-2 were pooled (Pool), concentrated (C) and dialyzed (D).

Aliquots of CRMP were gel filtered in 20 mM Hepes/KOH buffer, pH 7, 25-100 mM NaCl or in F-buffer, prior each experiment to remove contaminating proteins and aggregates, but also for buffer exchange. An example of gel filtration of CRMP in 20 mM Hepes/KOH buffer, pH 7, 25 mM NaCl is shown (Figure 8.12; Table 8.5).

The fractions (0.5 ml) were analyzed by SDS-PAGE (Figure 8.12, panel B) and by dynamic light scattering (DLS). The protein concentration was determined with the Bradford method (Table 8.5). The elution profile showed the presence of a first peak with a low absorbance that eluted in the column void volume. This peak, containing aggregated CRMP (Figures 8.12, panel A), was followed by the main peak containing most of the protein (Figure 8.12, panel A). The final protein peak contained residual CRMP, but also contaminants and was discarded. Fractions 21-24 were pooled and concentrated (Figures 8.12, panel B; Table 8.5). The CRMP preparation was used for the experiments after storage for 15-18 h on ice at 4°C or was flash-frozen in liquid nitrogen and transferred at -80°C for later use.

DLS analysis of individual fractions from the Superose12 column and of the sample after concentration showed that CRMP is not monomeric (Figure 8.12, panel C; Table 8.5). The calculated radius of CRMP in solution was 5.1-5.6 nm, corresponding to a mass of 150-193 kDa, assuming a spherical particle. This calculated mass could correspond to that of a compact tetramer or of a non-spherical dimer. The latter conclusion would be consistent with the fact that CRMP forms an elongated dimer in the crystals (Figure 8.2).

A similar behavior was observed for CRMP gel filtered in 20 mM Hepes/KOH buffer, pH 7, 50 or 100 mM NaCl or in F-buffer no ATP.

Table 8.5. Size exclusion chromatography of CRMP on Superose12 column and determination of the apparent mass by DLS. CRMP1 was gel filtered on Superose12 column in 20 mM Hepes/KOH buffer, pH 7, 25 mM NaCl; protein concentration was determined with the Bradford method; DLS conditions; temperature, 15°C; sensitivity, 80%; solvent, NaCl 0.2%, pH, 7; concentration, 0.1-2.4 mg/ml. The mass of 57.78 for monomeric CRMP (8-525) was calculated as in Table 8.2.

Sample	*mg/ml*	*ml*	*mg*	*yield, %*	*R, nm*	*Calculated mass, kDa*	*Oligomeric state*
CRMP1/8-525	9.62	0.4	3.84	100.00	7.5	371	6.42
17	0.12	0.5	0.06	1.56	24	6154	106.50
21	0.2	0.5	0.1	2.60			
22	1.14	0.5	0.57	14.81	5.6	193	3.34
23	2.37	0.5	1.18	30.80	5.4	173	2.99
24	1.74	0.5	0.87	22.61	5.5	183	3.17
25	0.45	0.5	0.23	5.85	5.3	168	2.9
26	0.28	0.5	0.14	3.64	5	147	2.54
27	0.22	0.5	0.11	2.86	5.1	151	2.61
28	0.08	0.5	0.04	1.04			
Pool 21-24	1.28	1.6	2.04	53.22	5.5	185	3.20
after concentration	2.82	0.65	1.83	47.64	5.7	196	3.39

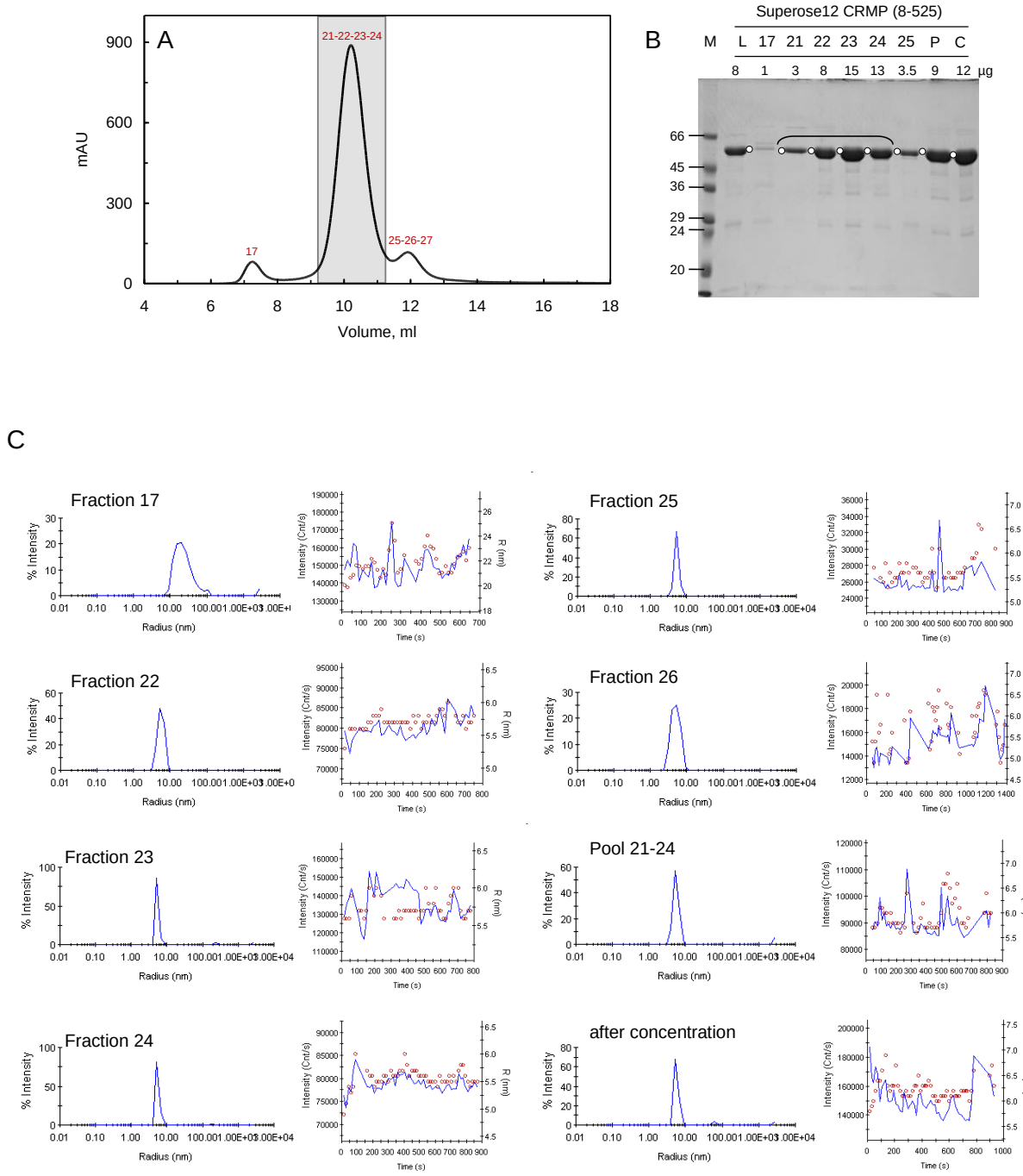

Figure 8.12. Size exclusion chromatography of CRMP1/8-525. An aliquot of CRMP solution (10 mg/ml) purified by GSH-Sepharose affinity chromatography was gel filtered on a Superose12 column connected to an FPLC apparatus in 20 mM Hepes/KOH buffer, pH 7, 25 mM NaCl. Panel A: elution profile of the chromatography obtained by monitoring A_{280}; fractions pooled are in the shaded area. Panel B: SDS-PAGE analysis of the sample loaded (L), of individual fractions (numbered as in panel A); fractions 21-24 were pooled (P) and concentrated (C). The amount of protein loaded in each lane, as calculated from the protein concentration determined with the Bradford method, is indicated. Panel C: DLS analysis of individual fractions from the Superose12 column, of the pooled fractions and after concentration. DLS conditions: temperature, 15°C; acquisition time, 15 s; sensitivity, 80%; solvent, NaCl 1%; pH, 7; concentration, 0.1-2.5 mg/ml. The calculated radius of the individual fractions and that of the pooled fractions before and after concentration and the corresponding mass is indicated in Table 8.5.

8.4. Study of the interaction between the isolated MO domain and CRMP 8-525 form by Ni-NTA affinity chromatography

Schimdt et al. (2008) demonstrated that CRMP1-5 interact with MICAL by co-immunoprecipitation experiments (Figure 8.4, panel A). Furthermore, it was shown that addition of CRMP/8-525 (as GST-fusion protein) to cell lysates expressing MOCHLIM form of mouse MICAL1 led to a rdecrease of H_2O_2 produced by MICAL NADPH-dependent activity, leading to the proposal that CRMP could be the substrate of the monooxygenase/hydroxylating activity of MICAL (Schmidt et al., 2008).

The absorption spectrum of flavoenzymes is very sensitive to changes in the FAD environment (Chapter 6), which may induced by bound ligand. Thus, we tested the effect of CRMP on the absorption spectrum of the MO form of human MICAL1.

Prior the addition of CRMP to MO solution, the absorption spectrum of the individual proteins was recorded (Figure 8.13, panels A and B). When a stoichiometric amount of CRMP was added to MO (18 μM) in 20 mM Hepes/KOH buffer, pH 7, the solution immediately became opalescent, indicating that the interaction between MO and CRMP caused protein aggregation. The addition of 100 mM NaCl to the sample was sufficient to remove the turbidity, suggesting that the interaction between MO and CRMP was probably due to their opposite charges at neutral pH (MO, pI 9; CRMP, pI 5), rather than to a specific interaction. The absorption spectra of MO before and after the addition of CRMP were similar to each other indicating that the interaction at this ionic strength is weak or that, MICAL-CRMP complex formation does not alter the FAD enviroment (Figure 8.13, panel C).

Next we tested the effect of CRMP on the absorption spectrum of MOCH that has a lower pI than MO (MOCH, pI 7.67) in 20 mM Hepes/KOH, buffer, pH 7, 100 mM NaCl. The lower positive charge of MOCH than MO at this pH should decrease non specific interactions.

CRMP was added at different final concentrations (1-20 μM) to a MOCH solution (17 μM). The absorption spectrum of MOCH did not significantly change during the titration (Figure 8.13, panel D). Only a small increase of absorbance was observed when CRMP was added to a final concentration >10 μM, maybe due to the formation of turbidity. Thus, specific and strong interaction between MO or MOCH and CRMP could not be readily detected with this approach.

CRMP-MICAL interaction was also tested by Ni-NTA Sepharose affinity chromatography by taking advantage of the presence of His_6-tag at the C-terminus of MO. A solution containing equimolar amounts of MO and CRMP was incubated with Ni-NTA Sepharose in 20 mM Hepes/KOH buffer, pH 7, 100 mM NaCl and proteins were eluted with increasing concentrations of imidazole (0-500 mM). Control samples using MO or CRMP alone were also carried through the same procedure.

CRMP was found to interact with the resin and started to elute by applying 40 mM imidazole both in the absence and presence of MO (Figure 8.14). MO eluted when imidazole concentration was increased from 80 to 500 mM. Thus, under these conditions we could not detect any interaction between MO and CRMP, probably due to the high ionic strength of the medium selected to prevent the non specific interaction observed in 20 mM Hepes/KOH buffer, pH 7 (see above).

Subsequently, the experimental set-up was modified to prevent the non specific binding of CRMP to Ni-NTA Sepharose by adding 20 mM imidazole and to promote the interaction between MO and CRMP. In this case, prior the addition of CRMP, the MO solution was incubated in batch with Ni-NTA Sepharose resin (1 ml) in 20 mM Hepes/KOH buffer, pH 7 to allow its binding to the resin in a random fashion, which should have prevented aggregation with CRMP at low ionic strength allowing for complex formation. As done for the previous experiment, control samples were set-up. The proteins were eluted by increasing NaCl concentration with addition of buffer containing 500 mM imidazole as final step.

As expected MO eluted by applying 500 mM imidazole (Figure 8.15). Most of CRMP was now present in the unbound fractions (Figure 8.15) and only a small amount of CRMP eluted with 500 mM NaCl and imidazole when MO was present (Figure 8.15).

These results suggested that the interaction between MO and CRMP is weak. However, it is possible that the CH, LIM and C-terminal regions of MICAL are required for formation of CRMP-MICAL complex. In this respect, experiments are in progress to test the interaction between CRMP and MOCH, MOCHLIM and full-length forms of MICAL.

The fact that MICAL-MO and CRMP do not form a tight complex does not rule out that they may transiently interact, as expected if CRMP is a MICAL substrate.

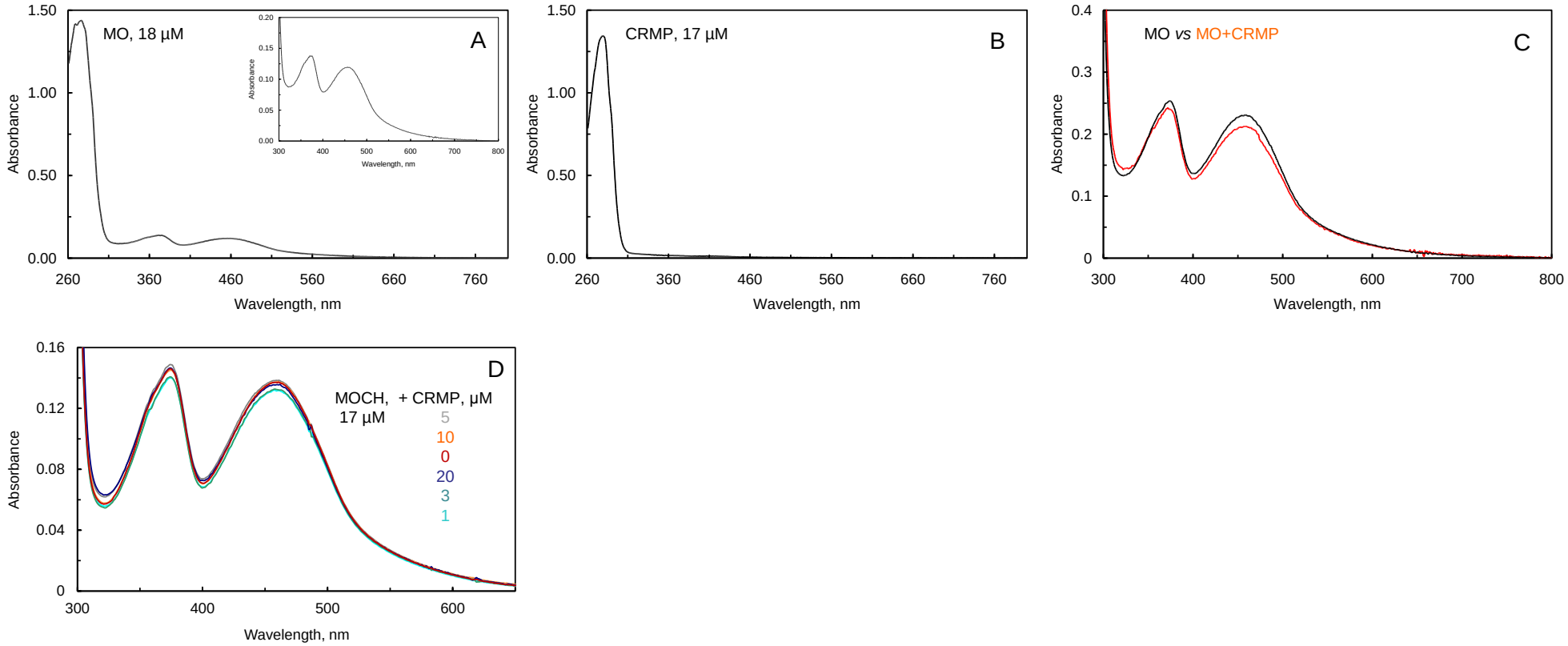

Figure 8.13. Studies of the CRMP1/8-525 interaction with MO and MOCH forms. The absorption spectra of MO (1 mg/ml, 18 µM, panel A) and CRMP (1 mg/ml, 17 µM, panel B) in 20 mM Hepes/KOH buffer, pH 7, 100 mM NaCl were recorded. In panel C the comparison of absorption spectrum of MO before (black line) and after the addition of CRMP (red line) is shown. The absorption spectrum of MOCH alone (red line, 17 µM) and after incubation with varying concentrations of CRMP (1, 3, 20, 5, 10 and 20 µM) in 20 mM Hepes/KOH buffer, pH 7, 100 mM NaCl at 17°C are shown in panel D.

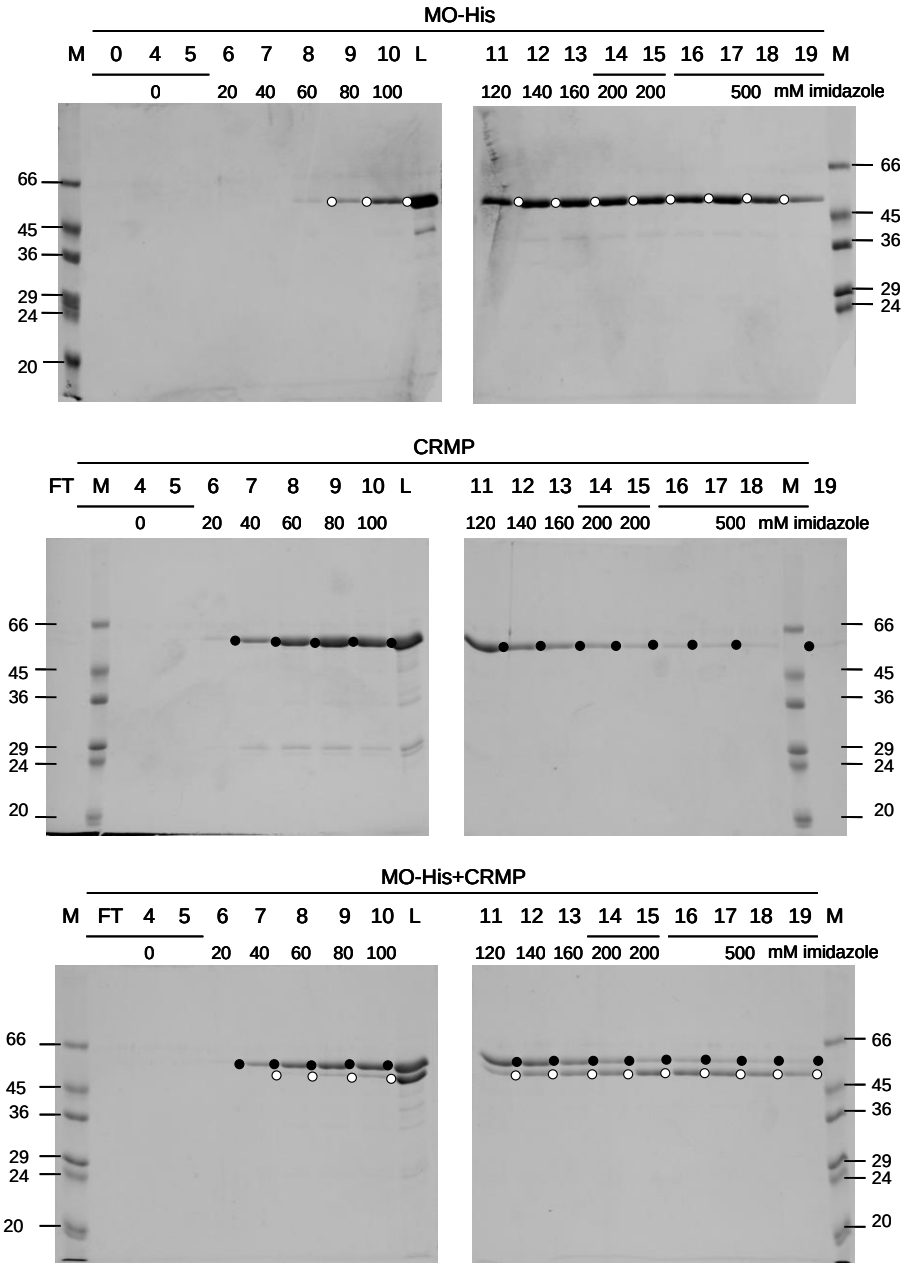

Figure 8.14. Study of the interaction between MO and CRMP1/8-525 by Ni-NTA affinity chromatography. SDS-PAGE analysis of the samples collected during the interaction assay between MO and CRMP on Ni-NTA Sepharose resin in 20 mM Hepes/KOH buffer, pH 7, 100 mM NaCl. L, sample incubated with the resin; FT, unbound proteins; the imidazole concentrations used for proteins elution are indicated; ○, MO-His; ●, CRMP.

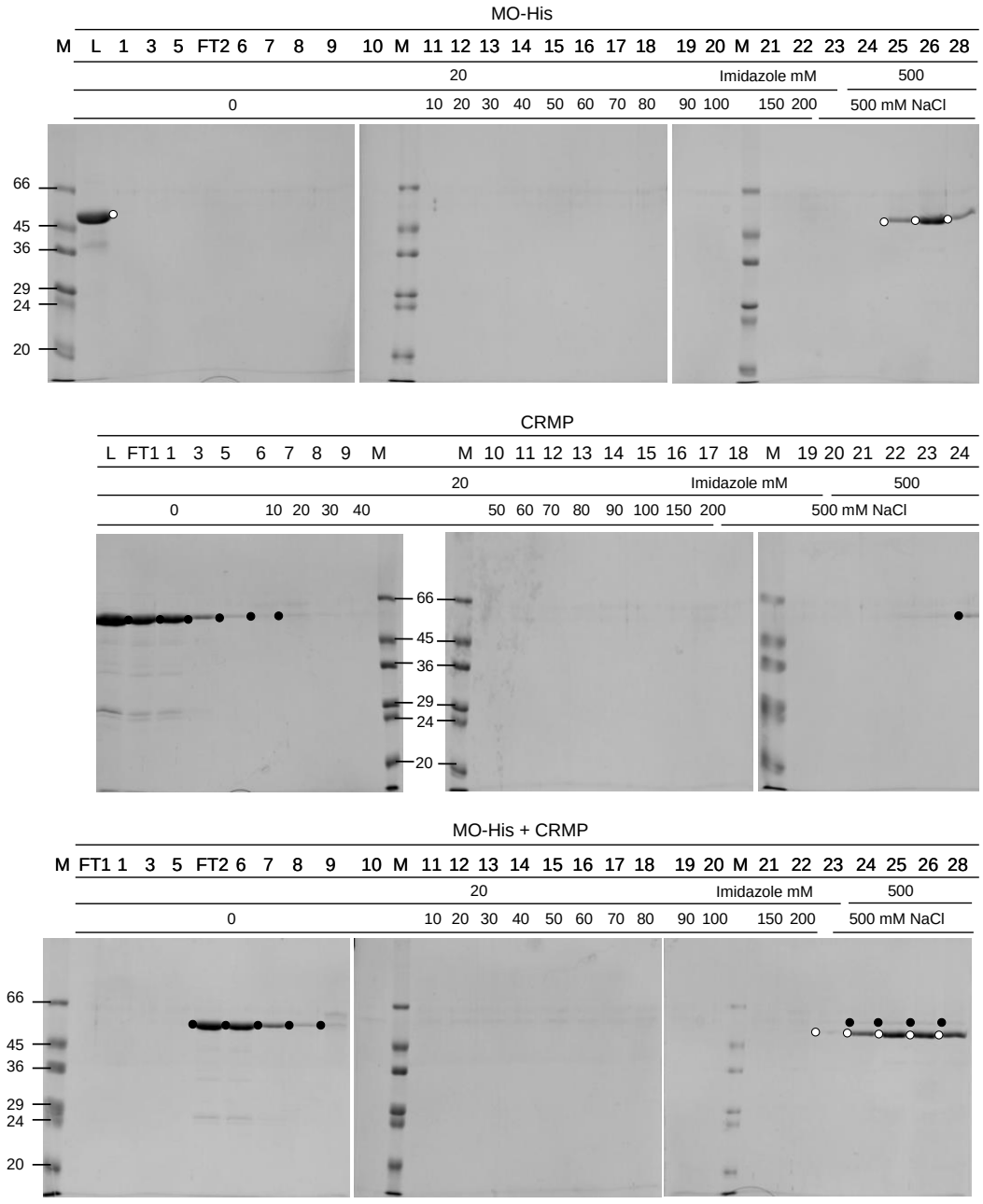

Figure 8.15. Study of the interaction between MO and CRMP1/8-525 by Ni-NTA affinity chromatography. SDS-PAGE analysis of the samples collected during the interaction assay between MO and CRMP on Ni-NTA Sepharose resin in 20 mM Hepes/KOH buffer, pH 7. L, sample incubated with the resin; FT, unbound proteins; the NaCl concentrations and that of imidazole used for proteins elution are indicated; ○, MO-His; ●, CRMP.

8.5. Study the interaction between MO, MOCH forms and CRMP1/8-525 form by measuring the NADPH oxidase activity

We tested the effect of CRMP (8-525) on the NADPH oxidase activity of MO and MOCH. The oxidation of NADPH by MO and MOCH was measured as a function of CRMP under various conditions.

Prior to each experiment, CRMP solution was gel filtered on a Superose12 column both to remove the aggregates and residual contaminants and to transfer CRMP in 20 mM Hepes/KOH buffer, pH 7 with varying NaCl concentrations (25, 50 and 100 mM) and in F-buffer (without ATP). MO and MOCH solutions stored in buffer B, in which they were stable, were diluted in 40 mM Hepes/KOH buffer pH 7 to lower the ionic strength and yield a buffer composition similar to that of CRMP. Full buffer exchange of MO and MOCH in the same buffer as that of CRMP was not required due to the addition of a very small volume of MICAL solution to each assay (1-2 µl to 120 µl). The v/[E] values of the NADPH oxidase activity of MO and MOCH were measured in the presence of 100 µM NADPH and varying CRMP concentrations (from 0 to 50 µM) in 20 mM Hepes/KOH buffer, pH 7 supplemented with 25, 50, 100 or 200 mM NaCl and in F-buffer by recording the entire absorption spectrum was recorded every 10 s at 25°C to detect artifacts (e.g. formation of turbidity). The changes of A_{340} values were used to calculate the initial reaction velocity. Standard NADPH oxidase activity assays of MO and MOCH were carried out in 20 mM Hepes/KOH buffer, pH 7 (no CRMP) every 1-1.5 h to check the stability of the enzyme dilutions.

For MO, we observed up to 90% inhibition of the NADPH oxidase activity with increasing CRMP concentrations in 20 mM Hepes/KOH buffer, pH 7 (I, 4.4 mM). The inhibitory effect of CRMP progressively decreased as the ionic strength of the medium increased (Figure 8.16, panel A). Interestingly, the activity of MO was weakly stimulated (up to 35%) by CRMP when its concentration was <15 µM in 20 mM Hepes/KOH buffer, pH 7, 200 mM NaCl (I, 204.4 mM) and in F-buffer (I, 60 mM) (Figure 8.16, panel A). However, at higher CRMP concentrations the inhibitory effect seemed to prevail (Figure 8.16, panel A). To try to quantify the strength of the interaction between CRMP and MO in the ionic strength regime that leads inhibition, the v/E calculated in the presence of CRMP (v/E_c) was subtracted from that calculated in the absence of CRMP (v/E_o). The resulting values showed reasonable hyperbolic dependence on CRMP concentration (Figure 8.16, panel B). The data were fitted to Eq.9 that describes ligand binding to determine the apparent dissociation constant (K_d) of the MO-CRMP complex. The calculated K_d values were 0.13 ± 0.01 µM in the absence of NaCl, 8.88 ± 1 µM with 25 mM NaCl and 17.68 ± 2.6 µM with 50 mM NaCl (Figure 8.16, panel B). For the conditions that led to activity increase the v/E_c-v/E_o values were fitted to Eq.9 and the calculated K_d were 4.34 ± 0.18 µM with 200 mM NaCl and 8.20 ± 1.5 µM in F-buffer (Figure 8.16, panels C and D).

A qualitatively similar behavior was observed for MOCH, but the stimulatory effect exerted by CRMP was observed at lower ionic strength (20 mM Hepes/KOH buffer, pH 7, 50 mM NaCl; I, 54.4) (Figure 8.16, panel E). The calculated K_d for MOCH-CRMP complex were 0.76 ± 0.1 µM with 10 mM NaCl and 21.94 ± 1.73 µM with 25 mM NaCl (Figure 8.16, panel F). CRMP stimulated (≈20%) the NADPH oxidase activity of MOCH in 20 mM Hepes/KOH buffer, pH 7 supplemented with 50 (I, 54.4 mM) and 100 mM NaCl (I, 104.4 mM) and in F-buffer (I, 60 mM) (Figure 8.16, panel E) and the calculated K_d for

MOCH-CRMP complex in the presence of 100 mM NaCl and in F-buffer were 19.6 ± 3 μM and 5.9 ± 1 μM, respectively (Figure 8.16, panels G and H).

The data indicated that CRMP interacts with MO and MOCH leading to inhibition of the NADPH oxidase activity at low ionic strength and to a weak stimulation at higher ionic strength. These results suggested that the interaction between the proteins leading to inhibition is electrostatic in nature. In fact the inhibitory effect exerted by CRMP switched to a weak activation of MOCH at ionic strength lower than that required for MO that correlates with the total charge of the proteins at neutral pH (MO, pI 9; MOCH, pI 7.67).

The inhibitory effect of CRMP on MO and MOCH due to non specific interactions at the lower ionic strength would explain the decrease of H_2O_2 observed by Schmidt et al., (2008) when CRMP was added to cell extracts containing MOCHLIM. The observed increase of activity was too small to be consistent with the hypothesis that CRMP is the substrate of a monooxygenase activity of MICAL or a strong activator.

The activation of MICAL by CRMP was very weak. However, the kinetic parameters k_{cat} and K_{NADPH} of the NADPH oxidase activity of MOCH in the presence of CRMP in F-buffer were determined to obtain further information on how the activity of MOCH was increased by CRMP. The calculated parameters k_{cat} and K_{NADPH} in the presence of CRMP (15 μM) were 1.73 ± 0.05 s^{-1} and 349 ± 23 μM to be compared with 1.73 ± 0.14 s^{-1} and 459 ± 66 μM in its absence (Figure 8.17) . These results indicated that the increase (≈25%) of the NADPH oxidase activity of MOCH observed previously (Figure 8.16, panel E) was due to a very small decrease of the K_m value for NADPH due to MICAL-CRMP interaction.

If CRMP was the substrate of the postulated monooxygenase activity of MICAL, we would have expected to a significant decrease of the K_m for NADPH and a dramatic increase of the k_{cat} value (Chapter 6), as observed for enzymes of PHBH class and also with MICAL in the presence of F-actin (Chapeter 7).

As part of the preliminary survey of MICAL-CRMP interaction, we also tested the effect of CRMP on the rate of NADPH consumption in the presence of F-actin in F buffer.

When F-actin (4 μM) was present, the calculated v/[E] values decreased by increasing CRMP concentration up to 20 μM (25% of inhibition); with higher concentration of CRMP the velocity of the NADPH oxidation increased to the values of the measured in its absence (Figure 8.18). Thus, with actin, the stimulatory effect of CRMP was reverted to an inhibition of the NADPH oxidation reaction catalyzed by MOCH in a CRMP concentration dependent manner (Figure 8.18). However, the NADPH was rapidly oxidized at a rate (≈15 s^{-1}) similar to that measured in the presence of F-actin (Chapter 8) compared to that measured in F-buffer in the absence or presence of CRMP (Figures 8.17 and 8.18). This observation indicate that the interaction between MOCH and F-actin is favored, and only a small fraction of MOCH binds to CRMP preventing its interaction with F-actin and thus, leading to a decrease (up to 25%) of its activity (Figure 8.18).

Overall, the data obtained by studying the effect of CRMP1/8-525 on the NADPH oxidase activity of MO and MOCH forms of MICAL indicated that an interaction between MO and MOCH with CRMP takes place. Such interaction leads to an inhibition of the NADPH oxidase activity at low ionic strength due to

the opposite charge of the proteins. Thus, the decrease of H_2O_2 production in lysates of cells expressing MICAL forms and CRMP1/8-525 observed by Schmidt et al., (2008) was probably due an inhibition of the NADPH consumption rather than a moonoxygenase/hydroxylase activity of MICAL in which CRMP would be the substrate. At higher ionic strength, the activity of MO and MOCH is inhibited when CRMP is present at high concentration (Scheme 8.1), but stimulation up to 25% occurs with lower CRMP concentrations (Scheme 8.1). Interestingly, in the presence of F-actin the enhanced NADPH consumption by MOCH is decrease up to 25% by CRMP. This suggests a competition between F-actin and CRMP to interact with MICAL, in which the interaction with F-actin is favored resulting in its depolymerization and enhancement of the NADPH oxidase (H_2O_2-producing) activity of MICAL (Scheme 8.1). However, it is possible that the presence of the LIM domain and C-terminal region of MICAL are required for the stabilization the MICAL-CRMP complex having a different (stronger) effect on MICAL activity.

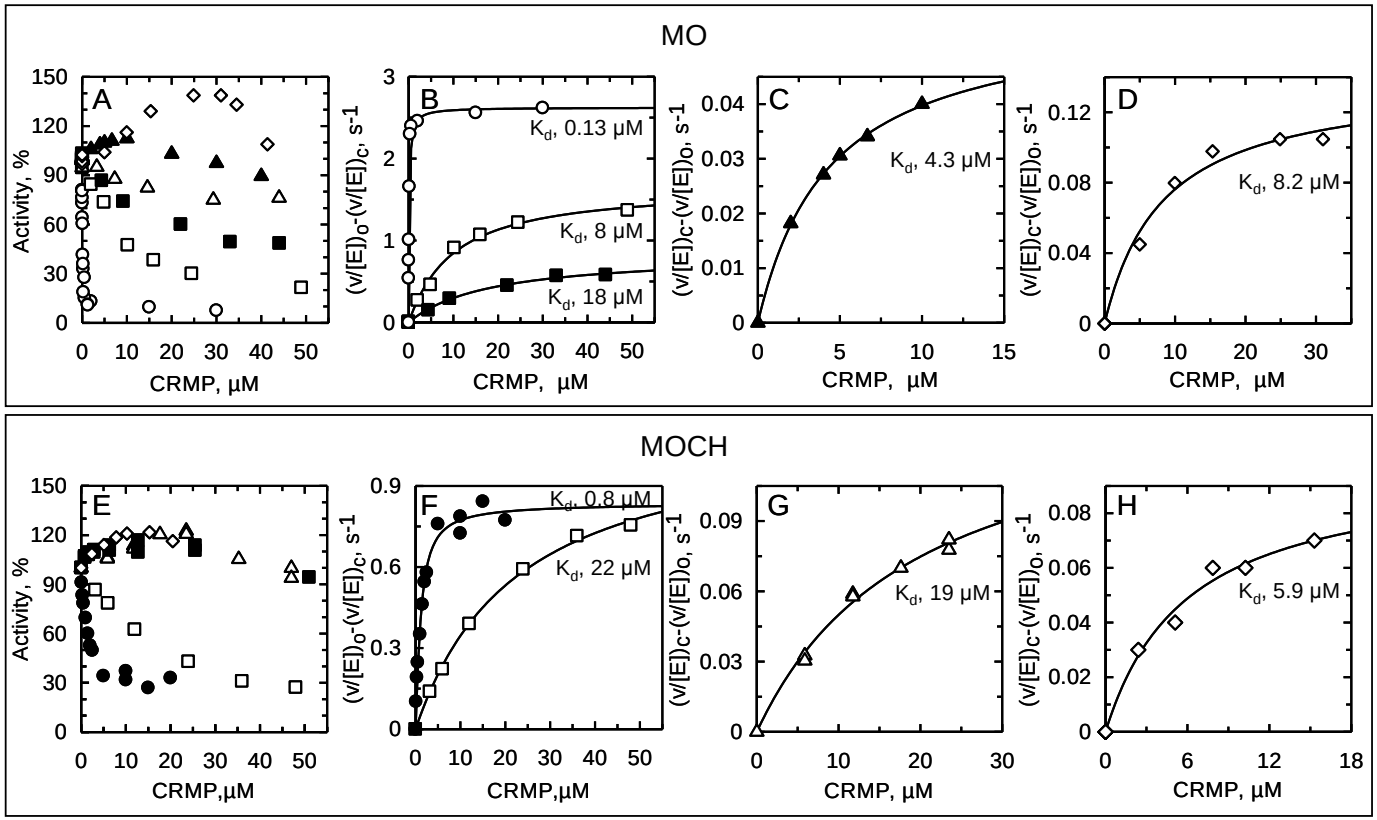

Figure 8.16. Effect of CRMP1/8-525 on the NADPH oxidase activity of MO and MOCH forms at varying ionic strength and ionic composition of the buffer. The initial velocity of the NADPH oxidase activity of MO and MOCH was measured in the presence of a fixed concentration of NADPH (100 μM) and varying CRMP concentration in 20 mM Hepes/KOH buffer, pH 7 (○), supplemented with 10 mM NaCl (●), 25 mM (□), 50 mM (■), 100 mM (Δ) and 200 mM (▲) and in F-buffer (◊). The activity measured in the absence of CRMP is taken as 100% of the activity (panels A and D). The K_d values of the MO- or MOCH-CRMP complex are calculated as described in the text (panels B-D and F-H).

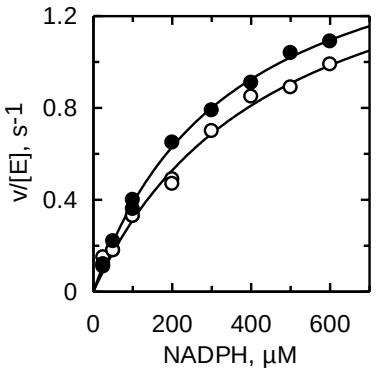

Figure 8.17. Effect of CRMP1/8-525 on the steady-state kinetic parameters k_{cat} and K_{NADPH} of the NADPH oxidase activity of MOCH. The calculated v/[E] values of the NADPH oxidation reaction in the absence (○) and in the presence of 15 µM CRMP (●) at varying NADPH concentration in F-buffer were fitted to Eq2 and the calculated kinetic parameters are indicated in the text.

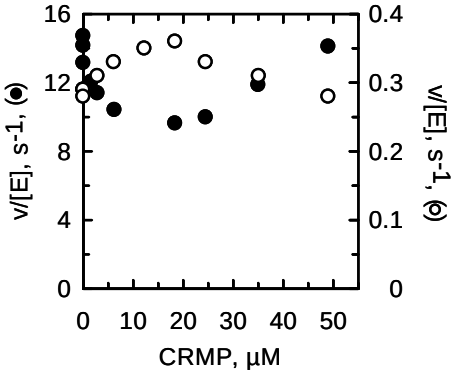

Figure 8.18. Effect of CRMP1/8-525 on the NADPH oxidation reaction catalyzed by MOCH in the presence of F-actin. The initial velocity of the NADPH oxidation reaction were measured in F-buffer in absence (○) and presence of F-actin (4 µM, ●) with fixed concentration of NADPH (100 µM) and by varying CRMP concentration.

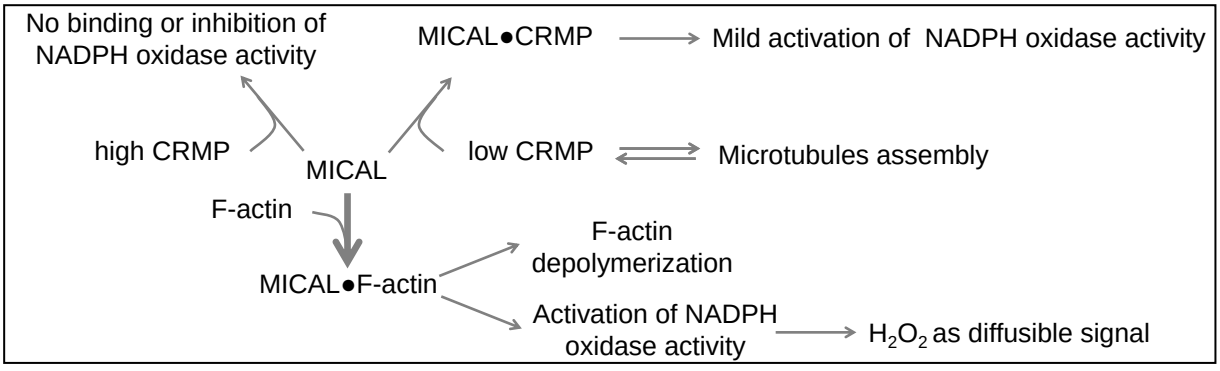

Scheme 8.1. Schematic representation of possible mechanisms of action of MICAL and CRMP for the control of cytoskeleton dynamics in response to semaphoring signaling pathway.

9. Discussion and conclusions

The aim of this work was to produce and purify the full-length human MICAL1 protein and its truncated forms (MO, the isolated MO domain; MOCH, comprising the MO and CH domains; MOCHLIM, lacking the C-terminal region) to determine for the first time: (i) the catalytic properties of human MICAL 1; (ii) the effect of the CH and LIM domains and the C-terminal region on the catalytic properties of the N-terminal monooxygenase-like domain and (iii) to open the way to study how MICAL interacting proteins can modulate its activities.

We engineered the DNA coding human MICAL1 for the expression of the full-length protein and the form lacking the C-terminal region carrying the His_6-tag at their C-terminus, as previously done for the production of the isolated MO domain (Zucchini et al., 2011) and of the form comprising the MO and CH domains (Vitali 2012). Two forms of MOCHLIM were constructed, MOCHLIM2 and MOCHLIM4, spanning residues 1-771 and 1-783, respectively.

On the basis of the results of pilot experiments, MOCH, MOCHLIM comprising 1-783 residues and the full-length MICAL1 were produced in *E.coli* BL21(DE3) cells in the presence of GroE to favor protein folding.

The proteins were purified by affinity chromatography on Ni-NTA Sepharose resin followed by gel filtration on a Superose12 column (on a small scale; for MO, MOCH and MOCHLIM) or on a Superdex200 column (on a large scale, for MOCHLIM) or by anion exchange chromatography (for MICAL) to obtain homogeneous protein preparations. MOCHLIM form and to a lesser extent the full-length form were sensitive to proteolytic degradation. The addition of 0.5% of a protease inhibitors cocktail to the enzyme preparation after each chromatographic and dialysis step and the presence of 1 mM PMSF in buffer solutions allowed us to obtained stable protein preparations to carry out their characterization. All MICAL forms were stable after concentration up to ≈5 mg/ml by ultrafiltration and after dialysis against 50 mM Na-phosphate buffer, pH 7.5, 100 mM NaCl, 10% glycerol, 1 mM EDTA, 1 mM DTT, 1 mM PMSF. Mass spectrometry analysis of the purified MICAL forms confirmed their integrity with the N-terminal sequence corresponding to that of MICAL1 after post-traslational removal of Met1.The absorption spectrum of all MICAL forms showed the characteristic long-wavelength absorption band due to the formation of the charge-transfer complex (CT) between FAD and Trp400 (Nadella et al. 2005; Siebold et al., 2005) and absorbance maxima at 375 and 458 nm in the visible region. Small differences were observed in the absorbance maxima in the UV region, which is influenced by the amino acidic composition of the proteins so that the maxima were at 273, 276, 278 and 280 nm for MO, MOCH, MOCHLIM and MICAL, respectively. The fact that the absorption spectra in the visible region of the final MICAL forms were very similar to that of the isolated MO domain indicated that the presence of the CH, LIM domains and of the C-terminal region did not perturb the FAD environment of the N-terminal domain of MICAL. For the isolated MO domain it has been previously demonstrated that 1 mol of FAD was bound per mol of the purified protein. The calculated extinction coefficient was 8.1 $mM^{-1}cm^{-1}$ at 458 nm (Zucchini et al., 2011). These results were confirmed with MO preparations produced during the present work. More importantly, also the MOCH, MOCHLIM and the full-length

MICAL showed a stoichiometry of ≈0.8 mol of FAD per mol of protein with the protein concentration determined with the Bradford method, which likely overestimates the protein content by 15-25%. Similar values of the extinction coefficient at 458 nm were determined for MICAL forms (7.9 ± 0.22 mM^{-1} cm^{-1}, 8.1 ± 0.07 mM^{-1} cm^{-1} and 7.6 ± 0.56 mM^{-1} cm^{-1} for MOCH, MOCHLIM and MICAL, respectively, with the protein denatured with TCA to release the FAD and 8.02 $mM^{-1}cm^{-1}$ (MOCH), 8.4 $mM^{-1}cm^{-1}$ (MOCHLIM) and 8.4 $mM^{-1}cm^{-1}$ (MICAL) when the proteins were denatured in buffer containing guanidine). The MOCHLIM and full-length proteins contained also zinc ions with a stoichiometry consistent with the expected 2 zinc ions bound to the LIM domain.

The purified proteins were stable after long-term storage at -80°C or after incubation up to 24 h on ice at 4°C, as demonstrated by their absorption spectra, activity and by SDS-PAGE analysis.

MO and MOCH forms were monomeric in solution as demonstrated by gel filtration and by DLS experiments. MOCHLIM and MICAL were found to be dimeric by gel filtration. For full-length MICAL the result was confirmed by DLS. Instead, DLS showed that the presence of the LIM domain causes MOCHLIM to oligomerize yielding dimers, trimers, tetramers and higher order aggregates. This observation is in agreement with the the tendency of such domain to aggregate as well as to stabilize various oligomeric states depending on the protein concentration (Mathews et al., 2013).

All MICAL forms were able to catalyze a NADPH oxidase activity. The catalytic efficiency (k_{cat}/K_{NADPH}) of the NADPH oxidase activity catalyzed by MICAL forms progressively decreased (from ≈163 $s^{-1}mM^{-1}$ to ≈18.5 $s^{-1}mM^{-1}$, ≈15.3 $s^{-1}mM^{-1}$ and ≈0.75 $s^{-1}mM^{-1}$ for MO, MOCH, MOCHLIM and MICAL, respectively) mainly due to an increase of the K_m for the NADPH (MO, ≈20 μM; MOCH ≈134 μM; MOCHLIM, ≈230 μM; MICAL, ≈375 μM). MO, MOCH and MOCHLIM forms showed similar k_{cat} values (≈3 s^{-1}). Instead, a 10-fold drop of the k_{cat} was observed for the full-length protein (≈0.3 s^{-1}).The pH profiles of $1/K_{NADPH}$ and k_{cat}/K_{NADPH} that were similar in shape for MICAL forms and they appeared to reflect the overall charge of the protein, which plays a major role for NADPH bnding to enzymes of the PHBH family. MO and MOCH showed a similar pH profile of the k_{cat} with similar pK_a values and revealed a greater sensitivity of the MO domain to the ionic strength and ionic composition of the medium compared to that of the other forms. The k_{cat} of MOCHLIM was little sensitive to pH between pH 6 and 9, with values similar to the maxima values observed for MO and MOCH. At pH lower than 6 also the k_{cat} decreased as observed for the other truncated forms. These result suggests that at this pH value LIM, which becomes less negatively charged, may lose its interaction with the rest of the protein, leading to that the decrease of k_{cat} observed with MO and MOCH at acidic pH. Instead, the k_{cat} of the full-length MICAL remained lower compared to the values measured with the truncated forms in the entire pH range we could explore, and it increased from a low value at pH 6-8 as the pH decreased. It is possible, that as the pH lowers the C-terminal region becomes less negatively charged so that its interaction with the positively changed MO could be weakened leading to the observed increase of k_{cat}.

Studies of the effect of solvent viscosity on the kinetic parameters of the NADPH oxidase activity of the MO domain suggested the presence of conformational changes that take place during the catalytic cycle between substrate binding and NADP release, which contribute to determine the value of the parameter

(Zucchini et al., 2011). On the basis of the known properties of PHBH and the structures of MICAL-MO in the oxidized and reduced state (Nadella et al., 2005; Siebold et al., 2005), in a minimal scheme, the predicted conformational changes may be: (i) movement of Trp400 to allow hydride transfer from the NADPH nicotinamide ring to the flavin and (ii) the subsequent "flavin in"/"flavin out" transition. The effect of the solvent viscosity on the kinetic parameters of the NADPH oxidase reaction catalyzed by MOCH, MOCHLIM and MICAL confirmed that the NADPH oxidase reaction catalyzed by the MO domain of MICAL1 is solvent sensitive. The CH and LIM domains and the C-terminal region of MICAL partially suppressed the viscosity effect on k_{cat}/K_{NADPH} in a fashion that may be explained by their progressively lower affinity for NADPH. Interestingly, the effect of solvent viscosity on the k_{cat} was similar for all MICAL forms demonstrating that it is unlikely that the drop of kcat of full-length MICAL is due to a decrease of the chemical steps of the reaction.

The study of the pH and solvent viscosity dependence of the NADPH oxidase reaction catalyzed by MICAL forms led us to conclude that the observed changes in the values of the kinetic parameters are not due to changes of the optimal pH and/or in the rate determining steps of the reaction taking place in the MO domain. The increase of the K_m for NADPH correlates with a decrease of the positive charge of the protein due to the presence of the acidic CH, LIM and C-terminal domain. The 10-fold decrease of the NADPH oxidase activity observed for the full-length MICAL is in agreement with the proposal that the C-terminal region has an inhibitory function on the activity of the MO domain (Schmidt et al., 2008; Giridharan et al., 2012). Our experiments indicate that the observed lowering of k_{cat} is likely due to the presence of a conformational equilibrium between an inactive/close (a) and active/open (b) conformation of MICAL in the free state (Scheme 9.1), which is shifted 9:1 toward the inactive conformation in solution so that only a 10% of MICAL would be present in the catalytically active state (Scheme 9.1). In fact the value of k_{cat} reflects the actual concentration of the active enzyme present in solution. These conformations, which are expected to be in rapid equilibrium with each other so that their relative cncentrations would remain constant in solution, depend on the position of the C-terminal region.

In spite of the fact that the MICAL MO domain is structurally related to PHBH, the prototype of FAD-containing aromatic monooxygenases and that it share with it the high sensitivity of NADPH binding to ionic composition and ionic strength and catalytically relevant conformational changes, all MICAL forms have an unusually high NADPH oxidase activity for a monooxygenase in the absence of the substrate to hydroxylate suggesting that they function as true oxidases. The differences between monooxygenases and oxidases may be very subtle and depend on the ability of being reduced by NADPH even in the absence of the hydroxylating substrate and the abitity to stabilize the Flavin 4a-hydorperoxide intermediate, which are linked to the fine details of the active site architecture. It should be noted that the overall structure of MICAL MO is similar to that of PHBH, but the active sites of the two enzymes are different as well as the details of their topologies (Figure 2.3 in Chapter 2), which suggest a greater degree of flexibility of MO compared to PHBH (Nadella et al., 20155, Siebold et al., 2005). Thus, a PHBH-like module could have been recruited in MICAL to generate a NADPH oxidase that can be finely regulated by modulating

NADPH binding and catalysis through electrostatics and by modulating the catalytically relevant conformational changes as in PHBH.

A unique feature of MICAL proteins is their ability to catalyze a NADPH-dependent F-actin depolymerizing activity. We have demonstrated that all MICAL forms were able to catalyze a NADPH-dependent depolymerization of actin filaments. F-actin greatly stimulated the rate of NADPH consumption by all MICAL forms, leading to a (≈10-fold) increase the k_{cat} and to a decrease of the K_m for NADPH (10-50 μM *vs* 400-900 μM in the absence of F-actin). As a result, MO, MOCH and MOCHLIM forms are similar to each other with respect to the K_{NADPH} measured in the presence of F-actin (4 μM), and k_{cat} values vary within a factor of 2-3 (20 s^{-1}, 26 s^{-1} 15 s^{-1} and 8 s^{-1} for MO, MOCH , MOCHLIM and full-length MICAL,, respectively). The apparent K_m for actin was also similar for MO, MOCH and MOCHLIM (≈4 μM) indicating that the main site of MICAL interaction with F-actin is its MO domain. Thus,the presence of the CH and LIM domains, which mediate the interaction with F-actin in actin-binding proteins, did not alter the affinity of MICAL for F-actin and the N-terminal monooxygenase-like domain is sufficient for the interaction. This is in contrast with the proposal that the CH and LIM domains are required to present the physiological substrate to the catalytic domain (Siebold et al., 2005), but it is in agreement with the fact that single CH or LIM domains are not able to bind F-actin. In fact, cytoskeleton proteins that interact with F-actin or with actin binding proteins (ABP) contain tandem CH and LIM domains (Bamburg et al., 2000). Thus, the presence of single CH and LIM domains in MICAL proteins is another unusual feature of MICAL proteins.

For the full-length MICAL F-actin stimulates the rate of the NADPH oxidation reaction catalyzed by MICAL by lowering the K_m for NADPH to a value of ≈30 μM, which is similar to those calculated for the truncated forms. The apparent k_{cat} was ≈8 s^{-1} that is only 2-3-fold lower than those of the other forms. Interestingly, assuming that the K_m value reflects the K_d, the affinity for F-actin was 10-fold lower (≈30 μM) than that measured for MO, MOCH and MOCHLIM. Also this effect could be explained by the conformational equilibrium between an inactive and active conformation of the full-length MICAL in the free state (Scheme 9.1 and Figure 1.8 in Chapter 1). The higher K_m for actin of MICAL could reflect the coupled equilibria between the inactive(a)/active(b) conformations and between the formation of F-actin/$MICAL_{active}$ (c) complex and MICAL in the active conformation (b) (Scheme 9.2). Only in the active (b) conformation of MICAL the actin binding site of the MO domain would be physically accessible. This time binding of F-actin would shift the equilibrium towards the active species, justifying the fact that k_{cat} of MICAL is only 3-fold lower than that measured with the other forms.

Interestingly, actin depolymerization catalyzed by MO and MOCH led to the release of actin monomer (G-actin), while the incubation of F-actin with MOCHLIM and the full-length protein in the presence of NADPH led to the formation of actin fragments of approximately 240 kDa suggesting that they function as severing proteins.. We can speculate that part of the actin filament is physically protected by the presence of the LIM domain and the C-terminal region of MICAL reducing the number of site on the actin filament that can interact with the MO domain. As a result several actin monomers could not be

modified by the NADPH oxidation reaction catalyzed by the MO domain bound to actin and, thus, they remain associated to yield the observed fragments.

In all cases, the amount of NADPH rapidly oxidized by MICAL forms exceeded that of the actin present. This result can be explained as due to: (i) a case of substrate recycling; (ii) enhanced NADPH oxidation leading to both the hydroxylation (monooxygenase activity) of F-actin residues and the H_2O_2 production (NADPH oxidase activity) at a similar rate or (iii) enhanced NADPH oxidase activity. If F-actin Met 44 (and Met 47) were the substrate of the monooxygenase/hydroxylating activity of the N-terminal domain of MICAL, as proposed for the Drosophila and mouse proteins (Hung et al., 2013; Lee et al., 2013), we would have expected rapid oxidation of a molar amount of NADPH corresponding to that of actin (or twice its concentration), followed by a slow oxidation of NADPH at the same rate as that observed in the absence of F-actin. The mass spectrometry analyses of actin samples treated with MICAL forms and NADPH revealed that a maximum of two residues are oxidized per actin molecule. Actin Met44 and Met47 are modified but that also several other Met and Trp residues are oxidized with similar probability. The oxidation of several residues, which are all in proximity of the interface between actin monomers (Figures 7.17 and 7.18 in Chapter 7), would suggest that their modification depends on *in situ* H_2O_2 production through the NADPH oxidase activity of MICAL. This is in contrast with the proposal of the specific conversion of Met44 (and Met 47) to methionine sulfoxide (Scheme 9.3) by a hydroxylase activity for the Drosophila and mouse MOCH forms, in which the resulting R-methionine sulfoxide residue is reverted to methionine through R-specific methione sulfoxide reducatase (Hung et al., 2013; Lee et al., 2013) (Scheme 9.3; Figure 8.8 in Chapter 8). However, it is possible that MICAL binds to F-actin in such a way that the first residue being hit by released H_2O_2 could be Met44 (or Met 47), which belong(s) to loop D, at the interface between actin monomers in the filament. As a result of preferential modification of Met 44 (and/or Met47), disassembly of the filament would locally take place, causing MICAL-MO release and inhibition of its NADPH oxidase activity. This process would further limit uncontrolled actin oxidation. The precise geometry of MICAL/F-actin interaction would control the stereochemistry of Met oxidation to yield methionine sulfoxide with excess of the R enantiomer, which could be repaired by R-specific methionine sulfoxide reductase.

Overall it appears that, in the cell, MICAL can catalyze a basal NADPH oxidase activity in the free state. This activity is enhanced by the binding of MICAL to F-actin, which catalyzes depolymerization of actin filaments, even in the absence of activating proteins. The removal of the interaction between the C-terminus and the N-terminal catalytic domain of MICAL by interactor proteins, like the cytoplasmic portion of plexin, in response to semaphorin signaling would shift the inactive/active equilibrium toward the active form favoring its interaction with F-actin and thus, promoting its local depolymerization.

Several proteins have been identified as MICAL interactors (CasL, GTPases, NDR, CRMP), which could modulate its activity. With purified MICAL forms now available, it will be possible to identify specific interactors and to study in detail their effect on the activities catalyzed by the MO domain. In this respect, preliminary experiments were carried out to start to study the interaction between MICAL and CRMP. Experiments in COS7 cells demonstrated that the interaction between MICAL1 interact with CRMP1-5

proteins and that such interaction leads to reorganization of the cytoskeleton also in the absence of semaphorin stimulation (Schmidt et al., 2008). For CRMP2 it has been proposed that the H_2O_2 produced by the NADPH oxidase activity of MICAL modulates the activity of CRMP2 by oxidizing a Cys residue, which would stimulate its phosphorylation and, as a consequence, promote microtubules disassembly (Morinaka et al., 2011). Instead, CRMP1 has been proposed to be possible substrate of the monooxygenase/hydroxylase activity of MICAL due to a decrease of H_2O_2 produced in the presence of NADPH in lysates of COS7 cells expressing MICAL1 and CRMP1 compared to that measured in cells expressing only MICAL1 or CRMP (Schmidt et al., 2008). Thus, it was proposed that hydroxylation of CRMP1 by MICAL1 would be responsible for the observed synergistic action of MICAL and CRMP in cells collapse. We produced and purified the mouse CRMP1 form comprising residues 8-525 used by Schmidt et al. (2008) to show the quenching of H_2O_2 production by MICAL. Our experiments demonstrated that CRMP1 and MICAL1 MO and MOCH interact, but in a complex way. At low ionic strength, CRMP1 caused an inhibition of the NADPH oxidase activity due to non specific interactions depending on the opposite charge of the proteins. At higher ionic strength, the non specific interactions were removed and CRMP (up to 15 μM) led to a weak stimulation (≈25%) of the NADPH oxidase activity of MO and MOCH, which was followed by an inhibition at higher CRMP concentrations. The stimulatory effect of CRMP on the activity of MO and MOCH was due to a small decrease of the K_m for NADPH. If CRMP were the hydroxylatable substrate of the monooxygenase activity of the N-terminal monooxygenase-like domain of MICAL we would have expected a significant increase of k_{cat} and a significant decrease of the K_m for the NADPH. Interestingly, when F-actin was present, the stimulatory effect of CRMP was reverted to an inhibition of NADPH oxidation. From this observation we can speculate that CRMP and F-actin compete for binding to MICAL and that the formation of MICAL/F-actin complex is favored.

In general these results suggested that CRMP1/8-525 is not the substrate of a hydroxylase activity of the MO domain of MICAL1 and the observed inhibitory effect on the NADPH consumption by MO and MOCH could explain the decrease of the H_2O_2 production detected in cell lysates. The interaction between CRMP and MO or MOCH seems weak (estimated of K_d are in the microM range (Figure 8.16 in Chapter 8), but it may be explained by the absence of the LIM domain and C-terminal region of MICAL, which could be the protein region at which the interaction between MICAL and CRMP takes place. It is possible that CRMP can interact with the C-terminal regions of MICAL removing the autoinhibitory effect exerted on the N-terminal catalytic domain, leading to activation of the NADPH oxidase activity of MICAL also in the absence of semaphor-plexin interaction or maintaining MICAL in a conformation to that would promote its binding to plexin to potentiate the signal transduction.

The H_2O_2 produced by MICAL could modulate the ability of CRMP to promote microtubules assembly indirectly by inhibiting phosphatase activity though oxidation (Figure 8.8 in Chapter 8). In this respect, the NADPH oxidase H_2O_2-producing activity of MICAL that should be enhanced when bound to the cytoplasmic side of plexin thorugh its C-terminal region could also maintain CRMP in the phosphorylation state (by inhibiting phosphatases) and thus destabilize the microtubules. In such way

actin and microtubules cytoskeleton component could be linked and controlled by MICAL activity in response to semaphoring-plexin signaling.

Our studies revealed that MICAL may be an authentic NADPH oxidase rather than a monooxygenase and that it exhibits such activity even in the free state.

In order to evaluate the relevance of MICAL NADPH oxidase activity in the absence/presence of F-actin in the cell, we searched the literature for estimates of the cellular concentrations of NADPH and F-actin. For both species the published values vary over several orders of magnitude. For F-actin, concentrations varying from μM to mM were reported depending on cell type and cell localization (Koelster et al., 2009). Also the reported NADPH concentrations varied from 30 μM in brain (Klaidman et al., 1995) to 300 μM in liver (Slater 1967) and 900 μM in suprachiasmatic nucleolus cell lines (SCN2.2) (Wise et al., 2004). NADPH concentrations also depend on the metabolic conditions, which influence the activity of NADPH generating or consuming enzymes (Ying et al., 2008). By considering the highest NADPH concentration of 900 μM, the free full-length MICAL would exhibit a low, but not neglible, NADPH oxidase (H_2O_2-producing) activity, which would be controlled by local NADPH levels. Such activity would remain low even after the removal of C-terminal interaction upon its interaction with plexin activated by semaphorin, which would probably corresponds to the activity of the MOCHLIM form. The NADPH concentration could also control the activity of MICAL upon F-actin binding, if local NADPH concentration were < 100 μM. Thus, NADPH levels in the cell can control H_2O_2 produced by the NADPH oxidase activity of free MICAL and also cytoskeleton dynamics by regulating the F-actin depolymerizing activity of MICAL.

With purified MICAL forms it will be possible to better understand the reaction mechanism of F-actin depolymerization, to identify MICAL interactors and to determine their mutual effects. In this respect, it will be interesting to clarify the catalytic properties of full length MICAL in complex with CRMP1 (or 2) and MICAL and of MICAL with other proteins such as CasL, NDR which are involved in the integrin pathway and apoptosis, respectively.

Inhibition of MICAL has been proposed to be beneficial to prevent neurodegenerations associated with, e.g., spinal cord injury or even Amyotrophic lateral sclerosis (Kaneko et al., 2006; Schmidt et al., 2009) and even some cancer forms (Ashida et al., 2006; Lundquist et al., 2014). Recently, a compound named CCG1423 that had been shown to inhibit cancer cells proliferation (Lundquist et al., 2014) has been proposed to be a potent inhibitor (K_i, 1.57 μM) of MICAL2 activity (Lundquist et al., 2014). In these experiments, the inhibition studies had to be carried out in the presence of F-actin to enhance the rate of NADPH oxidation catalyzed by the MO domain of MICAL2 to measurable levels. This set-up certainly complicates the interpretation of the data. The higher k_{cat} and lower K_{NADPH} of human MICAL1 forms, even in the absence of F-actin, compared to those of the still poorly characterized MICAL2 and 3, makes MICAL1 better suited than other MICAL isoforms for detailed structure-function studies aiming to dissect the catalytic mechanism of the reaction that is associated with its monooxygenase-like domains and to, e.g., search for inhibitors of potential medical interest. For example, we tested the effect of

CC1423 on the NADPH oxidase activity of human MICAL MO and MOCH forms in the absence of F-actin and we could not confirm the results of Lundquist et al. with MICAL2. The similarity between the catalytic domains of MICAL isoforms would suggest that the the effect observed on MICAL2 could be an artifact due to the intrinsic low activity of MICAL2 MO domain even in the presence of F-actin or to the presence of F-actin itself.

Finally, with homogeneous preparations of the various MIAL1 forms available it will be possible to initiate structural studies of the proteins in the free state, in complex with its interactors and F-actin by using the potent techniques now available (e.g.: small-angle X-ray scattering or cryo-electron microscopy) for structure determination even in the case of proteins that resist cystallyzation such as conformationally heterogeneous proteins, weak protein-protein complexes and complexes with F-actin.

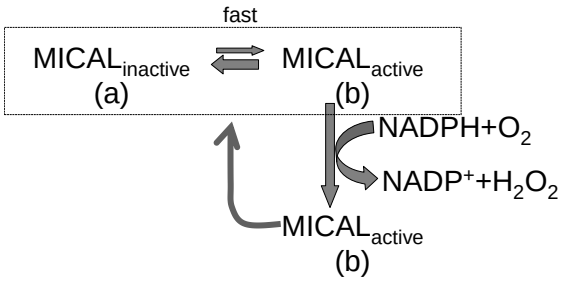

Scheme 9.1. Conformational equilibrium between the inactive (a) and active (b) conformation of MICAL in the free state. Only the active form would react with NADPH and molecular oxygen, but at the end of the catalytic cycle active MICAL would rapidly equilibratewith the inactive form so that the relative concentrations of active/inactive conformations would be independent from NADPH concentration.

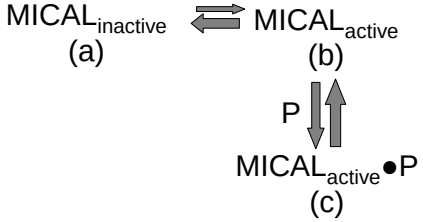

Scheme 9.2. Conformational equilibrium between the inactive (a), active (b) conformation of MICAL in the free state and in complex with interacting protein (c). F-actin (P) would be able to shift the equilibrium between the inactive and active form of full-length MICAL increasing the concentration of the active species.

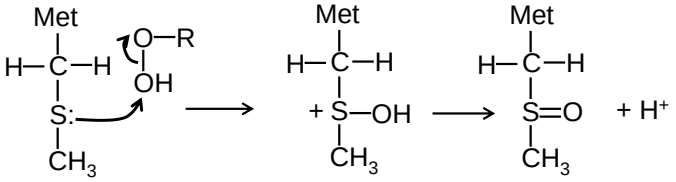

Scheme 9.3. Mechanism of the reaction for the oxidation if methionine to methionine sulfoxide in a monooxygenase (R-OOH, FAD 4a hydroperoxide) or by H_2O_2 (ROOH, hydrogen peroxide).

10. Materials and Methods

10.1. Microbiology and Molecular biology techniques

For microbiology and molecular biology methods protocols reported in Sambrook, J et al., (1988) and Ausubel, F.M., et al., (2005) were used.

Ultrapure water produced with a MilliQ Reagent water system (Millipore, Billirica, MA, USA) was used to prepare all solutions, while growth media were prepared with deionized water produced with a Elix 5 (Millipore) apparatus.

Growth medium

LB medium (Luria Bertani)
Tryptone 10g/l, NaCl 10g/l and Yeast extract 5g/l.

Antibiotic solutions

Ampicillin (Amp) 100 mg/ml in ultrapure H_2O; the solution is sterilized with a 0.22 μm filter (sterile syringe filter with cellulose-acetate membrane, VWR);
Chloramphenicol (Chl) 25 mg/ml in ethanol.
Antibiotic solutions are divided in aliquots and stored at -20°C.

Preparation of E.coli Rosetta (DE3) and BL21(DE3) competent cells with the $CaCl_2$ method

Solutions
- 0.1 M $CaCl_2$ sterile solution, stored at -20°C;
- DMSO (Sigma, D-8418, St. Louis, MI, USA).

Procedure
The night before the experiment:
- remove an aliquot of *E.coli* Rosetta(DE3) or BL21(DE3) cells stored at -80°C as glycerol stocks;
- inoculate the cells on a LB (for BL21(DE3)) or LB-Amp (for Rosetta(DE3)) plate and incubate overnight at 37°C;
- inoculate 100 ml of LB or selective LB medium with a single colony from the plate;
- incubate at 37°C under stirring (220 rpm);
- monitor cell growth by measuring the optical density at 600 nm (OD_{600}) at different times;

When the culture reaches a OD_{600} value of 0.4-0.5:
- transfer the culture into 250 ml bottle for Sorvall rotor SLA1500 and centrifuge at 4000 rpm for 10 min at 4°C (Sorvall RC6 Plus);
- discard the supernatant and resuspend the pellet in 0.1 M $CaCl_2$ (20 ml);
- transfer the suspension into a 50 ml sterile centrifuge tube and centrifuge at 4500 rpm for 10 min at 4°C (rotor SS34);
- discard the supernatant and resuspend the pellet in 0.1 M $CaCl_2$ (4 ml);

The cells are ready to be transformed with the plasmid.

For a later use of the competent cells:
- add 35 μl of DMSO per ml of competent cells suspension;
- incubate 15 min on ice;
- add 35 μl of DMSO per ml of competent cells;
- distribute 600 μl aliquots in cryotubes;
- flash-freeze in liquid nitrogen and store at -80°C.

E.coli Rosetta(DE3) and BL21(DE3) competent cells trasformation

Solutions
- TE buffer: 10 mM Tris/HCl, pH 8, 1 mM EDTA sterilized in autoclave;
- plasmid solution (0.2-0.6 μg/μl);
- *E.coli* competent cells;
- LB medium;
- selective LB plates.

Procedure
- thaw an aliquot of *E.coli* competent cells or use freshly prepared competent cells;
- thaw the desiderate plasmid solutions and, if needed, dilute it in TE buffer to have 1-50 ng of DNA in 1-50 μl;
- set-up the transformation mixture:

	Negative control	sample
Plasmid	-	1-50 μl
Competent cells	200 μl	200 μl

- mix gently and incubate for 30 min on ice;
- carry out the thermal shock at 42°C for 90 s;
- incubate for 2 min on ice;
- add 800 μl of LB medium;
- incubate for 45 min at 37°C;
- centrifuge at 13000 rpm for 2 min at 4°C in a microfuge (Heraeus Biofuge Pico, Chandler, AZ, USA) ;
- discard the supernatant and resuspend the pellet in 200 μl of LB medium;
- spread on selective LB plates;
- incubate overnight at 37°C.

Preparation of E.coli DH5α competent cells with the RbCl method

E.coli DH5α strain is used for the maintenance and propagation of the plasmids. The strain is mutated in the gene coding RecA protein involved in the recombination process and in the gene coding EndA endonuclease. This method is used to transform *E.coli* cells when high transformation efficiency is required, e.g. during cloning.

Solutions
- Solution A: 10 mM MOPS, pH 6.5, 10 mM RbCl (sterilized in autoclave);
- Solution B: 10 mM MOPS, pH 6.5, 10 mM RbCl, 50 mM $CaCl_2$ (sterilized in autoclave);
- Solution B + glycerol: 7 ml of Solution B + 1 ml of 80% glycerol (freshly prepare for use and maintained on ice).

Procedure
The night before the experiment:
- remove an aliquot of *E.coli* DH5α cells stored at -80°C as glycerol stocks;
- inoculate the cells on a LB plate and incubate overnight at 37°C;
- inoculate 80 ml of LB or selective LB medium with a single colony from the plate;
- incubate at 37°C under stirring (220 rpm);
- monitor cell growth by measuring the optical density OD_{600} at different times;

When the culture reaches a OD_{600} value of 0.3-0.5;
- transfer and split the culture in 50 ml sterile centrifuge tube and centrifuge at 6500 rpm for 10 min at 4°C (Sorvall RC6 Plus, rotor SS34);
- discard the supernatant and resuspend the pellet in 20 ml of Solution A;
- centrifuge at 6500 rpm for 10 min at 4°C (rotor SS34);
- discard the supernatant and resuspend the pellet in 20 ml of Solution B;
- incubate 30 min on ice;
- centrifuge at 6500 rpm for 10 min at 4°C (rotor SS34);
- discard the supernatant and resuspend the pellet in 4 ml of Solution B + glycerol;

- split in aliquots of 200 µl in eppendorf tubes and store at -80°C
The cells are ready to be transformed with the plasmid.

E.coli DH5α competent cells trasformation

The procedure is similar to that described for *E.coli* Rosetta(DE3) and BL21(DE3) cells with the following modifications:
- carry out the thermal shock at 37°C for 1 min;
- add 1 ml of LB medium;
- incubate for 1 h at 37°C;
- spread 120 µl (1/10) of sample on selective LB plate;
- centrifuge the remaining sample at 13000 rpm for 3 min at 4°C;
- discard the supernatant;
- resuspend the pellet in 200 µl of LB medium (9/10);
- spread on selective LB plates;
- incubate at 37°C overnight.

Table 10.1 E.coli strains.

E.coli strains	*Genotype*	*Marker*
DH5α	*recA*⁻ *endA*⁻	-
BL21 (DE3)[a]	F⁻ *ompT hsdSB* (*rB*⁻ *mB*⁻) *gal dcm* (DE3)	-
Rosetta (DE3)[a]	F⁻ *ompT hsdSB*(*rB*⁻ *mB*⁻) *gal dcm lacY1* (DE3) pRARE6 (CmR)	Chl

[a]Studier et al., 1986

Table 10.2 Properties of the plasmids used.

Plasmid	*Vector*	*Marker*	*Dimensions, bp*	*Encoding proteins*
pJET-MICAL	pJET1.2 (Thermo scientific)	Amp	6205	Full length human MICAL1, 1-1068 aa
pET-MICAL	pET23b (Novagen)	Amp	6791	
pJET-MOCHLIM2	pJET1.2	Amp	5311	MO, CH and LIM domain of human MICAL1, 1-771 aa
pET-MOCHLIM2	pET23b	Amp	5933	
pJET-MOCHLIM4	pJET1.2	Amp	5347	MO, CH and LIM domain of human MICAL1, 1-783 aa
pET-MOCHLIM4	pET23b	Amp	5897	
pET-MOCH	pET23b	Amp	5434	MO and CH domains of human MICAL1
pET-MO	pET23b	Amp	5054	MO domain of humanMICAL1
EFS10	pGEX-6P (GE Healthcare)	Amp	6673	Mouse CRMP1 8-875 aa
EFS11	pGEX-6P	Amp	6673	Mouse CRMP1 8-875 aa, mut 49-56
EFS12	pGEX-6P	Amp	6535	Mouse CRMP1 8-825 aa
EFS13	pGEX-6P	Amp	6535	Mouse CRMP1 8-825 aa, mut 49-56
p18	pBR22	Chl	3773	GroES-GroEL of *E.coli*
pRARE	pRIG	Chl	4629	tRNA per Ile, Gly, Arg, Leu e Pro

Table 10.3 Primers used for the amplification of the cDNA of human MICAL1 coding MICAL-MOCHLIM and the full length protein forms. Restriction sites are indicated: *Eco*RI (bold), *Nde*I (italic), *BamH*I (underlined) and *Xho*I (double underlined). The start and the stop codons are highlighted in grey. The lower case types indicate the mismatch with respect to the DNA template. The melting temperature (T_m) is calculated with the formula indicated in the text.

primer	*sequence*	*Tm*
MICAL Fw new	5′cc**gaattc***cat**ATG*GCTTCACCTACCTCCACCAACCCAGCGCATGCCC 3′	70.5
MICALMOCHLIMRev1	5′ GCTGgaTcCCTacTcGaGGTCTGTCTGGGGCAGGTGC 3′	71.5
MICALMOCHLIMRev2	5′ TCTCggaTccTtactcGAGCTCCGGACTCTCAGGGCCTCTATCGCTGC 3′	71.3
MICALMOCHLIMRev4	5′AGGCgGatccctactcGAGGCCTGGTGGCATGCTATTCTCACTTGGTG 3′	68.5
MICALFLRev	5′ GGTACAgGATcCTtacTCGagCTGGGCCCCTGTCCCCAAGGC 3′	70.3

Table 10.4. Primers used for sequencing of pDON-hMICAL1, pUC-MOCH, pJET-MOCHLIM and pJET-MICAL.

Primer	*Sequence*	*plasmid*
MICCt Fw	5′-CGGTGCAGGAATTGAATCTG-3′	pDON-hMICAL1
M13 (-21) Fw	5′- TGTAAAACGACGGCCAGT -3′	pUC-MOCH
M13 Rev	5′- CAGGAAACAGCTATGACC -3′	
pUCFw1	5′- CGCAATTAATGTGAGTTAGCTC -3′	
pUCFw2	5′- GTGGTAGCAGGGAGTGAC -3′	
MOCH rev	5′- CTTCACCATCCAGGCTGCATC -3′	pUC-MOCH and pJET derivatives
pJET Fw	5′-CGACTCACTATAGGGAGAGCGGC -3′	pJET derivatives
pJET Rev	5′-AAGAACATCGATTTTCCATGGCAG -3′	
MOCH Fw	5′- TCGTGTGCAAGAGAAGCATG -3′	pJET-MICAL
MICFL Rev	5′- AGCTTGAGGGCTCTGGAC -3′	

10.2. Engineering of the DNA coding MICAL and preparation of the plasmids for the production of MICAL-MOCHLIM and MICAL-FL forms

Plasmids purification by midi prep

E.coli DH5α cells are transformed with the plasmids of interest for their purification using the Midi-Prep Kit (Qiagen, Milano, Italy). Aliquots of competent *E.coli* DH5α cells are transformed with ≈60 ng of plasmid DNA. The trasformants clones are selected on LB plates containing suitable antibiotics (Table 10.2).

Solutions
- RNAse 100 µg/ml;
- Buffer P1 (Resuspension Buffer): 50 mM Tris/HCl, pH 8.0, 10 mM EDTA;
- Buffer P2 (Lysis Buffer): 200 mM NaOH, 1% (w/v) SDS;
- Buffer P3 (Neutralization Buffer): 3 M K-acetate, pH 5.5;
- Buffer QBT (Equilibration Buffer): 50 mM MOPS, pH 7, 750 mM NaCl, 0.15% (v/v) isopropanol, 0.15% Triton X-100;
- Buffer QC (Wash Buffer): 50 mM MOPS, pH 7, 1 M NaCl, 0.15% (v/v) isopropanol;
- Buffer QF (Elution Buffer): 50 mM Tris/HCl, pH 8.5, 1.25 M NaCl, 15% (v/v) isopropanol;
- TE buffer: 10 mM Tris/HCl, pH 8, 1 mM EDTA (sterile);
- Na-acetate: 3 M Na-acetate, pH 5.3 (sterile);
- 70% EtOH: ethanol 70% (v/v), stored at -20°C;
- 100%EtOH: absolute ethanol, stored at -20°C.

Procedure
The night before plasmid DNA preparation a single colony of trasformant *E.coli* DH5α cells is used to inoculate 100 ml of selective LB medium and cells are grown overnight at 37°C under stirring (220 rpm).

For plasmid purification proceed as follows:

- transfer the culture in a 250 ml sterile centrifuge bottle and centrifuge at 5000 rmp for 15 min at 4°C (rotor SLA1500);
- discard the supernatant and resuspend the pellet in 4 ml buffer P1 containing RNAse conserved on ice (e.g., 4 ml buffer P1 + 4 µl of RNAse 100 µg/ml);
- transfer the suspension in a 50 ml centrifuge sterile tube (rotor SS34);
- add 4 ml buffer P2, mix gently and incubate for 5 min at RT;
- add 4 ml buffer P3 (stored on ice), mix gently and incubate for 15 min on ice;
- centrifuge at 13000 rpm for 30 min at 4°C;
- equilibrate the Qiagen-tip 100 column with 4 ml buffer QBT;
- transfer the supernatant in a 50 ml sterile tube;
- centrifuge at 13000 rpm for 15 min at 4°C;
- add the supernatant on the Qiagen-tip 100 column;
- wash with 20 ml buffer QC (2 washes of 10 ml);

- elute the DNA with 5 ml buffer QF in a 50 ml sterile tube for Sorvall centrifuge;
- add 3.5 ml of isopropanol for plasmid DNA precipitation;
- centrifuge at 13000 rpm for 30 min at 4°C;
- discard the supernatant and wash the pellet with 4 ml 70% EtOH;
- centrifuge at 13000 rpm for 10 min at 4°C;
- discard the supernatant and air-dry the pellet near the bunsen flame;
- resuspend the pellet in 500 µl TE buffer;
- centrifuge at 3000 rpm for 3 min at 4°C;
- transfer the sample in a 2 ml sterile eppendorf tube and measure the volume;
- add 1/10 of volume of Na-acetate and 2 volumes of 100% EtOH (stored at -20°C);
- incubate the sample for 1 h at least at -20°C;
- centrifuge at 13000 rpm for 15 min at 4°C in a microfuge;
- discard the supernatant and wash the pellet with 1 ml of EtOH 70% (stored at -20°C);
- centrifuge at 13000 rpm for 15 min at 4°C in microfuge;
- remove the supernatant and air-dry the pellet near the bunsen flame;
- resuspend the pellet in 100 µl TE buffer;
- determine the plasmid concentration spectrophotometrically;
- split up in 2-3 aliquots and stored at -20°C.

DNA quantitation

DNA concentration is determined by measuring the absorbance value at 260 nm taking into account that 50 ng/µl DNA solution absorbs 1 at 260 nm. An aliquot (8 µl) of the sample is diluted 100-fold in TE buffer (792 µl) and the absorption spectrum is recorded with HP8453 diodearray spectrophotometer (Hewlett Packard, Agilent, La Jolla, CA, USA). The quality of the DNA plasmid preparation is verified by calculating the A_{260}/A_{280} ratio, which must be ≥ 1.8 for pure DNA, and by restriction analysis.

Restriction analysis

Restriction enzymes and their corresponding buffers used for the analysis of plasmids and their derivatives are indicated in the following table:

Restriction enzyme	*U/µl*	*Manufacturer*	*Working temperature, °C*
*BamH*I	15	Amersham Pharmacia	30
*Nde*I	20	New England BioLabs	37
*Pvu*I	10	New England BioLabs	37
*Sca*I	10	Fermantas	37
*Sph*I	10	Fermentas	37
*Xho*I	10	Fermantas	37

Solutions
- Buffer K (Amersham Pharmacia, now GE Healthcare, Little Chalfont,UK) for *BamH*I: 200 mM Tris/HCl, pH 8.5, 100 mM $MgCl_2$, 10 mM DTT, 1000 mM KCl;
- Buffer NEB3 (New England BioLabs, Ipswich,USA) for *Pvu*I: 50 mM Tris/HCl, pH 7.9, 100 mM NaCl, 10 mM $MgCl_2$, 1 mM DTT;
- Buffer NEB4 (New England BioLabs) for *Nde*I: 200 mM Tris-acetate, pH 7, 500 mM K-acetate, 100 mM Mg-acetate, 10 mM DTT;
- Buffer R (Fermentas, Vilnius, Lithuania) for *Xho*I: 10 mM Tris/HCl ,pH 8.5, 10 mM $MgCl_2$, 100 mM KCl e 0.1 mg/ml BSA;
- Buffer H (Fermentas) for *Sca*I and *Sph*I: 500 mM Tris/HCl, pH 8.5, 1000 mM KCl, 100 mM MgCl, 10 mM DTT;
- Loading Dye 10X (LD10X): 0.25% (w/v) blu di bromofenolo, 30% (v/v) glycerol in H_2O.
- GeneRuler 1 Kb DNA ladder (Fermentas): mixture of DNA fragments with a size ranging from 250 to 10000 bp;
- TE Buffer: 10 mM Tris/HCl, pH 8.0 (25°C), 1 mM EDTA, sterile.

Procedure
- thaw aliquots of the solutions of the plasmid of interest;

- If needed, prepare a dilution of the sample in H_2O to obtain a final concentration between 30 and 100 ng/µl;
- prepare the samples as follows, by adding the enzyme last:

Plasmid	1-4 µl
Buffer 10x	1 µl
Restriction enzyme	1 µl
H_2O to a final volume of	10 µl

- incubate for 1 h at the working temperature for the enzyme (see table above) in a thermomixer (Eppendorf, Cambridge, UK) or a thermostatted bath;
- add 1 µl of LD10x at the end of the single digestion to block the reaction, to load the sample and to add dye that will allow monitoring the electrophoretic migration of the samples.

For the double digestion proceed as follows:
At the end of the single digestion add:

Buffer 10x	2 µl
Restriction enzyme	1 µl
H_2O to a final volume of	20 µl

- incubate for 1 h at optima temperature for the enzyme;
- add 2 µl of LD10x.

At the end of the double digestion for the triple add:

Buffer 10x	3 µl
Restriction enzyme	1 µl
H_2O to a final volume of	30 µl

- incubate for 1 h at the working temperature for the enzyme;
- add 3 µl of LD10x.

Analytical electrophoresis on 1% agarose gel

The analysis of DNA fragments obtained by PCR or plasmid digestion is done by agarose gel electrophoresis.

Materials
- Electrophoresis apparatus: Submarine Mini Horizontal HE33B (Hoefer-Amersham).

Solutions
- Buffer TAE 50X: 200 mM Tris-acetate, pH 8.5, 1 mM EDTA, made up by mixing 242 g Tris, 57.1 ml acetic acid, 100 ml 500 mM EDTA, pH 8 to a final volume of 1 l with H_2O. The solution is sterilized in the autoclave
- Ethidium bromide (EtBr): ethidium bromide 0.5 mg/ml in H_2O.

Procedure
- prepare TAE 1X buffer: 8 ml TAE50X buffer + 392 ml ultrapure H_2O;
- add 0.5 g of agarose (Sigma A9539) to 50 ml of TAE1X buffer;
- melt under stirring on a hot plate;
- allow cooling under stirring by transferring to another plate;
- add 50 µl of EtBr when the temperature is ≈ 40°C;
- pour into the gel casting mold and allow solidifying;
- load samples and apply 80 V for 1.5 h until the band of the dye reaches the end of the gel;
- visualize the bands on a transilluminator (Vilber Lourmat, Marne-la-Vallée, France) and record the photograph of gel (Kodak Digital Science 1D; Rochester, New York, USA).

Polymerase Chain Reaction

Materials
- thermocycler (Gene Amp PCR 2400, Applied Biosystem, Foster City, CA, USA);

Solutions
- *Pfu* Ultra DNase (Agilent, La Jolla, CA, USA), DNA polymerase from *Pyrococcus furiosus*, 40 U/µl.
- Pfu Buffer 10X (Agilent).
- dNTPs, (Takara, Madison, WI, USA), 2.5 mM each;

- pDON201-MICAL1 13 ng/µl TE buffer;
- oligonucleotide primers, 100 µM each (see Table 10.3).

Primers are designed using the program OligoCalc, (www.basic.northwestern.edu/biotools/OligoCalc.html) that calculates the percentage of G+C and the presence of potential hairpin formation. The melting temperature T_m is calculated using the following formula, which take into account the presence of mismatches, the percentage of GC (%GC) and the number of nucleotides of the oligo (N):

$$T_m = 81.5 + 0.41(\%GC) - {}^{675}\!/_{N} - \%mismatch$$

Procedure
- prepare the reaction mixture as follows:

	Product				
	MOCHLIM2		*MOCHLIM4*		*MICAL*
pDON201-MICAL (13 ng/ µl), µl	2.5	5	2.5	5	10
Oligo MICAL Fw new (10 µM), µl	2	2	2	2	8
Oligo MICALLIM Rev2 (10 µM), µl	2	2	-	-	-
Oligo MICALLIM Rev4 (10 µM), µl	-	-	2	-	-
Oligo MICALFL Rev(10 µM), µl	-	-	-	-	8
dNTPs (2.5 mM each), µl	4	4	4	4	16
Pfu Ultra Buffer 10X, µl	5	5	5	5	20
Pfu DNA Polymerase (2.5 U/µl), µl	1	1	1	1	4
H_2O	33.5	31	33.5	31	134
Total volume, µl	50	50	50	50	200

The solutions are added in the following order using Gilson pipettes equipped with sterile filter tips and a different set of pipettes aside for PCR for the addition of primers:
- sterile H_2O, Pfu ultra buffer, dNTPs, primers, template DNA, Pfu Polymerase;
When the reaction mixture is >50 µl:
- aliquot 50 µl of the sample in PCR tubes.
For the amplification:
- transfer the sample into thermocycler;
- set-up the following conditions: initial denaturation, 1 min at 95°C; cycle 1-30, 30 s at 95°C, 30 s at 60°C and 6 min at 68°C; final extension 10 min at 68°C.
At the end of the PCR reaction the DNA fragments are purified by agarose gel electrophoresis followed by extraction and purification with Illustra GFX PCR DNA and Gel Band Purification Kit (GE Healthcare, Little Chalfont, UK).

Preparative agarose gel electrophoresis

The procedure is the same as that described for analytical agarose gel electrophoresis but with the following modifications:

- use TAE1X buffer that has been sterilized in autoclave to prepare the gel and the running buffer;
- add 10 µl of EtBr 0.5 mg/ml to the agarose solution rather than 50 µl to limit the photodegradation of DNA fragments;
- carry out the electrophoresis at 60 V rather than 80 V;
To check if sufficient separation of DNA fragments has been obtained during the electrophoresis run, switch off the power and examine the gel with a hand held UV lamp (λ 254 nm). If DNA fragments are sufficiently separated:
- excise the bands containing the DNA fragments of interest with a blade previously cleaned with 100% EtOH;
- transfer the bands into sterile eppendorf tubes, previously weighted to determine the amount (in mg) of gel.

Purification of DNA fragments

Illustra GFX PCR DNA and Gel Band Purification kit (GE Healthcare) is used to purify the DNA fragments of interest. The kit is designed for the purification and concentration of DNA fragments from PCR or enzymatic digestion and from agarose gels. It is important to control the solution pH, which must be ≤7.5 for an efficient binding of the DNA to the silica membrane and the successive elution in H_2O or in a buffer at pH 8.

Materials
- GFX Illustra spin column.

Solutions (stored at RT)
- Capture buffer type 3 containing pH indicator;
- Wash Buffer: 10 ml 100% EtOH + 2.5 ml of wash buffer;
- Elution Buffer type 4: 10 mM Tris/HCl, pH 8;
- Elution Buffer type 6: nuclease free H_2O;
- Na-acetate: 3 M Na-acetate pH 5.3 (sterilized in autoclave);

Procedure
- add the calculated volume of capture buffer to each sample (i.e.: 10 µl/10 mg of gel);
- incubate at 60°C in a thermomixer until the agarose gel is dissolved (≈20 min) mixing every 3 min. Check the color of the solution that must be yellow; if the color of solution is pink adjust the pH by adding Na-acetate.
- centrifuge at 13000 rpm for 1 min in microfuge at RT;
- load each sample onto a spin column placed in a 2 ml eppendorf tube;
- centrifuge at 13000 rpm for 1 min at RT;
- discard the flow through;
- load 500 µl of wash buffer;
- centrifuge at 13000 rpm for 1 min at RT;
- discard the eluate;
- place the column in a new eppendorf tube;
- load 10-50 µl of elution buffer type 4 or 6 and incubate for 1 min at RT;
- centrifuge at 13000 rpm for 2 min at RT;
- prepare samples for the electrophoresis analysis:

DNA solution	2 µl
TE buffer	7 µl
LD10x	1 µl

- store DNA solution at -20°C.

Quantitation of DNA obtain from the purification

To determine the concentration of the DNA fragments after the purification step, aliquots of a pUC18 vector solution (50 ng/µl) linearized with *Eco*RI are loaded on the analytical agarose gel (1%) to have a range between 25 and 200 ng of DNA.

The samples are prepared as follows:	*MOCHLIM2*		*MOCHLIM4*		*MICAL*		*pUC18EcoRI*			
pUC18/*Eco*RI (50 ng/µl), µl	-	-	-	-	-	-	0.5	1	2	4
MOCHLIM2	3	5	-	-	-	-				
MOCHLIM4	-	-	3	5	-	-				
MICAL	-	-	-	-	3	5				
TE, µl	6	4	6	4	6	4	8.5	8	7	6
LD 10X, µl	1	1	1	1	1	1	1	1	1	1
Total volume, µl	10	10	10	10	10	10	10	10	10	10
pUC18, ng							25	50	100	200

Cloning of the cDNA coding for MOCHLIM and MICAL in pJET1.2 blunt-end vector

The DNA fragments encoding MOCHLIM and full-length MICAL obtained from PCR and purified were cloned in pJET1.2/blunt-end cloning vector (CloneJET PCR cloning kit, Thermo Scientific Fermentas, Waltham, MA, USA). The CloneJET PCR Cloning kit presents a series of advantages such us: (i) a positive selection system, in that the vector contains a lethal gene that is disrupted by ligation of the DNA insert into the cloning site; (ii) blunt-end PCR products generated by proofreading DNA polymerase (e.g., Pfu Polymerase) can be directly ligated in just 5 min with the pJET1.2 blunt linearized vector included in the kit. The kit also contains a "PCR product" to be used as positive control to verify the efficiency of the blunting and ligation steps.

Sticky-end cloning protocol for positive control

- Set up the "blunting reaction mixture" on ice:

	Positive control
Reaction Buffer 2x, µl	10
Control "PCR product" (24ng/ µl) µl	2 (48 ng)
pJET1.2/blunt cloning vector (50 ng/ µl), µl	1 (0.05 pmol ends)
Water, nuclease free, µl	5
DNA Blunting enzyme , µl	1
Total volume, µl	18

- centrifuge at 13000 rpm in microfuge for 3 min at 4°C;
- incubate the mixture at 70°C for 5 min;
- chill on ice;
- set-up the ligation reaction mixture on ice by adding the following to the blunting reaction mixture:

pJET1.2/blunt cloning vector (50 ng/ µl), µl	1 (0.05 pmol ends)
T4 DNA Ligase (5 U/ µl), µl	1
Total volume, µl	20

- centrifuge the mixture at 13000 rpm in for 1 min at 4°C;
- incubate the ligation mixture at 22°C in a thermomixer for 15 min;
- transform *E.coli* DH5α competent cells with 5 µl of the ligation mixture (as described previously);
- select transformants on LB-Amp (100 µg/ml) plates.

Blund-end cloning protocol for MOCHLIM and MICAL

- Set up the "ligation reaction mixture" on ice using the solutions including in the kit

	MOCHLIM2	*MOCHLIM4*	*MICAL*
Reaction Buffer 2x, µl	10	10	10
MOCHLIM2 (2338 bp, 25 ng/µl)	4 (100 ng)	-	-
MOCHLIM4 (2437 bp, 17 ng/µl)	-	6 (102 ng)	-
MICAL (3200 bp, 65 ng/ µl), µl	-	-	3 (195 ng)
pJET1.2/blunt cloning vector (50 ng/ µl), µl	1	1	1 (0.05 pmol ends)
Water, nuclease free, µl	4	2	5
T4 DNA Ligase (5 U/ µl), µl	1	1	1
Total volume, µl	20	20	20

- centrifuge the mixture at 13000 rpm for 1 min at 4°C in microfuge;
- incubate the ligation mix at 22°C in a thermomixer for 15 min;
- transform *E.coli* DH5α competent cells with 5 µl of the ligation mix and the transformants are selected on LB-Amp (100 µg/ml) plates.

Analysis of the transformants by colony PCR

To check the presence of the correct plasmid in the *E.coli* cells transformed with the ligation mix, the trasformants are analysed by colony PCR. The same method is used to verify the cloning of cDNA fragments encoding MOCHLIM and MICAL in pET23b vector.

Solutions
- Go Taq Polymerase: DNA Polymerase from *Thermus aquaticus* (Promega, Madison, WI, USA) 5 U/ µl;
- Go Taq buffer 5x (Promega);
- dNTPs (Takara) 2.5 mM each;
- pJETFw primer (included in CloneJET PCR cloning kit, Table 10.4), 10 µM;
- pJETRev primer (included in CloneJET PCR cloning kit, Table 10.4), 10 µM;
- T7 fw (Amersham Pharmacia) primer, 5′-TAATACGACTCACTATAGGG-3′, 10 µM;
- T7 terminator (Amersham Pharmacia) primer, 5′-GCTAGTTATTGCTCAGCGG-3′, 20µM.

Procedure
- set up the following Master Mix:

	Master Mix
GoTaq Buffer, µl	100
H_2O, µl	327
dNTPs, µl	40
pJETFw, µl	10
pJETRev, µl	10
GoTaq , µl	3
Total volume, µl	500

- distribute 20 µl aliquots of the Master Mix into PCR tubes;
- inoculate a colony of *E.coli* DH5α into one of the PCR tubes (negative control);
- add 60 ng of a well characterized plasmid derivative that has the same vector, but that contains a different insert into another PCR tube (positive control);

For each construct, 10 transformants are analyzed.
- pick up the colony and replicate it on a selective LB plate and then dissolve the rest of the cells in a PCR tube containing the Master Mix;

Amplify the desired DNA fragments using the same PCR conditions as those used for their initial production. At the end:
- add 2 µl of LD10X to each PCR tube;
- analyze by agarose gel electrophoresis;
- choose the clones containing the correct insert for the subsequent storage in glycerol at -80°C, midi prep and restriction analysis.

Two positive clones for each plasmid will be sequenced. The pJET derivatives containing the DNA coding for MOCHLIM and the full-length MICAL were sequenced by Primm srl (Milano, Italy) using the Sanger method with ddNTPs labeled with fluorophores and separated by capillary electrophoresis. The plasmid solution (50 µl) to provide must have a concentration of 150 ng/µl in H_2O. An aliquot (3 µl) of such plasmid solution is diluted in TE buffer up to 10 µl and 1 µl of LD10X is added for (1%) agarose gel electrophoresis. The image of the gel must be sent to Primm with the sample to be sequenced. pJETFw and pJETRev (1 µM, 30 µl) primers were also sent to Primm for sequencing of the samples. For each sequencing reaction 10 µl of primer solution is used. To complete sequencing, three specific primers (Table 10.4) have been designed.

Subcloning of fragments encoding MOCHLIM (1-771 aa), MOCHLIM (1-786 aa) and the full-length MICAL in pET23b vector

pJET derivates containing the correct DNA fragment coding for MOCHLIM2, MOCHLIM4 and full-length MICAL were used for subcloning into a pET23b vector, in order to express the eterologous proteins with a C-terminal His-tag in *E.coli* cells.

Aliquots of pET23b , pJET-MOCHLIM2, pJET-MOCHLIM4 and pJET-MICAL plasmid are digested with *Nde*I restriction enzyme, followed by *Xho*I. For pJET-MICAL, at the end of the double digestion, the sample was precipitated, resuspended in H_2O and incubated with *Pvu*I to discriminate between the pJET vector (2990 bp) and the DNA fragments encoding MICAL (3200 bp).

For the first digestion with *Nde*I the following samples were prepared:

	pET23b	*MOCHLIM2*	*MOCHLIM4*	*MICAL*
pET23b (20 µg/µl), µl	20	-	-	-
pJET-MOCHLIM2 (1.1 µg/µl), µl	-	9	-	-
pJET-MOCHLIM4 (0.6 µg/µl), µl	-	-	16	-
pJET-MICAL (1.08 µg/µl)	-	-	-	10
NEB4 buffer	12	12	12	12
*Nde*I (20 U/µl)	1	1	1	1
H_2O	87	98	91	97
Total volume, µl	120	120	120	120

- incubate 1h and 30 min at 37°C;
- withdraw an aliquot (3 µl) of each sample, add TE buffer (6 µl) and LD10X (1 µl);
- load the samples on agarose gel and start the electrophoresis;

In the mean time:

- add 1 µl of *Nde*I to the remaining reaction mixture and incubate for 1 h at 37°C;

If the digestion with *Nde*I was successful after 1 h (as judged by analytical electrophoresis):

- inactivate *Nde*I by incubating the reaction mixture at 60°C for 20 min;
- prepare the second digestion by adding to the samples:

	pET23b	*MOCHLIM2*	*MOCHLIM4*	*MICAL*
pET23b *Nde*I, µl	120	-	-	-
pJET-MOCHLIM2/*Nde*I	-	120	-	-
pJET-MOCHLIM4/*Nde*I	-	-	120	-
pJET-MICAL/*Nde*I, µl	-	-	-	120
Buffer R	14	14	14	14
*Xho*I (10 U/µl)	1	1	1	1
H_2O	5	5	5	5
Total volume, µl	140	140	140	140

- incubate for 1 h and 30 min at 37°C;
- withdraw 3 µl from each sample, add TE buffer (6 µl) and LD10X (1µl) and analyze electrophoretically;

In the mean time:

- add 1 µl of *Xho*I to the remaining reaction mixture and incubate for 1 h at 37°C;

If the second digestion was successful:

- inactivate *Xho*I by incubating the reaction mixture at 80°C for 20 min.

After the double digestion, for pET23b, pJET-MOCHLIM2 and pJET-MOCHLIM4 samples, proceed as follows:

- add LD10x (10 µl) to each sample;
- load each sample on preparative agarose gel and purify the fragments of interest with the Illustra GFX PCR DNA and Gel Band Purification kit.

pJET-MICALFL was further digested with *Pvu*I:

- divide the reaction mixture in two aliquots;
- add 10 µl of Na-acetate, H_2O to a volume of 100 µl and 1 ml of cold 100% EtOH to each sample;
- incubate for 1 h at least at -20°C;
- centrifuge at 13000 rpm for 15 min at 4°C;
- discard the supernatant and add 1 ml of 70% EtOH;
- centrifuge at 13000 rpm for 15 min at 4°C;
- discard the supernatant and dry on air the pellet;
- resuspend the pellet in 30 µl TE buffer;
- set up the digestion reaction with *Pvu*I:

	MICAL
pJET-MICAL/*Nde*I/*Xho*I, µl	48
NEB3 buffer, µl	7
BSA (1 mg/ml), µl	7
*Pvu*I (10 U/µl), µl	1
H_2O, µl	7
Total volume, µl	70

- incubate for 1 h and 30 min at 37°C;
- withdraw an aliquot (3 µl) for the analytical agarose gel electrophoresis;
- add 1 µl of *Pvu*I to the remaining reaction mixture and incubate for 1 h at 37°;
If the digestion with PvuI after 1 h was successful:
- add LD10x (7 µl) to the sample, load on preparative agarose gel and purify the fragment of interest.

The purified DNA fragments were ligated using 60 ng of pET23b vector and two different molar vector:insert ratios (1:2 and 1:4) for each plasmid.

Materials
T4 Ligase: DNA Ligase of T4 phage (5 U/µl, Fermentas);
T4 Ligase Buffer 10X: 400 mM Tris/HCl , pH 8, 100 mM $MgCl_2$, 100 mM DTT, 5 mM ATP.

Procedure
- set up the following reaction mixtures in eppendorf tubes:

	pET23b	*MOCHLIM2*		*MOCHLIM4*		*MICAL*	
pET23b *Nde*I/*Xho*I/*Pvu*I (30ng/µl), µl	2	2	2	2	2	2	2
pJET-MOCHLIM2 *Nde*I/*Xho*I (80 ng/µl), µl	-	1.5	3	-	-	-	-
pJET-MOCHLIM4 *Nde*I/*Xho*I (60 ng/µl), µl	-	-	-	1.5	3	-	-
pJET-MICAL/*Nde*I/*Xho*I (40ng/µl), µl	-	-	-			3	6
T4 ligase buffer	3	3	3	3	3	3	3
T4 ligase (5 U/µl)	1	1	1	1	1	1	1
H_2O	24	22.5	21	22.5	21	21	18
Total volume, µl	30	30	30	30	30	30	30

- incubate over-night at 16°C.

For each sample an aliquot (4 µl) of the reaction mixture is used to transform *E.coli* DH5α cells made competent with the RbCl method. The trasformants are selected on LB-Amp (100 µg/ml) plates, and then analyzed by colony PCR using T7 promoter and T7 terminator primers to identify clones containing the correct insert. Among the positive clones, two are used to purify the plasmid by midi prep, followed by restriction analysis. The plasmid preparations will be used for the expression of MICAL forms proteins in *E.coli* cells.

10.3. Production of human MICAL1 forms in Escherichia coli cells

E.coli Rosetta (DE3) and BL21(DE3) cells are used for the production of the truncated MO, MOCH and MOCHLIM forms and the full-length human MICAL1 for the production of the proteins with the His_6-tag at their C-terminus.

Preparation of cell culture for the expression of MICAL forms in 2.5 l flasks

E.coli Rosetta(DE3) cells that have been made competent with $CaCl_2$ method are transformed with pET derivatives encoding MICAL forms. BL21(DE3) competent cells are transformed with p18 plasmid encoding GroE (Castanié et al., 1997) first, then transformed with pET23b derivatives coding for MICAL forms (Table 10.2).

Procedure
- transfer ≈30 colonies of transformants in 50 ml of LB medium supplemented with Amp (0.1 mg/ml) and Chl (0.25 mg/ml);
- incubate the flask in an incubator at 25°C under stirring (220 rpm) and monitor the cells growth by measuring the OD_{600};

When OD_{600} is ≈1:
- add 50 µl of ampicillin solution (100 mg/ml) and transfer the flask at 4°C.

The day after:
- harvest the cell cultures under sterile conditions;
- resuspend the pellet in 10 ml of LB medium;
- inoculate 500 ml of selective LB with 5 ml of cell suspension to have an initial OD_{600} of ≈0.05;
- incubate at 25°C under stirring (220 rpm);

When the OD_{600} is ≈1:
- add 500 µl of Amp stock solution (100 mg/ml) and 500 µl of 1 mM IPTG (0.1 mM final concentration);
- transfer the cell culture at 15°C;
- add 500 µl of Amp every 8-15 h;
- monitor the cell growth by measuring OD_{600};
- harvest the cells 24 after IPTG addition.

Preparation of cell culture for the expression of MICAL forms in 12 l fermentor

Preparation of the preculture
- transfer ≈30 colonies of *E.coli* Rosetta (DE3) or BL21(DE3, p18) cells freshly transformed with pET23b derivatives encoding MICAL forms (Table 10.2) in two 2 l flask containing 300 ml of selective LB medium;
- incubate the flask in an incubator at 25°C under shaking (220 rpm) and monitor the cells growth by measuring the OD_{600};

When OD_{600} is ≈1:
- add 300 µl of ampicillin solution (100 mg/ml) and transfer the flask at 4°C.

Preparation of fermentor and cells growth
- position the fermentor vase containing 12 l of sterile LB medium in the MF100 fermentor (New Brunswick Scientific, Enfield, CT, USA);
- connect the aeration system and the bath thermostatted at 25°C;
- equilibrate at 25°C under stirring (140 rpm);
- harvest the cells from the preculture under sterile conditions (centrifugation at 6000 rpm for 10 min at 4°C, rotor SLA1500);
- remove the supernatant and resuspend the pellet in 30 ml LB medium;
- add the antibiotics and the suspension under sterile conditions to the fermentor;
- set-up stirring at 140 rpm and the airflow 5-6 l/min;

When OD_{600} is ≈1:

- lower the temperature to 15°C;
- add 12 ml of IPTG solution (100 mM) and 12 ml of ampicillin solution (100 mg/ml);
- add 12 ml of ampicillin solution every 12 h;
- follow the cells growth by measuring OD_{600};
40 h after the addition of IPTG solution:
- harvest the culture using 1 l bottles for Beckamn Avanti J-20 (Beckman, Brea, CA, USA) centrifuge equipped with JLA 8.1 rotor at 6000 rpm for 10 min at 4°C;
- remove the supernatant and resuspend the pellet with saline solution (200-250 ml) and transfer the suspension in centrifuge tube and centrifuge at 6000 rpm for 15 min at 4°C (rotor SLA1500);
- remove the supernatant, weight out the pellet and store the cells at -20°C.

Total cell extracts preparation

The aliquots of culture used to measure the OD_{600} before and after the addition of IPTG solution are used for the preparation of total cell extracts for the analysis of the time-course of protein production by SDS-PAGE. The samples are prepared as follows:

- transfer the sample (1-1.4 ml) in an eppendorf tube;
- centrifuge at 13000 rpm for 3 min at 4°C;
- discard the supernatant and resuspend the pellet in a volume of SB1x calculated as follows:
  OD_{600} x 100 x sample volume (ml)
- mix with vortex;
- incubate at 100°C for 10 min;
- centrifuge at 13000 rpm for 30s;
- store at -20°C for SDS-PAGE.

10.4 Small and large-scale purification of MICAL forms

Small-scale purification of MICAL forms

Small-scale homogenization of E.coli cells (2-6 g) by sonication

Materials
- Branson Ultrasonic Sonifier250 (Branson, Darbury, CA, USA) equipped with a microtip;
- DNase: Deoxyribonuclease from bovine pancreas type II-S (Sigma D4513);

Solutions
- Protease inhibitor cocktail, EDTA free (Sigma P8849).
- buffer A: 50 mM Na-phosphate, pH 7.5, 100 mM NaCl, 10% glycerol;
- homogenization buffer: buffer A + DNase (few crystals), protease inhibitors cocktail (50 µl/g of cells), 1 mM PMSF, 1 mM 2-ME, 5 or 20 mM imidazole;

Procedure
- resuspend the cells in 2.5 ml homogenization buffer/g cells;
- transfer the suspension into a glass tube and place on an ice-salt mixture;
- sonicate for 4 min (eight 30 s cycles); instrument setting: power, 60 W; output, 60%; duty cycle, constant; the temperature is maintained below 5°C by waiting between sonication cycles.
At the end of sonication:
- add 2.5 ml homogenization buffer/g cells;
- mix gently and transfer to 50 ml centrifuge tubes uge and centrifuge at 18000 rpm for 1 h at 4°C (rotor SS34);
- recover the supernatant (crude extract), measure the volume and check the pH;
- transfer 1 ml of supernatant in an eppendorf tube for the determination of protein concentration by the Bradford method and for the analysis by SDS-PAGE.

Small-scale purification of MICAL forms - Ni-NTA affinity chromatography

Materials
- Ni-NTA Sepharose resin (HisPur Ni-NTA Resin, Thermo Fisher Scientific);
- column for chromatography (2x9 cm);
- HP8354 diodearray spectrophotometer connected to a thermostatted bath at 17°C.

Solutions
- buffer A: 50 mM Na-phosphate, pH 7.5, 100 mM NaCl, 10% glycerol;
- buffer A + 20, 100, 200 and 500 mM imidazole;

Procedure
This procedure is used to check the productivity of the cells expressing MICAL forms and in preliminary experiments during the set-up of the purification procedure.
- add Ni-NTA Sepharose resin (1 or 2 ml) equilibrated in buffer A + 5 or 20 mM imidazole to the crude extract obtained by sonication (see above);
- incubate on a wheel (6 rpm) for 1 h at 4°C;
- transfer the resin into the column and let it pack;
- collect the flow-through (FT);
- elute the proteins by applying 5 volumes of:
    Buffer A+ 5 or 20 mM imidazole
    Buffer A + 20 mM imidazole
    Buffer A + 100 mM imidazole
    Buffer A + 200 mM imidazole
    Buffer A + 500 mM imidazole

1 or 2 ml fractions are collected and analyzed by (1) recording the absorption spectrum with a hp8453 diodearray spectrophotometer at 17°C, (2) SDS-PAGE and (3) measuring the NADPH oxidase activity (see below).

For MOCHLIM:
- pool the fractions containing most of the protein based on their absorption spectrum;
- concentrate the sample to a final volume of 1-2 ml with a CentriconYM30 filter device by centrifugations at 3500xg in a swing-out rotor (Labfuge, Heraeus) for 10 min at 4°C each;
- analyze the sample before and after concentration as described for the individual fractions and by determining the protein concentration with the Bradford method;
- store the sample overnight on ice at 4°C.

MOCHLIM preparations obtained by Ni-NTA affinity chromatography (see above) were further purified by gel filtration on a Superose12 column or by anion exchange chromatography on a MonoQ column.

Small-scale final purification of MOCHLIM - Gel filtration

Materials
- Superose12 column for FPLC, cutoff 10000-30000, stationary phase 24ml: dextran and agarose (microsphere diameter 8-12 μm) (Amersham Pharmacia);
- FPLC Akta apparatus (GE Healthcare);
- HP8453 diodearray spectrophotometer and Cary100 spectrophotometer (Varian, Mulgrave, Australia);

Solutions
- buffer B: 50 mM Na-phosphate, pH 7.5, 100 mM NaCl, 10% glycerol, 1 mM EDTA, 1 mM DTT

Procedure
- load the sample (200-500 μl) on a Superose12 column equilibrated in buffer B;
- inject the sample and elute at a flow rate of 0.5 ml/min collecting 0.5 ml fractions;
- analyze the fractions by recording the absorption spectrum at 17°C and by SDS-PAGE;
- pool the fractions containing most of MOCHLIM;
- centrifuge at 18000 rpm for 10 min at 4°C (SS34);
- concentrate the sample to a final concentration >2 mg/ml with a Centricon YM30 device;

- analyze the sample before and after concentration by (1) recording the absorption spectrum, (2) measuring the standard NADPH oxidase activity, (3) determining protein concentration with the Bradford method and (4) by SDS-PAGE;
- slip the sample in 0.2 ml aliquots;
- flash-freeze in liquid nitrogen;
- store at -80°C.

Small-scale final purification of MOCHLIM - Anion exchange chromatography

Materials
- MonoQ anion exchanger column (Amersham Pharmacia);
- FPLC Akta apparatus (GE Healthcare);
- HP8354 diodearray spectrophotometer and Cary100 spectrophotometer;

Solutions
- buffer A: 50 mM Na-phosphate, pH 7.5, 10% glycerol, 1 mM EDTA, 1 mM DTT
- buffer A + 1 M NaCl;

Procedure
The MonoQ column is equilibrated with buffer in which the protein is conserved.
- load the sample (0.5-2 ml) in the loading loop;
- injetct the sample;
- flow 5 ml of buffer A + 25 or 100 mM NaCl at a flow rate of 0.5 ml/min;
- apply a linear gradient form 25 or 100 to 500 mM NaCl in 60 column volume;
- collect 0.5-1 ml fractions;
Then proceed as described for the gel filtration on Superose12 column.

Large-scale purification of MICAL forms - Ni-NTA Sepharose affinity chromatography

Homogenization of E.coli cells (20-40g) by sonication

Materials
- Rosette cooling cell (250 ml) (Branson);
- Branson Ultrasonic Sonifier250;
- DNase: Deoxyribonuclease from bovine pancreas type II-S (Sigma D4513);

Solutions
- Protease inhibitor cocktail, EDTA free (Sigma P8849).
- buffer A: 50 mM Na-phosphate, pH 7.5, 100 mM NaCl, 10% glycerol;
- homogenization buffer: buffer A + DNase (few crystals), protease inhibitors cocktail (50 µl/g of cells), 1 mM PMSF, 1 mM 2-ME, 5 or 20 mM imidazole;

Procedure
The procedure is the same as that described for the homogenization of 2-6 g cells with the following modifications:
- transfer the cell suspension in a rosette cooling cell that allows a good efficiency of mixing and cooling of the sample during sonication;
- place the rosette cell on ice and layer salt only on the top of bulk ice;
- sonicate for 8.5 min (seventeen 30 s cycles).

Large-scale purification of MOCH - Ni-NTA affinity chromatography

The purification of the MO form was carried out as described in Zucchini et al., 2011.

Materials
- Ni-NTA Sepharose resin (Ni Sepharose 6 Fast Flow, GE Healthcare);
- dialysis membranes (Spectra/Por MWCO 12-14000, Spectrum Laboratories, Inc. Rancho Dominguez, CA, USA) previously washed in ultrapure water;
- XK16 column (1.6x19 cm; Amersham Pharmacia);

- peristaltic pump Pump P-1 (Amersham Pharmacia);
- fraction collector Bromma 2111 Multirac (LBK, Uppsala);
- FPLC Akta apparatus (GE Healthcare);
- HP8354 diodearray and Cary100 spectrophotometers connected to thermostated bath set at 17°C.

Solutions
- Buffer A: 50 mM Na-phosphate, pH 7.5, 100 mM NaCl, 10% glycerol;
- Buffer A + 20 mM imidazole;
- Buffer A + 500 mM imidazole;
- Buffer B (dialysis buffer): 50 mM Na-phosphate, pH 7.5, 100 mM NaCl, 10% glycerol, 1 mM EDTA, 1 mM DTT;

Procedure
- load the crude extract on the Ni-NTA Sepharose column with a peristaltic pump at a flow rate of ≈42 ml/h at 4°C, in the cold room;
- wash with 1 column volume of buffer A + 5 mM imidazole, 1 mM 2-ME (flow rate: 40 ml/h) collecting 5-7 ml fractions;
- wash with 10 column volumes of buffer A + 20 mM imidazole at 4°C (overnight, flow rate: 9 ml/h) collecting 5-7 ml fractions;
- connect the column to the Akta apparatus for FPLC and to a thermostatted bath (5°C);
- load pump A with buffer A + 1 mM 2-ME and pump B with buffer A + 500 mM imidazole, 1 mM 2-ME;
- flow 1 column volume of buffer A + 20 imidazole (5 % buffer B);
- apply a linear imidazole gradient: from 20 to 200 mM imidazole in buffer A in 10 column volumes with a flow rate of 1 ml/min and collecting 2 ml fractions;
- analyze the collected fractions by: (1) recording the absorption spectrum and (2) by SDS-PAGE;
- pool the purest MOCH containing fractions on basis of absorption spectrum;
- centrifuge at 18000 rpm for 10 min at 4°C (rotor SS34);
- concentrate to 4-6 mg/ml by ultrafiltration in an Amicon apparatus equipped with YM30 membrane, the sample is kept on ice and under gently stirring (60 rpm).

At the end of concentration:
- centrifuge at 18000 rpm for 10 min at 4°C (rotor SS34);
- dialyze overnight against 2 l of buffer B at 4°C;
- centrifuge at 18000 rpm for 15 min at 4°C (rotor SS34);
- split sample in 0.2-0.5 ml aliquots;
- flash-freeze in liquid nitrogen;
- store at -80°C.

At this stage only trace amounts of contaminating proteins are present, which can be removed by gel filtration on a Superose12 column or by anion exchange chromatography.

Final MOCH purification - Gel filtration

Aliquots up to 500 µl of MOCH preparation obtained by Ni-NTA affinity chromatography are gel filtered on a Superose12 column in buffer B as described previously for small-scale purification of MOCHLIM. Individual fractions and the final sample are analyzed by (1) recording the absorption spectrum, (2) SDS-PAGE, (3) measuring the standard NADPH oxidase activity and (4) by dynamic light scattering (DLS).

Analysis of samples by dynamic light scattering (DLS)

Dynamic light scattering measures the dimensions of particles in solution based on the analysis of the brownian motions that determine the movement of the particles. When light pass through moving particles it is "scattered". This scattering and its decay depends on the dimension of the particles in solution (fast small molecules will lead to a wider scattering than slowly moving larger molecules) and on the composition of solvent. DLS allow to determine the radius of the particle, from which calculates its

mass assuming a globular particle. In addition DLS can also be used to monitor the stability and the tendency of the sample to aggregates under various conditions, such as sample concentration, buffer composition and pH.

Materials
- 50 µl quartz cuvette;
- Dynapro MS/X apparatus (Protein Solutions, Lakewook, NJ, USA);

Solutions
- buffer;
- protein solution: 0.1-5 mg/ml.

Procedure
Data acqusition
- set up the instruments parameters for the acquisition of data through the Dynamic V5 interface that controls the:

Acquisition time	15 s
Sensitivity	80%
Temperature	15°C
Solvent	10% glycerol (for protein stored in buffer B) Water (for protein stored in 20 mM Hepes/KOH buffer, pH 7)
pH	7

- centrifuge 100 µl of buffer at 13000 rpm for 10 min at 4°C;
- transfer 60 µl of the supernatant into the cuvette;
- start the acquisitions of the signal and stop after the acquisition of at least 20 measures validated by the instrument;

This measurement is carried out to check the presence of particles and the stability of the instrument. For the proteins samples the procedure is the same of that described for the buffer. At the end of the data acquisition the software can calculate number of particle in solution and their radius, along with the degree of polydispersity of each species. To calculate the mass of each particle the thickness of the water shell (0.2 nm) is subtracted from the radius calculated by the software.

Final MOCH purification - Anion exchange chromatography

MOCH preparation after Ni-NTA chromatography can be further purified by anion exchange chromatography on a MonoQ column.

Materials
- dialysis membrane (Spectra/Por MWCO 12-14000, Spectrum Laboratories) previously washed in ultrapure water;
- MonoQ anion exchanger column (Amersham Pharmacia);
- FPLC Akta apparatus (GE Healthcare);
- HP 8354 diodearray spectrophotometer connected to a thermostatted bath at 17°C.

Solutions
- buffer A: 20 mM Na-phosphate, pH 7.5;
- buffer A + 40 mM NaCl (dialysis buffer);
- bufferA + 1 M NaCl.

Procedure
- thaw an aliquot of 0.8 ml MOCH solution obtained by Ni-NTA affinity chromatography;
- centrifuge at 18000 rpm for 10 min at 4°C (SS34 rotor, Sorvall RC6 Plus);
- recover the sample and analyze it by (1) recording the absorption spectrum, (2) determining the protein concentration with the Bradford method and (3) SDS-PAGE;

- transfer the sample into dialysis membrane;
- dialyze against 500 ml of buffer A + 40 mM NaCl for 4 h at 4°C;
- repeat the previous step;
- dialyze against 1.5 l of buffer A + 40 mM NaCl for 16 h at 4°C;
- centrifuge at 18000 rpm for 10 min at 4°C (rotor SS34).

For the chromatography of sample proceed as describe previously for final small-scale purification of MOCHLIM.

Large-scale purification of MOCHLIM - Ni-NTA affinity chromatography

The details of the protein purification by Ni-NTA Sepharose resin are discussed in Chapter 4.
The MOCHLIM4 form (1-783, which will be indicated as MOCHLIM) is purified as indicated for MOCH, with the following modifications:
- add 1 mM PMSF to buffer A and buffer A + 20, 50 and 500 mM imidazole;
- elute MOCHLIM by applying a linear gradient of imidazole from 50 to 200 mM in 9 column volumes;
- add 0.5% protease inhibitors cocktail to the pooled fractions and at the end of the dialysis.

At this stage MOCHLIM preparation shows the presence of contaminating proteins with a mass of ≈22 kDa that can be removed by gel filtration on a small-scale on a Superose12 column and on a large-scale on a Superdex200 column.

Final MOCHLIM purification - Small-scale gel filtration

Aliquots up to 500 µl of MOCHLIM preparation obtained by Ni-NTA affinity chromatography are gel filtered on a Superose12 column in buffer B as described previously for small-scale purification, with the following modifications:

- add 0.5% of protease inhibitors cocktail to the polled fractions;
- concentrate in a Amicon apparatus (3 ml) by ultrafiltration rather than in a CentriconYM30 filter device.

Final MOCHLIM purification - Large-scale gel filtration

Materials
- Superdex 200 prep grade resin (GE Healthcare);
- XK16column, height 100 cm, diameter 1.6 cm (Amersham Pharmacia);
- peristaltic pump Pump P-1 (Amersham Pharmacia);
- fraction collector Bromma 2111 Multirac (LBK, Uppsala);
- HP 8354 diodearray spectrophotometer.

Solutions
- buffer B + 1 mM PMSF: 50 mM Na-phosphate buffer, pH 7.5, 100 mM NaCl, 10% glycerol, 1 mM EDTA, 1 mM DTT, 1 mM PMSF;

Procedure
- load the sample 2-3 ml onto the column containing 150ml of Superdex200 resin equilibrated in buffer B + 1 mM PMSF;
- flow buffer B + 1 mM PMSF with a flow rate of 0.5 ml/min;
- collect 1.5-3 ml fractions;
- analyze the fraction by (1) recording the absorption spectrum and (2) SDS-PAGE;
- pool the fractions containing most of MOCHLIM as judge by the absorption spectrum of the individual fractions;
- add 0.5% of protease inhibitors cocktail;
- centrifuge at 18000 rpm for 10 min at 4°C;
- concentrate the sample to 3-5 mg/ml in Amicon apparatus equipped with YM30 membrane;
- analyze the sample befor and after concentration as for the fractions and determine the protein concentration with the Bradford method;
- split the sample in 0.2-0.5 ml aliquots;
- flash-freeze in liquid nitrogen and stored at -80°C.

Large-scale purification of MICAL - Ni-NTA affinity chromatography

The details of the protein purification by Ni-NTA Sepharose resin are discussed in Chapter 4.
The full-length form of MICAL is purified as indicated for MOCH, with the following modifications:
- add 1 mM PMSF to buffer A and buffer A + 20 and 500 mM imidazole;
- elute MOCHLIM by applying a linear gradient of imidazole from 20 to 200 mM in 10 column volumes;
- add 0.5% protease inhibitors cocktail to the pooled fractions and at the end of the dialysis.

At this stage MICAL preparation shows the presence of contaminating proteins and it is further purified by anion exchange chromatography on a MonoQ column as described previously for MOCH or on a large-scale on a Q-Sepharose resin.

Final MICAL purification - Large-scale anion exchange chromatography

Materials
- XK16 column (1.6x19 cm, GE Healthcare) containing Q-Sepharose Fast flow resin (GE, Healthcare);
- Akta apparatus for FPLC (GE Healthcare);
- HP8453 diodearray spectrophotometer connected to a thermostatted bath at 17°C.

Solutions
- buffer A: 50 mM Na-phosphate, pH 7.5, 1 mM PMSF;
- buffer A + 100 mM NaCl;
- buffer A + 1 M NaCl.

Procedure
- load the sample onto the column containing Q-sepharose resin (10 ml) equilibrated with buffer A+ 100 mM NaCl in cold room;
- flow 2 volumes of buffer A + 100 mM NaCl by gravity and collect 5 ml fractions;
- connect the column to FPLC apparatus, of which pump A was washed with buffer A and pump B with buffer A + 1 M NaCl, and to a thermostatted bath at 10°C;
- flow 5 volumes of buffer A + 100 mM NaCl with a flow rate of 1 ml/min and collect 2 ml fractions;
- elute proteins by applying a first linear gradient from 100 to 500 mM NaCl in 60 column volumes and a second gradient from 500 to 1000 mM NaCl in 5 column volumes and collect 2 ml fractions;
- analyze the individual fractions by (1) recording the absorption spectrum and (2) by SDS-PAGE;
- pool the fractions enriched in MICAL;
- add 0.5% of protease inhibitors cocktail to the pooled fractions;
- centrifuge the sample at 18000 rpm for 10 min at 4°C;
- concentrate the sample up to 5 mg/ml in Amicon apparatus equipped with YM30 membrane;
- centrifuge the sample at 18000 rpm for 10 min at 4°;
- dialyze the sample against 2 l of buffer B overnight at 4°C;
- split the sample in 0.2-0.5 ml aliquots;
- flash-freeze in liquid nitrogen and store at -80°C.

Before and after concentration and dialysis analyze the sample as done for the individual fractions and determine the protein concentration with the Bradford method.

10.5. N-terminal sequencing and mass determination of MICAL forms

The N-terminal sequence and the mass of MICAL forms are determined by mass spectrometry in the laboratory of Prof. Gabriella Tedeschi (Università degli Studi di Milano, Dipartimento di Scienze Veterinarie e Sanità Pubblica). For the determination of the N-terminal sequence of protein in solution and of the mass of the intact protein 100 and 10 pmole of sample are required, respectively. For the analysis, the samples had to be stored in a buffer with low ionic strength and devoid of components such as glycerol and DMSO for technical reasons. In our case, buffer with high ionic strength was required to maintain the stability of MICAL forms, thus for their analysis proteins were concentrated to ≈150 μM

(≈10-20 mg/ml) in 50 mM Na-phosphate buffer, pH 7.5, 100 mM NaCl, in a way that samples can be dilute at low ionic strength for their analysis by mass spectrometry.

Protein preparation - Gel filtration on Sepharose G25(medium) column

Materials
- PD10, Sepharose G25 column (1.9x11 cm, 9 ml; GE Healthcare);
- HP 8453 diodearray spectrophotometer;
- Microcon centrifugal filter YM30 (Millipore).

Solutions
- equilibration buffer: 50 mM Na-phosphate, pH 7.5, 100 mM NaCl.

Procedure
- equilibrate PD10 column with 50 ml (5 volumes) of equilibration buffer;
- load ≤ 500 µl volume of sample (0.75-1.5 mg);
- elute with 0.5 ml aliquots of equilibration buffer;
- collect 1.5 ml in the first fraction;
- collect 0.5 ml in the next fractions;
- record the absorption spectrum of the individual proteins;
- pool the fractions containing the protein;
- concentrate the sample in a microcon filter device by centrifugation at 12000xg at 4°C in microfuge to reach a final concentration of 50-150 µM (10-20 mg/ml, 0.05 ml, 0.5-1 mg);
- flash-freeze the sample and store at -80°C until analysis.

Before and after concentration the sample is analyzed by (1) recording the absorption spectrum, (2) determining the protein concentration with the Bradford method and (3) SDS-PAGE.

Mass spectrometry analysis

The N-terminal sequence of MICAL forms was determined with a pulsed-liquid sequencer equipped with a PTH analyser (Procise model 491, Applied Biosystems, Foster City, CA, USA) either after SDS-PAGE and electrotransfer on polyvinyldifluoride membranes (ImmobilonP, Merck-Millipore, see below) or on 50-150 µM protein samples that had been gel filtered in 50 mM sodium phosphate buffer, pH 7.5, 100 mM NaCl and concentrated. Concentrated MICAL solutions were also used for mass determination of the intact protein by an AUTOFLEX III MALDI-TOF instrument (Bruker Daltonics, Milano, Italy). After dilution, each sample was loaded onto a MALDI plate with a matrix of sinapinic acid in 0.1% trifluoroacetic acid: acetonitrile (2:1). Mass spectrometry analysis was carried out on a Bruker Daltonics Reflex IV instrument (Bruker Daltonics,) equipped with a nitrogen laser, operating in positive mode. Each spectrum was accumulated for at least 200 laser shots and Bruker peptide calibration standards were used for calibration.

10.6. Quantitation of FAD content and the extinction coefficient at 458 nm of human MICAL1 forms

Among essentials steps for the characterization of flavin-containing enzymes are (i) the determination of the stoichiometry of the bound flavin cofactor and (ii) their extinction coefficient in the visible region. Several methods are available in the literature in order to achieve such goals (Aliverti et al., 1999), which mainly differ for the method of protein denaturation for the release of flavin-bound cofactor. Moreover, the flavin stoichiometry and the degree of purity of protein preparation can be determined from the UV/Vis ratio of the absorption spectrum under native and denaturating conditions.

Determination of the theoretical UV/Vis ratio for MICAL forms

We use the expasy tool Peptide Property Calculator (www.expasy.org/tools/protparam) to calculate the extinction coefficient at 280 nm of the apo-protein forms. The program calculates the extinction coefficient at 280 nm of the protein under denaturing conditions using the following formula:

$$E_{Mapo} = aE_{M,\,Tyr} + bE_{M,\,Trp} + cE_{M,\,Cys}$$

Where a, b and c are the number of tyrosine, tryptophan and cystein residues per mol of protein and $E_{Tyr,\,Trp,\,Cys}$ are the molar extinction coefficient of the residues at 280 nm.

The ε_{280} of holoproteins is calculated by adding the ε_{280} of 22.7 $mM^{-1}cm^{-1}$ of free FAD in 3 M guanidine (obtained from 5 experimental determinations by 2-fold dilution of 20 μM FAD solution in 20 mM Tris/HCl, pH 8, 500 mM NaCl, 6 M guanidine).

$$\varepsilon_{280}^{holoMICAL} = \varepsilon_{280}^{apoMICAL} + \varepsilon_{280}^{FAD}$$

To determine the theoretical UV/Vis ratio in denaturing conditions the ε_{280} of the holoprotein is divided by the ε_{448} of 11.9 $mM^{-1}cm^{-1}$ of the free FAD in 3 M guanidine. The calculated UV/Vis ratio expected for MICAL forms are indicated in Table 10.5

Table10.5. Theoretical values of the UV/Vis (A_{280}/A_{448}) ratio expected for human MICAL1 and MO, MOCH and MOCHLIM forms when different percentage of apoprotein is present. The extinction coefficient at 280 nm ($\varepsilon_{280}^{holoMICAL}$) was calculated with ProtParam tool at www.expasy.ch and the extinction coefficient at 280 and 448 nm of free FAD in 3 M guanidine was experimentally determined (5 determinations).

f holo	*f apo*	ε_{280}^{FAD}	ε_{448}^{FAD}	$\varepsilon_{280}^{holoMO}$	A_{280}/A_{448}	$\varepsilon_{280}^{holoMOCH}$	A_{280}/A_{448}	$\varepsilon_{280}^{holoMOCHLM}$	A_{280}/A_{448}	$\varepsilon_{280}^{holoMICAL}$	A_{280}/A_{448}
1	0	22.7	11.9	68.87	7.69	89.84	9.46	100.81	10.38	125.91	12.49
0.95	0.05	21.57	11.31		8.00		9.85		10.82		13.05
0.9	0.1	20.43	10.71		8.34		10.30		11.32		13.66
0.85	0.15	19.30	10.12		8.72		10.79		11.87		14.36
0.8	0.2	18.16	9.52		9.14		11.34		12.50		15.13
0.75	0.25	17.02	8.93		9.62		11.97		13.20		16.02
0.7	0.3	15.89	8.33		10.18		12.69		14.01		17.02
0.65	0.35	14.76	7.74		10.81		13.52		14.94		18.19
0.6	0.4	13.62	7.14		11.55		14.49		16.03		19.54
0.55	0.45	12.49	6.55		12.43		15.63		17.31		21.15
0.5	0.5	11.35	5.95		13.48		17.01		18.85		23.07

Determination of the theoretical UV/Vis ratio for native MICAL forms

We assume that the extinction coefficient at 280 nm calculated under denaturing conditions is the same as that of native protein. The molar extinction coefficient for the holoprotein forms is calculated by adding the extinction coefficient of free FAD at 280 nm (ε_{280} = 21 $mM^{-1}cm^{-1}$) to the extinction coefficient calculated for the apoprotein:

$$\varepsilon_{280}^{holoMICAL} = \varepsilon_{280}^{apoMICAL} + \varepsilon_{280}^{FAD}$$

The UV/Vis ratio (A_{280}/A_{458}) is calculated by dividing the extinction coefficient of holoprotein at 280 nm (Table 10.5) by the extinction coefficient at 458 nm of 8.1 $mM^{-1}cm^{-1}$ determined for the MO form (Zucchini et al., 2011)

$$UV/Vis = \varepsilon_{280}^{holoMICAL} / \varepsilon_{459}^{holoMICAL}$$

Protein	A_{280}/A_{458}
MO	10.5
MOCH	14
MOCHLIM	16
MICAL	18

Protein denaturation with 5% TCA

Solutions
- TCA10%;
- protein solution ≈ 20 µM in 50 mM Na-phosphate buffer, pH 7.5, 100 mM NaCl.

Materials
- HP 8453 diodearray or Cary 100 spectrophotometers connected to a thermostatted bath at 25°C.

Procedure
Protein solutions are freshly gel filtered in 50 mM Na-phosphate buffer, pH 7.5, 100 mM NaCl on a Superose12 column as described previously.

- record the absorption spectrum of MICAL solution (≈20 µM);
- transfer 120-400 µl of protein solution into an eppendorf tube;
- add 1 volume 10% (w/v) TCA solution;
- incubate for 15 min at RT;
- centrifuge at 13000 rpm for 15 min at 4°C;
- transfer the supernatant in a clean eppendorf tube;
- centrifuge at 13000 rpm for 15 min at 4°C;
- transfer directly the supernatant in a quartz cuvette;
- record the absortion spectrum of the supernatant;
- calculate the concentration of FAD:

$FAD, mM = A_{448} / \varepsilon_{448}^{FAD,TCA5\%}$; where $\varepsilon_{448}^{FAD,TCA5\%}$ is the extinction coefficient of 9.7 $mM^{-1}cm^{-1}$ of free FAD in 5% TCA calculated from 5 experimental determinations by 2-fold dilution of FAD (20 µM) in 10%TCA;
- calculate the stoichiometry of FAD bound to the enzyme by dividing the concentration of FAD by that of the starting enzyme determined with the Bradford method by taking into account the protein mass and the 2-fold dilution factor: $FAD/MICAL = (mM, FAD)/(mM, MICAL * 0.5)$;
- calculate the extinction coefficient of bound FAD by dividing the A_{458} of the starting MICAL solution by FAD concentration by taking into account the 2-fold dilution factor:

$\varepsilon_{458}^{MICAL} = A_{458}^{nativeMICAL} * 0.5 / mM, FAD$.

Protein denaturation in buffer containing 3 M guanidine

Solutions
- guanidine buffer: 20 mM Tris/HCl, pH 8, 500 mM NaCl, 6 M guanidine;
- protein solution ≈ 20 µM in 50 mM Na-phosphate buffer, pH 7.5, 100 mM NaCl, 10% glycerol, 1 mM EDTA.

Materials
- Spectrophotometer HP 8453 (Hewlett Packard) or Cary 100 (Varian).

Procedure
Protein solutions are freshly transferred in 50 mM Na-phosphate buffer, pH 7.5, 100 mM NaCl, 10% glycerol, 1 mM EDTA by gel filtration on a Superose12 column or on a SephadexG25 column as described previously.

- record the absorption spectrum of MICAL solutions (150-400µl; ≈20 µM);
- add 1 volume of guanidine buffer and mix well;
- record the absorption spectra for ≈60 min every 1-10 min;
- calculate the concentration of FAD:

$FAD, mM = A_{448} / \varepsilon_{448}^{FAD,3Mguanidine}$; $\varepsilon_{448}^{FAD,3Mguanidine}$ is the extinction coefficient 11.9 $mM^{-1}cm^{-1}$ of free FAD in guanidine buffer determined experimentally;

- calculate the stoichiometry of FAD bound to the enzyme by dividing the concentration of FAD by that of the starting enzyme determined with the Bradford method by taking into account the 2-fold dilution factor: $FAD/MICAL = (mM, FAD)/(mM, MICAL * 0.5)$;
- calculate the extinction coefficient of bound FAD by dividing the A_{458} of the starting MICAL solution by FAD concentration by taking into account the 2-fold dilution factor:

$\varepsilon_{458}^{MICAL} = A_{458}^{nativeMICAL} * 0.5 / mM, FAD$

10.7. Quantitation of zinc ions content of MICAL forms

The determination of Zn^{2+} content of the samples was carried out following the procedure reported in Homsher., R. and Bennie., Z. (1985, Spectrophotometric investigation of sensitive complexing agents for the determination of zinc in serum. Clin. Chem. 31, 1310-1313) modified to reduce the final volume of the assays.

Solutions
- 1 M Hepes/KOH buffer pH 8;
- TCA10%;
- 5BrPAPS 86 mM (1 mg/ml, dissolved in water);
- Zn^{++} stock solution: 1g/l (standard zinc solution for atomic absorption spectroscopy, Sigma 18827);
- Zn^{++} working solution: 50 mg/l, prepared by dilution of 20-fold of Zn^{++} stock solution in water;
- Buffer: 50 mM Na-phosphate, pH 7.5, 100 mM NaCl;
- buffer +TCA: 25 mM Na-phosphate buffer, 50 mM NaCl, 5% TCA;
- MICAL form solution ≈ 20 µM.

Materials
- HP 8453 and Cary100 spectrophotometer thermostatted at 25°C.

Preparation of Zn^{++} standard solutions and calibration
- prepare the standard zinc solutions at different concentration in NaPi buffer as described in the table:

Sample	*Zn^{++} working solution*	*Buffer*	*Total volume*	*Zn^{++}*	
	ml	*ml*	*ml*	*mg/ml*	*µM*
Buffer	0	5	5	-	-
1	0.15	5	5.15	1.456	22.13
2	0.1	5	5.1	0.98	14.19
3	0.05	5	5.05	0.495	7.52
4	0.03	5	5.03	0.28	4.53
5	0.02	5	5.02	0.199	3.03
6	0.01	5	5.01	0.099	1.516

- dilute 2-fold the sample with 10% TCA:

Zn++ standard solution	*sample*	*10%TCA*	*Zn^{++}*	
	ml	*ml*	*mg/ml*	*µM*
blank	Buffer, 0.5	0.5	-	-
1	1, 0.5	0.5	0.73	11.1
2	2, 0,5	0.5	0.49	7.10
3	3, 0.5	0.5	0.25	3.76
4	4, 0.5	0.5	0.14	2.26
5	5, 0.5	0.5	0.1	1.52
6	6, 0.5	0.5	0.05	0.76

For the blank sample:
In a plastic cuvette:
- add 0.7 ml of 1 M Hepes/NaOH buffer, pH 8 and 0.05 ml of 5 BrPAPS (125 µM final concentration);
- record the absorption spectrum and the A_{550} value (A_{550} 1);
- add 0.2 ml of buffer diluted 2-fold in 10%TCA;
- record the absorption spectrum and the A_{550} value (A_{550} 2);
- calculate the value of the blank: A_{550} blank= A_{550} 2- A_{550} 1(0.75/0.9);
Each sample:
- add 0.7 ml of 1 M Hepes/NaOH buffer, pH 8 and 0.05 ml of 5 BrPAPS (125 µM final concentration);
- record the absorption spectrum and the A_{550} value (A_{550} 1);
- add 0.2 ml of Zn^{++} standard solution;
- record the absorption spectrum and the A_{550} value (A_{550} 2);
- calculate the final A_{550} (A_{550}X) value by taking into the account the dilution and the A_{550} of the blank: A_{550}X= [A_{550} 2- A_{550} 1(0.75/0.9)]- A_{550} blank;
- divide the resulting A_{550} value by the extinction coefficient of the zinc-PAPS complex of 130 $mM^{-1}cm^{-1}$ to determine the concentration of zinc present in the sample.
This procedure is used for all zinc standard solutions and the blank sample is repeated after two zinc standard solutions to ensure that the blank A_{550} value is similar for all the samples analyzed.

The following figure shows an example of the calibration curve obtained with zinc standard solutions.

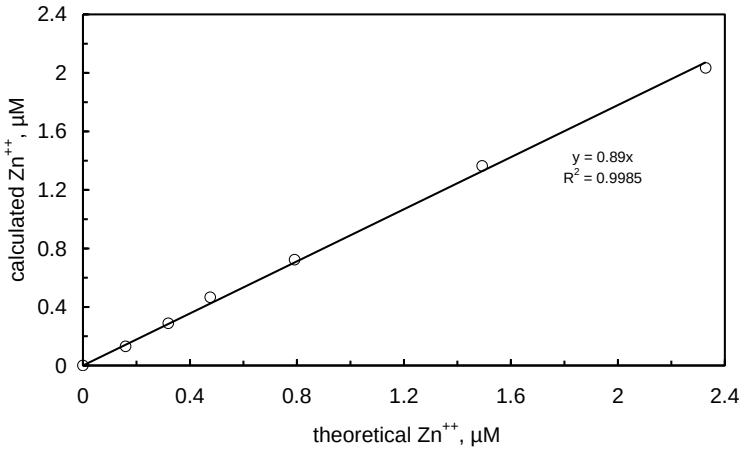

Procedure for the determination of the zinc content of MICAL forms
- denature the protein with TCA5% as described previously;
For zinc quantitation:
- determine the blank A_{550} value as described for the calibration curve;
To quantify the zinc content of the sample, in a 1 ml cuvette:
- add 0.7 ml of 1 M Hepes/NaOH buffer pH 8 in 1 ml plastic cuvette;
- add 0.05 ml of PAPS;
- record the absorption spectrum and sign the A_{550} value (A_{550} 1);
- set-up the following samples individually:

Sample	*Buffer +TCA*	*SN, ml*
1	-	0.2
2	0.05	0.15
3	0.1	0.1
4	0.150	0.05

- determine the A_{550} value (A_{550} 2);
- calculate the zinc content as described previously.

As a part of the method set-up we quantified the amount of zinc in sample obtained by denaturation of MO and MOCH forms, which lack the LIM domain and thus, the associated zinc ions. To ensure that zinc does not precipitate with 5%TCA, control sample was carried out with MO form in which a known amount of zinc was added to the protein solution prior protein denaturation:

	Volume, µl	*µM*
MO, 28 µM	300	13
Zn working solution, 765 µM	20	5
10% TCA	320	
Total volume	640	

The supernatant obtained after incubation for 15 min at RT and centrifugation and the zinc content is determined as described previously.

Control samples were also set-up during each experiment by adding a known amount of zinc standard solution to the supernatant obtained after protein denaturation. Here, an example of the sample set-up is shown:

	"SN only"	"SN+Zn^{++}"	"Zn^{++} only"
SN , 28 μM	75	75	-
Buffer +TCA	75	-	75
Zn^{++} standard solution 19 µM	-	75	75
Total volume	150	150	150

The zinc content was determined using 0.1 ml of each sample.

10.8. Production of mouse CRMP1 forms in Escherichia coli cells

E.coli BL21(DE3) cells made competent with $CaCl_2$ method are freshly transformed with pGEX derivatives (Table 10.2) encoding mouse CRMP1 forms.

Preparation of the preculture
- transfer ≈30 colonies of transformants in a 500 ml flask containing 50 ml of selective LB;
- incubate the flask under stirring (220 rpm) at 25 °C and monitor cell growth by measuring the optical density at 600 nm (OD_{600});

When the cell culture reaches an OD_{600} value of 1:
- add 50 µl of ampicillin solution (100 mg/ml) and transfer the flask in the cold room overnight.

Preparation of the culture
- transfer the preculture in a falcon tube and centrifuge in a swing-out rotor at 3500xg for 10 min at 4°C (Labofuge 400 Heraeus, Chandler, AZ, USA);
- remove the supernatant and resuspend the pellet in 10 ml of LB;
- transfer, under sterile conditions, 5 ml of suspension in a 500 ml of selective LB broth in a 2.5 l flask to have an initial OD_{600} value of ≈0.05;
- transfer the flask in the incubator under stirring (220 rpm) at 25°C;

When the OD_{600} value is ≈1:
- add 500 µl IPTG solution (1 mM final concentration) and 500 µl Amp solution;

16 h after the addition of the IPTG solution:
- transfer the culture in 500 ml centrifuge bottles and centrifuge at 6000 rpm for 15 min at 4°C (rotor SLA 3000);
- discard the supernatant, resuspend the cells with saline solution (0.9% NaCl, 30-40 ml) and pool in a centrifuge tube;
- centrifuge at 6000 rpm for 15 min at 4°C;
- discard the supernatant and weight the cells;
- store at -20°C.

10.9. Purification of mouse CRMP1 forms

Small-scale purification of CRMP forms - Glutathione-Sepharose affinity chromatography

The crude extract is obtained by homogenization of 2 g of *E.coli* BL21(DE3) cells expressing CRMP forms as described for the small-scale purification of MICAL forms.

Materials
- Glutathione Sepharose 4B resin (GE Healthcare) equilibrated in lysis buffer;

Solutions
- Lysis Buffer: 50 mM Hepes/KOH, pH 7.5, 150 mM KCl;
- Elution Buffer: 50 mM Tris/HCl, pH 8.5, 15 mM reduced glutathione (GSH);
- Protease inhibitor cocktail (EDTA free), 50 µl/g cells.

Procedure
- resuspend the resin (0.5 ml/g of cells) in 1 volume of lysis buffer and transfer to a falcon tube;
- add the crude extract (CE);
- incubate for 1 h on a wheel at 6 rpm and 4°C;
- centrifuge in the swing-out rotor at 500xg for 5 min at 4°C;
- remove the supernatant containing unbound proteins (flow-through);
- add 5 ml of lysis buffer and gently mix for 3 min at RT;
- centrifuge in swing-out rotor at 500xg for 5 min at 4°C;
- remove the supernatant (wash 1, W1);
- repeat the last three steps twice for a total of three wash steps (W1 above, W2, W3);
- add 1 ml of elution buffer;
- incubate for 1 h on a wheel at 6 rpm and 4°C;
- centrifuge in the swing-out rotor at 500xg for 5 min at 4°C;
- recover the supernatant (elution 1, E1);
- repeat the last four steps twice for a total of three elution steps (E1 above, E2 and E3).

Fractions collected during the chromatography are analysed by (1) recording the absorption spectrum, (2) SDS-PAGE and (3) determining protein concentration with Bradford method.

Large-scale purification of CRMP (8-525) form

The crude extract is obtained by sonication of 20-30 g of *E.coli* BL21(DE3) cells that had produced the mouse CRMP1 (8-525) form following the same procedure indicated for the homogenization of *E.coli* cells containing MICAL forms (see above).

Materials
- column (14 x 1.7 cm; BioRad, Hercules, CA, USA);
- Glutathione Sepharose 4B resin (GE Healthcare) equilibrated in lysis buffer.

Solutions
- Lysis Buffer: 50 mM Hepes/KOH, pH 7.5, 150 mM KCl;
- Elution Buffer: 50 mM Tris/HCl, pH 8.5, 15 mM glutathione reduce (GSH).
- Cleavage Buffer: 50 mM Tris/HCl, pH 7, 150 mM NaCl, 1 mM EDTA, 1 mM DTT;
- Prescission Protease (2 U/µl, GE Healthcare, stored at -20°C), which is a GST-fusion protein to allow its binding to GSH-Sepharose resin and its separation from the cleaved GST-fusion protein;
- Equilibration buffer: 50 mM Tris/HCl, pH 7;
- Dialysis Buffer: 20 mM Hepes/KOH, pH 7.5, 300 mM NaCl, 10 % glycerol, 1 mM DTT (Stenmark et al., 2007).

Procedure
- resuspend the resin (0.5 ml/g cells) in 1 volume of lysis buffer;
- incubate for 1 h on a wheel at 6 rpm at 4°C;
- centrifuge in a swing-out at 500xg for 5 min at 4°C;
- remove the supernatant containing unbound proteins (flow-through, FT);
- add 50 ml of lysis buffer to the resin and gently mix for 3 min at RT;
- centrifuge in swing-out rotor at 500xg for 5 min at 4°C;

- remove the supernatant (wash 1, W1);
- add 50 ml of lysis buffer to the resin and gently mix for 3 min at RT;
- centrifuge in swing-out rotor at 500xg for 5 min at 4°C;
- remove the supernatant (wash 2, W2);
- add 50 ml of lysis buffer to the resin and gently mix for 3 min at RT;
- pour the suspension into the column, let it pack under flow to fully remove the unbound proteins (W3);
- resuspend the resin in 10 ml of elution buffer;
- transfer the suspension in a falcon-type tube;
- incubate for 15 min on a wheel at 4°C;
- pour the suspension into the column, let it pack under flow and collect bound proteins (E1);
- repeat the last four steps two more times (E2 and E3);
- add 5 ml of elution buffer and collect eluate 4 (E4);
- add 3 ml of elution buffer and collect eluate 5 (E5).

The collected fractions are analyzed by (1) recording the absorption spectrum, (2) SDS-PAGE and (3) determining protein concentration with Bradford method. Fractions containing CRMP (8-525) are pooled and dialyzed against 2 l of cleavage buffer for 20-22 h at 4°C.
To separate CRMP from GST protein at the end of the dialysis:
- remove aggregated proteins by centrifugation at 18000 rpm for 10 min at 4°C (rotor SS34);
- determine the protein concentration with the Bradford method;
- set-up the reaction mixture with prescission protease by adding 10 µl of the protease per mg of GST-fusion protein;
- incubate for 16 h at 4°C in cold room.
To the reaction mixture:
- add 10 ml of GSH-Sepharose equilibrated in equilibration buffer;
- incubate on a wheel for 1 h at 4°C;
- pour the suspension into the column, let it pack under flow and collect the unbound proteins, flow-through (FT);
- flow 40 ml of equilibration buffer and collect 5 ml fractions;
- analyze the FT and individual fractions as described previously;
- add fractions enriched in CRMP to the flow-through;
- centrifuge at 18000 rpm for 10 min at 4°C;
- concentrate the sample to ≈10 mg/ml in an Amicon ultrafiltration apparatus equipped with YM10 membrane;
- centrifuge at 18000 rpm for 10 min at 4°C;
- dialyze against 2 l of dialysis buffer for 16 h at 4;
- recover the sample by centrifugation;
- split the sample in 0.5 ml aliquots;
- flash-freeze in liquid nitrogen and store at -80°C.
The pooled fractions and the sample after concentration and dialysis are analyzed as described for the individual fractions.

At this stage CRMP preparation showed small traces of contaminating proteins and aggregates. Aliquots of CRMP solution obtained by GSH-Sepharose affinity chromatography were further purified by gel filtration on a Superose12 column.

Final CRMP (8-525) purification - Gel filtration

Prior each experiments aliquots up to 500 µl of CRMP (8-525) preparation obtained by affinity chromatography are gel filtered on a Superose12 column in 20 mM Hepes/KOH buffer, pH 7 + 25-100 mM NaCl or in F-buffer no ATP (9.5 mM Tris/HCl buffer, pH 7.7, 45 mM KCl, 0.18 mM $CaCl_2$, 1.18 mM $MgCl_2$, 1.3 mM DTT) as described for MOCHLIM.

The individual fractions and the final sample are analyzed (1) by recording the absorption spectrum, (2) DLS, (3) SDS-PAGE and (4) determining the protein concentration with the Bradford method.

The final CRMP preparation is flash-frozen in liquid nitrogen in 0.5 ml aliquots and stored -80°C or stored overnight on ice at 4°C to if it will be used the day after for experiments.

10.10. Preparation of G- or F-actin solution

Solutions

G-, F- and polymerization buffers are prepared from the following stock solutions:
- 10 mM Tris/HCl buffer, pH 8;
- 100 mM Tris/HCl buffer, pH 7.5;
- 2 M KCl;
- 10 mM $CaCl_2$;
- 20 mM $MgCl_2$;
- 85 mM ATP pH 7 (concentration spectrophotometrically determined; stored at -20°C);
- 100 mM DTT in 50 mM Na-acetate buffer (stored at -20°C);
- G-buffer: 5 mM tris/HCl, pH 8, 0.2 mM $CaCl_2$, 0.2 mM ATP, 1 mM DTT;
- Polymerisation buffer 10X: 50 mM Tris/HCl, pH 7.5, 500 mM KCl, 20 mM $MgCl_2$, 10 mM ATP, 5 mM DTT;
- F-buffer: 0.9 ml G buffer + 0.1 ml F buffer, 9 mM Tris/HCl, pH 8.0, 0.18 mM $CaCl_2$, 45 mM KCl, 1.8 mM $MgCl_2$, 1.3 mM DTT, 1.1 mM ATP;
- G-actin (AKL99, Cytoskeleton, Acoma St. Denver, CO, USA), 1 mg in 5 mM Tris/HCl, pH 8.0, 0.2 mM $CaCl_2$, 0.2 mM ATP, 5% (w/w) sucrose, 1% (w/w) dextran;
- G-pyrenyl-actin solution (AP05-A, Cytoskeleton) 20 mg/ml in 5 mM Tris/HCl, pH 8.0, 0.2 mM $CaCl_2$, 0.2 mM ATP, 5% (w/w) sucrose, 1% (w/w) dextran was diluted to desiderate final concentration in G buffer.

Equipment
- Beckman TL100 ultracentrifuge (Beckman, Brea, CA, USA), equipped with a TLA 100.3 rotor;
- fluorimeter Cary Eclipse (Varian);
- Dynapro MS/X.

Procedure
- resuspend 1 mg of lyophilized G-actin in 100 µl of cold ultrapure water (freshly drawn from MilliQ Reagent water system apparatus, Millipore) to have a G-actin 10 mg/ml stock solution; if pyrenyl-actin is used dissolve 1 mg of lyophilized protein in 50 µl of cold water to have a 20 mg/ml stock solution;
- centrifuge at 13000 rpm for 3 min at 4°C;
- dilute G-actin or G-pyrenyl-actin stock solution to desired final concentration in G buffer (0.2-2 mg/ml) in an eppendorf type for ultracentrifugation (357448, Beckman);
- incubate 1 h on ice;
- centrifuge at 100000 x g (55000 rpm) for 1 h at 4°C in Beckman TL100 ultracentrifuge equipped with a TLA 100.3 rotor;
- transfer the supernatant into a clean eppendorf tube;
- determine the protein concentration with the Bradford method;
- add 1/10 of volume of polymerisation buffer to the G-actin solution;
- incubate 1 h at 25°C in a Thermomixer.

Polymerization can be monitored by dynamic light scattering; for G-pyrenyl-actin polymerization is monitored in a Cary Eclipse fluorimeter (λ_{ex}= 365 nm; λ_{em}= 407 nm).
At the end of the polymerization F-actin solution is maintained on ice or at 25°C.

<u>Monitoring the aggregation state of actin</u>

DLS is used to monitor the polymerization of actin and the effect of MICAL forms on the oligomeric state of actin in a kinetic mode.

Procedure
- set-up the instruments parameters:

Acquisition time	15 s
Sensitivity	50%
Temperature	25°C
Solvent	H_2O or PBS buffer
pH	8

- measure the DLS signal (intensity and average radius of the particles in solution) of G-buffer solution (20 valid acquisitions);
- transfer 120 µl of G-actin solution (0.1-0.18 mg/ml, 2-4.5 µM; after ultracentrifugation) in the cuvette;
- measure the DLS signal for 10 min;
- add 12 µl of polymerization buffer and mix gently with a Gilson P200 pipette equipped with a cut tip;
- follow the increase of DLS signal of the solution until it reaches a maximum and constant value.

If the effect of MICAL forms on the aggregation state of actin is under study:
- add 1.2 µl of 10 mM NADPH solution (100 µM);
- monitor DLS signal for at least 5 min;
- add 1-5 µl of enzyme solution;
- monitor the DLS signal every 15 s for ≈30 min.

At the end:
- transfer the sample into a eppendorf tube;
- centrifuge at 13000 rpm for 15 min at 4°C;
- recover the supernatant and monitor the DLS signal.

Preparation of actin samples for mass spectrometry analysis

To determine the residues of actin that are modified upon incubation with MICAL forms, actin samples are precipitated with cold acetone:methanol to block the reaction at a specific time. The actin samples were prepared at a concentration of ≈1 mg/ml (23 µM), which was the concentration required for their analysis by mass spectrometry carried out in the laboratory of Prof. Gabriella Tedeschi (Dipartimento di Scienze veterinarie e Sanità Pubblica, Università degli Studi di Milano).

Materials
- spectrophometer hp 8453 thermostatted at 25°C.

Solutions
- G- or F-actin solution ≈ 1 mg/ml (23 µM);
- 10 mM NADPH in 20 mM TrisOH (100-200 µM final concentration);
- Catalase 1 mg/ml stock solution in 20 mM Hepes/KOH buffer pH 7 stored at -20°C;
- Catalase working solution 0.1 mg/ml obtained by 10-fold dilution of the stock solution G- or F-buffer;
- MICAL forms stored in buffer B (50 mM Na-phosphate, pH 7.5, 100 mM NaCl, 10% glycerol, 1mM EDTA, 1 mM DTT); Protein solutions was diluted to appropriate concentration in buffer B to add 1 µl of enzyme to 120 µl of actin sample; the final concentrations of MICAL proteins are indicated in the figures legends (Chapter 7);
- Acetone:Methanol: 8 ml acetone (100%) + 1 ml methanol (100%) conserved at -20°C.

Procedure
In a 0.2 ml cuvette:
- transfer 120 µl of G- or F-actin solution;
- record the absorption spectrum and incubate for 2 min;
- add 1-2 µl of 10 mM NADPH (100-200 µM final concentration) and gently mix;
- record the absorption spectrum and incubate for 3 min and check that no changes occur in the absorption spectrum;
- add 1 µl of 0.1 mg/ml catalase (0.83 µg/ml) and mix gently;
- record the absorption spectrum and incubate for 2 min;
- add 1 µl of enzyme solution and record the absorption spectrum to check the formation of turbidity and/or aggregates and record spectra every 20 s to limit the radiation damage of sample;

At the desired time, to block the reaction:

- transfer the sample into a eppendorf tube containing 10 volumes of cold acetone:methanol (e.g., 120 µl sample + 1200 µl acetone:methanol);
- incubate the sample at -20°C for 15-20 h;
- centrifuge at 13000 rpm for 30 min at 4°C (15 min + 15 min);
- discard the supernatant;
- resuspend the pellet in 500 µl of cold acetone:methanol;
- incubate at -20°C for 2 h;
- centrifuge at 13000 rpm for 30 min at 4°C (15 min + 15 min);
- discard the supernatant;
- dry the pellet on air under a hood near a Bunsen burner;
- store the samples at -20°C.

Analysis of actin by mass spectrometry.

This part of the experiments were carried out in laboratory of Prof. G. Tedeschi

For mass determination of the intact protein mass, each actin sample was diluted 10-fold in water and loaded onto a MALDI plate with a matrix of sinapinic acid in 0.1% trifluoroacetic acid: acetonitrile (2:1). Mass spectrometry analysis was carried out on a Bruker Daltonics Reflex IV instrument (Bruker Daltonics,) equipped with a nitrogen laser, operating in positive mode. Each spectrum was accumulated for at least 200 laser shots and Bruker peptide calibration standards were used for calibration. For analysis and identification of the actin modification sites, precipitated protein samples were resuspended in 50 mM ammonium bicarbonate, reduced, alkylated and digested overnight with trypsin (sequence grade), at 37 °C, using a protease: protein ratio (1:10). Tryptic digests were extracted with 50% acetonitrile in 0.1% trifluoroacetic acid, desalted/concentrated on a µZipTipC18 (Millipore) and mass spectrometry analysis was carried out on a Bruker Daltonics Reflex IV instrument (Bruker Daltonics,) equipped with a nitrogen laser, operating in positive mode. Each spectrum was accumulated for at least 200 laser shots and Bruker peptide calibration standards were used for calibration. The identification of the corresponding peptides was carried out using the theoretical fingerprint of actin digested with trypsin with Expasy tools (www.expasy.org, Gasteiger E., Hoogland C., Gattiker A., Duvaud S., Wilkins M.R., Appel R.D. & Bairoch A. (2005) Protein Identification and Analysis Tools on the ExPASy Server in *The Proteomics Protocols Handbook* (Walker, J. M., ed) pp. 571-607 Humana Press).

10.11. NADPH oxidase activity of MICAL forms

MOCHLIM and MICAL preparations (3-5 mg/ml) stored in buffer B (50 mM Na-phosphate buffer, pH 7.5, 100 mM NaCl, 10% glycerol, 1 mM EDTA, 1 mM DTT) are diluted to 1 mg/ml in the same buffer to measure the NADPH oxidase activity. Instead, MO and MOCH solutions are gel filtered on a SepharoseG25 column to transfer the proteins transfer the protein in 20 mM Hepes/KOH, pH 7, 10% glycerol, 1 mM EDTA, 1 mM DTT.

<u>Standard NADPH oxidase activity</u>

Materials
- HP 8453 diodearray and Cary100 spectrophotometers connected to circulating bath set at 25°C.

Solutions
- Assay buffer: 40 mM Hepes/KOH, pH 7;
- NADPH stock solution: 10 mM NADPH in 20 mM TrisOH;

Procedure

The initial velocity of NADPH oxidation is continuously monitored at 340 nm (ε_{340} = 6.23 $mM^{-1}cm^{-1}$) when the Cary100 spectrophotometer is used, when HP 8453 diodearray spectrophotometer is used the entire absorption spectrum of the reaction is recorded every 10 sec and the absorbance trace at 340 nm is used to calculate the initial velocity of the reaction.

The reaction mixture is set-up into 1 ml quartz cuvette as follows:
- add 0.5 ml of assay buffer and 0.49 ml of H_2O;
- mix and incubate at 25°C for 5 min;
- add 10 µl of 10 mM NADPH (100 µM final concentration);
- monitor the absorbance at 340 nm (for Cary100) or record the absorption spectra (for HP8453) for 2 min;
- add 1-10 µl of protein solution.

The initial velocity is expressed as v/E in s^{-1}, where v is the initial velocity of the reaction and E is the total enzyme concentration in the assay determined with the Bradford method and using the theoretical protein mass.

Determination of kinetic parameters of the NADPH oxidase activity of MICAL forms

Materials
- HP 8453 diodearray and Cary100 spectrophotometers connected to circulating bath set at 25°C.

Solutions
- Assay buffer: 40 mM Hepes/KOH, pH 7;
- NADPH stock solution: 10 or 50 mM NADPH in 20 mM TrisOH;
- NADPH 1-5 mM obtained by dilution of the 50 mM NADPH stock solution in H_2O.

Procedure

To determine the apparent steady-state kinetic parameters k_{cat} and K_m for NADPH (K_{NADPH}), the NADPH concentration was varied between 10-600 µM NADPH. For high NADPH concentrations 50 mM NADPH stock solution is used and care is taken to add less than 20 µl/ml assay mixture to avoid altering the pH of the reaction. Enzyme solutions are concentrated to add less than 50 µl/ml assay to start the reaction. The reaction was monitored at 340 nm for NADPH concentrations between 10 and 200 µM. For higher concentration of NADPH the reaction was monitored at 374 nm (ε_{360} = 2.1 $mM^{-1}cm^{-1}$) and at 380 nm (ε_{380} = 1.3 $mM^{-1}cm^{-1}$). When the Cary100 spectrophotometer is used identical reactions are carried out and monitored at the two wavelengths in the overlapping range (with duplicates); when HP 8453 diode array spectrophotometer is used, the absorption spectra of the reaction are recorded every 10 s and the initial velocity of the reaction is calculated from the traces obtained at different wavelengths.

After inspection of double reciprocal plots (Eq.1), the data of v/E were fitted to the Michaelis-Menten equation (Eq.2).

Eq. 1 $$\frac{E}{v} = \frac{K_m}{k_{cat}} * \frac{1}{S} + \frac{1}{k_{cat}}$$

Eq.2 $$\frac{v}{E} = \frac{k_{cat} * S}{K_m + S}$$

where: S is the varying substrate concentration; E is the total enzyme concentration in the assay with the protein concentration determined with the Bradford method and the known protein mass; k_{cat} is the apparent turnover number and K_m is the Michaelis-Menten constant for NADPH.

The Grafit 4.0 software (Erithacus Software Ltd, Horley, UK) was used to determine the kinetic parameters and the associated errors. The k_{cat}/K_{NADPH} was calculated with error propagation according to Bevington (1969).

Effect of the ionic strength on the NADPH oxidase activity of MOCH

Solutions
- Assay buffer: 40 mM Hepes/KOH, pH 7;
- NaCl: 1 M NaCl solution;
- Na-acetate: 1M Na-acetate, pH 7;
- Imidazole-acetate buffer: 200 mM imidazole/acetate, pH 7;
- Tris-acetate buffer: 200 mM Tris/acetate, pH 7;
- NADPH stock solution: 10 mM NADPH in 20 mM TrisOH;
- NADPH 1 mM: 100 µl of NADPH 10 mM + 900 µl of H_2O.

The effect of ionic strength on the NADPH oxidase activity of MOCH was studied by measuring the initial velocity of the reaction in the presence of varying concentration of NADPH and of (1) 20 mM Hepes/KOH buffer, pH 7 (I, 4.4 mM) + NaCl (10-100 mM; I, 29.4-104.4 mM) or Na-acetate (100-250 mM; I, 104.4-254.4 mM), (2) imidazole-acetate buffer pH 7 (50-150 mM; I, 27-81 mM) and (3) Tris-acetate buffer pH 7 (50-200 mM; I, 45-180 mM). The ionic strength of reaction medium was calculated as described in Ellis, K.J., et al 1982.

The effect of imidazole-acetate buffer on the slope of double reciprocal plots $(k_{cat}/K_{NADPH})/(k_{cat}/K_{NADPH})_0$ as a function of ionic strength was well fitted to the limiting case of the Debye Hückel equation (Norby et al., 1997 and Eq 3),

Eq. 3 $$\log(k_{cat}/K_M) = z_E * z_S * \sqrt{I} - \log(k_{cat}/K_M)_0$$

Where: k_{cat}/K_M is the value of the parameter obtained in the presence of a given ionic strength (I); $(k_{cat}/K_M)_0$ is the value of the parameter calculated at zero ionic strength; z_E and z_S are the charge of the enzyme acive site and that of ligand, respectively. For NADPH z_S is -3 or -4 at pH 7.

pH dependence of NADPH oxidase activity of MICAL forms

Solutions
- Mixed Buffer A 2x: 20 mM acetic acid, 10 mM Tris, 10 mM imidazole;
- Mixed Buffer B 2x: 25 mM formic acid, 10 mM tris, 10 mM imidazole;
- NADPH stock solution 10 or 50 mM in 20 mM TrisOH buffer.

The pH dependence of the steady-state kinetic parameters of the NADPH oxidase activity of MICAL forms is studied in mixed buffer that ensures a constant ionic strength over the entire pH range explored (Ellis et al., 1982). In the light of the fact that the ionic strength of any single buffer significantly varies over its useful pH range. Figure 10.X show the plot of ionic strength of the single mixed buffer A as a function of pH to compare with that of complete mixed buffer A and B (Figure 10.X) in which the ionic strength is essentially constant over the pH range form 4.5 to 10. Moreover, the pK_a value for a single buffer varies with temperature and thus, it is important to take into account temperature difference in the calculation of pK_a values using the following relationship:

$$pK_{RT} = pK_T + (RT - T)DT$$

Where RT, T and DT are: the required temperature, the temperature at which the determination was made and the change in pK_a values per degree, respectively (Ellis and Morrison 1982).

The NADPH oxidase activity of MICAL is very sensitive to ionic strength and ions composition, thus mixed buffer A and B are designed to maintain the ionic strength low and constant over the entire pH range investigated by calculating the total charge of the buffer and its ionic strength as a function of pH using the following formula and are indicated in Table 10.5:

$$\text{Total charge} = \left[HA^{z+1}\right](z+1) + \left[A^{z}\right]z + \left[HB^{z'+1}\right](z'+1) + \left[B^{z'}\right]z' + \left[HC^{z''+1}\right](z''+1) + \left[C^{z''}\right]z''$$

$$\text{Ionic strength} = 0.5\left\{\left[HA^{z+1}\right](z+1)^2 + \left[A^{z}\right]z^2 + \left[HB^{z'+1}\right](z'+1)^2 + \left[B^{z'}\right]z'^2 + \left[HC^{z''+1}\right](z''+1)^2 + \left[C^{z''}\right]z''^2 + |\text{total charge}|\right\}$$

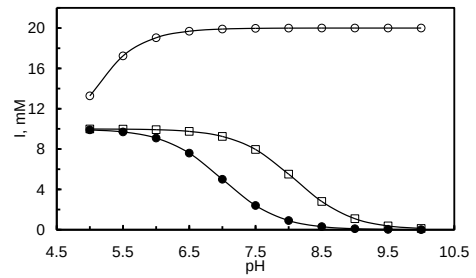

Figure 10.1. Plot of the ionic strength of the single components of mixed buffer A as a function of pH.
○, 20 mM acetic acid; ●, 10 mM imidazole; □, 10 mM Tris.

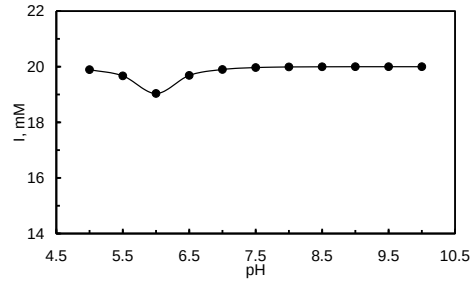

Figure 10.2. Plot of the ionic strength of mixed buffer A as a function of pH. Composition of mixed buffer A: 20 mM acetic acid, 10 mM imidazole, 10 mM Tris.
.

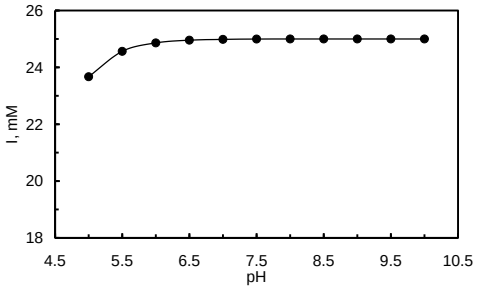

Figure 10.3. Plot of the ionic strength of mixed buffer B as a function of pH. Composition of mixed buffer B: 25 mM formic acid, 10 mM imidazole, 10 mM Tris.

Na-acetate is added to maintain the ionic strength constant at 10 and 12.5 mM for mixed buffer A and mixed buffer B, respectively. For mixed buffers A at pH >6.5 NaOH is added and small amount of HCl (<2 mM) is added to obtain pH 5-6. Mixed buffer B is designed to have an initial pH value of 4.3 in order to add only NaOH solution to reach the desired pH values.

The kinetic parameters of the NADPH oxidation reaction catalyzed by MICAL forms are determined in mixed buffer A and mixed buffer B by varying NADPH concentration as described in the previously.

The v/E values obtained at each pH are fitted to the Michaelis-Menten equation (Eq 2) and the resulting kinetic parameters (k_{cat}, K_{NADPH} and k_{cat}/K_{NADPH}) are fitted to the following equations to determine the pH dependence of the reaction.

Eq 4: $Y = [A_1 * 10^{-2pH} + A_2 * 10^{-(pH + pKa1)} + A_3 * 10^{-(pKa1 + pKa2)}]/[10^{-(pKa1 + pKa2)} + 10^{-(pH + pKa1)} + 10^{-2pH}]$

Eq. 5 : $Y = [A * 10^{(pH - pKa)}]/[1 + 10^{(pH - pKa)}]$

Eq. 6: $Y = [A_1 + A_2 * 10^{(pH-pKa)}]/[1 + 10^{(pH-pKa)}]$

Eq. 7: $Y = [A_1 * 10^{(pKa1-pH)}/ (1 + 10^{(pKa1-pH)}) + A_2 * 10^{(pKa2-pH)}]/ (1 + 10^{(pKa2-pH)})]$

Eq 4. was used to describe the pH profile of the kcat of MO and MOCH. It describes the pH dependence of the parameter that increases from a non-zero value at low pH (A_1) to a maximum (A_2), as a group with pK_{a1} deprotonates, and decreases to another non-zero value (A_3) as a second group with pK_{a2} deprotonates.

Eq.5 was used for the pH profile of the k_{cat} calculated for MOCHLIM. The value of the parameter increases from zero to an upper limit (A) as one group deprotonates.

Eq. 6 was used to describe the pH profile of the k_{cat} calculated for MICAL. The value of the parameter decreases from un upper limit (A_1) at low pH to a lower limit (A_2) when a single group dissociates.

Eq. 7 was used to describe the pH dependence of the k_{cat}/K_{NADPH} and $1/K_{NADPH}$ for all MICAL forms. The value of the parameter decreases from an upper limit (A_1+A_2) at low pH to a second value (A_2) as a group with pK_{a1} deprotonates and decreases to zero as a second group with pK_{a2} also deprotonates.

Table 10.5. Composition of mixed buffer A (20 mM acetic acid, 10 mM imidazole, 10 mM Tris) and B (25 mM formic acid, 10 mM imidazole, 10 mM Tris) stock solution:.

A

					pH										
	Concentration, mM	pK_a	charge		5	5.5	6	6.5	7	7.5	8	8.5	9	9.5	10
Acetic acid	20	4.70	0	acid	6.72	2.76	0.96	0.32	0.10	0.03	0.01	0.00	0.00	0.00	0.00
			-1	base	13.28	17.24	19.04	19.68	19.90	19.97	19.99	20.00	20.00	20.00	20.00
Imidazole	10	7	1	acid	9.90	9.69	9.09	7.60	5.00	2.40	0.91	0.31	0.10	0.03	0.01
			0	base	0.10	0.31	0.91	2.40	5.00	7.60	9.09	9.69	9.90	9.97	9.99
Tris	10	8.09	1	acid	9.99	9.97	9.92	9.75	9.25	7.95	5.51	2.80	1.09	0.37	0.12
			0	base	0.01	0.03	0.08	0.25	0.75	2.05	4.49	7.20	8.91	9.63	9.88
				charge	6.62	2.43	-0.03	-2.34	-5.65	-9.61	-13.57	-16.89	-18.81	-19.59	-19.87
				\charge\	6.62	2.43	0.03	2.34	5.65	9.61	13.57	16.89	18.81	19.59	19.87
				Ionic strength, mM	19.89	19.67	19.04	19.68	19.90	19.97	19.99	20.00	20.00	20.00	20.00
				NaAcetate, mM	0.11	0.33	0.96	0.32	0.10	0.03	0.01	0.003	0.001	0.000	0.000
				I total, mM	20.00	20.00	20.00	20.00	20.00	20.00	20.00	20.00	20.00	20.00	20.00

B

					pH										
	Concentration, mM	pK_a	charge		5	5.5	6	6.5	7	7.5	8	8.5	9	9.5	10
Formic acid	25	3.75	0	acid	1.33	0.44	0.14	0.04	0.014	0.004	0.0014	0.0004	0.00014	4.45E-05	1.41E-05
			-1	base	23.67	24.56	24.86	24.95	24.98	24.99	24.99	24.99	24.99	24.99	24.99
Imidazole	10	7	1	acid	9.90	9.69	9.09	7.60	5	2.40	0.90	0.31	0.1	0.031	0.01
			0	base	0.099	0.31	0.91	2.40	5	7.60	9.09	9.69	9.90	9.97	9.99
Tris	10	8.09	1	acid	9.99	9.97	9.92	9.75	9.25	7.95	5.51	2.80	1.09	0.37	0.12
			0	base	0.008	0.026	0.081	0.25	0.75	2.05	4.48	7.20	8.91	9.63	9.87
				charge	-3.77	-4.89	-5.85	-7.61	-10.73	-14.64	-18.58	-21.89	-23.81	-24.59	-24.86
				\charge\	3.77	4.89	5.85	7.61	10.73	14.64	18.58	21.89	23.81	24.59	24.86
				Ionic strength, mM	23.67	24.56	24.86	24.95	24.98	24.99	24.99	24.99	24.99	24.9	24.99
				NaAcetate, mM	1.33	0.44	0.14	0.044	0.014	0.0044	0.0014	0.0045	0.0001	4.45E-05	1.41E-05
				I total, mM	25	25	25	25	25	25	25	25	25	25	25

Effect of viscosity on the NADPH oxidase reaction of MICAL-MOCH

Solutions
- Buffer stock solution: 80 mM Hepes/KOH, pH 7;
- Assay buffer: 40 mM Hepes/KOH, pH 7 (25 g buffer stock solution + 25 g H_2O);
- Assay buffer + 10, 20, 30, 40, 50% glycerol (w/w);
- NADPH stock solution: 10 or 50 mM NADPH in 20 mM TrisOH;
- NADPH 2 mM: NADPH stock solution is diluted in H_2O.

The v/E values obtained by varying NADPH concentration in the presence of different glycerol concentrations were fitted to Eq (8) (Eser and Fitzpatrick, 2010). The relative viscosity (η_{rel}) values for glycerol have been obtained from the literature (Sheely, 1932).

$$\text{Eq. 8}\quad \frac{v}{E} = \frac{k_{cat} * S}{[K_m * (1 + m * \mu) + S * (1 + n * \mu)*]}$$

Where $\mu = (\eta_{rel} - 1)$; m and n are the effect of viscosity on k_{cat}/K_m and k_{cat} respectively. The m*μ and n*μ values correspond to $(k_{cat}/K_m)_0/(k_{cat}/K_m)_\eta$ and $(k_{cat})_0/(k_{cat})_\eta$ respectively, calculated at different relative viscosity values, which indicate the ratio of the value of the parameter in the absence and in the presence of viscogen at a given concentration. Note that in the original equation μ was $(\eta_{rel}^2 - 1)$, due to a printing error.

Study the effect of F-actin on the NADPH oxidation reaction catalyzed by MICAL forms

Materials
- HP8453 diode array and Cary100 spectrophotometers connected to theromostatted bath at 25°C.

Solutions
- F-buffer (9.5 mM Tris/HCl, pH 7.7, 45 mM KCl, 0.18 mM $CaCl_2$, 1.18 $MgCl_2$, 1.1 mM ATP, 1.33 mM DTT);
- NADPH 10 mM in 20 mM TrisOH;
- F-actin solution (0.2 or 1.3 mg/ml, 4 or 30 μM);
- MICAL proteins stock solutions (2-4 mg/ml) stored in buffer.

Procedure
F-actin solutions were prepared as described previously and maintained on ice during the experiments.

To determine the intial velocity of the NADPH oxidation reaction catalyzed by MICAL forms in the presence of F-actin the enzyme solutions were diluted in buffer B (50 mM Na-phosphate, pH 7.5, 100 mM NaCl, 10% glycerol, 1 mM EDTA, 1 mM DTT). MOCH dilution (0.03 mg/ml, 0.4 μM) is prepared for each single assay carried out in the presence of F-actin due to the instability of the enzyme at this concentration. MOCHLIM is diluted to 0.2 mg/ml, 2 μM and MICAL to 1.3 mg/ml, 10 μM in buffer B. For all MICAL forms the standard NADPH oxidase activity is measured in a Cary100 spectrophotometer in parallel to the assay carried out with HP8453 diode array spectrophotometer in the presence of F-actin to verify the stability of their activity under standard conditions and eventually, to correct the intial velocity measured in the presence of F-actin by taking into the account the partial loss of the activity due to the low concentration of protein solutions required to carry out the assys in the presence of F-actin.

To determine the effect of F-actin on the apparent steady-state kinetic parameters k_{cat} and K_m for NADPH of MICAL forms, the initial velocity of the NADPH consumption is determined by varying NADPH concentration (10-400 μM) in the presence of a fixed concentration of F-actin (4 μM). The NADPH oxidation is monitored by recording the absorption spectra of the reaction every 10 s to detect the formation of turbidity and/or aggregates over time, which would affected the calculation of the reaction velocities. The v/E values are calculated from the absorbance changes at 340 nm.

To determine the apparent K_m for F-actin the v/E values are determined in the presence of a fixed concentration of NADPH (200 μM) by varying F-actin concentration (1-30 μM) in F-buffer.

An example of the experimental set-up to measure the rate of NADPH consumption in the presence of F-actin is described:
In a 0.2 ml cuvette:
- add 120 μl of F-actin solution;
- record the absorption spectrum for 2 min;
- add 2.5 μl of 10 mM NADPH (200 μM final concentration) and mix gently;
- record the absorption spectrum and incubate for 3 min;
- add 1 μl of the enzyme dilution and mix gently;
- record the absorption spectra every 10 s;
- calculate the v/E value from the absorbance trace at 340 nm.

The calculated v/E values are fitted to the Michaelis-Menten equation (Eq.2) after inspection of double reciprocal plots (Eq.1).

10.12. Study of the interaction between MICAL-MO or MOCH and CRMP/8-525

Study of the interaction by Ni-NTA affinity chromatography

Method 1

Materials
- Ni-NTA Sepharose resin HisPur Ni-NTA Resin (Thermo Fisher Scientific);
- HP 8453 diode array spectrophotometer.

Solutions
- buffer A: 20 mM Hepes/KOH buffer, pH 7;
- buffer A + 100 mM NaCl pH 7;
- buffer A + 20, 40, 60, 80, 100, 120, 140, 160, 200 and 500 mM imidazole, prepared by mixing buffer A and buffer A + 500 mM imidazole (pH 7).

Sample preparation
- gel filter CRMP and MO on a Sepharose G25 (medium) column (PD10) in buffer A, as previously described;
- record the absorption spectrum of the individual fractions;
- pool the fractions enriched in the protein;
For MO-only and CRMP-only samples:
- dilute the protein solution to 1 mg/ml in buffer A and a final volume of 1 ml;
- record the absorption spectrum;
For MO+CRMP sample:
- add to 0.5 ml of MO solution (2 mg/ml) to 0.5 ml of CRMP solution (2 mg/ml);
- record the absorption spectrum.

Set-up of interaction assay
- distribute in three eppendorf tubes 1 ml of Ni-NTA Sepharose 50% suspension in buffer A+ 100 mM NaCl;
- let the resin settle and remove the supernatant;

- add 1 ml of MO-only, CRMP-only and MO+CRMP solutions to each tube;
For each sample:
- resuspend the resin by gently mixing;
- incubate on a wheel for 1h at 6 rpm and 4°C;
- pour the suspension into an empty column;
- let the resin pack under flow and collect the flow-through (FT);
- apply:

buffer A + 100 mM NaCl	5x0.5 ml
buffer A + 100 mM NaCl + 20 mM imidazole	1x0.5 ml
buffer A + 100 mM NaCl + 40 mM imidazole	1x0.5 ml
buffer A + 100 mM NaCl + 60 mM imidazole	1x0.5 ml
buffer A + 100 mM NaCl + 80 mM imidazole	1x0.5 ml
buffer A + 100 mM NaCl + 100 mM imidazole	1x0.5 ml
buffer A + 100 mM NaCl + 120 mM imidazole	1x0.5 ml
buffer A + 100 mM NaCl + 140 mM imidazole	1x0.5 ml
buffer A + 100 mM NaCl + 160 mM imidazole	1x0.5 ml
buffer A + 100 mM NaCl + 200 mM imidazole	2x0.5 ml
buffer A + 100 mM NaCl + 500 mM imidazole	4x0.5 ml

- collect 0.5 ml fractions;
- analyze 20 µl of each fraction by SDS-PAGE.

Method 2

Materials
- Ni-NTA Sepharose resin HisPur Ni-NTA Resin, Thermo Fisher Scientific);
- HP 8453 spectrophotometer.

Solutions
- buffer A: 20 mM Hepes/KOH buffer, pH 7, 20 mM imidazole;
- buffer A + 10, 20, 30, 40, 50, 60, 70, 80, 90, 100, 150, 200 and 500 mM NaCl.
- buffer A + 500 mM NaCl, 500 mM imidazole.

Sample preparation
MO and CRMP solutions are gel filtered on PD10 column in buffer A.
Prepare MO and CRMP solutions to a final concentration of 0.5 mg/ml (1 ml).

Set-up of interaction assay
- distribute 1 ml aliquots of Ni-NTA Sepharose 50% suspension in buffer A in three eppendorf tubes;
- let the resin to settle and remove the supernatant;
To two resin aliquots:
- add 1 ml of 0.5 mg/ml MO;
- incubate on a wheel for 1 h at 6 rpm and 4°C;
For each suspension, to remove any unbound proteins:
- pour the suspension in an empty chromatography column;
- let the resin pack under flow and collect the flow-through;
- wash with 5x0.5 ml buffer A;
- resuspend the resin in 0.5 ml of buffer A;
- transfer the suspension into eppendorf tubes;
- let the resin settle and discard the supernatant;
To one aliquot of resin add 0.5 ml of buffer A and this will be the MO-only sample.
To the second aliquot add 0.5 ml of CRMP (0.5 mg/ml) and this will be the MO+CRMP sample.
To the third Ni-NTA Sepharose aliquot that had been set aside at the beginning of the experiment, add 0.5 ml of CRMP (0.5 mg/ml in buffer A) and this will be the CRMP-only sample.
For each one of the three samples:
- mix gently;
- incubate on a wheel for 1 h at 6 rpm and 4°C;
- pour the suspension into an empty column, let the resin pack collecting the flow-through;
- wash with 5x0.5 ml buffer A;

- apply 0.5 ml each of buffer A containing 10, 20, 30, 40, 50, 60, 70, 80, 90, 100, 150, 200 and 500 mM NaCl;
- apply 5x0.5 ml buffer A + 500 mM NaCl, 500 mM imidazole;
- collect 0.5 ml fractions and analyze 20 µl by SDS-PAGE.

Study of the interaction between MO or MOCH and CRMP1/8-525 by measuring the NADPH oxidase activity of MICAL forms

The interaction between MO or MOCH and CRMP/8-525 is also studied by measuring the NADPH oxidation reaction catalyzed by MICAL forms in the presence of CRMP/8-525 under different conditions.

Protein preparations
Prior each experiment aliquots of CRMP/8-525 preparation obtained by GSH-Sepharose chromatography were gel filtered in 20 mM Hepes/KOH buffer, pH 7 supplemented with 10, 25, 50, 100 mM NaCl or in "F-buffer no ATP" (9.5 mM Tris/HCl, pH 7.7, 45 mM KCl, 0.18 mM $CaCl_2$, 1.18 mM $MgCl_2$, 1.33 mM DTT) on a Superose12 column to remove the small amounts of aggregates and contaminating proteins and to transfer CRMP into the desired buffer, MICAL forms preparations stored at -80°C after gel filtration on a Superose12 column in buffer B (50 mM Na-phosphate, pH 7.5, 100 mM NaCl, 10% glycerol, 1 mM EDTA, 1 mM DTT) were used. Buffer exchange of enzyme solutions was not required to due to the addition of a small volume of enzyme to the reaction mixture (1 µl to 120 µl).

NADPH oxidase activity assays in the presence of CRMP/8-525

Materials
- HP8453 diode array spectrophotometer at 25°C.

Solutions
- 20 mM Hepes/KOH buffer, pH 7;
- 20 mM Hepes/KOH buffer, pH 7 + 10, 25, 50, 100, 200 mM NaCl;
- F-buffer;
- NADPH 10 mM in 20 mM TrisOH.

Procedure
The NADPH oxidase activity of MO and MOCH is measured in the presence of a fixed concentration of NADPH (100 µM) and by varying CRMP concentration (1-50 µM) in the indicated buffers. Every 1-1.5 h the standard NADPH oxidase activity of MO and MOCH is measured.

The activity assay is set-up in 0.2 ml cuvette as follows:
- add 120 µl of CRMP solution or dilute CRMP solution at desired concentration in the same buffer to a total volume of 120 µl;
- record the absorption spectrum for 2 min;
- add 1.5 µl of 10 mM NADPH solution (100 µM final concentration) and incubate for 3 min;
- add 1-2 µl of MO or MOCH solution;
- record the absorption spectrum of the reaction every 10 sec.

The v/E values are calculated as described before.

To determine the apparent K_d for MO- or MOCH-CRMP complex when CRMP has an inhibitory effect, the v/E values measured in the presence of CRMP are subtracted to that measured in its absence, vice-versa when a stimulatory effect is observed. The resulting v/E values are fitted to the following equation:

Eq.9 $$EL = \frac{E_{tot} + L_{tot} + K_d \pm \sqrt{(E_{tot} + L_{tot} + K_d)^2 - 4E_{tot}L_{tot}}}{2E_{tot}}$$

Where E_{tot} is the total enzyme concentration; L is the total concentration of the ligand; EL is the concentration of the enzyme-ligand complex; K_d is the dissociation constant for the enzyme-ligand complex. The increase or decrease of v/E is taken as proportional to EL concentration so that E_{tot} is the maximum value of v/E.

10.13. Miscellaneous techniques

Determination of the protein concentration with the Bradford method

Preparation of the Bradford reagent

Solutions
- 85% (w/v) phosphoric acid;
- 100% methanol;
- H_2O;
- Coomassie Brilliant Blue G-250.

Procedure for 1 l of Bradford reagent solution
- dissolve 100 mg of Coomassie Brilliant Blue in 50 ml 100% methanol;
- add 100 ml 85% phosphoric acid;
- add 850 ml of H_2O;
- mix under stirring at least for 2 h at RT;
- filter the solution through a 0.22 µm filter paper and store at 4°C.

Preparation of standard curve and protein samples

Solutions
- Bradford reagent;
- 0.15 M NaCl;
- BSA 0.5 mg/ml.

Materials
- Cary100 spectrophotometer.

Procedure
A range of BSA concentrations (0-6 mg) is used to draw the calibration curve.
In eppendorf tubes:
- add 100 ul (for blank) or 100-x ul of 0.15 M NaCl;
- add 0-x ul of BSA;
- add 1 ml of Bradford reagent;
- incubate for 15-20 min at RT;
- record the A_{595};
- plot the A_{595} as a function of the µg of BSA present in each assay to draw the calibration curve;
- set-up the sample as described for BSA by using aliquots of different volumes for each sample;
- record the A_{595} values;
- check the reproducibility and linearity of the A_{595} values as a function of sample volume added;
- determine the protein concentration of sample using the equation obtained from the linear portion of the calibration curve.

Polyacrylamide Gel Electrophoresis in the presence of Sodium Dodecyl Sulfate (SDS-PAGE)

Materials
- SE 260 electrophoretic apparatus for SDS-PAGE (Amersham, GE);
- dual gel caster SE 245 (Hoefer-Amersham, GE);

Solutions
- 30%AcA+bisAcA: 29.9% (w/v) acrylamide, 0.8% (w/v) N-methylenbisacrylamide;
- 0.5 M Tris/HCl buffer, pH 6.8;
- 1.5 M Tris/HCl buffer, pH 8.8;
- 10% SDS: 10% (w/v) SDS in H_2O;
- AxS: 10% (w/v) ammonium persulphate in H_2O;
- TEMED: N,N,N',N'-tetramethylethylenediamine
- Running buffer 10X: 250 mM Tris, 1.92 M glycine, pH 8.2;
- Running buffer: 10-fold dilution of running buffer 10x in H_2O supplemented with 0.1% SDS (w/v);
- SB4X: 0.5 M Tris/HCl, pH 6.8, 8% SDS (w/v), 40% glycerol (v/v), 20% 2-ME (v/v), 0.005% bromophenol blue (w/v), stored at -20°C;
- staining solution: 40% methanol (v/v), 10% acetic acid (v/v), 0.1% Comassie Blue R-250 (w/v);
- destaining solution: 40% methanol (v/v), 10% acetic acid (v/v).

Procedure
- set-up the following mixture to prepare the running gel for two mini gels (8x10 cm or 10x10 cm; 1 mm thinck)

	AcA+bisAcA	
	10%	12%
H_2O, ml	8.1	6.7
1.5 M Tris/HCl pH 8.8, ml	5	5
AcA+bisAcA, ml	6.6	8
SDS, ml	0.2	0.2
TEMED, ml	0.01	0.01
AxS, ml	0.1	0.1

When the running gel is polymerized
- set-up the following mixture to prepare the stacking gels

	AcA+bisAcA
	4%
H_2O, ml	6.1
0.5 M Tris/HCl pH 6.8, ml	2.5
AcA+bisAcA, ml	1.3
SDS, ml	0.1
TEMED, ml	0.01
AxS, ml	0.05

At the end of the polymerization:
- place the gel onto apparatus for electrophoresis;
- fill the upper and lower chambers of the apparatus with running buffer;
- load the samples;
- apply 20 mA per gel until the BBF reaches the running gel;
- apply 40 mM until the BBF is at the end of running gel;
- incubate the gel in the staining solution for at least 1 h under stirring;
- transfer the gel in the destaining solution.

Blot transfer onto polyvinylidene difluoride (Immobilon) membrane

Materials

The material being used is washed with ultrapure water and the electrophoretic apparatus is also rinsed with 100% methanol followed by water.
- Whatman paper 3 MM (Millipore);
- polyvinylidene difluoride membrane (Immobilon P, Millipore);
- SE 260 electrophoretic apparatus (Amersham);
- Mini-Trans Blot (BioRad 170-3930);

Solutions

All the solution are freshly prepared immediately before the experiment.
- 1.5 M Tris/HCl buffer, pH 8.8 (filter the aliquot to use through 0.22 µm filter);
- 0.5 M Tris/HCl buffer, pH 6.8 (filter the aliquot to use through 0.22 µm filter);
- AcA + bisAcA 30% (use ultrapure AcA and bisAcA and filter the aliquot to use through a 0.22 µm filter);
- SDS 10% (w/v);
- Running buffer 10X: 0.25 M Tris, 1.9 M glycine;
- Running buffer 1X: dilute running buffer 10X 10-fold with H_2O and add 0.1% SDS;
- Mercaptoacetic acid;
- Methanol 100% (MetOH 100%);
- Transfer buffer: 10 mM CAPS, pH 11, 10% methanol, 0.25 mM DTT (DTT is added just before use);
- Staining solution: 40% methanol (v/v), 10% acetic acid (v/v) and 0.1% Comassie Blue R-250 (w/v);
- Destaining solution: 40% methanol (v/v), 10% acetic acid (v/v);

Procedure

- prepare the polyacrilamide gel at the desired % of AcA+bisAcA;
- store overnight at 4°C to ensure that all radical species are decayed;
- set-up the electrophoretic apparatus;
- add mercaptoacetic acid (2 mM) to the running buffer 1X and transfer it only in the upper chamber;
- load the sample (at least 30 µg of protein for the N-terminal sequencing) and carry out the electrophoresis as described previously;

At the end of the electrophoretic migration:
- equilibrate the gel in transfer buffer for 15 min at RT under gentle shaking;
- equilibrate filter papers (2 for 1 gel) in transfer buffer;
- activate the immobilon membrane:
    soak by capillarity in 100%MetOH and equilibrate for 3 min;
    transfer the membrane in ultrapure H_2O for 3 min;
    transfer the membrane in transfer buffer for 3 min;

For the electrotransfer:
- place on the gel cassette holder: filter pad/filter paper/gel/immobilon membrane/filter paper/filter pad;
- close the cassette firmly, being careful not to move the sandwich;
- transfer into the buffer tank of the minitrans blot apparatus;
- add the frozen Bio-Ice cooling unit;
- fill the tank with transfer buffer stored at 4°C;
- add a stir bar and place on a magnetic stirrer to help maintain even buffer temperature and ion distribution in the tank;
- put on the lid and apply 60 V for 2 h.

At the end of the electrotransfer:
- disassemble the blotting sandwich and remove the membrane;
- soak the membrane into staining solution for 5 min under gentle shaking;
- transfer the gel into staining solution to verify the efficacy of the electrotransfer;
- transfer the membrane into a small aliquots of the destaining solution and remove the unbound dye by replacing the destaining solution every few minutes until no Coomassie blue is released;
- wash thoroughly the membrane with several aliquots of ultrapure H_2O until no trace of acetic acid is detected;
- dry the membrane;
- place the membrane between two layers of filter paper and store at -20°C until analysis.

10.14. Technical notes

Ni-NTA Sepharose affinity chromatography

Preparation and regeneration(1)

Materials

- HisPur Ni-NTA Resin (Thermo Fisher Scientific);
- column (2x9 cm).

Solutions
- H_2O;
- equilibration buffer;
- MES buffer: 20 mM MES, pH 5, 100 mM NaCl;
- 20% EtOH: 20% ethanol (v/v).
The solutions are filtered with 0.22 µm and degassed.

Procedure
To equilibrate the resin:
- transfer the desired volume of 50% suspension of Ni-NTA Sepharose resin stored in 20%EtOH in an empty column and pack the resin;
- wash with at least 5 volumes of H_2O;
- equilibrate by flowing 5 volumes equilibration buffer;
- resuspend the resin in 1 volume equilibration buffer;
- transfer in a test tube;
- store at 4°C.
After usage to regenerate the resin flow:
- 5 volumes H_2O;
- 5 volumes MES buffer;
- 3 volumes 20%EtOH;
Resuspend the resin in 1 volume 20%EtOH, transfer to a plastic bottle and store at 4°C.

Preparation and regeneration(1)

Materials
- Ni-NTA Sepharose resin (Ni Sepharose 6 Fast Flow, GE Healthcare);
- XK16 column (1.6x19 cm, Amersham Pharmacia);
- peristaltic pump Pump P-1 (Amersham Pharmacia).

Solutions
- H_2O;
- equilibration buffer;
- Na-phosphate buffer + EDTA: 20 mM Na-phosphate buffer, pH 7.5, 500 mM NaCl, 50 mM EDTA;
- Na-phosphate buffer: 20 mM Na-phosphate buffer, pH 7.5;
- $NiSO_4$: 0.1 M $NiSO_4$;
- 20% EtOH: 20% ethanol (v/v).
The solutions are filtered with 0.22 µm and degassed.

Procedure
To equilibrate the resin:
- transfer the Ni-NTA Sepharose 50% suspension in 20%EtOH (30-60 ml) in a vacuum flask;
- wash 5 times with 1 volume H_2O;
- wash twice with 1 volume equilibration buffer;
- add 1 volume equilibration buffer;
- resuspend the resin and degas for ≈1 h;
- resuspend the resin and pour into the column containing 5 ml of degassed equilibration buffer;
- let the resin settle for ≈10 min, open the column and let the resin pack;
- flow 4 volumes equilibration buffer with a peristaltic pump at a flow rate of 150 ml/h;
- store the column at 4°C.
To regenerate the resin flow:
- 5 volumes Na-phosphate buffer + EDTA;
- 5 volumes Na-phosphate buffer;
- 5 volumes H_2O;
- 0.5 volumes $NiSO_4$;
- 5 volumes H_2O;
- 3 volumes 20%EtOH;

Resuspend the resin in 1 volume 20%EtOH, transfer into a plastic bottle and store at 4°C.

Gel filtration-Superose12 column

Materials
- Superose12 column for FPLC, fractionation range 10000-30000, stationary phase 24ml of dextran and agarose granules (microsphere diameter 8-12 μm) (Amersham Pharmacia);
- FPLC Akta apparatus (GE Healthcare).

Solutions
- 20% EtOH: 20% ethanol (v/v);
- H_2O;
- equilibration buffer.

The solutions are filtered under vaccum though 0.22 μm filter and degassed.

Procedure
- wash the FPLC pumps A and B with 20% EtOH;
- connect the column at a flow rate of 0.1 ml/min (50% B);
- flow 50 ml of EtOH 20%;
- wash pump A with H_2O;
- flow 50 ml water (0% B) at flow rate between 0.1 and 0.5 ml/min until the conductivity value is stable;
- wash pump A with equilibration buffer;
- flow equilibration (0% B) at flow rate between 0.1 and 0.5 ml/min at least 75 ml after that the conductivity value is stable;
- load the sample (200-500 μl) in the loading loop (500 μl);
- inject the sample and elute at a flow rate of 0.5 ml/min collecting 0.5 ml fractions.

At the end of the chromatography:
- wash the FPLC pump A with H_2O;
- flow 50 ml water (0% B) at flow rate between 0.1 and 0.5 ml/min until the conductivity value is stable;
- wash the FPLC pump A with 20% EtOH;
- flow 100 ml 20%EtOH (0% B) at flow rate between 0.1 and 0.3 ml/min until the conductivity value is stable;
- disconnect the column at a flow rate of 0.1 ml/min.

Calibration with standard proteins

Solutions
- standard proteins from the HMW and LMW Gel Filtration Calibration Kits (GE Healthcare): bovine thyroid thyroglobulin, 667000 Da; horse spleen ferritin, 395000 Da; rabbit muscle aldolase 191000 Da; bovine serum albumin BSA, 66000; hen egg ovoalbumin, 49400;
- buffer B: 50 mM Na-phosphate, pH 7.5, 100 mM NaCl, 10% glycerol, 1 mM EDTA, 1 mM DTT.

Procedure
- prepare protein standard solutions at a concentration of 10 mg/ml in buffer B;
- set-up the following protein standard mixtures:

Protein stock, μl	
Thyroglobulin	200
BSA	200
Buffer	200
Total volume, μl	600

Protein stock, μl	
Ferritin	200
Ovoalbumin	200
Buffer	200
Total volume, μl	600

Protein stock, µl	
Aldolase	200
Buffer	400
Total volume, µl	600

- inject 400 µl of one of the protein standard mixtures onto equilibrated Superose12 column and eluted with buffer B at 0.5 ml/min and collecting 0.5 ml fractions;
- draw the calibration curve using the elution volume of the standard proteins (Table 10.x) by plotting the Log of their mass as a function of the elution volume;

Table 10.6. Gel filtration of the standard proteins on a Superose12 column equilibrated and eluted with buffer B. The proteins were gel filtered in buffer B and their elution volume and molecular mass were used to draw the calibration curve shown in Figure 5.4.

Protein	*Molecular mass, Da*	*Elution volume, ml*
Thyroglobulin	667000	7.64
Ferritin	395000	10.48
Aldolase	191000	12.23
BSA	69800	12.99
Ovoalbumin	49400	13.44

Gel filtration-Superdex200 column

Materials
- Superdex 200 prep grade resin (GE Healthcare);
- XK16column (1.6x100 cm, Amersham Pharmacia);
- Packing reservoir (Amersham Pharmacia);
- peristaltic pump Pump P-1 (Amersham Pharmacia);
- Bromma 2111 Multirac fraction collector (LBK, Uppsala).

Solutions
- H_2O;
- EtOH 20%: 20% ethanol (v/v);
- buffer B + 1 mM PMSF: 50 mM Na-phosphate buffer, pH 7.5, 100 mM NaCl, 10% glycerol, 1 mM EDTA, 1 mM DTT, 1 mM PMSF;
- Tween 20.

The solutions are filtered with 0.22 µm and degassed.

Procedure
- transfer 150 ml of Superdex 200 resin into a vacuum flask;
- wash in batch 5-10 times with 1 volume H_2O;
- wash with 475 ml of water + 300 µl of Tween 20;
- resuspend the resin and degas for 30 min;
- attach packing reservoir to the column;
- resuspend the resin, pour the suspension into the column in a single step and cap the packing reservoir;
- connect the pump outlet to the inlet of the packing reservoir and open the column;
- flow buffer B + 1 mM PMSF at a flow rate of 2 ml/min for 2 h and 10 ml/min for 1 h;
- transfer at 4°C;
- load the sample;
- flow buffer B + 1 mM PMSF at 0.5 ml/min;
- collect 1.5-3 ml fractions;
- analyze the fraction by recording the absorption spectrum and by SDS-PAGE.

After use:
- flow at least 5 volumes H_2O at of 1-2 ml/min;
- flow 3 volumes 20% EtOH at 0.5 ml/min;
- resuspend the resin in 1 volume 20% EtOH, transfer in a plastic bottle and store at 4°C.

Anion exchange chromatography - MonoQ column connected to FPLC

Materials
- MonoQ anion exchanger column (Amersham Pharmacia);
- FPLC Akta apparatus (GE Healthcare, Little Chalfont, UK);

Solutions
- 20%EtOH: 20% ethanol (v/v);
- H_2O;
- buffer A: 20 or 50 mM Na-phosphate, pH 7.5;
- buffer A + 1 M NaCl.

The solutions are filtered with 0.22 µm and degassed.

Procedure
The MonoQ column is connected to FPLC Akta apparatus as described for Superose12 column in EtOH20%:
- fill pump A and B with 20% EtOH;
- flow 10 ml 20%EtOH (50% B) at a flow rate between 0.1 and 0.5 ml/min;
- fill pump A and B with 20% H_2O;
- flow 10 ml H_2O (50% B) at flow rate between 0.1 and 0.5 ml/min;
- wash pump A with buffer A;
- wash pump B with buffer A + 1 M NaCl;
- flow 5 ml of starting buffer (2 or 10 %B);
- equilibrate the column as follows:

Volume, ml	*%B*	*ml/min*	*Note*
0-5	2 or 10	0.5	%B depends on the
5-8	gradient up to 100	0.3	starting NaCl
8-13	100	0.3	concentration desired
13-16	Gradient down to 2or 10	0.3	
16-25	2-10	0.5	

At the end of the chromatography:
- apply a linear gradient from 100 to 2-10% buffer B in 10 ml;
- wash pump A and B with H_2O;
- flow 10 ml H_2O (50%B) at 0.5 ml/min;
- wash pump A and B with 20%EtOH;
- flow 10 ml 20%EtOH (50%B) at 0.3 ml/min;
- disconnect the column at a flow rate of 0.1 ml/min.

Anion exchange chromatography - Large-scale purification on Q-Sepharose resin

Materials
- Q-Sepharose Fast Flow resin (GE Healthcare);
- XK16 column (1.6x10 cm, GE Healthcare);
- Akta apparatus for FPLC (GE Healthcare).

Solutions
- 20%EtOH: 20% ethanol (v/v);
- H_2O;
- buffer A: 50 mM Na-phosphate, pH 7.5, 1 mM EDTA, 1 mM PMSF, 1 mM DTT (DTT and PMSF are added prior the use);
- buffer A + 1 M NaCl;
- equilibration buffer (buffer A + 100 mM NaCl) : 50 mM Na-phosphate, pH 7.5, 100 mM NaCl, 1 mM EDTA, 1 mM PMSF, 1 mM DTT;

The solutions are filtered with 0.22 µm and degassed.

Procedure
To equilibrate the resin:
- transfer the required amount of resin (50% suspension in 20% EtOH) into a vacuum flask;
- wash in batch with 1 volume H_2O 5 times;

- wash in batch with 1 volume equilibration buffer 3 times;
- resuspend in 1 volume of equilibration buffer;
- degas for ≈1 h;
- transfer into the column and let the resin settle;
- connect the column to the FPLC apparatus flowing buffer A+ 100 mM NaCl (10%B) at 0.1 ml/min;
- equilibrate the column as described for 10 ml of resin:

Volume, ml	*%B*	*ml/min*
0-40	10	1.5
40-70	gradient up to 100	1.5
70-120	100	1.5
120-150	Gradient up to 2or 10	1.5
150-230	10	1.5

- transfer the column at 4°C in the cold room.

For the chromatography of sample:

- load the sample and wash with 2 volumes of the equilibration buffer through gravity and collect fractions in the cold room;
- connect the column to a bath thermostatted at 10°C and to the FPLC apparatus;
- apply the following gradient (for a 10 ml column):

Volume, ml	*% B*	*Flow rate, ml/min*
0-50	2 or 10	1-1.2
50-650	gradient up to 50	1-1.2
650-750	gradient up to 100	1-1.2
750-760	100	1-1.2

- collect 5-2 ml fractions;

At the end of chromatography to regenerate the resin:

- apply a linear gradient from 100% to 10% buffer B in 5 volumes ml with a flow rate of 1-2 ml/min;
- flow 3 volumes equilibration buffer ;
- flow at least 5 volumes water;
- flow 5 volumes 20% EtOH;
- resuspend in 1 volume 20% EtOH, transfer into a plastic bottle and store at 4°C.

Glutathione-Sepharose affinity chromatography

Materials

- Glutathione(GSH)-Sepharose resin (Glutathione agarose, GE Healthcare);
- column (1.7xh 14 cm, BioRad);

Solutions

- H_2O;
- equilibration buffer (Lysis Buffer): 50 mM Hepes/KOH, pH 7.5, 150 mM KCl;
- Regeneration Buffer: 6 M guanidine hydrochloride solution in water;
- PBS: 10 mM Na_2HPO_4, 1.8 mM KH_2PO_4, 140 mM NaCl, pH 7.3, 2.7 mM KCl;
- 20% EtOH: 20% ethanol (v/v).

Procedure

To equilibrate the resin:

- transfer the resin (50% suspension in 20%EtOH) into the column;
- flow 5 volumes H_2O;
- flow 5 volumes equilibration buffer;
- resuspend the resin in 1 volume of equilibration buffer;
- transfer in a falcon tube and store at 4°C.

To regenerate the resin, flow:

- 3 volumes regeneration buffer;
- 3 volumes PBS;
- 3 volumes H_2O_2;
- flow 3 volumes of EtOH 20%;

Resuspend the resin in 1 volume of 20% EtOH, transfer in a plastic bottle and store at 4°C.

References

Aliverti, A., Curti, B. and Vanoni, M.A. Identifying and quantitating FAD and FMN in simple and complex flavoprotein. *Methods Mol Biol Biochem*., 1999, 131, 9-23.

Ashida, S., Furihata, M., Katagiri, T., Tamura, K., Anazawa, Y., Yoshioka, H., Miki, T., Fujioka, T., Shuin, T., Nakamura, Y., Nakagawa, H. Expression of novel molecules, MICAL2-PV (MICAL2 prostate cancer variants), increases with high Gleason score and prostate cancer progression. *Clin Cancer Res*. 2006, 12, 2767-2773.

Aguda, A.H., Burtnick, L.D. and Robinson, R.C. The state of the filament. *EMBO Rep*. 2005, 6, 220-6.

Ausubel, F.M., Brent, R., Kingston, R.E., Moore, D.D., Seidman, J.G., Smith, J.A., Sthrul, K. Current Protocols in Molecular Biology . John Wiley & Sons. Inc. Hoboken NJ. (2005).

Bach, I. The LIM domain: Regulation by association. Mech. Dev. 2000, 91, 5–17.

Ballou, D.P., Entsch, B., Cole, L.J. Dynamics involved in catalysis by single-component and two-component flavin-dependent aromatic hydroxylases. *Biochem Biophys Res Commun*. 2005, 338, 590-598.

Bamburg JR. Proteins of the ADF/cofilin family: essential regulators of actin dynamics. *Annu Rev Cell Dev Biol*. 1999, 15, 185-230.

Bamburg, J.R. and Bernstein, B.W. Roles of ADF/cofilin in actin polymerization and beyond. *Biol Rep*. 2010, 2, 62. Barile, M., Giancaspero, T.A., Brizio, C., Panebianco, C., Indiveri, C., Galluccio, M., Vergani, L., Eberini, I. and Gianazza, E. Biosynthesis of flavin cofactors in man: implications in health and disease. Curr Pharm Des. 2013,19, 2649-2675.

Beuchle, D., Schwarz, H., Langegger, M., Koch, I., Aberle, H. Drosophila MICAL regulates myofilament organization and synaptic structure. *Mech Dev*. 2007, 124, 390-406.

Bevington, P. R. (1969) *Data Reduction and Error Analysis for the Physical Sciences*, McGraw-Hill, New York.

Borisy, G.G. and Svitkina, T.M. Actin machinery: pushing the envelope. *Curr Opin Cell Biol*. 2000, 12, 104-12.

Bradford, M.M. A rapid and sensitive method for the quantitation of microgram quantities of protein utilizing the principle of protein-dye binding. *Anal Biochem*. 1976, 72, 248-254.

Bräutigam, L., Schütte, L.D., Godoy, J.R., Prozorovski, T., Gellert, M,, Hauptmann, G., Holmgren, A., Lillig, C.H. and Berndt, C. Vertebrate-specific glutaredoxin is essential for brain development. *Proc Natl Acad Sci*. 2011, 108, 20532-205037.

Brender, J.R., Dertouzos, J, Ballou, D.P, Massey, V, Palfey, B, Entsch, B, Steel, D.G, Gafni, A. Conformational dynamics of the isoalloxazine in substrate-free p-hydroxybenzoate hydroxylase: single-molecule studies. *J Am Chem Soc (JACS)* 2005, 127, 18171-18178.

Carlier, M.F., Ressad, F. and Pantaloni, D. Control of actin dynamics in cell motility. Role of ADF/cofilin. *J Biol Chem*. 1999, 274, 33827-33030.

Castanié, M.P, Bergès, H., Oreglia, J., Prère, M.F. and Fayet, O. A set of pBR322-compatible plasmids allowing the testing of chaperone-assisted folding of proteins overexpressed in *Escherichia coli*. *Anal Biochem*. 1997, 254, 150-152.

Cornils, H,, Stegert, M.R., Hergovich, A., Hynx, D., Schmitz, D., Dirnhofer, S. and Hemmings, B.A. Ablation of the kinase NDR1 predisposes mice to the development of T cell lymphoma. *Sci. Signal*. 3:ra47.

Deo, R.C., Schmidt, E.F., Elhabazi, A., Togashi, H., Burley, S.K. and Strittmatter, S.M. Structural bases for CRMP function in plexin-dependent semaphorin3A signaling. *EMBO J*. 2004, 23, 209-222.

Dominguez, R. & Holmes, K. C. Actin structure and function. *Annual review of biophysics.* 2011, 40, 169-86.

Eggink, G., Engel, H., Vriend, G., Terpstra, P., Witholt, B. Rubredoxin reductase of Pseudomonas oleovorans. Structural relationship to other flavoprotein oxidoreductases based on one NAD and two FAD fingerprints. *J. Mol. Biol.* 1990, *212*, 135–142.

Ellis, K.J. and Morrison, J.F. Buffers of constant ionic strength for studying pH-dependent processes. *Methods Enzymol 1982*, 87, 405-426.

Entsch, B., Cole, L. J. and Ballou, D. P.Protein dynamics and electrostatics in the function of p-hydroxybenzoate hydroxylase, *Archives of biochemistry and biophysics.* 2005, 433, 297-311.

Eser, B and Fritzpatrick, P.F. Measurement of intrinsic rate constants in the tyrosine hydroxylase reaction. *Biochemistry* 2010, 49, 645–652.

Fischer, J, Weide, T, Barnekow, A. The MICAL proteins and rab1: a possible link to the cytoskeleton? *Biochem Biophys Res Comm*. 2004, 328, 415–423.

Galkin, V.E., Orlova, A., Salmazo, A., Djinovic-Carugo, K. and Egelman, E.H. Opening of tandem calponin homology domains regulates their affinity for F-actin. *Nature and Structural Biology*. 2012, 17, 614-616.

Galkin, V. E., Orlova, A., Vos, M. R., Schroder, G. F. & Egelman, E. H. Near-atomic resolution for one state of f-actin, *Structure.*2015, 23, 173-82.

Gasteiger E., Hoogland C., Gattiker A., Duvaud S., Wilkins M.R., Appel R.D. & Bairoch A. (2005) Protein Identification and Analysis Tools on the ExPASy Server in *The Proteomics Protocols Handbook* (Walker, J. M., ed) pp. 571-607 Humana Press.

Gellert, M., Venz, S., Mitlöhner, J., Cott, C., Hanschmann, E.M. and Lillig, C.H. Identification of a dithiol-disulfide switch in collapsin response mediator protein 2 (CRMP2) that is toggled in a model of neuronal differentiation. *J Biol Chem*. 2013, 288, 35117-35125.

Gellert, M., Hanschmann, E.M., Lepka, K., Berndt, C. and Lillig, C.H. Gellert M, Hanschmann EM, Lepka K, Berndt C, Lillig CH. Redox regulation of cytoskeletal dynamics during differentiation and de-differentiation. *Biochim Biophys Acta*. 2015, 8, 1575-1587.

Gimona, M., Djinovic-Carugo, K., Kranewitter, W.J., Winder, S.T. Functional plasticity of CH domains. *FEBS J* 2002, 513, 98-106.

Giridharan, S.S., Rohn, J.L., Naslavsky, N., Caplan, S. Differential regulation of actin microfilaments by human MICAL proteins. *J. Cell Sci.* 2012, *125*, 614–624.

Grigoriev, I., Yu, K.L., Martinez-Sanchez, E., Serra-Marques, A., Smal, I., Meijering, E., Demmers, J., Peranen, J., Pasterkamp, R.J., van der Sluijs, P., Hoogenraad, C.C., Akhmanova, A. Rab6, Rab8, and MICAL3 cooperate in controlling docking and fusion of exocytotic carriers. *Curr. Biol.* 2011, *21*, 967–974.

Goujon, M., McWilliam, H., Li, W., Valentin, F., Squizzato, S., Paern, J., Lopez, R. A new bioinformatics analysis tools framework at EMBL-EBI. *Nucleic Acids Res.* 2010, *38*, W695–W699.

Goshima, Y.,,Nakamura, F,, Strittmatter, P. and Strittmatter, S.M. Collapsin-induced growth cone collapse mediated by an intracellular protein related to UNC-33. *Nature*. 1995**,** 376, 509-514.

Gu, Y., Hamajima, N. and Ihara, Y. Neurofibrillary tangle-associated collapsin response mediator protein-2 (CRMP-2) is highly phosphorylated on Thr-509, Ser-518, and Ser-522. *Biochemistry*. 2000, 39, 4267-4275.

Homsher, R. and Bennie Z. Spectrophotometric investigation of sensitive complexing agents for the determination of zinc in serum. *Clin. Chem*. 1985, 31, 1310-1313.

Huijbers, M.M, Montersino, S. Westphal, A.H., Tischler, D. and van Berkel WJ. Flavin dependent monooxygenases. *Arch Biochem Biophys*. 2014, 544, 2-17.

Hung, R.J., Terman, J.R. Extracellular inhibitors, repellents, and semaphorin/plexin/ MICAL-mediated actin filament disassembly. *Cytoskeleton* 2011, *68*, 415–433.

Hung, R.J., Yazdani, U., Yoon, J., Wu, H., Yang, T., Gupta, N., Huang, Z., van Berkel, W.J., and Terman, J.R. Mical links semaphorins to F-actin disassembly. Nature 2010, 463, 823-827.

Hung, R.J, Pak, C.W, Terman, J.R. Direct Redox Regulation of F-Actin Assembly and Disassembly by Mical. Science express.

Joosten, V, van Berkel, W. Flavoenzyme. *Curr Op Chem Biol*. 2007, 211, 195–202.

Ishida, H., Borman, M.A., Ostrander, J., Vogel, H.J., MacDonald, A.J. Solution structure of calponin homology domain (CH) from Smoothelin-like protein. *J Biol Chem*. 2008, 283, 20569-20578.

Jin, X., Zhang, J., Dai, H., Sun, H., Wang, D., Wu, J., Shi, Y. Investigation of the four cooperative unfolding units existing in the MICAL-1 CH domain. *Biophys. Chem.* 2007, *129*, 269–278.

Kaneko, S., Iwanami, A., Nakamura, M., Kishino, A., Kikuchi, K., Shibata, S., Okano, H.J., Ikegami, T., Moriya, A., Konishi, O., *et al*. A selective Sema3A inhibitor enhances regenerative responses and functional recovery of the injured spinal cord. *Nat. Med.* 2006, *12*, 1380–1389.

Kadrmas, J.L, Beckerle, M.C. The LIM domain: from the cytoskeleton to the nucleus. *Nature* 2004, 5, 920-931.

Khazaei, M.R., Girouard, M.P., Alchini, R., Ong Tone, S., Shimada, T., Bechstedt, S., Cowan, M., Guillet, D., Wiseman, P.W., Brouhard, G., Cloutier, J.F. and Fournier, A. E. Collapsin response mediator protein 4 regulates growth cone dynamics through the actin and microtubule cytoskeleton. *J Biol Chem*. 2014, 289, 30133-30143.

Kikuchi, K., Kishino, A., Konishi, O., Kumagai, K., Hosotani, N., Saji, I., Nakayama, C., Kimura, T. *In vitro* and *in vivo* characterization of a novel semaphorin 3A inhibitor, SM-216289 or xanthofulvin. *J. Biol. Chem.* 2003, *278*, 42985–42991.

Kirilly, D., Gu, Y., Huang, Y., Wu, Z., Bashirullah, A., Low, B. C., Kolodkin, A. L., Wang, H. & Yu, F. A genetic pathway composed of Sox14 and Mical governs severing of dendrites during pruning, *Nature neuroscience. 2009*, 12, 1497-505.

Klaidman, L. K., Leung, A. C. and Adams, J. D., Jr. High-performance liquid chromatography analysis of oxidized and reduced pyridine dinucleotides in specific brain regions, *Anal Biochem.* 1995, 228, 312-317.

Koestler, S. A., Rottner, K., Lai, F., Block, J., Vinzenz, M. & Small, J. V. F- and G-actin concentrations in lamellipodia of moving cells, *PloS one.* 2009, 4, e4810

Lee, B.C., Péterfi, Z., Hoffmann, F.W., Moore R.E., Kaya, A., Avanesov, A., Tarrago, L., Zhou, Y., Weerapana, E., Fomenko, D.E., Hoffmann, P.R. and Gladyshev, V.N. MsrB1 and MICALs regulate actin assembly and macrophage function via reversible stereoselective methionine oxidation. *Mol Cell*. 2013 51, 397-404.

Lin, Y.L. and Hsueh, Y.P. Neurofibromin interacts with CRMP-2 and CRMP-4 in rat brain. *Biochem Biophys Res Commun*. 2008, 369, 747-752.

Loria, R., Bon, G., Perotti, V., Gallo, E., Bersani, I., Baldassari, P., Porru, M., Leonetti, C., Di Carlo, S., Visca, P., Brizzi, M. F., Anichini, A., Mortarini, R. & Falcioni, R. Sema6A and Mical1 control cell growth and survival of BRAFV600E human melanoma cells, *Oncotarget.* 2015, 6, 2779-93.

Lundquist, M. R., Storaska, A. J., Liu, T. C., Larsen, S. D., Evans, T., Neubig, R. R. & Jaffrey, S. R Redox modification of nuclear actin by MICAL-2 regulates SRF signaling, *Cell.* 2014, 156, 563-76

Maniatis, T., Frisch, E.F., Sambrook, J. Molecular Cloning, a laboratory manual. Ed. (1988). Cold Spring Harbor Laboratory Press, Cold Spring Harbor, NY, USA.

Massey, V. The chemical and biological versatility of riboflavin. *Biochem Soc Trans*. 2000, 28, 283-296.

Majava1, V, Loytynoja1, N, Chen, W.Q, Lubec, G and Kursula, P. Crystal and solution structure, stability and post-translational modifications of collapsing response mediator protein 2. *FEBS j*. 2008, 275, 4583-4596.

Matthwes, J.M and Potts, J.R. The tandem β-zipper: modular binding of tandem domains and linear. *FEBS Letters*. 2013, 587, 1164-1171.

Matsudaira, P. Sequence from picomole quantities of proteins electroblotted onto polyvinylidene difluoride membranes, *J Biol Chem.* 262, 1987, 10035-10038.

McDonald, C.A, Liu, Y.Y and Palfey, B.A. Actin stimulates reduction of the MICAL-2 monooxygenase domain. Biochemistry *2013*, 52, 1437-1445.

McKay, G. A. & Wright, G. D. Catalytic mechanism of enterococcal kanamycin kinase (APH(3')-IIIa): viscosity, thio, and solvent isotope effects support a Theorell-Chance mechanism, *Biochemistry*, 1996. 35, 8680-5

McNicholas, S., Potterton, E., Wilson, K. S. & Noble, M. E. Presenting your structures: the CCP4mg molecular-graphics software, *Acta crystallographica Section D, Biological crystallography.* 2011, 67, 386-394.

Miura, R. Versatility and specificity in flavoenzymes: control mechanisms of flavin reactivity. *The Chemical Record*, Vol. 1, 183–194 (2001).

Morinaka, A., Yamada, M., Itofusa, R., Funato, Y., Yoshimura, Y., Nakamura, F., Yoshimura, T., Kaibuchi, K., Goshima, Y., Hoshino, M., Kamiguchi, H. & Miki, H. Thioredoxin mediates oxidation-dependent phosphorylation of CRMP2 and growth cone collapse, *Science signaling.* 2011, 4, ra26

Nadella, M., Bianchet, M.A., Gabelli, S.B., Barrila, J., and Amzel, L.M. Structure and activity of the axon guidance protein MICAL. *PNAS*. 2005, 102, 16830-16835.

Norby, J.G., Esmann, J. The effect of ionic strength and specific anions on substrate binding and hydrolytic activities of Na,K-ATPase. *J.Gen. Physiol*. 1997, 109, 555-570.

Ortiz-Maldonado, M., Entsch, B. And Ballou, D.P. Conformational changes combined with charge-transfer interactions are essential for reduction in catalysis by p-hydroxybenzoate hydroxylase. *Biochemistry*. 2003, 42, 11234-11242.

Palfey, B.A., Moran, G.R., Entsch, B., Ballou, D.P. and Massey, V. Substrate recognition by "password" in p-hydroxybenzoate hydroxylase. *Biochemistry*. 1999, 38, 1153-1158.

Palfey, B. A. & McDonald, C. A. Control of catalysis in flavin-dependent monooxygenases, *Archives of biochemistry and biophysics.* 2010, 493, 26-36

Pasterkamp, R.J., Kolodkin, A.L. Semaphorin junction: Making tracks toward neural connectivity. *Curr. Opin. Neurobiol.* 2003, *13*, 79–89.

Pasterkamp, R.J., Verhaagen, J. Semaphorins in axon regeneration: Developmental guidance molecules gone wrong? *Philos. Trans. R. Soc. Lond. Series B Biol. Sci.* 2006, *361*, 1499–1511.

Ponnusamy, R. and Lohkamp, B. Insights into the oligomerization of CRMPs: crystal structure of human collapsin response mediator protein 5. *J Neurochem*. 2013, 125, 855-868.

Puius, Y.A., Mahoney, N.M. and Almo, S.C. The modular structure of actin-regulatory proteins. *Curr Opin Cell Biol*. 1998, 10, 23-34.

Rahajeng, J., Panapakkam Giridharan, S.S., Cai, B., Naslavsky, N., Caplan, S. Important relationships between Rab and MICAL proteins in endocytic trafficking. *World Journal of Biological Chemistry* 2010, 26, 254-264.

Sampson, N. S. & Knowles, J. R. Segmental motion in catalysis: investigation of a hydrogen bond critical for loop closure in the reaction of triosephosphate isomerase, *Biochemistry*, 1992. 31, 8488-94.

Sancar, A. Structure and function of photolyase and in vivo enzymology: 50th anniversary. *J Biol Chem*. 2008, 283, 32153-32157.

Schmidt, E.F. and Strittmatter, S.M. The CRMP family of proteins and their role in Sema3A signaling. *Adv Exp Med Biol*. 2007, 600, 1-11.

Schmidt, E.F., Shim, S.O., Strittmatter, S.M. Release of MICAL autoinhibition by semaphorin-plexin signaling promotes interaction with collapsin response mediator protein. Neurosci. 2008, 28, 2287-2297.

Schmidt, E.R., Pasterkamp, R.J., van den Berg, L.H. Axon guidance proteins: Novel therapeutic targets for ALS? *Prog. Neurobiol.* 2009, *88*, 286–301.

Schreuder, H.A., Prick, P.A., Wierenga, R.K., Vriend, G., Wilson, K.S., Hol, W.G., Drenth, J. Crystal structure of the p-hydroxybenzoate hydroxylase-substrate complex refined at 1.9 A resolution. Analysis of the enzyme-substrate and enzyme-product complexes. *J. Mol. Biol.* 1989, *208*, 679–696.

Sharma, M., Giridharan, S.S., Rahajeng, J., Caplan, S., Naslavsky, N. MICAL-L1: An unusual Rab effector that links EHD1 to tubular recycling endosomes. *Commun. Integr. Biol.* 2010, *3*,181–183.

Siebold, C., Berrow, N., Walter, T., Harlos, K., Ray, J.O., Stuart, D., Terman, J., Kolodkin, A.L., Pasterkamp, R.J., and Jones, E.Y. High-resolution structure of the catalytic region of MICAL (molecule interacting with CasL), a multidomain flavoenzyme-signaling molecule. *PNAS*. 2005, 102, 16836-16841.

Simopoulos, T.T and Jencks, W.P. Alkaline phosphatise is an almost perfect enzyme. *Biochemistry*. 1994, 33, 10375-10380.

Sitnitsky, A.E. Solvent viscosity dependence for enzymatic reactions. *Physica A*, 2008, 387, 5483–5497.

Slater, T. F. Oxidized and reduced nicotinamide-adenine dinucleotide phosphate in tissue suspensions of rat liver, *Biochem J.* 1967, 104, 833-842.

Stenmark, P., Ogg,D., Flodin, S., Flores,A., Kotenyova, T., Nyman, T., Nordlund, P and Kursula, P. The structure of human collapsin response mediator protein 2, a regulator of axonal growth. *J Neurochem*. 2007, 101, 906-917.

Studier, F.W., Moffatt, B.A. Use of bacteriophage T7 RNA polymerase to direct selective high-level expression of cloned genes. *J Mol Biol*. 1986 189, 113-130.

Sun, H., Dai, H., Zhang, J., Jin, X., Xiong, S., Xu, J., Wu, J. and Shi, Y. Solution structure of calponin homology domain of Human MICAL-1. *J Biomolecular NMR* 2006, 36, 295-300.

Suzuki, T., Nakamoto, T., Ogawa, S., Seo, S., Matsumura, T., Tachibana, K., Morimoto, C., and Hirai, H. (2002) MICAL, a novel CasL interacting molecule, associates with vimentin. *J Biol Chem.* 2002, 277, 14933-14941.

Tamagnone, L., Comoglio, P.M. To move or not to move? Semaphorin signalling in cell migration. *EMBO Rep*. 2004, *5*, 356–361.

Terman, J.R., Mao, T., Pasterkamp, R.J., Yu, H.H., and Kolodkin, A.L. MICALs, a family of conserved flavoprotein oxidoreductases, function in plexin-mediated axonal repulsion. *Cell*. 2002, 109, 887-900.

Van Berkel, W., Kamerbeekb, N.M., Fraaije, M.W. Flavoprotein monooxygenases, a diverse class of oxidative biocatalysts. Journal of biotechnology *2006*, 124, 670–689.

Vanoni, M.A., Vitali, T., Zucchini, D. (2013) MICAL, the flavoenzyme participating in cytoskeleton dynamics. *Int J Mol Sci* 2013, 14, 6920-6959.

Voet, D. and Voet, J. (2012) *Biochemistry*, 4th edn, Wiley, New York.

Venci, D., Zhao, G. and Jorns, M.S. Molecular characterization of NikD, a new flavoenzyme important in the biosynthesis of nikkomycin antibiotics. *Biochemistry*. 2002, 41, 15795-15802.

Voet, D. & Voet, J. (2012) *Biochemistry*, 4th edn, Wiley, New York

Wang, J., Ortiz-Maldonado, M., Entsch, B., Massey, V., Ballou, D., Gatti, D.L. Protein and ligand dynamics in 4 hydroxybenzoate hydroxylase. *Proc. Natl. Acad. Sci. USA* 2002, *99*, 608–613

Wang, L.H. and Strittmatter, S.M. Brain CRMP forms heterotetramers similar to liver dihydropyrimidinase. *J Neurochem*. 1997, 69, 2261-2269.

Weide, T., Teuber, J., Bayer, M., Barnekow, A. MICAL-1 isoforms, novel rab1 interacting proteins. *Biochem. Biophys. Res. Commun.* 2003, *306*, 79–86.

Wierenga, R.K., Terpstra, P., Hol, W.G. Prediction of the occurrence of the ADP-binding beta alpha beta-fold in proteins, using an amino acid sequence fingerprint. *J. Mol. Biol.* 1986, *187*, 101–107.

Wise, D. D. and Shear, J. B. Circadian tracking of nicotinamide cofactor levels in an immortalized suprachiasmatic nucleus cell line, *Neuroscience.* 2004, 128, 263-268.

Xue, Y., Kuok, C., Xiao, A., Zhu, Z., Lin, S., Zhang, B. Identification and expression analysis of mical family genes in zebrafish. *J. Genet. Genomics* 2010, *37*, 685–693.

Yamamura, R., Nishimura, N., Nakatsuji, H., Arase, S., Sasaki, T. The interaction of JRAB/MICAL-L2 with Rab8 and Rab13 coordinates the assembly of tight junctions and adherens junctions. *Mol. Biol. Cell* 2008, *19*, 971–983.

Ying, W. NAD+/NADH and NADP+/NADPH in cellular functions and cell death: regulation and biological consequences, *Antioxid Redox Signal.* 2008, 10, 179-206.

Zhang, Z., Majava, V., Greffier, A., Hayes, R.L., Kursula, P. and Wang, K.K. Collapsin response mediator protein-2 is a calmodulin-binding protein. *Cell Mol Life Sci*. 2009, 66, 526-536.

Zhou, Y., Gunput, R.A., Adolfs, Y., Pasterkamp, R.J. MICALs in control of the cytoskeleton, exocytosis, and cell death. *Cell. Mol. Life Sci.* 2011, *68*, 4033–4044.

Zhou, Y., Adolf, Y., Pim Pijnappel, W.W.M., Fuller, S.J., Van der Schor, C.R., Li, W.K, Sugden, P.H., Smit, A,B., Hergovich, A., Pasterkamp, R.J. MICAL-1 is a Negative Regulator of MST-NDR Kinase Signaling and Apoptosis. *Mol Cell Biol*. 2011, 1389-1410.

Zucchini, D., Caprini, G., Pasterkamp, J., Tedeschi, G. e Vanoni, M.A. Kinetic and spectroscopic characterization of the putative monooxygenase domain of human MICAL-1. *Arch Biochem Biophys*. 2011, 515, 1-13.